8-4-2001

Characterization of Cu-Co-Cr-K Catalysts

Phuong Thanh Doan

CHARACTERIZATION OF Cu-Co-Cr-K CATALYSTS

By

Phuong Thanh Doan

A Thesis
Submitted to the Faculty of
Mississippi State University
in Partial Fulfillment of the Requirements
for the Degree of Master of Science
in Chemical Engineering
in the Dave C. Swalm School of Chemical Engineering

Mississippi State, Mississippi

August 2001

CHARACTERIZATION OF Cu-Co-Cr-K CATALYSTS

By

Phuong Thanh Doan

Approved:

_____
Hossein Toghiani
Associate Professor of Chemical Engineering
(Director of Thesis and Major Professor)

_____
Donald O. Hill
Professor of Chemical Engineering
(Committee Member)

_____
Rebecca K. Toghiani
Associate Professor of Chemical Engineering
(Graduate Coordinator of the Dave C. Swalm
School of Chemical Engineering
and Committee Member)

_____
Wayne A. Bennett
Dean of the College of Engineering

Name: Phuong Thanh Doan

Date of Degree: August 4, 2001

Institution: Mississippi State University

Major Field: Chemical Engineering

Major Professor: Dr. Hossein Toghiani

Title of Study: CHARACTERIZATION OF Cu-Co-Cr-K CATALYSTS

Pages in Study: 199

Candidate for Degree of Master of Science

The production of higher alcohols from synthesis gas over Cu-Co-Cr-K catalysts has been studied. The production rate of alcohol was measured in the flow reactor, operating at 250 to 350°C, 3500 to 8000 gas hourly space velocity, and 900 to 1800 psig. The productivity as a function of temperature, pressure, gas hourly space velocity, carbon dioxide content of the feed, and reaction time was also examined.

Physisorption data have been analyzed using the Langmuir model, the Brunauer-Emmett-Teller (BET) method, the Barret-Joyner-Halenda (BJH) method, and the de Boer and Halsey t-method. The surface areas of catalysts CB1(1), CB1(3), and CB1(1) after reaction were $39.9 \pm .9$ m^2/g, 28.9 ± 1.7 m^2/g, and 26.5 ± 0.3 m^2/g, respectively. Moreover, information such as pore size distribution, pore shape, monolayer volume, micropore volume and thickness of adsorption layer were also obtained. The atomic concentration and oxidation states of near surface species were established by X-ray Photoelectron Spectroscopy.

DEDICATION

To my beloved family - Ba, Mom, Thao, Tung, Jimmy,
and especially my Phong Lê.

ACKNOWLEDGEMENTS

TABLE OF CONTENTS

LIST OF TABLES

LIST OF FIGURES

xiii

CHAPTER I

INTRODUCTION

1.1.   Background

Since the early twentieth century, there have been growing concerns about the large amount of fuel consumption in the world, especially in the United States. Automobiles are number one on the list in fuel consumption. They also produce the most pollution and do the most harm to the environment. There are local and global consequences to this problem. Locally, smog, or fog that has become mixed and polluted with smoke, is very common in metropolitan areas. Globally, the phenomena of the greenhouse effect, or the absorption of solar radiation by the earth, preventing its dissipation into space. This has resulted in a gradual rise in the temperature of the atmosphere. As a result, alternative fuels have been developed as a solution to this widespread problem. However, alternative fuels from agricultural materials are often expensive due to the limitations of suitable land and processing costs (1). Oxygenates such as higher alcohols are promising as fuel additives, and can be produced from any carbon source, from methane to manure (2). The most conventional way of converting synthesis gas to higher alcohols is catalytic conversion in which the feed gas is syngas (mixture of carbon monoxide and hydrogen). Oxygenates have long been of practical

interest because of their direct use in fuel blends and as commercially important chemical intermediates (3).

The advantages of oxygenate use in fuel blends include improvement of volatility, drivability, hydrocarbon solubility, and water tolerance. Addition of higher alcohols can especially boost the octane number, eliminating the need for lead containing antiknock agents. This results in improved in combustion and reduction in carbon monoxide emissions. Other potential applications of higher alcohols include fuel for power generation, production of ethylene from methanol, and production of propylene from propanol (4, 5, and 6). Today, the utilization of higher alcohols as oxygenates in gasoline is commercially viable. These oxygenates can also be used directly as a transportation fuel, but require extensive modification of engines, fuel delivery systems, and storage and distribution systems. Oxygenates can be produced from any carbonaceous source, and can be economically produced from abundant coal reserves. Thus, a reduction in the dependence on imported oil and stabilization in petroleum prices are outcomes.

Various catalyst systems for oxygenates have been developed and investigated over the past 90 years. Generally, there are three main types of synthesis: modified methanol synthesis using a Cu/ZnO catalyst, modified methanation with MoS_2, and modified Fischer-Tropsh with either Fe or Co to produce higher alcohols. These modifications often involve the use of an alkali or group VIII metal (3). The future of oxygenate production from synthesis gas is dependent on the catalyst preparation, with high selectivity and durable lifetime as important features. The objective of this research

is to study Cu-Co-Cr-K catalysts through physisorption, surface characterization, and higher alcohol synthesis experiments. With the use of physisorption, information such as surface area, pore size distribution, monolayer volume, and average thickness of catalytic adsorption layer are investigated to determine the effect of catalyst preparation techniques. The atomic concentration as well as oxidation states of surface species are established by x-ray photoelectron spectroscopy (XPS). In addition, the effect of pressure, temperature, gas hourly space velocity, carbon dioxide, and carbon monoxide / hydrogen ratio on production rate of higher alcohols will be studied. Scanning electron microscopy (SEM) is used to determine the homogeneity of the catalyst and its deactivation behavior. The catalyst reducibility is also studied by temperature programmed reduction.

1.2.   References

1.   Glaviano, T., Bemis, G., Nix D., "California Energy Commission", (1999).

2.   Sheldon, R., <u>Chemicals from Synthesis Gas: Catalytic Reactions of CO and H$_2$</u>, (Reidel Publishing, Dordrecht, Holland: 1983).

3.   Herman, R., <u>Studies in Surface and Catalyst</u>, (Chapter 7, Elsevier, Amsterdam: 1990).

4.   Xiaoding, X., Doesburg, E., Scholten J., *Catalysis Today,* 2, 125, (1987).

5.   Zhou, P., "Summary of the Higher Alcohols Synthesis Workshop", US Department of Energy, Pittsburgh Energy Technology Center, (1994).

6.   Greene, M., *AIChE Journal*, 82, 46, (1982).

CHAPTER II

LITERATURE REVIEW

2.1.   Synthesis Gas Applications

Synthesis gas utilization for production of many chemicals is common due to its low cost. Synthesis gas offers two main routes, direct versus indirect, toward chemical production. Direct conversion of synthesis gas produces compounds containing paraffins, olefins, and oxygenates. The best-known conversion method is Fischer-Tropsch synthesis, which yields mixtures of linear alkanes and/or alkenes. Indirect synthesis gas conversion uses methanol, methyl formate, or formaldehyde as intermediates. For instance, methanol or methyl acetate reacts with carbon monoxide to form acetic acid and acetic anhydride, respectively (1).

2.2.   Synthesis Gas Generation

Synthesis gas conversions are based on three methods. First, the steam reforming process is carried out in a reactor similar to a process furnace, with commercial nickel-based catalyst filled tubes, which converts methane or higher hydrocarbons to carbon monoxide and hydrogen. The typical operating pressure is 350 psi, and a temperature of approphimately 800°C is necessary for the endothermic reaction. The governing equation for the reforming process is (2, 62):

$$CH_4 + H_2O + heat \rightarrow CO + 3\ H_2 \qquad\qquad 2.1$$

The second method for synthesis gas production is the partial oxidation of hydrocarbons. This process can utilize any hydrocarbon feed stock, but heavy fuel oil is generally used.

$$C_nH_{2n} + \tfrac{1}{2}\ n\ O_2 \rightarrow n\ CO + n\ H_2 \qquad\qquad 2.2$$
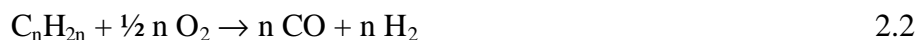
Coal gasification is the third synthesis gas conversion process and is the combination process of steam reforming and partial oxidation. One of the governing reactions, Equation 2.3, is extremely endothermic while the other, Equation 2.4, is strongly exothermic (2,3).

$$C(s) + H_2O \rightarrow CO + H_2 \qquad\qquad 2.3$$

$$C(s) + \tfrac{1}{2}\ O_2 \rightarrow CO \qquad\qquad 2.4$$

Each of these processes produces different molar ratios of carbon monoxide to hydrogen. However, this synthesis gas ratio is very important for catalytic reaction toward oxygenates, and can be altered via the water gas shift reaction (2).

$$CO + H_2O \Leftrightarrow CO_2 + H_2 \qquad\qquad 2.5$$

2.3. Higher Alcohol Synthesis Historical Review

Higher alcohol synthesis development from hydrogen and carbon monoxide was first discovered in the early twentieth century. However, the selectivity of the catalyst was quite low with many byproducts. In 1913, a patent was issued to BASF that described the production of alcohols, aldehydes, ketones, and acids using synthesis gas with alkalized oxide of cobalt or osmium catalyst at 10 to 20 MPa and 300 to 400°C. In 1923, Fischer and Tropsch developed a synthol process by using alkalized iron catalyst to

convert synthesis gas to alcohols at 10 MPa and 400 to 450°C. Although, the Fischer and

Tropsch iron catalyst was discovered in 1923, the production of alcohols did not appear

feasible until 1940 (38). Between 1935 and 1945, plants in Europe used ZnO/Cr_2O_3

doped with alkali salts to produce methanol and higher alcohols after BASF discovered

that ZnO/Cr_2O_3 alone produced a high yield of methanol. However, the severely high

pressure and short catalyst life were a drawback. In 1940, another synthol process was

developed with the conditions optimized toward linear higher alcohol production by

Farbenindustrie and Ruhrchemie in Germany (4). However, under low pressure, the

synthesis becomes hydrocarbon synthesis. After 1945, with the abundance of petroleum

and pure alcohol demands, higher alcohol synthesis from syngas became economically

unattractive. Thus, many plants were demolished. In 1950, with the increasing demand

for pure alcohol, high pressure methanol synthesis with zinc chromite (Zn/Cr_2O_3) catalyst

was developed. In the late 1960's, methanol synthesis continued to grow. A process

using synthesis gas derived from natural gas utilized low temperature, 250°C, low

pressure, 5 to 10 MPa, and $Cu/ZnO/Al_2O_3$ and $Cu/ZnO/Cr_2O_3$ catalysts (4, 5, 6).

In the early 1970's, under a great energy shock initiated by the Arab oil embargo,

the interest in higher alcohol synthesis and usage was renewed. There also was an

"extensive world-wide research effort" on synthesis gas as an alternative to crude oil. In

the early 1980's, with declining oil prices, higher alcohol synthesis research again

declined. Currently, higher alcohol synthesis is of interest due to the increasing

petroleum prices, environmental concerns, and gasoline additive octane demands (5).

2.4.   IFP Patent Catalyst

2.4.1.   IFP Patent Review

Institut Francais du Petrole (IFP) patents date back to 1974. The IFP Catalysts, comprised of an active phase consisting of mixed oxides of copper and a trivalent metal of aluminum, chromium, manganese, iron and cobalt, were studied for carbon monoxide conversion (8, 9). In 1978, a patent describing $Cu_1Co_1Cr_{0.8}K_{0.09}$ catalyst was published. The patent claimed that K could be replaced with Li or Na, and Cr, sometimes in combination with Zn, could be replaced by Fe, V, and Mn. The preparation was either via aqueous solution of Cu, Co and Cr salts, with an organic acid (citric acid for example), or via coprecipitation from an aqueous solution with metal salts (10, 11).

In 1981, another patent was issued in which the previous catalyst was modified with a rare earth metal and noble metals in the concentration range of 0.005 to 0.5 weight percentage. This catalyst contained copper, cobalt, a third metal M (Cr, Fe, Vn, Mn), a rare earth metal (La, Ce, Pr), and a fifth metal, A, which was either an alkali or alkali earth metal (Li, Na, K, Ca, or Ba). Following are the weight percentage range of these metals: Cu, from 20 to 60 percent; Co, from 5 to 50 percent; M, from 5 to 30 percent; N, from 5 to 40 percent; and A, from 0.1 to 5 percent. Some of these catalysts were prepared with about 0.5 to 15 % by weight of zinc (12, 13). In 1982, a similar patent was issued with two reactors in series. The products of the first reactor were fed to the second reactor to maximize both methanol and higher alcohol production (14). The same catalyst was modified again in 1983 by replacing Cr with Re, Al, and Zn, and adding Sc, Yb, Zr, Th to about a 0.02 to 0.8 percent by weight of rare earth metal (15).

Another catalyst was described in 1987 and was comprised of Cu, Co, Zn(B), Al(C), alkali or alkaline earth metal. The range of concentrations were 10 to 65 percent copper, 5 to 50 percent cobalt, 5 to 40 percent aluminum, and 1 to 50 percent zinc. Also, the ratio of alkali or alkaline earth metal to aluminum was 0 to 0.2 percent with the following ratios: Zn/Al = 0.4 – 2, Co/Al = 0.2 – 0.75, Cu / Al = 0.2 – 3. Zn could be partially or totally replaced by B (Cd or Mn^{2+}), and Al could be substituted by C (Cr, Mn^{3+}, or Ti) (16).

For all of the IFP catalysts, preparation of a homogeneous composition and avoidance of elemental segregation plays an active role in catalyst activity. The homogeneity of Co/Al within a 5 nm scale was reported in the 1983 patent by using STEM (scanning transmission electron microscopy) and ESCA (electron spectroscopy for chemical analysis) techniques. In the 1987 patent, a homogenous metal distribution was obtained with a relative variation of less than 15% on a 5 nm scale. Also, a spinal structure of AB_2O_4 (A = M^{2+}, B = M^{3+}) was observed based on similarity between the literature and obtained values from the STEM measurement (17).

Typical operating conditions for these catalysts are 50 to 150 bar, 220 to 350°C, and 4000 to 8000 GHSV with a ratio of H_2/CO of 0.5 to 4. The synthesis gas composition used was comprised of 66% H_2, 13% CO, 19% CO_2, and 2% N_2. A summary of the IFP catalyst performance is shown in Table 2.1. The patents also stated that the activation processes via reduction by continuously flowing H_2 are necessary to increase the catalyst activity. IFP reported that a range of 90 to 95 % selectivity with a production rate of 0.92 to 1.29 g/g cat hr of straight chain alcohols was obtained with low

Table 2.1. IFP Catalyst Performance (8-16)

Catalyst	P (MPa)	T (°C)	GHSV	MeOH %	EtOH %	Yield g/g hr
$Cr_{0.8}Cu_1K_{0.06}$	6	250	4000	91	7	0.114
$Cu_1Co_1Cr_{0.8}K_{0.09}$	6	250	4000	24	37	0.315
	6	270	4000	77	13	1.290
	12	250	4000	20	38	0.640
	12	250	8000	23	37	0.931
$Cu_1Co_1Cr_{0.8}K_{0.09}$ + cement	6	250	4000	22	41	0.286
$Cu_1Co_1Cr_{0.8}K_{0.09}$	6	250	4000	24	39	0.329
$Cu_1Co_{0.7}Zn_{0.3}Cr_{0.8}K_{0.09}$	6	250	4000	26	38	0.314
$Cu_1Co_1Mn_{0.8}K_{0.12}$	6	250	4000	24	39	0.276
$Cu_1Co_1Fe_{0.8}K_{0.12}$	6	250	4000	21	41	0.271
$Cu_1Co_1V_{0.8}K_{0.12}$	6	250	4000	20	33	0.314
$Cr_{0.4}Cu_1Co_{0.8}Al_1Ba_{0.1}$	6	250	4000	20	41	0.296
$Cu_1Co_1Cr_{0.5}La_{0.3}K_{0.09}$	6	250	4000	18	35	0.404
$Cu_1Co_1Cr_{0.5}La_{0.3}K_{0.09}$ + 0.05% Pt	6	250	4000	23	39	0.385
$Cu_1Co_1Cr_{0.5}Ce_{0.3}K_{0.09}$	6	250	4000	18	33	0.387
$Cu_1Co_1Mn_{0.5}Nd_{0.21}Pr_{0.09}K_{0.09}$	6	250	4000	18	39	0.335
$Cu_1Co_1Mn_{0.5}Nd_{0.21}Pr_{0.09}K_{0.09}$ + 0.03% Rh	6	250	4000	23	40	0.337
$Cu_1Co_1Fe_{0.8}La_{0.03}K_{0.12}$	6	250	4000	20	41	0.313
$Cu_1Co_1V_{0.5}La_{0.03}K0_{0.09}$	6	250	4000	19	34	0.393
$Cu_1Co_1V_{0.5}La_{0.03}K_{0.09}$ + 0.02% Pd	6	250	4000	23	39	0.363
$Cr_{0.2}Cu_1Co_{0.8}Al_{0.4}La_{0.8}Ba_{0.1}$	6	250	4000	20	33	0.398
$Cu_1Co_{0.5}Al_{0.95}Zn_{0.15}Na_{0.26}O_{3.2}$[I]	8	280	6900	-	56[*]	0.180
$Cu_{0.5}Co_{0.35}Al_{1.2}Zn_{0.5}Ca_{0.2}Mg_{0.4}Li_{0.34}$[II]	8	300	-	-	45[*]	0.105
$Cu_{0.8}Co_{0.3}Al_1Na_{0.132}Li_{0.132}$[II]	8	320	-	-	32[*]	0.280
$Cu_1Co_{0.5}Al_{0.6}Zn_{0.5}K_{0.05}O_{2.93}$[III]	6	290	3000	-	63[*]	0.110
$Cu_1Co_{0.4}Al_1Zn_{0.4}Na_{0.25}O_{3.43}$[III]	6	280	3000	-	49[*]	0.100
$Cu_{0.7}Co_{0.6}Al_{0.9}La_{0.3}Na_{0.17}Rb_{0.007}O_{3.19}$[III]	6	285	3000	-	70[*]	0.140
$Cu_{0.8}Co_{0.5}Al_{0.65}Na_{0.3}O_{2.45}$[III]	6	275	3000	-	72[*]	0.100
$Cu_{0.9}Co_{0.6}Al_1Zn_{0.2}V_{0.15}O_{.3.7}Na_{0.25}$[III]	6	285	3000	-	59[*]	0.130
$Cu_1Co_{0.7}Al_{1.1}Zn_{0.6}Fe_{0.1}Pr_{0.2}Ba_{0.02}K_{0.034}O_{4.44}$[III]	6	262	3000	-	66[*]	0.150
$Cu_{0.9}Co_{0.6}Al_{1.2}Th_{0.4}O_{4.33}Na_{0.45}$[III]	6	270	3000	-	62[*]	0.120
$Cu_{0.7}Co_{0.7}Al_{1.35}La_{0.3}Mn_{0.15}Na0_{.182}K_{0.044}O_{4.21}$[III]	6	256	3000	-	74[*]	0.140
$Cu_{1.3}Co_{0.3}Al_{0.65}Pr_{0.4}Fe_{0.15}O_{3.47}K_{0.127}$[III]	6	250	3000	-	39[*]	0.110
$Cu_1Co_{0.5}Al_{0.95}Zn_{0.15}Na_{0.26}O_{3.2}$[III]	6	280	3000	-	54[*]	0.120
$Cu_1Co_{0.5}Al_{0.95}Cr_{0.15}Na_{0.26}O_{3.28}$[III]	6	300	3000	-	49[*]	0.110
$Cu_{1.7}Co_{0.85}Al_{1.5}Ce_{0.1}Nd_{0.1}Th_{0.1}K_{0.15}O_{5.4}$[III]	6	255	3000	-	67[*]	0.130
$Cu_{0.8}Co_{0.7}Al_{1.25}Zr_{0.1}Re_{0.01}Zn_{0.2}Na_{0.38}O_4$[III]	6	285	3000	-	61[*]	0.105

[I] $H_2/(CO + CO_2) = 1.5$ and $CO_2/(CO + CO_2) = 0.25$
[II] $H_2/CO_2 = 2$ with 2% CO_2
[III] $H_2/(CO + CO_2) = 2$ and $CO_2/(CO + CO_2) = 0.14$
[*] $C_{2+}OH$

hydrocarbon selectivity. The selectivity by weight to higher alcohol is defined as the

ratio by weight of higher alcohol over the total weight of the formed alcohols. The first

catalyst, $Cu_1Co_1Cr_{0.8}K_{0.09}$, was deactivated very fast, and a slight improvement in the

deactivation process was observed with the next catalyst (10). Later, little deactivation

was observed, except during the start-up period for the two catalysts,

Cu/Co/Zn(B)/Al(C)/A/(M) and Cu/Co/Zn/Cr/M. The authors assumed that the addition of

the additives improves the long-term performance of catalysts, presumably via

hydrogenation of the surface carbonaceous species, resulting in diminished coke

deposition (6). During start-up, a highly exothermic effect was observed with an

excessive methanation reaction. Also, explicit amounts of water were produced via the

water gas shift reaction as stated in the 1987 patent.

Because of the high selectivity toward alcohols and high activity toward $C_{2+}OH$,

IFP catalysts are the most promising catalysts for higher alcohols synthesis under mild

reaction conditions. Also, with the IFP modification, the selectivity and long term

activity are not a major problem for large-scale industrial application (6). The IFP

catalyst is the only catalyst successfully tested in a demonstration plan (7000bbl/yr) with

97% selectivity of higher alcohols. However, no researcher has been able to replicate the

results claimed by IFP (15).

2.4.2. Calcinated Catalyst

Catalysts are prepared either by co-precipitation via a basic precipitating agent or

by the citric acid method (6). Air or nitrogen gas is used for the calcination process. Two

phases, HC (hydrotalcite) like crystalline and amorphous granular, are reported in the

literature (6). The crystalline and amorphous phases are transformed into spinels, AB_2O_4 ($A = M^{2+}$, $B = M^{3+}$). The transformation process begins when the HC-like phase loses most of its cobalt content, while the amorphous granular phase loses part of its copper content. Then, spinels are formed from both phases, sometimes with the presence of CuO. The M^{3+} ion in the spinel is reported to be Cr^{3+}, Al^{3+}, or Co^{3+} while M^{2+} ion is Cu^{2+}, Co^{2+}, or Zn^{2+}. Copper spinel is observed only at high calcination temperatures. The spinels containing both cobalt and copper have never been found in either aluminum or chromium-based catalysts. Finally, ZnO acts as a stabilizer especially on copper species possibly due to the epitaxial fixation of copper in the catalyst (6, 14).

2.4.3. Reduced Catalyst

Hydrogen gas is employed in the reduction process. After reduction, the metallic forms of both copper and cobalt were observed. Cobalt is more difficult to reduce while copper is easily reduced at temperatures below 200°C. The instability of the spinel is responsible for the slow reduction of cobalt. Thus, highly disperse cobalt and high probability of cobalt-copper structures, which are the active species for alcohol formation, are observed instead of the crystalline structure of cobalt itself. Also, due to the difficulty of reduction and thermal decomposition of spinels, the structure of cobalt-copper is maintained in the final catalyst. Possibly due to the interaction within the HC crystalline structure before calcination and within spinels after calcination, cobalt is still retained as small metallic crystalline (0.25 – 0.4 Å) and in ionic form. This eliminated the possibility of large cobalt particle formation, which is responsible for methanation and hydrocarbon formation (6). Higher alcohol catalysts are based on the homogeneous

spinel type mixed oxides, modified by incorporating alkali metals. Upon hydrogen

reduction and surface reconstruction under synthesis gas, the spinel phase is depleted of

its reducible metals and converted to highly dispersed clusters with depleted mixed

oxides support (29).

2.4.4. Reactive Sites

In higher alcohol synthesis, copper sites are responsible for hydrogen dissociative

chemisorption and CO associative adsorption since these are the main elements in

methanol synthesis. Metallic cobalt sites are responsible for CO dissociation, carbon-

carbon chain growth and hydrogenation since cobalt is the F-T synthesis metal. By

surface migration, the adsorbed CO molecule moves to an adsorbed alkyl group and

inserts between metal sites and alkyl group. Hence, cobalt and copper sites must be close

to each other (a few nm) for the possibility of this surface migration. Separation of the

two metals or the heterogeneous distribution during catalyst preparation will cause

selectivity deterioration for alcohol synthesis. Also, chain growth cannot take place on

the surface of potassium modified copper catalyst (6).

Metallic cobalt may also adsorb CO associatively. However, only a small amount

of oxygenates are formed from pure cobalt, indicating that adsorbed CO cannot be

inserted into the alkyl group to form alcohol. Thus, the copper sites are responsible for

the CO insertion, not cobalt sites. Also, the metal oxides are more active for CO and/or

CO_2 associative adsorption while transition metals are active in hydrogenation. It is also

reported that during start-up, a high rate of methanation occurs indicating that the active

sites might be produced by sites initially active for F-T synthesis. Later the selectivity for

12

higher alcohols gradually increases with decreasing selectivity of methanation, which in turn is explained by the increase in CO insertion sites and/or the oxidation of cobalt or copper sites due to the presence of water and CO_2 (6).

2.5.   Modified Fischer-Tropsch (F-T) Catalyst

Traditional F-T catalysts contain Fe, Co, Ni, and Ru metal, which produce long chain hydrocarbons with small amount of oxygenates. A considerable amount of oxygenates are also produced with the promotion of alkali metal. The products are primary straight-chain alcohols following an Anderson-Schulz-Flory (ASF) distribution. This distribution is characteristic of the linear condensation polymerization mechanism. Higher alcohols are difficult to optimize with modified F-T catalyst because of the restriction of ASF distribution (32, 34, and 37). In addition, high yields of alcohols and other oxygenated products are favored by high pressure, low temperature, high space velocity, and carbon monoxide-rich synthesis gas. However, these syntheses are usually operated at low pressure due to the volatile carbonyl formation, which may seriously damage activity and lifetime of catalysts if operating at high pressure. In addition, high temperature and pressure could increase carbon deposition from the iron group metals, resulting in catalyst disintegration. For instance, the carbon deposition rate of cobalt and nickel catalysts is prohibitively high at temperature above 250°C, 300°C for iron. Finally, hydrogen-rich synthesis gas should be used in order to minimize carbon deposition (38).

2.6. Modified Methanol Catalyst

The modified methanol catalyst has been known since 1920 and typically operates under high pressure, 10 to 20 MPa, and a temperature around 400°C (4). In the synthesis, methanol is the principal product with a small amount of secondary alcohols, isobutanol, ketones, ethers, and hydrocarbons. For the higher alcohol promotion or activation, one or more alkali metals, usually in oxide, hydroxide, or carbonate form, is essential. The basicity of spinel is also very important because it can reduce the formation of hydrocarbons. The maximum alcohol production was observed at unity synthesis gas ratio. Another type of modified methanol catalyst is the low temperature catalyst. The catalyst is mainly alkali modified copper (37, 64), generally operated at higher temperature and pressure than the Fischer-Tropsch synthesis, presumably due to the oxide stability at the presence of CO and H_2 (38).

2.7. Co-Cu Based Catalysts

Co-Cu based catalysts are utilized for the production of high purity alcohol, even though the purity decreases with the higher alcohol content. Table 2.2 shows a typical composition of alcohols for Cu-Co based and Co-free Cu based catalyst. It was observed that the higher alcohol and selectivity are favorable at low synthesis gas ratio. Higher ratios of 3.5 or more have damaging effects on both higher alcohol content and selectivity (29).

The Cu-Co based catalyst also produced a large amount of byproduct CO_2 and H_2O, but the selectivity toward high molecular weight alcohols was generally low (15, 16). The chain growth of higher alcohol formation is favored at high cobalt

concentration or low copper content, and/or alkali metal content (29). Many reported that

the selectivity of higher alcohols is directly related to the Co-Cu interaction (54-60). In

another words, the cobalt ions in combination with metallic Cu or the interaction phase

are important to oxygenates synthesis. The Cu-Co interaction formed after reduction is

the active site for the reaction (53) as mentioned earlier. Also, some researchers

mentioned that the unreduced cobalt ions are responsible for higher alcohol synthesis (58-

60).

Table 2.2. Typical Concentration of Alcohols (wt %)

	Cu-Co based catalyst	Cobalt free, copper based catalysts
(H_2 / CO)	2	<1
CH_3OH	57.5	53.5
C_2H_5OH	28.5	3.9
C_3H_7OH	7.1	3.1
C_4H_9OH	2.8	6.2
$C_5H_{11}OH$	1.2	3.8
$(C_6H_{13}OH)^+$	1.3	14.8
Hydrocarbons	0.3	4.3
Esters	0.7	10.1
Other Oxygenates	0.6	
	-----------	----------
	100 (anhydrous basis)	99.7 (+0.3% water)
Alcohol Purity	98.3	85.3
$(C_2H_5OH)^+$	40.4	31.9

It is also noted that the catalyst lifetime is dependent on the sulfur level in

synthesis gas. Sensitivity to sulfur poisoning is observed to vary with catalyst

composition for alcohol synthesis. Most catalysts appeared to be less sensitive to sulfur

poisoning than the Fischer-Tropsch catalyst (38). Different researchers favor different

catalysts. Some state that modified F-T catalyst and high temperature methanol catalysts

are least promising while others believe that both high and low temperature modified

methanol catalysts are the best higher alcohol catalysts (34). There is another type of

higher alcohol synthesis from synthesis of CO, H_2, and olefins called oxosynthesis.

Oxosynthesis was discovered in Germany during World War II, and uses catalysts similar

to the cobalt-base catalysts commonly used in Fischer-Tropsch synthesis (4). Thus, the

higher alcohol synthesis is mainly from F-T or modified methanol catalyst.

2.8.   Catalyst Characteristics

A catalyst cannot make an impossible reaction favorable or change the final

chemical equilibrium position. However, a catalyst can provide an alternative lower

energy pathway for a kinetically slow reaction. The catalyst increases the reaction rate

by lowering the activation energy of the rate-limiting step in the overall process. In the

absence of catalyst, the activation energies are too high for the reaction to occur at

temperatures where the thermodynamic equilibrium is favorable (2).   The relationship

between activation energy (E) and the reaction rate constant is expressed by the

Arrhenius equation:

$$k = A_o \exp (-E / RT) \hspace{4cm} 2.6$$

The processes that control the catalytic reaction are adsorption, formation and

breakup of activated complex, and desorption. The rate of each process is dependent on

the active sites on the catalyst surface. In other words, a catalyst must have a large

surface area, effectively bind to the reactants, stabilize the activated complex, and be able

to release the reaction products. It is also noted that the active catalyst species are not the same compounds that are added to the reaction as a "catalyst". After the induction period, the catalyst precursors are actually converted to the catalyst species.

2.9.   Higher Alcohol Synthesis Mechanisms

Higher alcohol synthesis is not just a one step direct reaction from carbon monoxide and hydrogen, but an extremely complicated series of reactions, which involve CO insertion to form a carbon-carbon bond, followed by sequential hydrogenation of the intermediate (5, 27). The three main mechanisms are dissociation (C – O bond breaking), association (hydrogenation / chain growth), and insertion (CO insertion / hydrogenation) (63). The general mechanism reaction sequences are proposed (2, 5, and 8):

$$CO + 2\ H_2 \rightarrow CH_3OH \qquad\qquad\qquad 2.7$$

$$CH_3OH + CO \rightarrow CH_3COOH \qquad\qquad\qquad 2.8$$

$$CH_3COOH + H_2 \rightarrow CH_3CHO + H_2O \qquad\qquad\qquad 2.9$$

$$CH_3CHO + H_2 \rightarrow CH_3CH_2OH \qquad\qquad\qquad 2.10$$
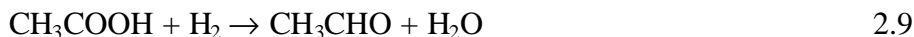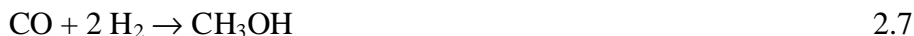
The precise oxygenates formation via synthesis gas mechanism is a chain growth polymerization in which the proposed initiation steps of both oxygenates and hydrocarbon are (6):

$$\tfrac{1}{2}\ H_2 + {^*S_H} \xrightarrow{k_H} H^* \qquad\qquad 2.11$$

$$CO + {^*S_A} \xrightarrow{k_A} CO^* \qquad\qquad 2.12$$

where $^*S_H$ is the H_2 dissociation site, S_A is the CO adsorption associative site, H^* is the adsorbed surface hydrogen atom, CO^* is the adsorbed surface molecule, k_H is the hydrogen dissociation rate constant, and k_A is the CO associative rate constant.

The formation of methanol involves the adsorbed molecule (CO*) and the adsorbed surface hydrogen atom (H*), where k_{MeOH} is the rate constant of methanol formation.

$$CO* + 4\ H* \xrightarrow{\ k_{MeOH}\ } CH_3OH \qquad 2.13$$
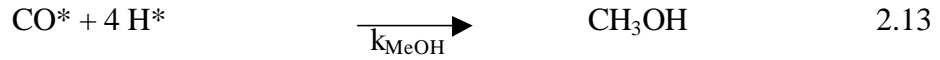
Following is the proposed mechanism for CO dissociation, which are necessary for hydrocarbon and essentially the formation of oxygenates.

$$CO* + S_D* \xrightarrow{\ k_D\ } C* + O* \qquad 2.14$$

$$2CO \Leftrightarrow CO_2 + C* \qquad 2.15$$

where S_D* is the CO dissociation site, $C*$ is the surface carbide species, $O*$ is the surface oxygen atom, and k_D is the CO dissociation rate constant.

The $C*$ species can also be found in the Boudourad reaction (Equation 2.15), which is not a major reaction, so Equation 2.14 is the main consideration.

The interaction between the carbide species ($C*$) and adsorbed surface hydrogen atoms (H*) leads to the formation of hydrocarbon.

$$C* + x\ H* \xrightarrow{\ k_{CHx}\ } CH_x* \qquad 2.16$$

where CH_x* is the partially hydrogenated carbon surface species ($1 < x < 4$), and k_{CHx} is the CH_x formation from $C*$ rate constant.

The final steps of oxygenates formation are via insertion of CO adsorbed molecules into the hydrocarbon chain.

$$CH_x* + CO* \xrightarrow{\ k_{CO}\ } CH_xCO* \qquad 2.17$$

$$CH_xCO + H* \xrightarrow{\ k_{H'}\ } C_2H_5OH \qquad 2.18$$
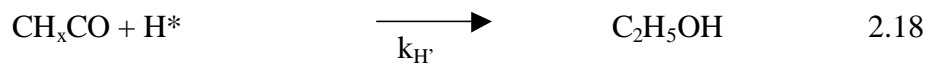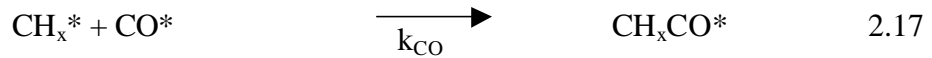
Higher oxygenates require the propagation steps of hydrocarbon and again CO insertion mechanism.

$$CH_x^* + CH_x^* \xrightarrow{k_P} C_2H_y^* \text{ or } C_nH_z^* \qquad 2.19$$

$$C_nH_z^* + CO^* \xrightarrow{k_{CO}} C_nH_zCO^* \qquad 2.20$$

$$C_nH_zCO^* + H^* \xrightarrow{k_{H'}} C_{n+1}H_{2n+3}OH \qquad 2.21$$

$$C_nH_z^* + H^* \xrightarrow{k_H} C_nH_{2n}C_nH_{2n+2} \qquad 2.22$$
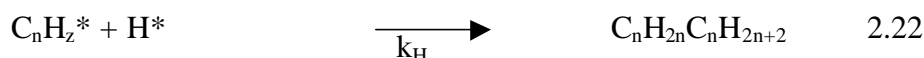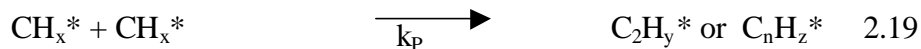
where k_P is the rate constant for the propagation step in the C-C chain growth via CH_x^* addition, k_{CO} is the rate constant of CO^* insertion, $k_{H'}$ is the rate constant for the hydrogenation of C_nH_zCO species, and k_H is the rate constant for the hydrogenation of $C_nH_z^*$ species.

Most of the higher alcohol mechanisms are straight chain primary alcohols with only a small amount of branched alcohols or iso-alcohols (30). Fischer suggested that isopropyl alcohol can be produced via acetic acid formation from acetone (19),

$$2CH_3COOH \rightarrow (CH_3)_2CO + CO_2 + H_2O \qquad 2.23$$

$$(CH_3)_2CO + H_2 \rightarrow (CH_3)_2CHOH \qquad 2.24$$
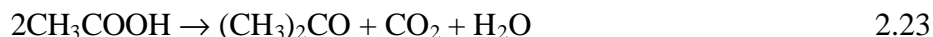
Higher iso-alcohols can be produced by further reaction between isopropyl alcohol with carbon monoxide and hydrogen.

In addition, the simplest mechanism of higher alcohol production is the condensation of two lower alcohol molecules with the formation of one higher alcohol molecule (64). The controlling reaction in the synthesis of higher alcohol formation is the condensation of two methanol molecules to produce ethanol via dehydration (19). This mechanism also produces one water molecule. Scientists were also able to

qualitatively predict the presence or absence of certain higher alcohols with simple addition rules (20).

$$2\ CH_3OH \rightarrow CH_3CH_2OH + H_2O \qquad\qquad 2.25$$

$$2\ CH_3OH \rightarrow (CH_3)_2O + H_2O \qquad\qquad 2.26$$

$$(CH_3)_2O \rightarrow CH_3CH_2OH \qquad\qquad 2.27$$

Enol condensation is another proposed mechanism, where methanol is the precursor for the chain initiator in the following expression (66, 67):

$$CH_3OH\ +\ CH_3CH_2OH \rightarrow CH_3CH_2CH_2OH + H_2O \qquad\qquad 2.28$$

A similar homologation of methanol by CO via a symmetric intermediate was proposed (22):

2.29
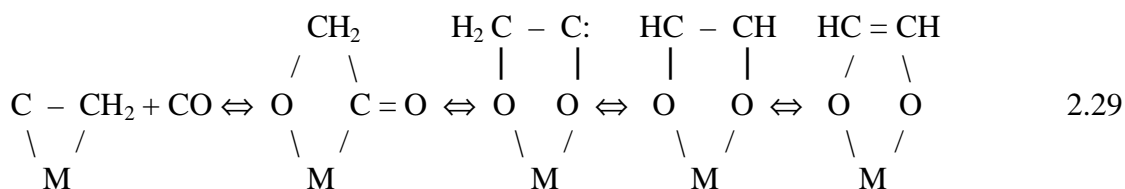
Another proposed mechanism is the aldol condensation. It was reported that aldol condensation would yield straight chain alcohols, especially butanol from two molecules of aldehyde. However, the aldol condensation, Equations 2.30 and 2.31, applied only to non-catalytic alcohol synthesis over alkali acetylides. Formaldehyde molecules in the second step of the following mechanism can also be derived from methanol (23).

$$2HCHO \rightarrow CH_2OHCHO \qquad\qquad 2.30$$

$$CH_2OHCHO\ +\ H_2 \rightarrow CH_3CHO + H_2O \qquad\qquad 2.31$$
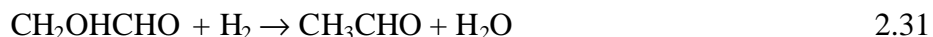
In general, the three proposed mechanisms for higher alcohol formation are CO insertion into a methyl-metal bond or into the C-O bond of methoxide, CO homologation of methanol via a symmetric intermediate, and aldol condensation via aldehydic coupling or alcohol species coupling (5).

The water gas shift reaction is always important in higher alcohol synthesis (6, 24). With the presence of water in higher alcohol synthesis, the reaction mechanism with or without initial CO_2 will definitely be altered (33). The water gas shift reaction mechanism is (6):

$$CO + H_2O \Leftrightarrow CO_2 + H_2 \tag{2.5}$$

$$CO_{(g)} \longrightarrow CO^* \underset{OH^*}{\longrightarrow} HCOO^* \longrightarrow CO_{2(g)} + H^* \underset{H}{\longrightarrow} H_{2(g)} \quad 2.32$$

$$CO + O^* \Leftrightarrow CO_2 + *empty\ site \tag{2.33}$$

$$H_2O + * \Leftrightarrow H_2 + O^* \tag{2.34}$$
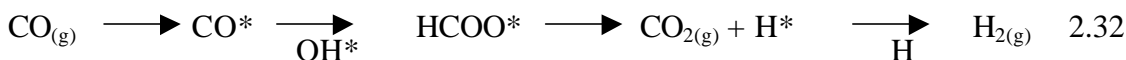
Equations 2.33 and 2.34 are the proposed mechanism via surface formate intermediates, and via surface O* species, respectively.

In summary, the hydrogenation of carbon monoxide may be presented in the following forms (35):

$$(2n + 1)\,H_2 + n\,CO \Leftrightarrow C_nH_{2n+2} + n\,H_2O \tag{2.35}$$

$$2n\,H_2 + n\,CO \Leftrightarrow C_nH_{2n} + n\,H_2O \tag{2.36}$$

$$2n\,H_2 + n\,CO \Leftrightarrow C_nH_{2n+1}OH + (n-1)\,H_2O \tag{2.37}$$

$$(n + 1)\,H_2 + 2n\,CO \Leftrightarrow C_nH_{2n+2} + n\,CO_2 \tag{2.38}$$

$$n\,H_2 + 2n\,CO \Leftrightarrow C_nH_{2n} + n\,CO_2 \tag{2.39}$$

$$(n + 1)\,H_2 + (2n - 1)\,CO \Leftrightarrow C_nH_{2n+1}OH + (n-1)\,CO_2 \tag{2.40}$$
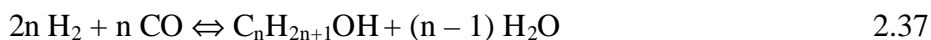
Extensive research has been focused on the mechanism determination with only slight success of gaining universal acceptance. The most supported proposal was the surface carbide mechanism for the formation of higher oxygenates and hydrocarbons (61). Many believe that the carbonyl insertion into metal-carbon bonds is thermodynamically favorable over carbonyl insertion into carbon-hydrogen bonds. The metal-carbon bonds are believed to be weaker than metal-hydrogen bonds. However, the process energy is influenced by many factors. One factor is that the C-H formation bond requires more energy than C-C bond formation (65). It is also believed that the barrier heights for metal-carbon bond insertion are much higher than the metal-hydrogen bond insertion due to the metal-alkyl bond being more directional than the metal-hydrogen bond (68).

2.10. Higher Alcohol Synthesis Thermodynamics

Higher alcohol synthesis produces selectively C_1-C_6 alcohols with the unavoidable byproducts of CO_2 and H_2O. Most of these reactions are strongly exothermic (29). Formation and change in Gibbs free energy (kcal / mole) starting from CO and H_2 are estimated based on the governing equations according to Xiaoding (4, 6):

$$CO + 2\,H_2 \rightarrow CH_3OH \tag{2.7}$$

$$\Delta G^\circ = -27.288 + 0.05838\,T \tag{2.41}$$

$$n\,CO + 2n\,H_2 \rightarrow C_nH_{2n+1}OH + (n-1)\,H_2O \tag{2.37}$$
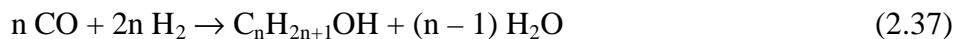
$$\Delta G^\circ = -38.386\,n + 11.098 + (5.982\,n - 0.144)10^{-2}\,T \tag{2.42}$$

$$n\,CO + (2n+1)\,H_2 \rightarrow C_nH_{2n+2} + n\,H_2O \tag{2.35}$$
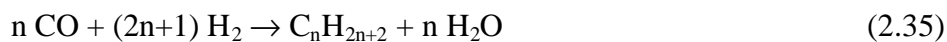
$$\Delta G^\circ = -38.386\,n + 35.158 + (5.982\,n - 0.144)10^{-2}\,T \tag{2.43}$$

$$n \, CO + 2n \, H_2 \rightarrow C_nH_{2n} + n \, H_2O \tag{2.36}$$

$$\Delta G^\circ = -38.386 \, n + 17.645 + (5.982 \, n - 3.434)10^{-2} \, T \tag{2.44}$$

$$CO + H_2O \rightarrow CO_2 + H_2 \tag{2.5}$$

$$\Delta G^\circ = -8.514 + (0.771) \, 10^{-2} \, T \tag{2.45}$$

$$CO_2 + 3 \, H_2 \rightarrow CH_3OH + H_2O \tag{2.46}$$

$$\Delta G^\circ = -18.774 + (5.067) \, 10^{-2} \, T \tag{2.47}$$

$$n \, CO_2 + 3n \, H_2 \rightarrow C_nH_{2n+1}OH + (2n - 1) \, H_2O \tag{2.48}$$
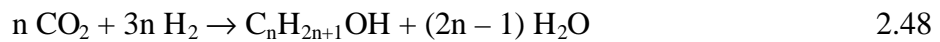
$$\Delta G^\circ = -29.872 \, n + 11.098 + (5.211 \, n - 0.144) \, 10^{-2} \, T \tag{2.49}$$

$$n \, CO_2 + (3n + 1) \, H_2 \rightarrow C_nH_{2n+2}OH + 2n \, H_2O \tag{2.50}$$
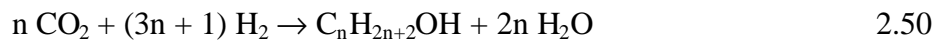
$$\Delta G^\circ = -29.872 \, n + 35.158 + (5.211 \, n - 0.144) \, 10^{-2} \, T \tag{2.51}$$

$$n \, CO_2 + 3n \, H_2 \rightarrow C_nH_{2n}OH + 2n \, H_2O \tag{2.52}$$
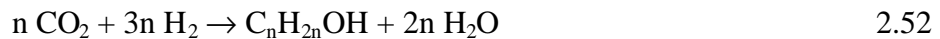
$$\Delta G^\circ = -29.872 \, n + 17.645 + (5.211 \, n - 3.434) \, 10^{-2} \, T \tag{2.53}$$

$$CH_3(CH_2)_{n-2}CH_2OH \rightarrow (CH_3)_2CH(CH_2)_{n-4}CH_2OH \tag{2.54}$$

$$\Delta G^\circ = -1.355 + (0.258) \, 10^{-2} \, T \tag{2.55}$$

These reactions are assumed to be the main formation routes with the possibility of other reactions such as hydrogenation, dehydration, dehydrogenation, oxidation, or esterification. A summary of the Gibbs free energy as well as reaction equilibrium constants is shown in Table 2.3.

$$K_{eq} = \exp(-\Delta G^\circ / RT) \tag{2.56}$$

Thermodynamically, the Gibbs free energy decreases in the order of methanol, higher alcohol, and F-T synthesis (C_nH_{2n}) at 523 K, which is the normal operating

Table 2.3. Gibbs Free Energy and Equilibrium Constant Values

Comp.	Gas	T (K)	ΔG° (kcal/mole)				K_{eq}			
			n = 1	n = 2	n = 3	n = 4	n = 1	n = 2	n = 3	n = 4
C_nH_{2n+1}	CO	473	0.3	-9.8	-19.9	-29.9	7.1E-01	3.3E+04	1.5E+09	6.9E+13
OH	H_2	523	3.2	-3.9	-11.0	-18.1	4.4E-02	4.1E+01	3.8E+04	3.5E+07
		573	6.2	2.1	-2.1	-6.2	4.5E-03	1.6E-01	6.1E+00	2.2E+02
		623	9.1	8.0	6.8	5.7	6.5E-04	1.6E-03	4.0E-03	9.8E-03
	CO_2	473	5.2	0.0	-5.3	-10.5	4.0E-03	1.0E+00	2.7E+02	6.9E+04
	H_2	523	7.7	5.1	2.5	-0.1	5.9E-04	7.3E-03	9.1E-02	1.1E+00
		573	10.3	10.2	10.2	10.2	1.2E-04	1.2E-04	1.2E-04	1.3E-04
		623	12.8	15.4	18.0	20.6	3.3E-05	4.0E-06	4.9E-07	6.1E-08
C_nH_{2n+2}	CO	473	24.4	14.3	4.2	-5.9	5.4E-12	2.5E-07	1.1E-02	5.3E+02
	H_2	523	27.3	20.2	13.1	6.0	3.9E-12	3.6E-09	3.3E-06	3.1E-03
		573	30.2	26.1	22.0	17.9	3.0E-12	1.1E-10	4.0E-09	1.5E-07
		623	33.1	32.0	30.9	29.8	2.4E-12	5.8E-12	1.4E-11	3.6E-11
	CO_2	473	29.3	24.0	18.8	13.6	3.0E-14	7.9E-12	2.0E-09	5.3E-07
	H_2	523	31.8	29.2	26.5	23.9	5.2E-14	6.5E-13	8.1E-12	1.0E-10
		573	34.3	34.3	34.3	34.3	8.1E-14	8.2E-14	8.3E-14	8.4E-14
		623	36.9	39.4	42.0	44.6	1.2E-13	1.5E-14	1.8E-15	2.2E-16
C_nH_{2n}	CO	473		-18.8	-28.9	-39.0		4.8E+08	2.2E+13	1.0E+18
	H_2	523		-14.5	-21.6	-28.7		1.2E+06	1.1E+09	1.0E+12
		573		-10.3	-14.4	-18.5		8.1E+03	3.0E+05	1.1E+07
		623		-6.0	-7.1	-8.2		1.3E+02	3.1E+02	7.7E+02
	CO_2									
	H_2	473		-9.0	-14.3	-19.5		1.5E+04	3.9E+06	1.0E+09
		523		-5.6	-8.2	-10.8		2.1E+02	2.6E+03	3.2E+04
		573		-2.1	-2.1	-2.1		6.1E+00	6.2E+00	6.2E+00
		623		1.4	4.0	6.6		3.1E-01	3.9E-02	4.8E-03
Water		473	-4.9				1.8E+02			
Gas		523	-4.5				7.5E+01			
Shift		573	-4.1				3.6E+01			
		623	-3.7				2.0E+01			

temperature for methanol synthesis and IFP catalysts. These above reactions are

thermodynamically controlled reactions. In reality, however, methanol synthesis

catalysts are observed to be very active and selective while F-T and higher alcohol

synthesis catalysts are not. It is concluded that higher molecular weight alcohol synthesis

is more thermodynamically favorable than low molecular weight alcohol synthesis. According to Table 2.3, the reactions are more favorable in the order of $C_nH_{2n} > C_nH_{2n+1}OH > C_nH_{2n+2}$ for the same n from either CO/H_2 or CO_2/H_2 gas. Also, CO/H_2 are more favorable for the reaction than CO_2/H_2. Methanol is one of the least thermodynamically favorable products of CO and CO_2 hydrogenation. More negative free energy change was observed for the formation of higher alcohols and hydrocarbons (28). By increasing the reaction temperature, the Gibbs free energy for both hydrocarbons and alcohols increase, but the equilibrium constant decreases rapidly, while the unfavorable equilibrium constant of the water gas shift reaction increases slightly. With increasing n values, the Gibbs free energy for both hydrocarbons and alcohols decreases, and leads to more favorable equilibrium. The synthesis of oxygenates must be kinetically controlled in order to minimize hydrocarbon formation (2). According to the isomerization equation, Equation 2.54, the equilibrium constant is slightly changed with temperature, or more unfavorable toward alcohol isomerization with increasing temperature (6). The production of alcohols is not just dependent on the selectivity of catalyst but also the kinetic factor. Thus, the thermodynamic considerations are not sufficient to establish the possible steps of the synthesis (4).

2.11. Effect of CO_2 in Synthesis Gas

Dow Chemical patent 8410932.5 in 1984 stated that catalyst activity of MoS_2/SiO_2K would be retarded with the utilization of a high CO_2 concentration. At high concentration of CO_2, CO conversion decreased, but the alcohol to hydrocarbon ratio was not significantly changed. At low concentration of CO_2, the CO conversion was

unchanged while the ratio of higher alcohols to methanol drastically decreased. In the absence of CO_2, however, the catalyst will have a lower initial activity and be deactivated at a rapid rate (5).

Another source also stated that a small concentration of CO_2 enhanced the yields of higher alcohols while large CO_2/CO ratios resulted in significant inhibition of higher alcohol production (31). The role of CO_2 in higher alcohol synthesis is still not clear, but it is reported that CO_2 in the feed gas affected the available active surface area. For instance, oxygen covered the active surface because CO_2 acts as an oxidizing agent. However, some CO_2 is probably necessary to maintain the selectivity (6). Addition of CO_2 also forces the production of water, which results in a substantial loss in carbon efficiency (64). By examining the methanol reaction rate, it is also concluded that CO hydrogenation is retarded by the presence of CO_2 but it is not true in reverse, due to the competitive adsorption of CO_2 on the active sites of catalyst (5).

2.12. Effect of Synthesis Gas Ratio (H_2/CO)

Synthesis gas ratio is an important parameter in higher alcohol synthesis. It can affect both reaction rates and activity. The reactions' stoichiometry, or synthesis gas ratio, should be between 0.6 and 3, depending on the involved carbon atoms and the product nature (29). A ratio of less than unity tends to decrease oxygenate yield while increasing alcohol selectivity (5). A change in the ratio will also affect the partial pressure of H_2 and CO under constant total pressure, thus the stoichiometry will be different for each reaction. Higher hydrogen partial pressure will eliminate coke formation, thus better activity will be obtained. Higher carbon monoxide partial pressure

26

favors the formation of high molecular weight compounds (4). H_2/CO will increase due to the favorable thermodynamics of the water gas shift reaction. By decreasing the H_2/CO ratio, CO insertion and C-C chain growth are more favorable, which then enhance the production of higher alcohols and/or hydrocarbons (6).

2.13. Effect of Pressure

An increase in total pressure will increase the equilibrium towards the product side, and increase the conversion (2). The change in Gibbs free energy will always be negative when pressure increases. Furthermore, a change in total pressure will not affect the water gas shift reaction but will change the equilibrium product distribution (6).

2.14. Effect of Temperature

The effect of temperature on reactions has been discussed in the thermodynamics section. Higher temperatures will enhance productivity. Some oxygenates will not be stable enough and will decompose at high temperatures. Thus the upper temperature limit to the synthesis of alcohols has to be set (4, 6) because high temperatures can also lead to catalyst deactivation due to sintering (37).

2.15. Effect of Space Velocity

Space velocity is inversely proportional to contact time between synthesis gas and catalyst surface. For kinetically controlled reactions, increasing the space velocity will increase total yield with the possibility of lowering conversion. For partial or total mass transfer controlled reactions, increasing the space velocity will increase the mass transfer to the core of the catalyst particles and suppress the secondary reactions. It has also been

27

observed that increasing the space velocity will increase higher alcohol selectivity. This is explained by the suppression of side reactions due to the shorter contact time, which reduces the chances of side reactions occurring. Consequently, higher purity products are obtained (4, 6, and 16).

2.16.   Effect of Alkali Promotion

Alkali metal plays an important role in the activity, selectivity, and lifetime of a catalyst, although in some cases alkali cations behave as poisons (65). They are responsible for creating a new way to form alcohols by introducing new basic sites. These sites are capable of associatively activating CO and capable of suppressing various unwanted side reactions. With an increased number of activated CO sites, total product yield will be enhanced (26). Alkali can also reduce the active hydrogen availability or activities by blocking the active sites for dissociative hydrogen adsorption. Thus, the interaction between carbon monoxide with the surface will be weaker and direct hydrogenation without dissociation of the CO will dominate the path-way. The CO dissociative adsorption on the catalyst surface is responsible for hydrocarbon production (65). Hence, alkali promoters prepare the surface in the way that creates alcohol synthesis pathways instead of hydrocarbon.

Higher alcohol production increases with the addition of alkali promoters in the order of Li, Na, K, Cs, Rb, the same order as their basicity. Catalyst doping with a small quantity of alkali usually increases the reaction rate in the order from Li to Rb, but when the optimized doping is exceeded, the reaction rate falls, and the activity sequence is reversed (4, 5, 21, 36). The promoter coverage should be at a level that justifies the

electronic states and does not block the active sites (65). The relative influence of various promoters is independent of the type of catalyst used.

In the case of dehydrogenation, the intrinsic presence of alkali can prevent coking. The surface alkali ions in melt form can initiate the reaction between coke and water vapor to produce CO and H_2. Adsorption of alkali metal ions donates electrons to the surface, thus increasing surface electron density and enhancing CO associative adsorption (36, 65). The promoter not only can alter the melting point of the catalyst active substance but can also alter its viscosity, thus, altering the rate of material exchange between the catalyst and synthesis gas. Sometimes, the addition of alkali metal can also prevent phase transformations in the catalyst (36). In summary, catalytic activity effects due to alkali promoter influences include alkali intrinsic catalytic effects, basic site creation, acid site neutralization, surface electronic properties modification, phase transformation prevention, reduction of volatility of the active component through formation of compounds, and modification of the physical properties of the active component melts (65).

2.17. Other Factors

Many researchers have provided significant understanding of the correlation between catalytic selectivity, activity, and properties of the catalyst (39): First, an optimal metal-oxygen bond is required for high selectivity in oxidation. A correlation between selectivity and metal-oxygen bond strength can be measured as the heat of reduction of oxides changed rates as a function of metal-oxygen bond lengths, or as a function of reduction degree (40). Also, the presence of M=O is important in many selective

oxidation catalysts (41, 42). Second, the correlation between selectivity and absence of

weakly adsorbed oxygen has been demonstrated by using temperature programmed

desorption. Weakly adsorbed oxygen is harmful to higher alcohol synthesis because it

causes combustion of adsorbed hydrocarbons (43, 44). Third, the activity of the catalyst

depends on the optimum density of active oxygen. Too many active oxygen sites will

cause excessive oxidation, and too few will result in an inactive catalyst (45).   Fourth,

the correlation between selectivity and electron binding energy of lattice oxygen has been

determined by XPS. The electron binding energy can be used as a measure of the

basicity of the lattice oxygen (46). Fifth, the acid-base properties will determine the

interaction strength of the reactants and products with the catalyst. Hence, it can

determine whether a reactant can be readily adsorbed, or a product can be readily

desorbed (47). Sixth, the ability of the catalyst to form shear structures facilitates the

oxidation and reduction cycles without any major structural change (48). Finally, the

selectivity of catalyst also is dependent on cation vacancy (49).

2.18.   References

1.   Keim, W., Industrial Chemicals via C_1 Processes, (Chapter 1, Fahey, D., Ed.,
        ACS Monograph 328, American Chemical Society, Washington, DC: 1987).

2.   Sheldon, R., Chemicals from Synthesis Gas: Catalytic Reactions of CO and H_2,
        (Reidel Publishing, Dordrecht, Holland: 1983).

3.   Falbe, J., *Philosophical Transaction Society of London*, 300, 205, (1981).

4.   Natta, G., Columbo, U., Pasquon, I., Catalysis, Emmett, P. H., ed., (Reinhold,
        Volume 5, Chapter 3, New York: 1957).

5.   Herman, R., Studies in Surface and Catalyst, (Chapter 7, Elsevier, Amsterdam:
        1990).

6. Xiaoding, X., Doesburg, E., Scholten J., *Catalysis Today,* 2, 125, (1987).

7. Ashmore, P. G., Catalysis and Inhibition of Chemical Reactions, (London, Butterworths: 1963).

8. Surgier, A., US Patent 3787332, (1974).

9. Surgier, A., US Patent 3899577, (1975).

10. Surgier, A., Courty, P., Freund, E., US Patent 4126581, (1978).

11. Surgier, A., Freund, E., US Patent 4122110, (1978).

12. Surgier, A., Courty, P., Freund, E., US Patent 4257920, (1981).

13. Surgier, A., Freund, E., US Patent 4291126, (1981).

14. Surgier, A., Freund, E., LePage, J., US Patent 4346179, (1982).

15. Courty, P., Durand, D., Freund, E., Surgier, A., GB Patent 2118061, (1983).

16. Courty, P., Durand, D., Surgier, A., Freund, R., US Patent 4659742, (1987).

17. Courty, P. Durand, D., Freund, E., Sugier, A., *Journal of Molecular Catalysis*, 17, 241, (1982).

18. Fischer, F., *Industrial and Engineering Chemistry,* 17, 574, (1925).

19. Frolick, P. K., Cryder, D. S., *Industrial and Engineering Chemistry*, 25, 1051, (1930).

20. Graves, G., *Industrial and Engineering Chemistry*, 23, 1381, (1931).

21. Vedage, F., Himelfard, P., Simmons, G., Klier, K., *ACS Symposium Series*, 279, 295, (1985).

22. Mazanec, T., *Journal of Catalysis*, 98, 115, (1986).

23. Fox, J. R., Pesa, F. A., Curatalo, B. S., *Journal of Catalysis*, 90, 127, (1984).

24. Courty, P., Marcilly, C., Preparation of Catalysts III, Poncelet, G., Grange, P., Jacobs, P., Eds., (Elsevier, Amsterdam: 1983).

25.	Nunan, J. G., Klier, K., Young, C-W., Himelfarb, P., Herman R., *Journal of the Chemical Society, Chemical Communications*, 193, (1986).

26.	Nunan, J. G., Gobdan, C. E., Klier, K., Smith, K. J., Young, C.-W., Himelfarb, P., Herman, R. G., *Journal of Catalysis*, 113, 410, (1988).

27.	Wender, I., *Catalysis Review - Science Engineering*, 14, 97, (1976).

28.	Klier, K., *Advances in Catalysis*, 31, 243, (1982).

29.	Courty, P., Forestiere, N. Kawata, N., Ohno, T., Raimbault, C., Yoshimoto, M., Industrial Chemicals via C_1 Processes, Fahey, D., Ed., (Chapter 4, ACS Monograph 328, American Chemical Society, Washington, DC: 1987).

30.	 Fujimoto, K., Oba, T., *Applied Catalysis*, 13, 289, (1985).

31.	Calverly, E., Smith, K., *Journal of Catalysis*, 130, 616, (1991).

32.	Sheffer, Gordon, Investigation of the Catalytic Behavior and Chemical Nature of Alkali Promoted Copper and Copper-Cobalt-Chromium Oxide Catalysts for the Conversion of Synthesis Gas to Methanol and Higher Alcohols, Doctor of Philosophy Dissertation, University of Iowa, (1989).

33.	Hansen J., Joensen, F., Natural Gas Conversion, Holmen, et. al, Ed., (Elsevier Science Publisher B.V., Amsterdam: 1991).

34.	Zhou, P., "Summary of the Higher Alcohols Synthesis Workshop", U. S. Department of Energy, Pittsburgh Energy Technology Center, (1994).

35.	Anderson, B., Catalysis, Emmett, P. H., ed., (Reinhold, Volume 4, Chapter 1, New York: 1957).

36.	Mross, W.-D., *Catalysis Review – Science Engineering*, 25, 591, (1983).

37.	Dombek, B., "Heterogeneous Catalytic Process for Alcohol Fuels from Syngas", Union Carbide Corp, U.S. Department of Energy, DOE/PC/90046-T8 to T15, U.S. Government Printing Office, Washington, DC, 1996.

38.	Anderson, R., Feldman, J., Storch, H., *Industrial and Engineering Chemistry*, 44, 2418, (1952).

39.	Kung, H., Studies in Surface Science and Catalysis, Delmon, B., Yates, J. T., ed., (Volume 45, Chapter 11, Elsevier, New York: 1989).

40.   Ziolkowski, J., *Journal of Catalysis*, <u>80</u>, 263, (1983).

41.   Mitchell, H., Trifiro, F., *Journal of The Chemical Society (A)*, 3183, (1970).

42.   Mori, K., Inomata, M., Miyamoto, A., Yurakami, Y*., Journal of Physical Chemistry*, <u>87</u>, 2564, (1983).

43.   Iwamoto, M., Yoda, Y., Tamazoe, N., Seiyama, T., *Journal of Physical Chemistry*, <u>82</u>, 2564, (1978).

44.   Yang, B. L., Kung, M. C., Kung, H. H., *Journal of Catalysis*, <u>89</u>, 172, (1984).

45.   Grasselli, K., Burrington, D., Tilley, J., *Advances in Catalysis*, <u>30</u>, 133, (1980).

46.   Zhdan, P. A., Shepelin, A. P., Osipova, Z. G., Sokolovskii, V. D., *Journal of Catalysis*, <u>58</u>, 8, (1979).

47.   Ai, M., Ikawa, T., *Journal of Catalysis*, <u>40</u>, 203, (1975).

48.   Haber, J., Jenas, J., Schiavello, M., Tilley, J., *Journal of Catalysis*, <u>82</u>, 395, (1983).

49.   Brazdil, J. F., Glaeser, L. C., Grasselli, R. K., *Journal of Catalysis*, <u>81</u>, 142, (1983).

50.   Harvey, E., <u>Spectrochemical Procedures</u>, (Glendate, California: 1953).

51.   Rossini, E., et. al., "Selected Values of Chemical Thermodynamic Properties", Circ. Natl. Bureau of Standards No. 500.

52.   Wang, J., <u>Mechanistic Investigation of Higher Alcohol Synthesis from CO/H$_2$ over Cobalt-Copper Based Catalysts</u>, Doctor of Philosophy Dissertation, University of Pittsburgh, (1994).

53.   Dalmon, A., Chaumette, P., Mirodatos., *Catalysis Today*, <u>15</u>, 101, (1992).

54.   Courty, P., Durand, D., Freund, E., Sugier, A., *Journal of Molecular Catalysis*, <u>17</u>, 241, (1982).

55.   Xu, X., Scholten, F., *Applied Catalysis*, <u>82</u>, 91, (1992).

56.   Di Cosimo, J. I., Apestegufa, C. R., *Journal of Catalysis*, <u>116</u>, 71, (1989).

57.   Baker, E., Burch, R., Niu, Y., *Applied Catalysis*, <u>73</u>, 135, (1991).

58.   Di Cosimo, J. I., Marchi, A. J., Apestegufa, C. R., *Journal of Catalysis*, 134, 594, (1992).

59.   Baker, E., Burch, R., Hibble, J., Loader, K., *Applied Catalysis*, 65, 281, (1990).

60.   Baker, E., Burch, R., Golunski, E., *Applied Catalysis*, 53, 279, (1989).

61.   Trevino, H., <u>Manganese as Promoter of the Formation of Higher Oxygenates from CO Hydrogenation over Rhodium Catalysts</u>, Doctor of Philosophy Dissertation, Northwestern University, Evanston, Illinois, (1997).

62.   Mann, M., "Technical and Economic Assessment of Producing Hydrogen and Reforming Syngas from the Battelle Indirectly Heated Biomass Gasifier", National Renewable Energy Laboratory, U.S. Department of Energy, DE95009275, U.S. Government Printing Office, Washington, DC, (1995).

63.   Akundi, M., "Investigation of Syngas Interactions in Alcohol Synthesis Catalysts", Xavier University of Louisiana, U.S. Department of Energy, DOE/MT/93013, U.S. Government Printing Office, Washington, DC, (1998).

64.   Barger, P., Spehlmann, B., Gajda, G., "Development of a Catalyst for Conversion of Syngas Derived Materials to Isobutylene", U.S. Department of Energy, DOE/PC/90042, U.S. Government Printing Office, Washington, DC, (1996).

65.   Klier, K., Herman, R., "Ethanol Synthesis and Water Gas Shift over Bifunctional Sulfide Catalysts", Lehigh University, U.S. Department of Energy, DOE/PC/91301, U.S. Government Printing Office, Washington, DC, (1995).

66.   Anderson, R., <u>Catalysis</u>, Emmett, P. H., ed., (Reinhold, Volume 4, Chapter 1, New York: 1957).

67.   Storch, H., Columbic, N., Anderson, R., <u>The Fischer-Tropsch Synthesis</u>, (Wiley, New York: 1951).

68.   Blomberg, M. R. A., Karlsson, C. A. M., Siegbaln, P. E. M., *Journal of Physical Chemistry*, 97, 9341, (1993).

69.   Satterfield, C., <u>Heterogeneous Catalysis in Industrial Practice</u>", (McGraw Hill, New York: 1991).

CHAPTER III

HIGHER ALCOHOL SYNTHESIS

3.1.   Catalyst Preparation

Catalyst CB1(1) was prepared by mixing 10 g of chromic anhydride, CrO_3, 28.35 g of copper nitrate, $Cu(NO_3)_2$, and 14.95 g of cobalt carbonate, $CoCO_3$. After all "precursor" metal salts were well mixed, 28.46 g of deionized water was added to the mixture and constantly stirred for about 4 minutes. The mixture was then left for degassing for 5 minutes. After the gas evolution had ceased, 6.83 g of citric acid was added. The solution was then heated for 10 minutes. After some amount of water evaporated, the resulting solution was dried in the oven for 2 hours at 200°C, and calcined at 450°C for 3 hours. To prepare the promoter, deionized water was added to 45% by weight KOH solution to obtain 2.5% by weight KOH solution. Then, the calcined catalyst was ground and impregnated with 25.2 g of 2.5% KOH solution. The remaining product was dried for 1 hour at 200°C. The catalyst powder was crushed and pelletized to 13 x 8 mm tablets under 10720 psi force. Each pellet was then broken into four pieces. The catalyst compositions were confirmed using atomic adsorption spectroscopy to be: 38.18 wt% Cu, 34.23 wt% Co, 25.41 wt% Cr, and 2.17 wt% K.

Catalyst CB1(2) was prepared by the similar procedure as catalyst CB1(1). Since the smaller beaker was used and gas evolution occurred, the solution in the beaker

overflowed. Half of the solution was then transferred to another beaker. Therefore, inhomogenity was observed and the catalyst was not suitable for the reactor testing. Instead, the CB1(2) sample was used to test the effect of promoter.

Catalyst CB1(3) was prepared by mixing 10 g of chromic anhydride, CrO_3, 28.35 g of copper nitrate, $Cu(NO_3)_2$, and 14.95 g of cobalt carbonate, $CoCO_3$. After all precursors were well mixed, 28.46 g of deionized water was and constantly stirred for about 20 minutes. After the gas evolution had ceased, 6.83 g of citric acid was added and waited for 3 minute. To promote the catalyst, 25.2 g of 2.5% by weight KOH solution was added to the mixture. The obtained solution was evaporated under vacuum in a 1200W rotary evaporator Brinkmann (B-461) for 10 hours at 70°C to form a thick slurry. The slurry was heated overnight in the oven at 100°C, but due to a furnace malfunction, the temperature dropped to 25°C. The next day, the solution was heated to 185°C for 2 hours. The obtained powder was transferred to a 1 inch Pyrex tube cylinder and heated with the air flow set at 190 cm^3/min. The temperature was ramped 5°C per min to 450°C and heated for 3 hours. Since the reaction is highly exothermic, the calcination temperature was continuously monitored with a thermocouple imbedded within the catalyst. It was observed that at approximately 260°C, the catalyst rapidly decomposed, and brown smoke with fumes was released. The calcined powder was crushed and pelletized to 5 x 5 mm tablets under 14500 psi force. Finally, the pellets were reheated with the given rate of air at 400°C for 2 hours.

3.2.   Experimental Apparatus

The schematic of the higher alcohol synthesis apparatus is shown in Figure 3.1.

First, synthesis gas was introduced into the 5 psig storage tank, while nitrogen gas was
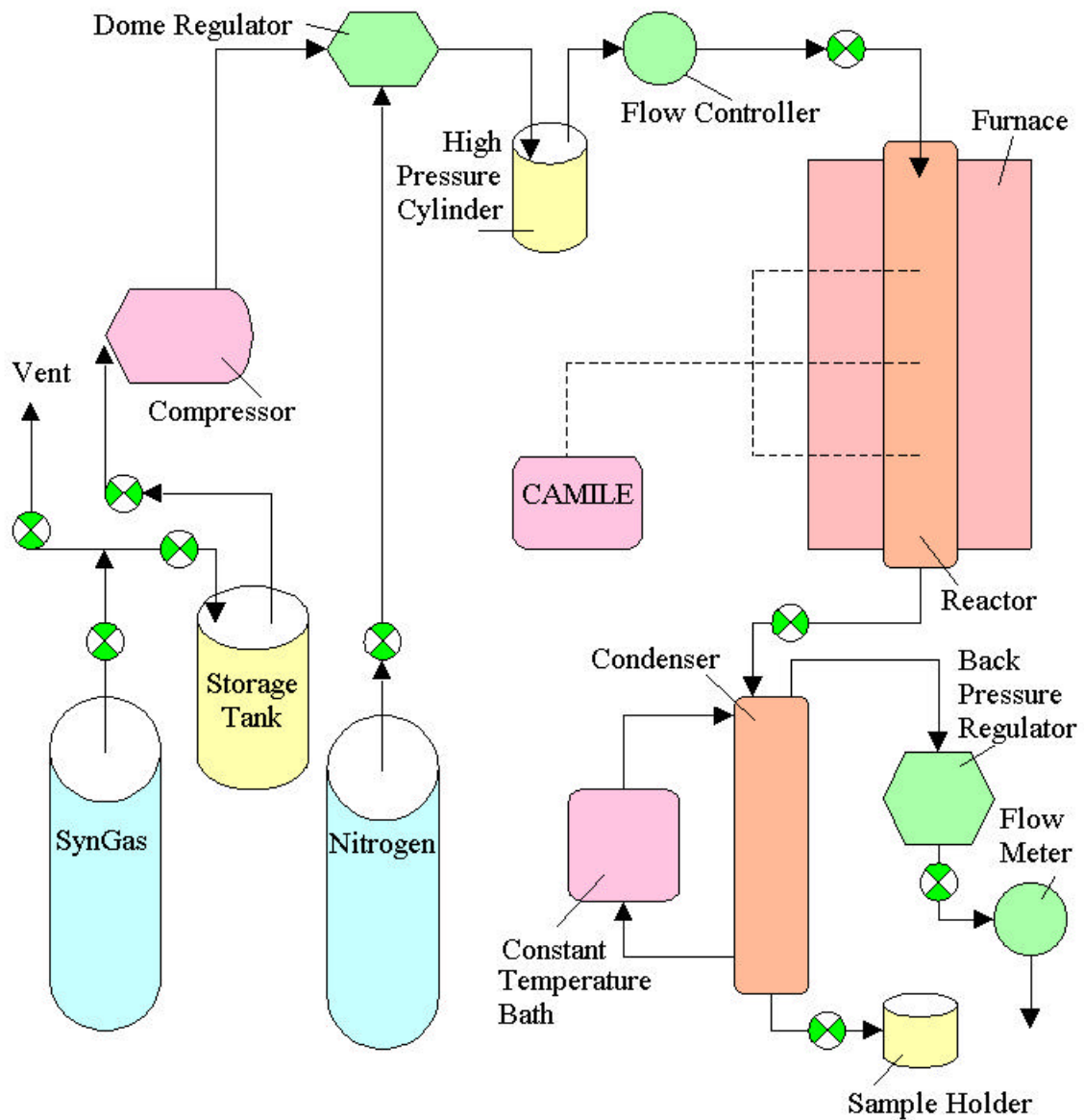
Figure 3.1. Schematic of Higher Alcohol Synthesis Process

used for pressure adjustment of the reactor. The synthesis gas mixture at less than 5 psig in storage tank was then introduced to a compressor. The high pressure discharge synthesis gas passed through a dome regulator, which was connected to a high pressure cylinder and a Brooks mass flow controller 5850TR. Synthesis gas was charged to the reactor, where it was heated by a three heating zone reactor furnace. The three heating zone temperatures of the furnace were controlled and individually monitored by a CAMILE Data Acquisition and Control System. The product gas from the reactor was introduced to the condenser, which condensed the liquid products by utilizing cooling water from the constant temperature bath. The liquid products were then collected in the sample holder and analyzed by using an HP 5890 GC with Poraplot Q column equipped with an HP 5971 Model mass spectrometer. The gas from the condenser then passed through a Tescom 2500 psi back pressure regulator and a Brooks 5850TR flow meter so that the outlet gas flowrate could be monitored.

The pilot scale reactor consisted of a 24 inch type 316 stainless-steel tube with 1 inch ID. The reactor was fully packed with glass beads and diluted with 5 g of catalyst in the reaction zone. The glass beads helped to eliminate the possibility of hot spot development. A central bore located at the center of the reactor allowed the placement of the thermocouples to monitor the temperature of the catalyst bed. The reactor could be operated up to 500°C and 2000 psig. The CAMILE Data Acquisition and Control System was used to monitor and control the process and also used as an integral part of the safe shutdown system. If the temperature exceeded the specified limit, the automatic shutdown sequences would be triggered.

The feed gas was a mixture of 2% nitrogen, 13% carbon dioxide, 66% carbon monoxide, and 19% hydrogen by volume. A gas mixture of 52% hydrogen and 48% carbon monoxide by volume was also used to investigate the effect of the carbon dioxide free synthesis gas on the reaction. The charging of the feed gas to the storage tank was accomplished using a purge valve to maintain the gas pressure inside the tank at a pressure lower than the storage tank pressure. A back pressure regulator located downstream of the reactor was used to maintain the elevated reactor pressure. The sampling of the product stream was accomplished using a valve assembly, which was designed so that either a liquid or a gas sample could be taken. The obtained liquid product was then analyzed by GC/MS.

Due to the oxide nature of the catalyst, the catalyst was reduced in situ with a 3 to 5% hydrogen/balance nitrogen mixture at the flowrate of 450 cm^3/min for 44 hours at 220°C and 200 psig. This served to increase surface copper metal, remove any impurities, and ensure catalyst stability. After the catalyst had been reduced, the system was cooled to room temperature, then pressurized with synthesis gas to the desired operating pressure. The desired flowrate had also been set using the mass flow controller. Again, the process temperatures and pressure were monitored and allowed to reach steady state at each set of operating conditions.

3.3.   Results and Discussion

The reaction was performed at pressures ranging from 900 to 1800 psig and temperatures in the range of 275 to 355°C. The experimental conditions and obtained reaction data are shown in Table 3.1 in which both production rate and weight percentage

are tabulated along with temperature, pressure, space velocity, and inlet gas composition. The reaction kinetics are also influenced by the catalyst shape, pore characteristics, age, sintering, and internal depositions. The analysis data from Table 3.1 at high temperature of catalyst CB1(1) is used for temperature effect discussion only and excluded from other discussions due to the exothermicity and run-away behavior of the reaction.

Table 3.1. Experimental Conditions and Reaction Data

Sample ID	T °C	P psig	GHSV	H₂	CO	CO₂	N₂	Yield g kg-cat⁻¹ hr⁻¹	Water	C₁OH	C₂OH	C₃₊OH
					Feed Gas (vol. %)				Liquid Products (wt. %)			
CB(1)R2#1	282	1750	3500	66	19	13	2	25.3	77.6	13.2	3.2	6.0
CB(1)R2#2	281	1750	3500	66	19	13	2		59.6	23.0	5.6	11.9
CB(1)R2#3	281	1750	3500	66	19	13	2	25.3	67.2	19.3	3.6	9.9
CB(1)R2#4	281	1750	3500	66	19	13	2	7.0	68.4	16.3	3.0	12.3
CB(1)R2#5	281	1750	3500	66	19	13	2		66.9	15.7	3.0	14.3
CB(1)R3#1	292	1750	3500	66	19	13	2	76.9	62.3	21.7	5.1	10.9
CB(1)R3#2	292	1750	3500	66	19	13	2	16.4	60.9	22.8	5.3	11.1
CB(1)R3#3	380	1750	3500	66	19	13	2	204.6	85.6	4.2	1.5	8.8
CB(1)R3#4	359	1750	4000	66	19	13	2		89.7	1.2	0.8	8.3
CB(1)R4#1	321	1750	8000	66	19	13	2	210.1	57.0	22.8	7.2	13.0
CB(1)R4#2	341	1750	8000	66	19	13	2	260.7	54.4	26.4	8.5	10.6
CB(1)R4#3	339	1750	8000	66	19	13	2	270.0	56.5	26.9	8.4	8.2
CB(3)R1#1	253	1800	6700	66	19	13	2	35.4	78.1	5.3	4.9	11.7
CB(3)R1#2	251	1800	6700	66	19	13	2	36.0	71.0	7.4	7.2	14.3
CB(3)R1#3	268	1800	6700	66	19	13	2	84.3	63.7	14.9	9.6	11.7
CB(3)R1#4	266	900	4000	66	19	13	2	50.0	51.0	19.1	13.1	16.8
CB(3)R1#5	271	900	4000	52	48			35.0	52.0	18.2	13.6	16.2
CB(3)R1#6	271	900	4000	52	48			11.5	52.1	17.4	14.0	16.6
CB(3)R1#7	271	900	4000	52	48			11.0	46.2	20.9	17.1	15.8
CB(3)R1#8	271	900	4000	52	48			14.0	48.6	18.4	17.0	16.0
CB(3)R1#9	269	900	4000	52	48			8.5	44.7	19.6	18.8	16.9
CB(3)R1#10	279	900	4000	52	48			24.0	45.9	22.6	15.7	15.9
CB(3)R1#11	279	1775	4000	52	48			41.6	31.1	28.8	20.3	19.8
CB(3)R1#12	279	1775	4000	52	48			30.0	23.8	31.2	23.8	21.2

C_1OH is methanol, C_2OH is ethanol, $C_{3+}OH$ is other alcohols.

3.3.1. Effect of Temperature

No temperature gradients were observed during pretreatment, but during the synthesis gas reaction, excessive exotherms were observed. The catalyst zone temperature of CB1(1) reaction rapidly rose to 525°C in 15 minutes after the operating temperature reached 250°C.   This was most likely due to the methanation or hydrocarbon formation. In order to prevent this runaway reaction, Stiles et al. (9) recommended that the CO gas content be held below 12% by volume so that the unreacted hydrogen acts as a heatsink to dissipate heat, but higher CO gas content is recommended for formation of higher alcohols. After exothermicity ceased, the operating temperature had to be increased in order to achieve the normal yields because the earlier operating temperature was no longer activating the catalyst.

The average performance of the catalysts within a temperature range is shown Figure 3.2 in which high temperature is more favorable for the average alcohol production rate. The production rate of methanol and higher alcohols increased for both catalysts CB1(1) and CB1(3). For CB1(3) catalyst, methanol rate increased from 2.2 to 10.8 g kg-cat^{-1} hr^{-1} while ethanol increased from 2.1 to 7.9 g kg-cat^{-1} hr^{-1}, and C3+OH increased from 4.7 to 7.3 g kg-cat^{-1} hr^{-1} when temperature increased from 250 to 280°C. The production rate of CB1(1) catalyst was much higher compared to CB1(3) catalyst with an increase in temperature. For CB1(1) catalyst, the methanol rate increased from 3.5 to 62.7 g kg-cat^{-1} hr^{-1} while ethanol increased from 0.7 to 19.9 g kg-cat^{-1} hr^{-1}, and C3+OH increased from 1.9 to 26.2 g kg-cat^{-1} hr^{-1} when temperature increased from 280 to 325°C. However, at 280°C, catalyst CB1(3) yielded a higher production rate of
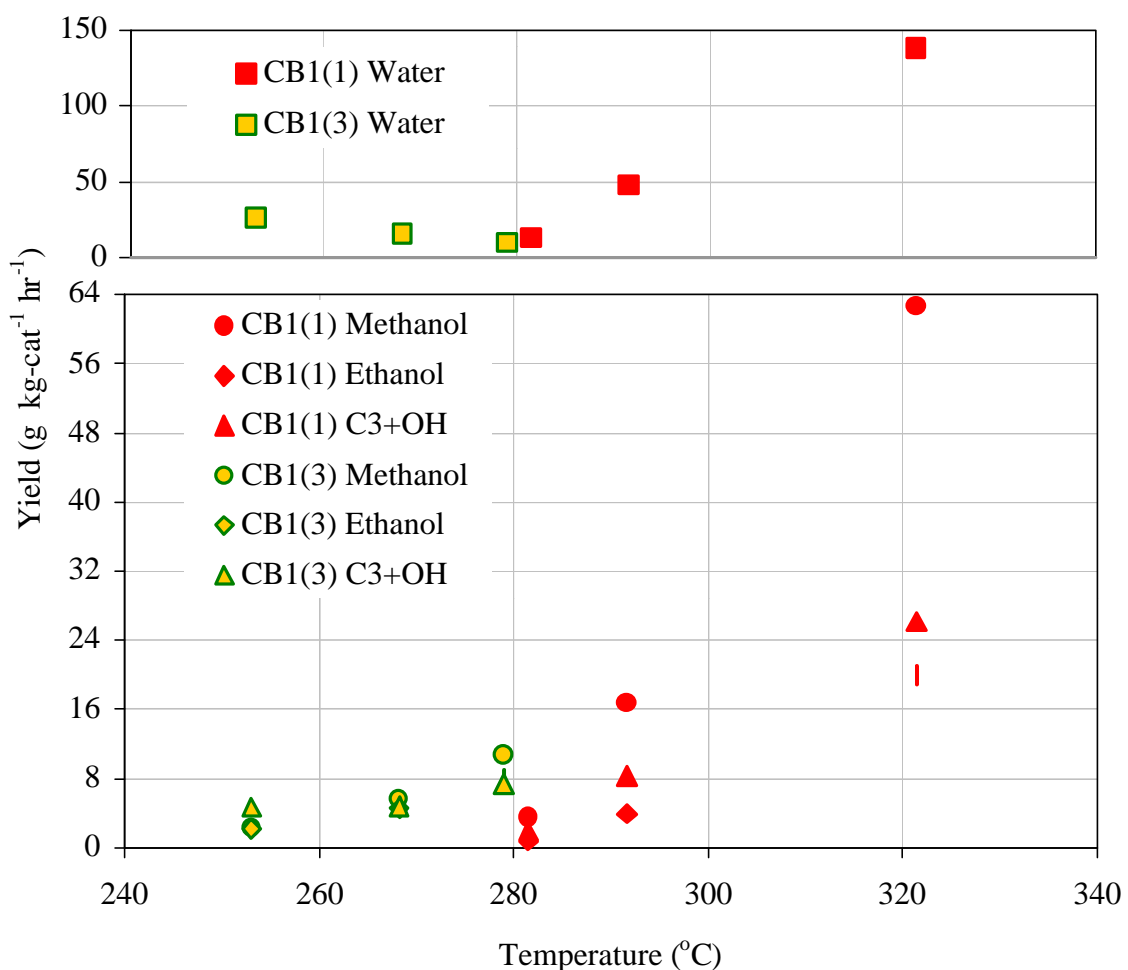
Figure 3.2. Average Yields as Function of Temperature

alcohols compared to that of CB1(1) catalyst since the exothermic reaction had been

occurred earlier in CB1(1) reaction. Thus, 285°C was the initial reaction temperature of

CB1(1). The highest yield of alcohols for CB1(1) is obtained at 325°C, but the catalyst

will be sinter and not be stable at this temperature. It was also observed that the water

production rate decreased from 26.6 to 9.8 g kg-cat^{-1} hr^{-1} for the CB1(3) catalyst while it

increased from 13.1 to 138.2 g kg-cat^{-1} hr^{-1} for the CB1(1) catalyst. Therefore, higher

temperature enhances productivity of alcohols, but can also lead to catalyst deactivation due to sintering (1), or simply the alcohol synthesis reaction will change to methanation synthesis or other hydrocarbon synthesis. The catalysts have a limited range of operating temperature from 275 to 300°C since the catalyst deactivation due to sintering is normally a concern above 300°C for copper catalysts (6).

3.3.2. Effect of Pressure

The effect of pressure on higher alcohol production is shown in Figure 3.3. Increasing the pressure will shift the equilibrium toward the product side and change the product distribution (2, 3). At approximately 1800 psig, methanol production of CB1(3) catalyst was higher while ethanol production was lower to that of CB1(1) catalyst with CO_2 syngas. The production rates of methanol, ethanol, C3+OH, and water were 10.1, 2.2, 6.3, and 40.6 g kg-cat^{-1} hr^{-1}, respectively, for CB1(1) catalyst, and 4.78, 3.77, 6.53, 36.8 g kg-cat^{-1} hr^{-1}, respectively, for CB1(3) catalyst. As the pressure increased from 900 to 1750, the average productivity of CB1(3) increased from 4.3 to 4.78 g kg-cat^{-1} hr^{-1} for methanol, from 3.4 to 3.77 g kg-cat^{-1} hr^{-1} for ethanol, and from 3.4 to 6.53 g kg-cat^{-1} hr^{-1} for C3+OH. The water production rate also increased. Therefore, the efficiency of the operation is not significantly enhanced by high pressure. The expected productivity was not obtained for both catalysts due to the operating pressure range of 900 to 1800 psig. However, the results are in agreement with Stiles et al. (9), who stated that the best operating pressure for methanol and higher alcohols in the 20-30 wt% range is 2500-3500 psi, and in the range of 1200-1500 psi, the productivity is unacceptably low but a high ratio of higher alcohol.
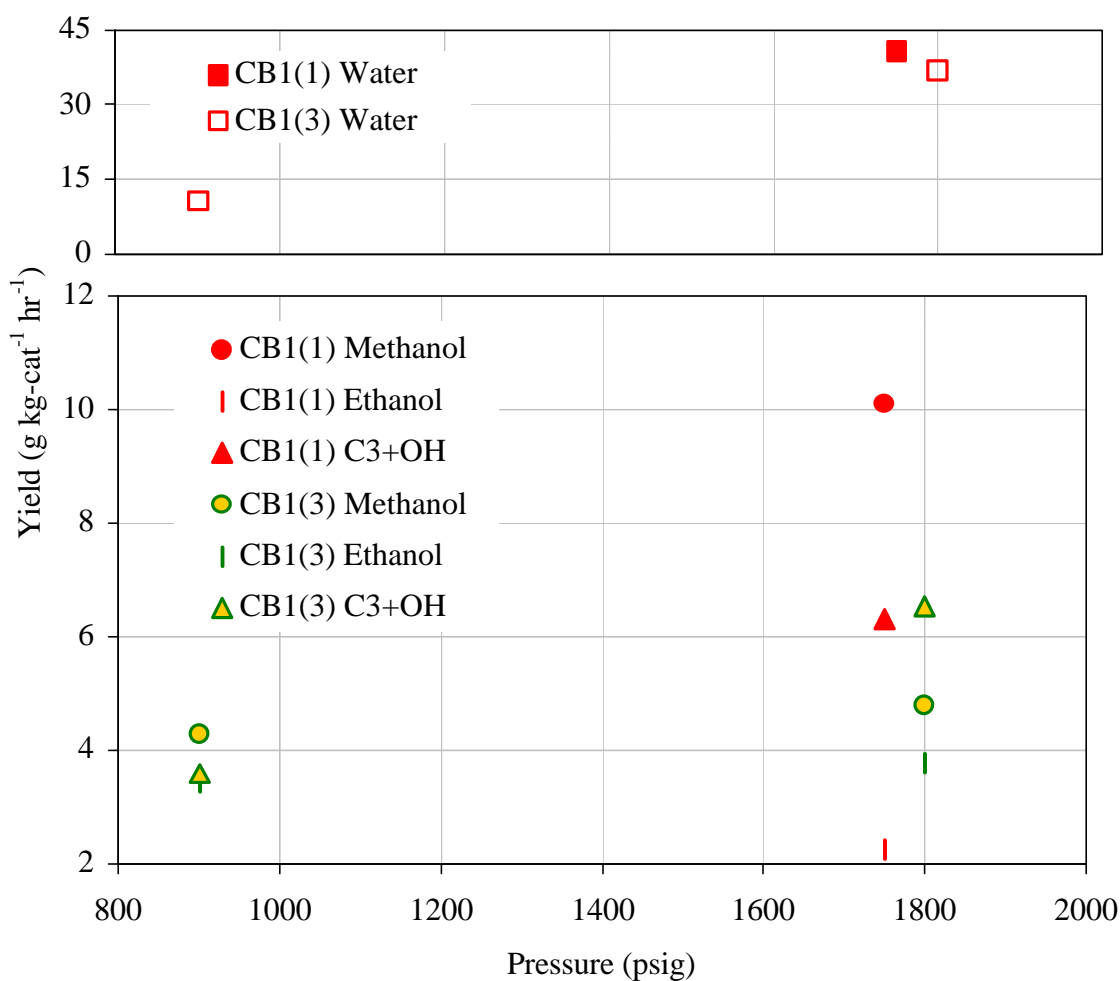
Figure 3.3. Production Rates as a Function of Pressure

The yields from CB1(3) catalyst as a function of pressure at constant GHSV of 4000 hr^{-1} are shown in Figure 3.4. According to Stiles et al. (9), methanol production is sharply increased with the pressure, while higher alcohol production is slightly higher than at low pressure. Instead, methanol production increased from 3.4 to 10.1 g kg-cat^{-1} hr^{-1}, while ethanol production rate increased from 2.8 to 7.9 g kg-cat^{-1} hr^{-1}, and C3+OH production rate increased from 2.8 to 7.4 g kg-cat^{-1} hr^{-1} as the pressure increased from

900 to 1750 psig in the reaction with CO_2 free syngas. While alcohol yields significantly increased, the water production rate slightly changed from 8.4 to 9.8 g kg-cat^{-1} hr^{-1}. Thus, an increase in pressure does have a significant effect on higher alcohol yields in this case. At 900 psig and 4000 h^{-1}, the alcohols and water productivity are higher with the presence of CO_2 in syngas. The productivity of methanol, ethanol, and C3+OH were 9.6, 6.5, and 8.4 g kg-cat^{-1} hr^{-1}, respectively in CO_2 syngas compared to 3.4, 2.8, and 2.4 g kg-cat^{-1} hr^{-1}, respectively, in CO_2 free syngas.
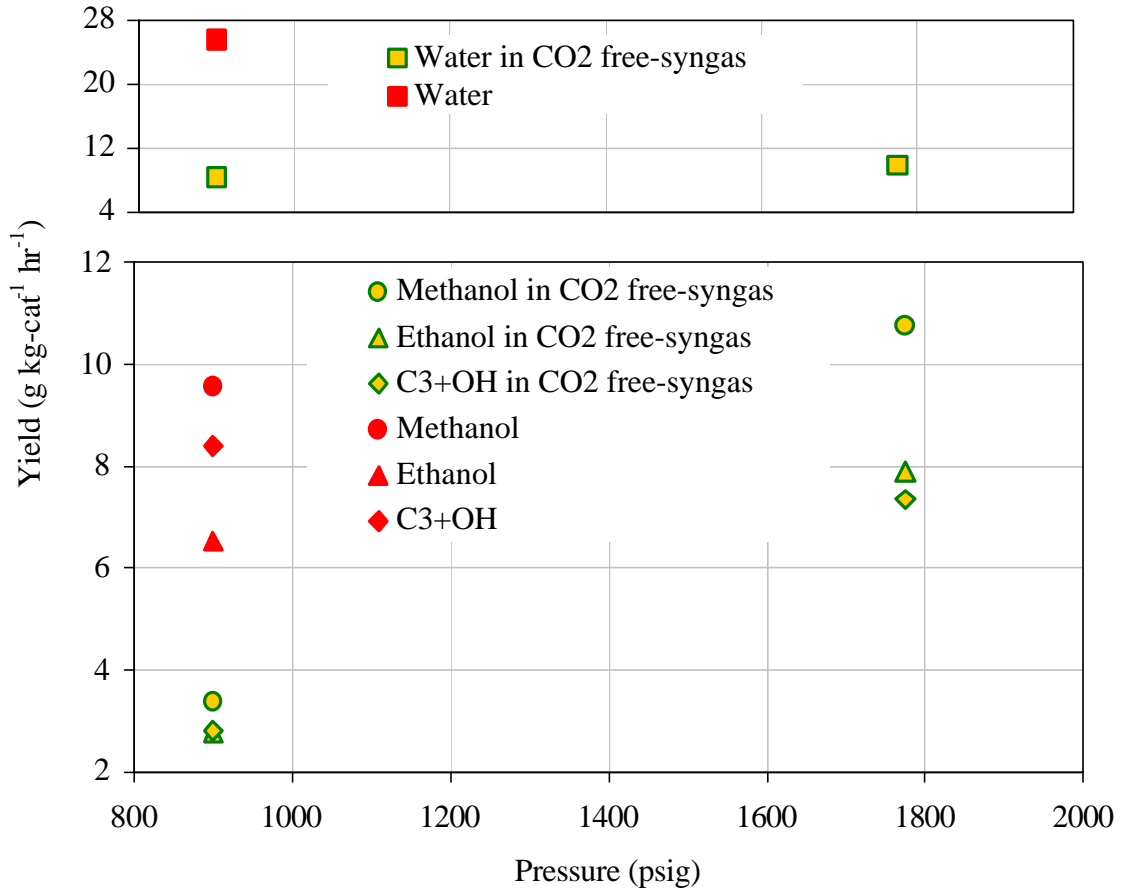
Figure 3.4. Average Yields of CB1(3) Catalyst at 4000 GHSV

3.3.3. Effect of Gas Hourly Space Velocity

The effect of gas hourly space velocity on alcohol productivity is shown in Figure 3.5. The average production rate of methanol at 8000 h^{-1} of CB1(1) is much greater than those at 3500 h^{-1}, while higher alcohol productivity increased slightly. The productivity of methanol, ethanol, and C3+OH at 8000 h^{-1} of CB1(1) were 62.6, 19.9, and 26.2 g kg-cat^{-1} hr^{-1}, respectively compared to 10.1, 2.2, and 6.3 g kg-cat^{-1} hr^{-1} at 3500 h^{-1}. The increase in production rate may also be due to the temperature effect since the operating temperature range of CB1(1) is 280 to 340°C. In contrast, the alcohol productivity decreased for CB1(3) catalyst; however, this may due to the effect of carbon dioxide in syngas. So, it is concluded that increasing the space velocity does significantly alter the alcohol productivity. Nevertheless, the increase in productivity can not prove that the reactions are kinetically controlled or either partial or total mass transfer controlled (3).

Figure 3.6 shows that the alcohol rate increased with an increase in GHSV at 1800 psig with the presence of CO_2. Increasing GHSV also increased the ratio of methanol to higher alcohol. Methanol productivity of CB1(1) increased from 5.6 to 62.6 g kg-cat^{-1} hr^{-1}; ethanol increased from 1.2 to 19.9 g kg-cat^{-1} hr^{-1}; C3+OH increased from 3.3 to 26.2 g kg-cat^{-1} hr^{-1}, and water increased from 20 to 138 g kg-cat^{-1} hr^{-1}. There is no alcohol above butanol. The results are not in agreement with the idea of side reaction suppression due to the shorter contact time because the side reactions occur in the mass transfer controlled region (3, 4, and 5). Also, the increase in ethanol productivity is in contradiction with Smith et al. (16), who stated that in order to improve the selectivity with respect to higher alcohol, low space velocities have to be used for Cu/ZnO catalysts.

In addition, similar productivity was obtained from CB1(1) at 3500 psig and CB1(3) at 6700 psig. Therefore, CB1(1) catalyst is more active toward alcohol productions.
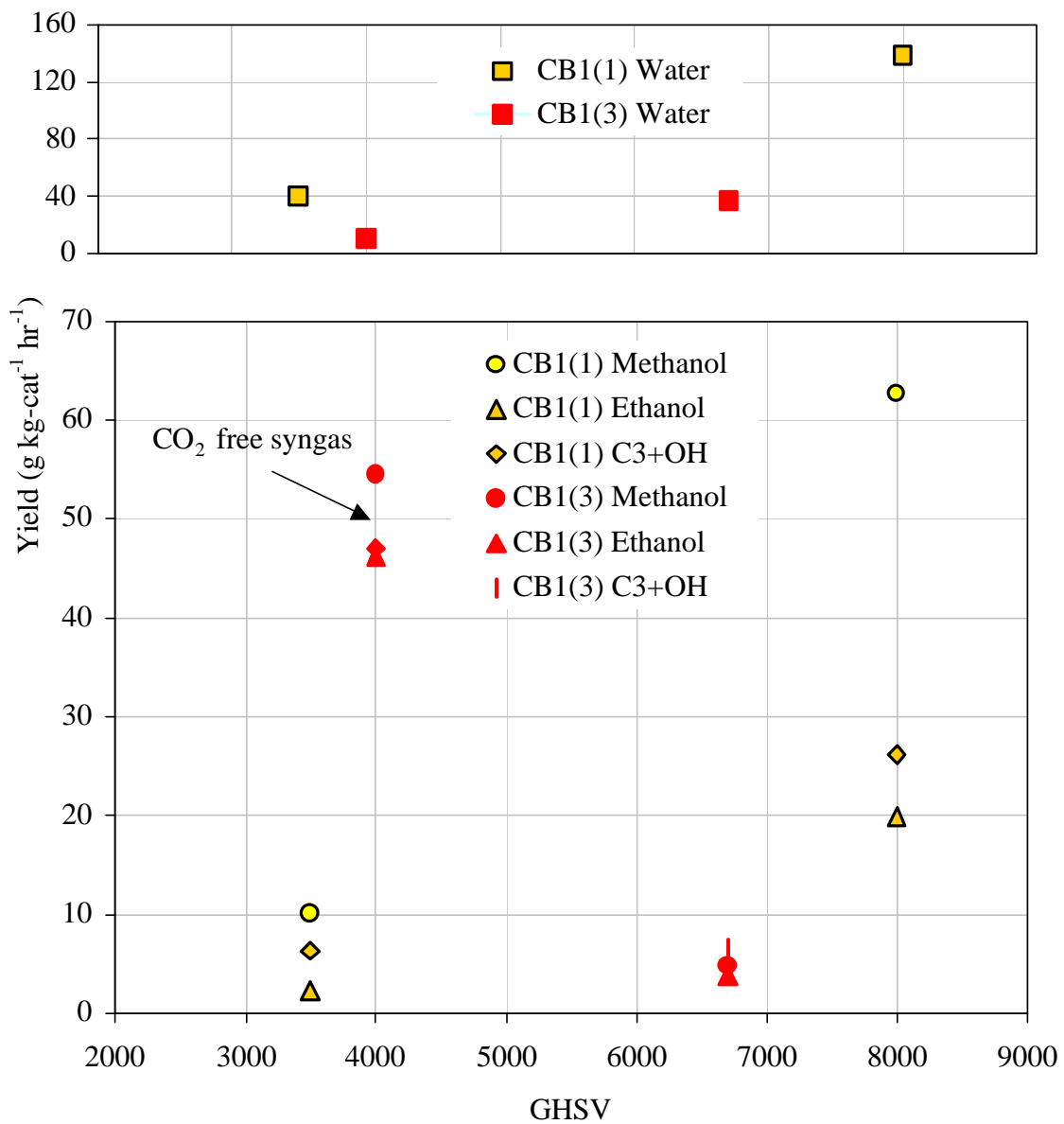
Figure 3.5. Average Yields as a Function of GHSV
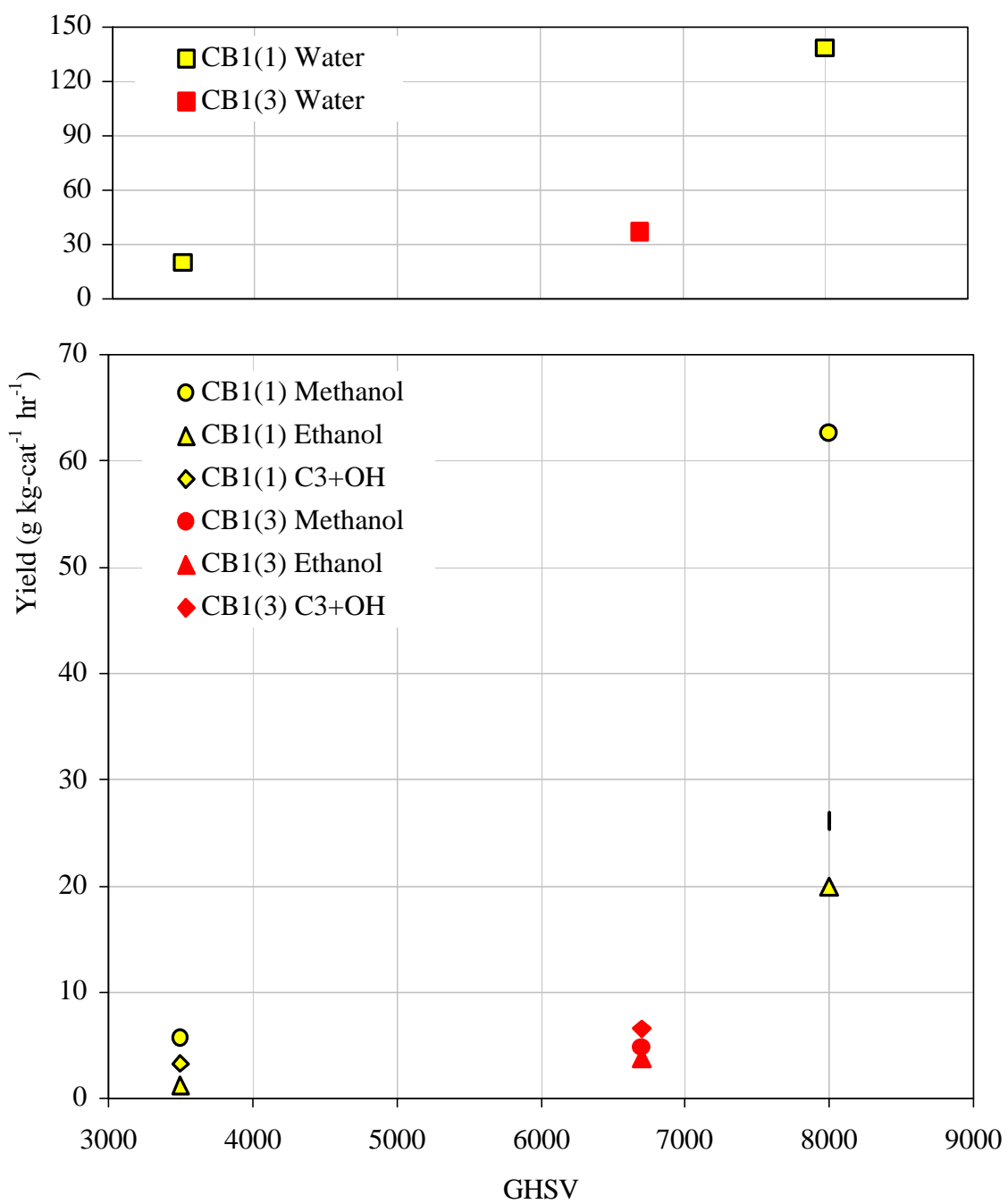
Figure 3.6. Average Yields at 1800 Psig in the Presence of CO_2

3.3.4. Effect of Carbon Dioxide

The effect of carbon dioxide on productivity is shown in Figure 3.7. The data indicated methanol and higher alcohol productivity are higher in CO_2-free syngas. The results are in agreement with Calverly et al. (6), who noted that high concentrations of CO_2 inhibit the yield of higher alcohols. Klier et al. (2) also stated that the presence of carbon dioxide in the synthesis gas is not necessary. Increases in both methanol and higher alcohol indicate that common sites and/or intermediates are involved for both syntheses. The low productivity in the presence of CO_2 is also explained by the fact that CO hydrogenation is retarded by the presence of CO_2, which is due to the competitive adsorption of CO_2 on the active sites of catalyst (7). Likewise, Tronconi et al. (14) observed decreasing higher alcohol yields when adding CO_2 over Zn-Cr-K oxide catalyst at $400^{\circ}C$ due to the poisoning of active sites by water via the water gas shift reaction. In contrast, Courty et al. (15) reported that the presence of carbon dioxide does not affect the alcohol yields over Cu-Co-Cr oxide catalyst. The decrease in methanol yield in CO_2 syngas is also confirmed by Coreron et al. (11), who stated that methanol production is maximized at 2% of CO_2 then rapidly decreases in copper-zinc catalyst reaction, which may be due to the decreasing CO partial pressure by CO_2 addition (6). Thus, CO_2 acts as a promoter at low concentration (12), and the catalyst activity would be retarded at high CO_2 concentration, but the deactivation is more severe with prolonged exposure to CO_2-free syngas (13). Unfortunately, the degree of CO_2 contribution to higher alcohol synthesis has not yet been confirmed. Addition of CO_2 also forced the production of water, which resulted in a substantial loss in carbon efficiency (8), and was harmful to

higher alcohol ratio (10). Thus, the higher alcohol synthesis feed should be free from CO_2 in order to optimize the production.
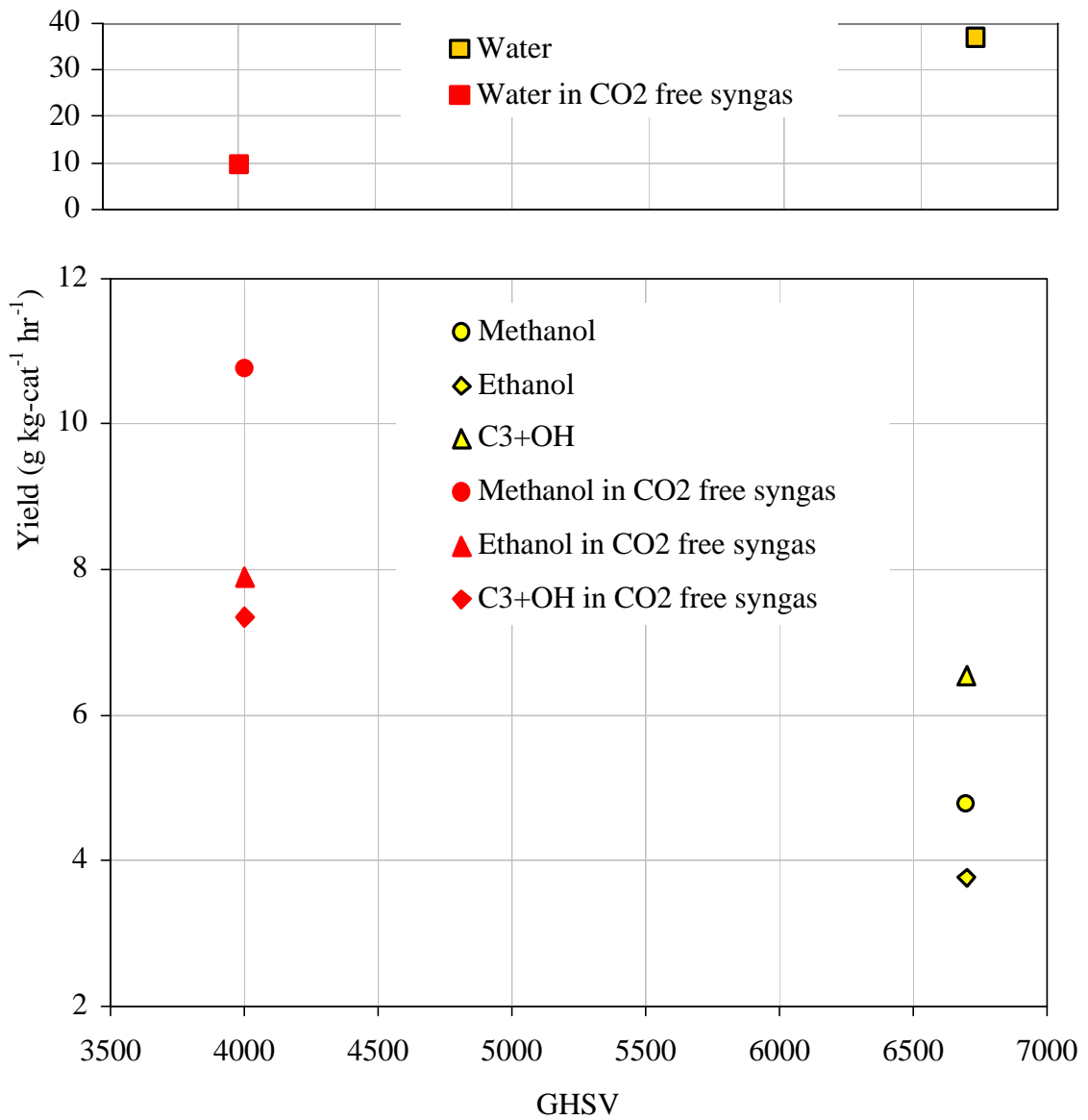
Figure 3.7. Average Yields of CB1(3) Catalyst at 1800 Psig

3.3.5. Effect of Reaction Time

According to Figures 3.8 to 3.10, the total yield and weight percentages of methanol, ethanol, C3+OH, and water are in the range of 1 to 27, 1 to 8.5, 6 to 11, and 54 to 90 g kg-cat^{-1} hr^{-1}, respectively for CB1(1) catalyst with CO_2 syngas. The methanol productivity obtained from CB1(3) catalyst is lower than CB1(1) while both ethanol and C3+OH productivity remained the same. Thus, methanol productivity is more favored with CB1(1).

The deactivation behavior of catalyst CB1(1) is shown in Figure 3.8. The maximum yield is obtained after about 94 hours from the time of the first yield. Methanol weight percentage reached a maximum after 24 hours, and then slightly decreased. The weight percentage of ethanol slightly increased and stayed constant during the run. The weight percentage of C3+OH oscillated slightly. Similar trends were observed for yield and selectivity of CB1(3) catalyst at 1800 psig, 6700 h^{-1}, and 250 to 270°C with CO_2 syngas. These results are shown in Figure 3.9. The maximum yield is observed after 30 hours. Methanol increased with time while higher alcohol slightly decreased. Figure 3.10 is the time effect of CB1(3) under low pressure and GHSV. Again, the maximum yield is obtained after 48 hours, and the distribution of yields and weight percentages are also obtained with time.

51
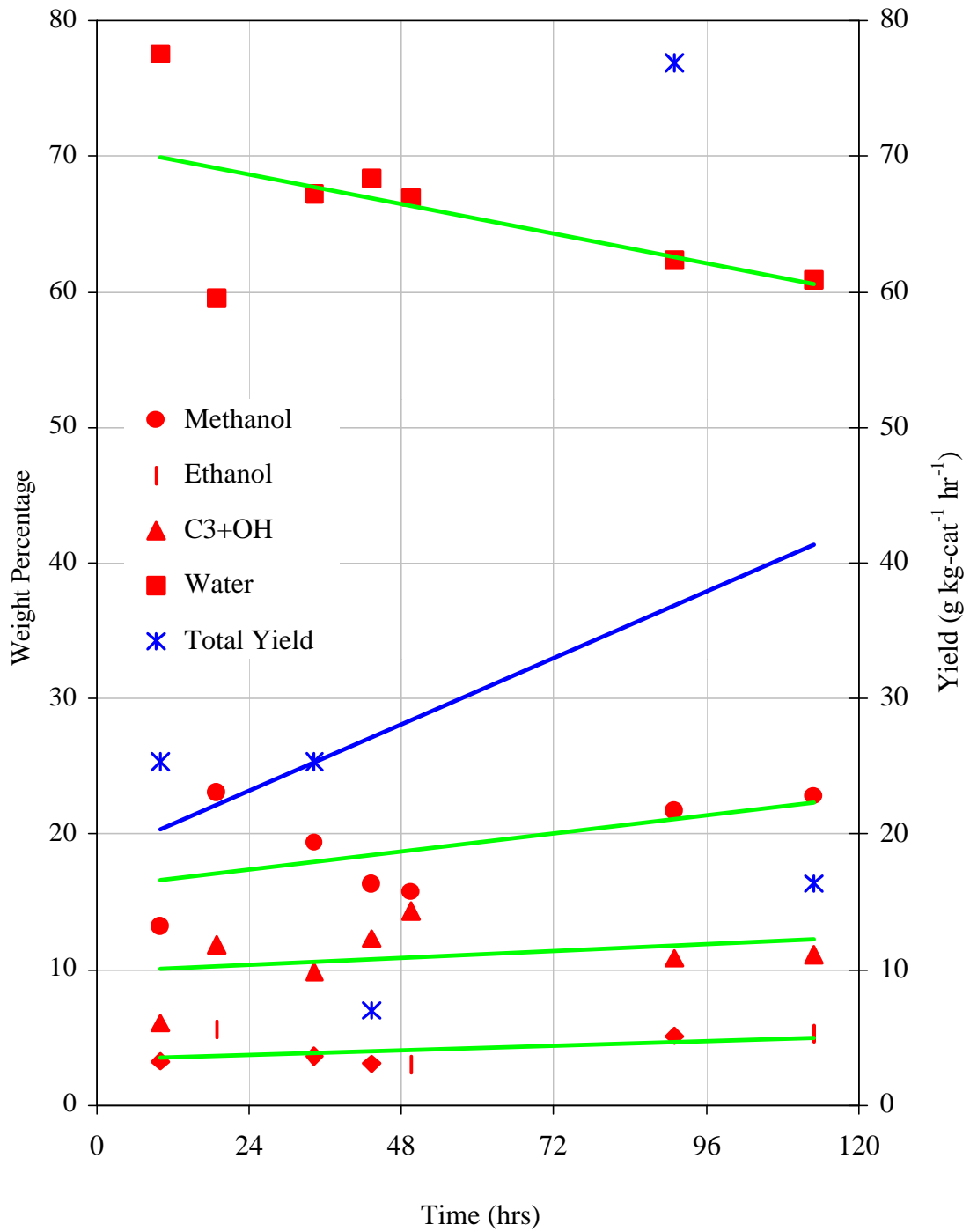
Figure 3.8. Production Rates of CB1(1) Catalyst at 1750 psig,
3500 GHSV, and 280 to 290°C with the CO_2 Syngas
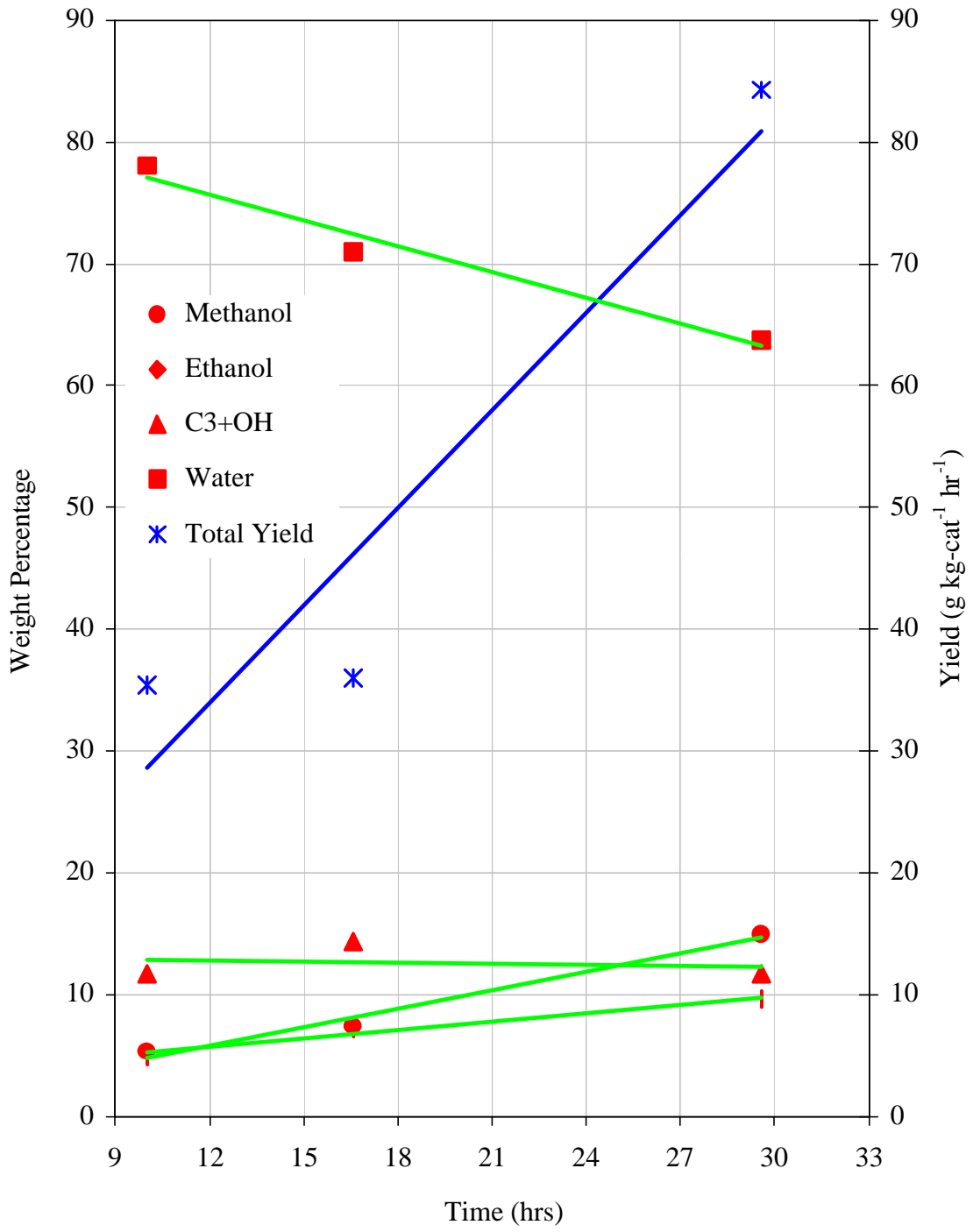
Figure 3.9. Production Rates of CB1(3) Catalyst at 1800 Psig,
6700 GHSV, and 250 to 270°C with CO_2 Syngas
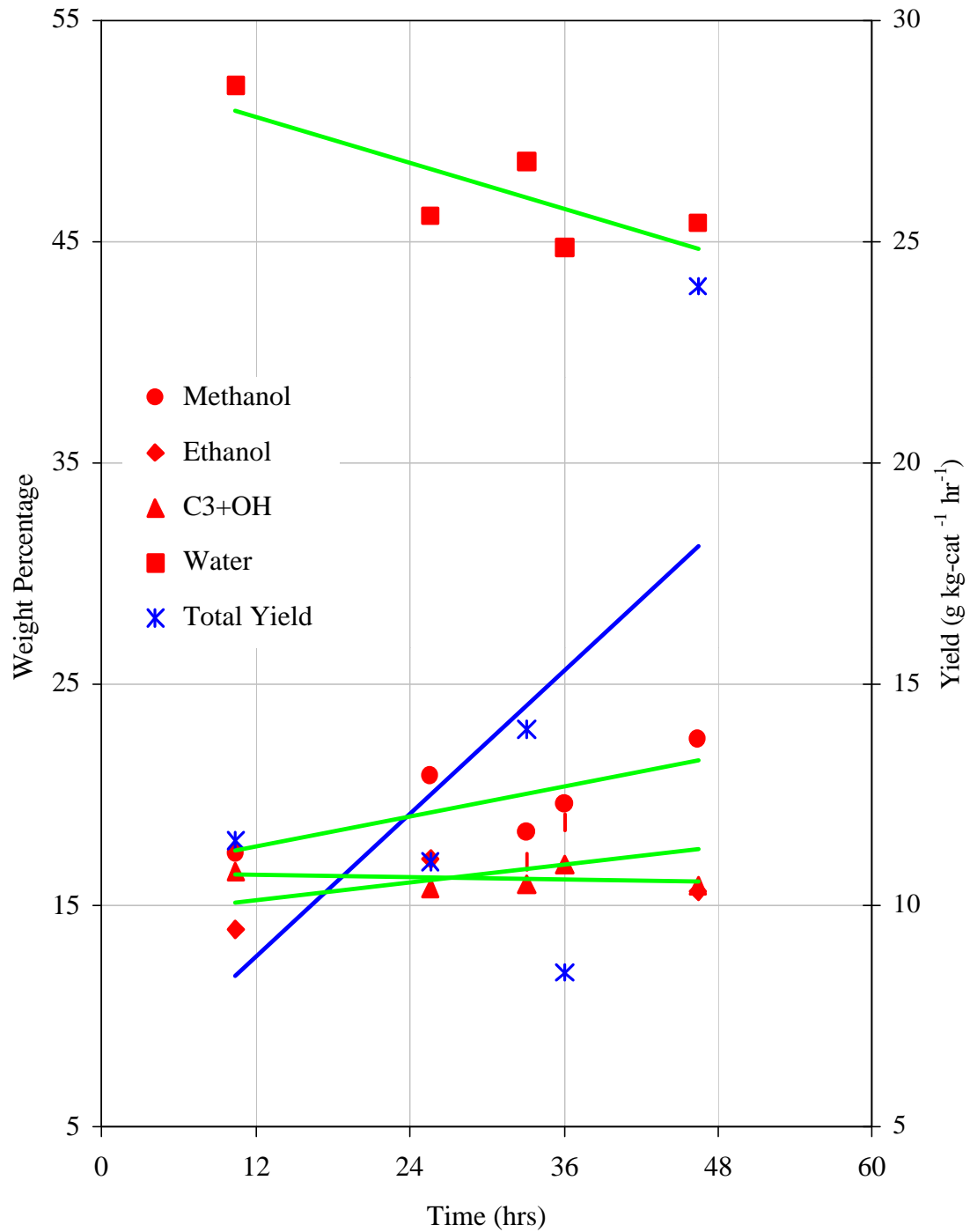
Figure 3.10. Production Rates of CB1(3) catalyst at 900 psig, 4000 GHSV, and 265 to 270°C with CO_2-Free Syngas

3.4.   Temperature Programmed Reduction

The temperature programmed reduction of the catalyst was performed by Quantachrome using a Chembet 3000. A mixture of 5 mol % hydrogen in nitrogen was flowed over the sample with a flowrate of approximately 70 cm^3/min. The temperature was linearly increased at the rate of 20°C/min to the setpoint temperature of 900°C, and 10°C/min to the setpoint of 270°C. These temperatures and rates were chosen to provide a better understanding of the reduction process at different ramping rates. The signal in mV is monitored according to the reducibility of metal species in catalyst.

The TPR profiles for the calcined catalyst at 270 and 900°C are reported in Figures 3.11 and 3.12. The similarity between the two broad peak profiles is observed. These broad peaks may be due to the combination of many reduced metal peaks within the range of reduction temperature. No minor or individual metal reduction peaks were observed. The catalyst started to reduce at 191°C at the ramping rate of 10°C/min, and 173°C at the ramping rate of 20°C. Thus, the catalyst is reduced at lower temperature at the faster rate. The rate appears to have the major influence on the reducibility of catalyst. At 250°C, the bulk reduction occurred in 48.5 minutes. At 900°C, the reduction time is more than 43.5 minutes in which the broad peak is starting from 191°C and extended 887°C. This indicated that the mixture of metals in the catalyst is reduced at different temperatures. However, the reducibility of individual metals remained unknown.
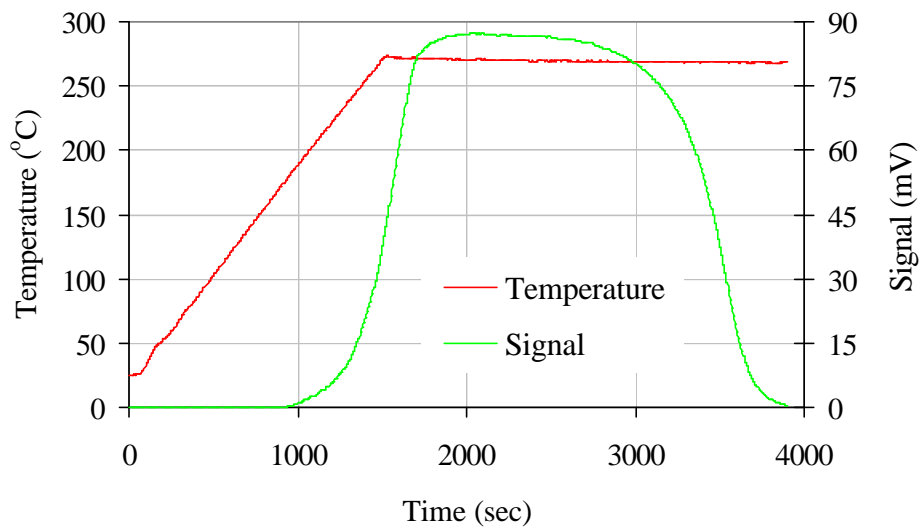
Figure 3.11. Temperature Programmed Reduction of CB1(3) at 270°C
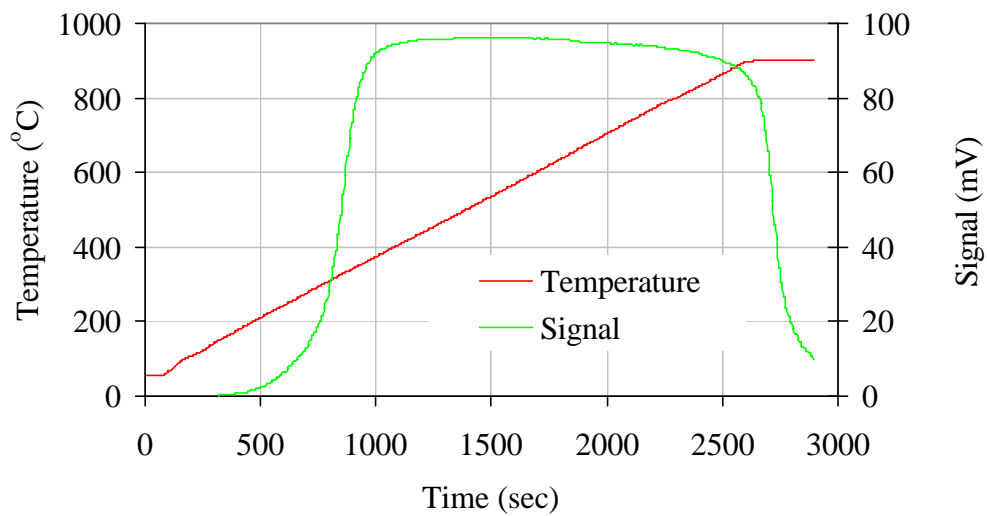
Figure 3.12. Temperature Programmed Reduction of CB1(3) at 900°C

3.5.   Scanning Electron Microscopy

Scanning Electron Microscopy is a powerful method, which can yield a great deal of morphological, physical, and chemical information about a catalyst's surface. The image obtained from SEM is due to the electrons ejected from the surface during interactions. The interactions are characterized into two groups. The first interaction is the elastic collision, which produces backscattered electrons. The primary beam electrons interact with the sample nucleus or an outer shell electron and bounce back with a negligible energy loss.   The second interaction is the inelastic collision, which yields secondary electrons in which a substantial energy loss occurs during collision. The backscattered electrons possess energies similar to the incident beam and subsequently may interact with specimen atoms to produce secondary electrons. The backscattered electron signal is weaker than the secondary electron signal due to the linear travel path. Similar to XPS, an electron from the inner shell is ejected by the beam and an electron from an outer shell will fill the vacancy. The difference in the energy of initial and final state of transition electron may be emitted as x-radiation (19).

3.5.1.   Instrumentation

The topographic information about the catalyst surface was examined with a Leo Stereoscan 360 Scanning Electron Microscope. The image is obtained when the sample surface is swept in a raster pattern with a focused beam of high-energy electrons. A raster is swept across the surface in a straight horizontal direction, then returned to its original position and shifted downward by a standard increment. The process is repeated until the desired surface has been scanned (18). The interaction between the beam and

surface produces a large number of electrons, which are eventually converted to the electronic signals shown on a cathode ray tube. The signal is then stored in the computer system and converted to an image (33).

Figures 3.13 through 3.15 show the micrographs, taken at 2000 and 5000 times of magnification of fresh CB1(1), aged CB1(1), and fresh CB1(3), respectively. Since these analyses cannot be used alone to interpret the chemical composition, the obtained micrographs are used to provide the basic understanding of the surface structure of the catalyst. It is noted that the catalyst surface is covered with small white crystallites of cobalt oxide, Co_3O_4 (17). The surface crystallites could also be copper or chromium since the potassium concentration is much smaller compared to other metals. However, no literature has been found to support this idea. In addition, the size of these small crystallites grew larger by agglomeration in the used catalyst, which may be due to sintering after the reaction. This observation is in agreement with Galarrage (17), who indicated that temperature could cause agglomeration of these small crystallites, which leads to catalyst deactivation under high temperature. The agglomeration is also caused by the inhomogenity distribution of metal precursors.
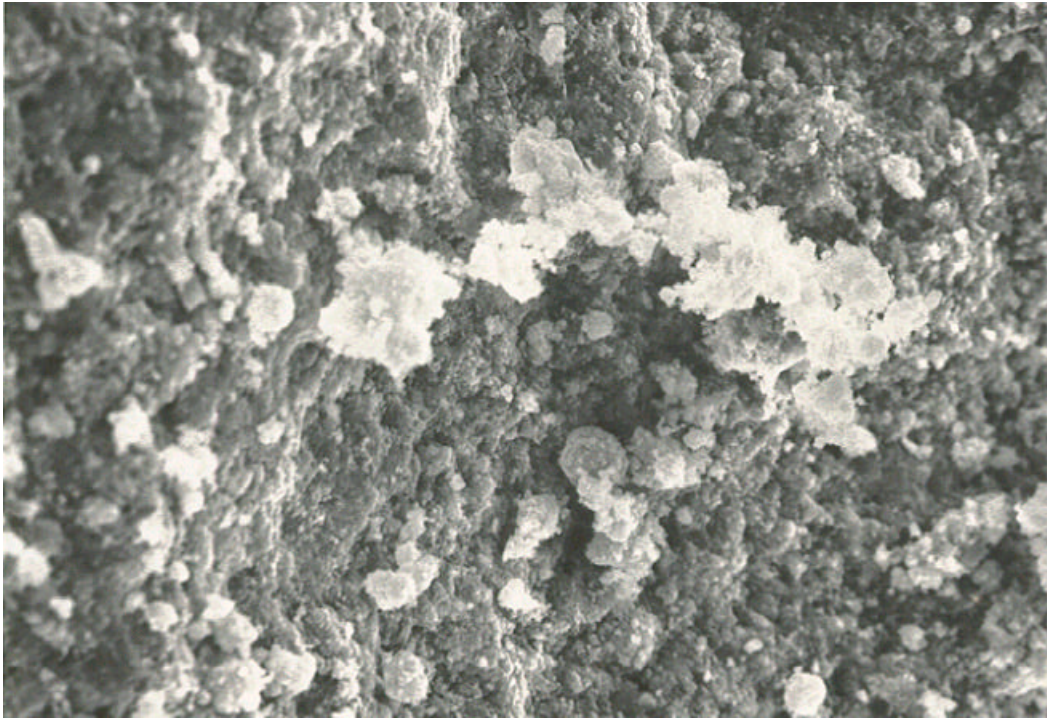
Figure 3.13. Micrograph of Fresh CB1(1) at 2000x Magnification
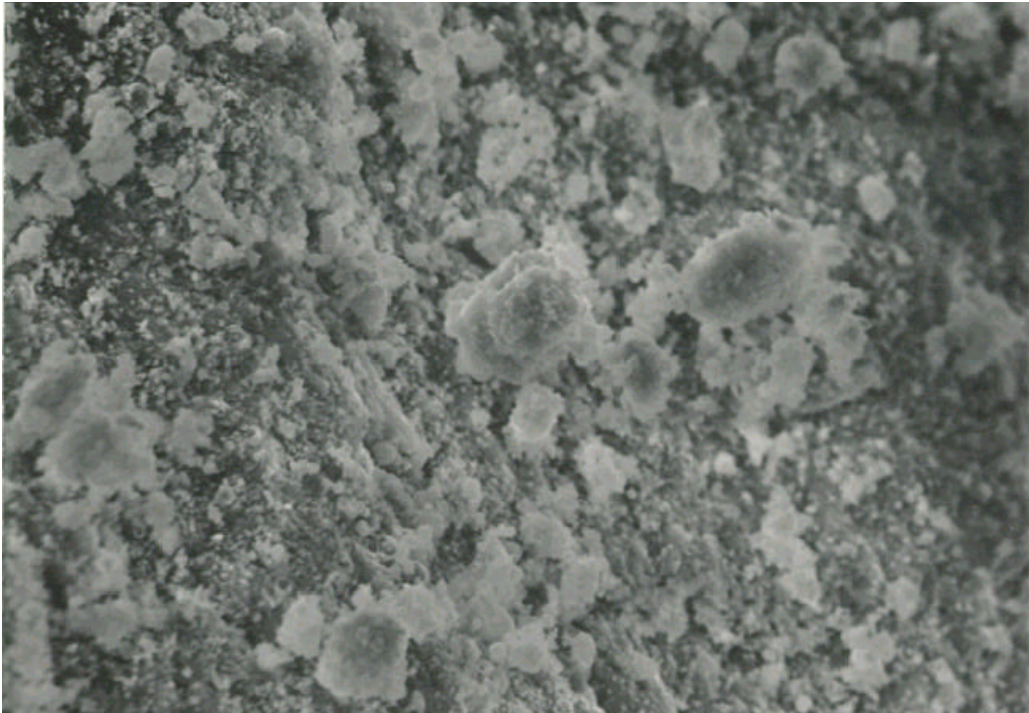
Figure 3.14. Micrograph of Aged CB1(1) at 2000x Magnification
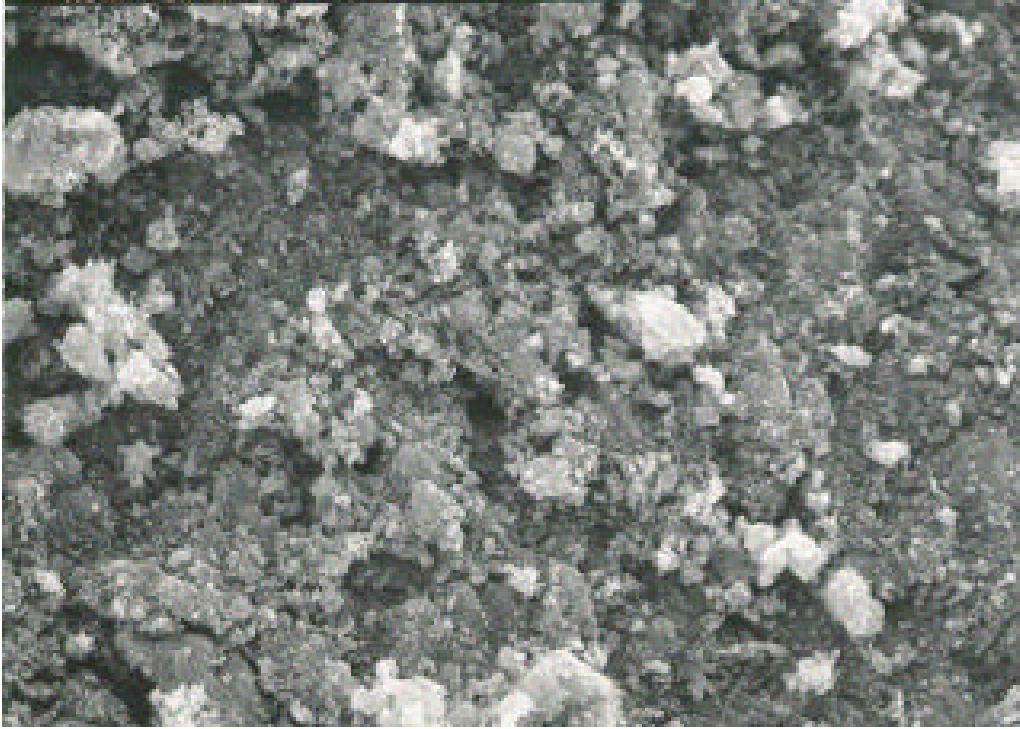
Figure 3.15. Micrograph of Fresh CB1(3) at 5000x Magnification

3.6. References

1. Dombek, B., "Heterogeneous Catalytic Process for Alcohol Fuels from Syngas", Union Carbide Corp, U.S. Department of Energy, DOE/PC/90046-T8 to T15, U.S. Government Printing Office, Washington, DC, 1996.

2. Sheldon, R., Chemicals from Synthesis Gas: Catalytic Reactions of CO and H$_2$, (Reidel Publishing, Dordrecht, Holland: 1983).

3. Xiaoding, X., Doesburg, E., Scholten J., *Catalysis Today,* 2, 125, (1987).

4. Natta, G., Columbo, U., Pasquon, I., Catalysis, Emmett, P. H., ed., (Reinhold, Volume 5, Chapter 3, New York: 1957).

5. Courty, P., Durand, D., Surgier, A., Freund, R., US Patent 4659742, (1987).

6. Calverly, E., Smith, K., *Journal of Catalysis*, 130, 616, (1991).

7. Herman, R., Studies in Surface and Catalyst, (Chapter 7, Elsevier, Amsterdam: 1990).

8. Barger, P., Spehlmann, B., Gajda, G., "Development of a Catalyst for Conversion of Syngas Derived Materials to Isobutylene", U.S. Department of Energy, DOE/PC/90042, U.S. Government Printing Office, Washington, DC, (1996).

9. Stiles, A. B., Chen, F., Harrison, J. B., Hu, X., Storm, D., *Ind. Eng. Chem. Res.*, 30, 811, (1991).

10. Pasquon, I., Dente, M., *Journal of Catalysis*, 1, 508, (1962).

11. Coteron, A., Hayhurst, A. N., *Chemical Engineering Science*, 49, 209, (1994).

12. Takagawa, M., Ohsugi, M., *Journal of Catalysis*, 107, 161, (1987).

13. Klier, K., Chatikavanij, V., Herman, R. G., Simmons, G. W., *Journal of Catalysis*, 74, 343, (1982).

14. Tronconi, E., Ferlazzo, N., Forzatti, P., Pasquon, I., *Ind. Eng. Chem. Res.*, 26, 2122, (1987).

15. Courty P., Arlie, J. P., Convers, P., Mikitenko, P., Sugier, A., *Hydrocarbon Processing*, 63, 105, (1984).

16. Smith, K. J., Anderson, R. B., *Journal of Catalysis*, 85, 428, (1984).

17. Galarrage, C.E., Heterogeneous Catalyst for the Synthesis of Middle Distillate Hydrocarbons, M. S. Thesis, University of Western Ontario, London, (1998).

18. Skoog, D., A., Holler, F. J., Nieman, T. A., <u>Principles of Instrumental Analysis</u>, (fifth edition, Harcourt Brace College Publishers, Florida: 1998).

19. Postek, M. T., Howard, K. S., Johnson, A. H., McMichael, K. L., <u>Scanning Electron Microscopy: A Student Handbook</u>, (Ladd Research Industries, Inc: 1980).

20. Klier, K., Herman, R. G., Vedage, G., US Patent 4843101, (1989).

CHAPTER IV

PHYSISORPTION

4.1.   Physisorption Theory

Gas adsorption is a complex phenomenon where adsorbate gases are in contact

with adsorbent solid. The adsorbate gas attaches and forms a bond on the solid surface.

Gas adsorbate can also penetrate into the adsorbent pores to determine the adsorbent

accessible surface area (1, 2) since most of the adsorbents have extremely porous bodies

with a large internal surface area. In the adsorbent bulk, the balance forces of molecules

are associated with their neighbors. At the surface, the molecules are bound to the inner

molecules at one side and leave unbalanced molecular forces on the other side. These

molecular forces create the attractive forces of the adsorbate to the surface called the van

der Waals attraction. In other words, the adsorbate molecules attach themselves to the

adsorbent surface by physisorption (physical adsorption). At high temperature, the

adsorbate molecule forms a covalent bond or shares electrons with the adsorbent surface

creating a phenomenon called chemisorption (chemical adsorption) (2 ,3 , and 10).

The nature of physisorption follows a van der Waals' interaction, and includes

both dispersion and attraction forces. Physisorption is a neutral process where the

molecules interact with surfaces without sharing or exchanging electrons, thus the

individual character of molecules is preserved. It is characterized as a reversible

exothermic process with a low heat of adsorption (heat of condensation). Adsorption increases with decreasing temperature and increasing pressure (1, 2, 3, and 8).

To determine the characteristics of the adsorbent, the adsorption and desorption isotherms must be established. The isotherm is the standard volume adsorbed as the function of relative pressure. Relative pressure is defined as the ratio of actual gas pressure over the saturated vapor pressure of adsorbate (P_o), under constant temperature (liquid nitrogen temperature at atmospheric pressure). The isotherm shapes reveal not only the pore structure of adsorbent, but also the adsorption and desorption process (2).

4.1.1. Rate of Adsorption

The rate of adsorbate gas penetrating into the adsorbent surface can be determined from the collision rate of the gas molecules at the adsorbent surface (25). The number of molecular collisions, Z, is given by the Herz-Knudsen equation from kinetic theory.

$$Z = n \, \nu / 4 \qquad\qquad\qquad 4.1$$

In which ν and n are obtained from the following equations,

$$\nu = (8RT / \pi M)^{1/2} = 14500 \, (T / M)^{1/2} \qquad\qquad\qquad 4.2$$

$$n = P / kT = 7.24 \times 10^{16} \, P / T \qquad\qquad\qquad 4.3$$

where Z is the molecular collision number ($cm^{-2} \, s^{-1}$), ν is the average velocity of gas molecules (cm/s), n is the number of molecules in 1 cm^3 of ideal gas, M is molecular weight of gas the adsorbate (g/mol), T and P are operating temperature (K) and pressure (Pa), and k is the Boltzmann constant (1.38×10^{-23} J/K).

Adsorption Isotherm

Adsorption isotherms from physisorption, which are shown in Figure 4.1, follow

one of six forms (2, 3, 4, 9, and 10). The first five types were proposed by S. Brunauer,

L. S. Deming, W. S. Deming, and E. Teller (BDDT) (5), and the sixth isotherm was

observed recently (2, 9). Type I is a Langmuir isotherm with very small pores or

microporous adsorbent. The adsorbate uptake rate depends on the accessible micropore

volume instead of the internal surface area at which adsorption occurs by filling

micropores in order of increasing sizes. Sometimes, the hysteresis loop is presented at

the near saturation pressure region due to the presence of mesopores with an upper size

restriction (2, 4, and 9).
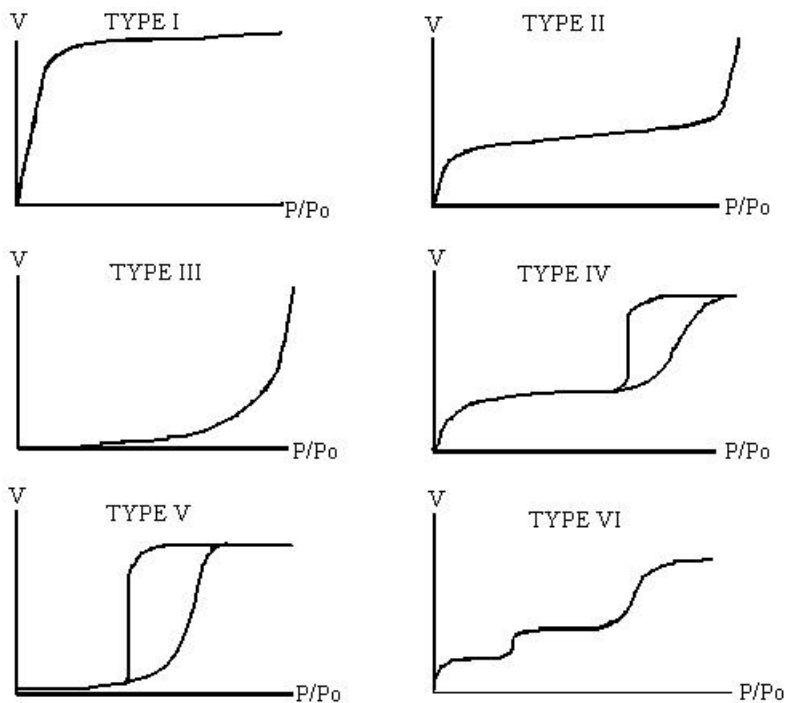
Figure 4.1. Isotherm Types

66

Type II and IV isotherms are the form observed for either nonporous or macroporous adsorbents with unrestricted monolayer-multilayer adsorption. In the nonporous isotherm, the desorption curve traces the adsorption curve, and the adsorption volume rapidly increases at low relative pressure of less than 0.01 due to the first energetic region interaction followed by the interaction with less energetic regions. When the monolayer of adsorbed adsorbate is completed, multilayers are forming at the sharp knee of the isotherm. As the relative pressure approaches unity, an abrupt rise indicates the bulk condensation of adsorbate gas to liquid. Instead of retracing the adsorption curve, the mesoporous or macroporous behavior shows a wide hysteresis loop indicating the filling and emptying effects of the pores by capillary condensation (2, 4, and 9).

Type III and V isotherms do not have the sharp knee shape, implying stronger adsorbate-adsorbate interactions than adsorbate-adsorbent. Type VI is the isotherm of a nonporous solid associated with layer by layer adsorption on a highly uniform surface. The step's sharpness is dependent on the system and the temperature. It is also noted that, in some cases, isotherms without hysteresis loops do not show that the adsorbent is nonporous, for instance, adsorbents with conical or closed-end pores (2, 4, and 9).

4.1.3. Hysteresis Loop

Hysteresis loops are associated with capillary condensation in the multilayer region, pore filling and the emptying mechanism of physisorption isotherm. The micropore filling effects occur at the low relative pressure up to a unity relative pressure. Thus, the meniscus begins to form and increases steadily toward the pore entrance with

67

increasing relative pressure. The evaporation process involves the same series of steps in the reverse direction of condensation (9).

The shape of the hysteresis loop implies the existence of certain states. The major hysteresis loops correspond to different pore shapes, represented in IUPAC, and shown in Figure 4.2. Type A hysteresis is attributed to cylindrical or tubular pore type of adsorbents with a narrow distribution of uniform pores, and is signified by steep and narrow parallel adsorption and desorption curves. Type B has a long flat plateau adsorption with a steep desorption curve. This is a complex structure of pores with interconnected networks or inkbottle shape. Type C presents the aggregates of adsorbents that contain parallel plates, slit shape pores, or wide capillaries (> 500Å). Type D is also associated with slit shape pores but contains mainly the pores in micropore region (9).
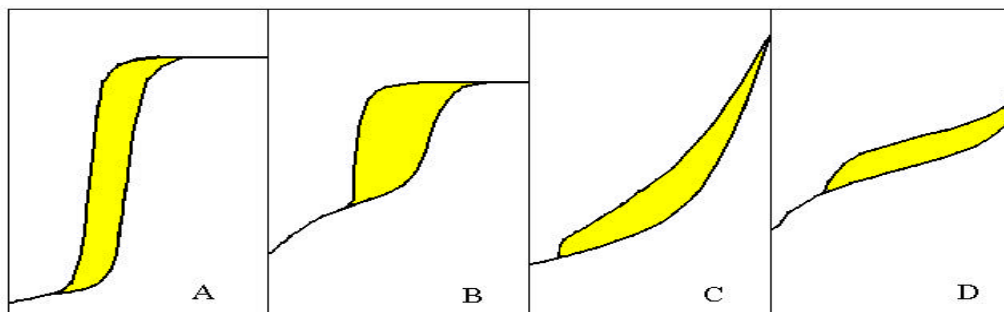
Figure 4.2. Hysteresis Loops

The lower limit of the hysteresis loop or the closing point is dependent on both of the adsorbate gas and the operating temperature. Increasing temperature will reduce the

size of the hysteresis loop. In the case of nitrogen, the hysteresis loop is closed at

relative pressure of 0.4 (9). However, most hysteresis loops close before the relative

pressure approaches 0.3 in the absence of micropores (4, 6). Pores can be varied in size

and shape from one adsorbent to another. Depending on the shape of either cylindrical

pores or slit pores, pore size is expressed in terms of diameter or width. Pores with

diameters or widths of less than 20 Å are micropores. Intermediate pores between 20 Å

and 500 Å are mesopores, and macropores are the pores with openings exceeding 500 Å

(2, 4).

4.1.4. Langmuir Model

The Langmuir method was developed (7) based on the assumption that gases form

only a monolayer and each site adsorbs only one molecule. Langmuir proposed that the

gas molecules strike the unoccupied adsorption sites and remain attached on the

adsorbent surface for a finite length of time due to the inelastic collision. The

evaporation or desorption rate is assumed to be the same as the rate of condensation or

adsorption, and also the heat of adsorption is independent of coverage (10). The

adsorption phenomenon thereby depends on the rate at which the molecules strike the

surface and the rate at which they leave the surface, which is shown in following equation

(2, 4, and 8):

$$V_a = V_m\, b\, P\, /\, (1 + bP) \qquad\qquad 4.4$$

where V_a is the adsorption volume of gas at relative pressure (cm^3), V_m is the monolayer

volume of gas adsorbed (cm^3), b is an empirical constant, and P is the adsorption pressure

(mmHg).

The previous equation can be rearranged into linear form (5),

$$P / V_a = 1 / V_m b + P / V_m \qquad\qquad 4.5$$

When $b = C / P_o$, where P_o is the saturated pressure of adsorbate at adsorption temperature (mmHg), the Langmuir or Type I isotherm is obtained:

$$P / (P_o W) = 1 / (W_m C) + P / (P_o W_m) \qquad\qquad 4.6$$

The constant C and monolayer weight are be calculated from the above equation. The Langmuir isotherm is referred to as the limiting adsorption due to the chemically bound monolayer completion, and has not been recommended for microporous physisorption. The adsorbent specific surface area, S, in cm^2/g, is (9):

$$S = V_m \, \sigma \, N_A / m V_o \qquad\qquad 4.7$$

$$S = W_m \, \sigma \, N_A / m \, M \qquad\qquad 4.8$$

where V_m is the monolayer volume of gas adsorbed (cm^3), σ is the cross section area of an adsorbate molecule ($Å^2$/molecules), N_A is Avogadro's constant (6.023×10^{23} molecules/mol), m is the mass of adsorbent sample (g), V_o is the molar volume of gas ($22414 \ cm^3$/mole), W_m is the monolayer weight of gas adsorbed at relative pressure (g), and M is the molecular weight of adsorbate (g/mol).

By assuming close packing at the adsorbent surface, the mean area per molecule of adsorbate gas, σ, is calculated using Equation 4.9 (13). A list of selected parameters of adsorbate gases is given in Table 4.1.

$$\sigma = 1.091 \times 10^6 \ (M / N_A \ \rho)^{2/3} \qquad\qquad 4.9$$

The density of liquid adsorbate is written as:

$$\rho = \rho_C \ [1 + 0.75 \ (1 - T_i / T_C) + 1.75 \ (1 - T_i / T_C)^{1/3}] \qquad\qquad 4.10$$

where ρ_C is the critical density of liquid adsorbate (g/cm^3), T_C is the critical temperature (K), and T_i is the adsorption temperature (K).

Table 4.1. Gas Parameters of Selected Adsorbates (4)

Gas	Molecular Weight (g/mol)	Critical temperature (K)	Critical Density (g/cm^3)
Hydrogen (H_2)	2.016	33.3	0.031
Oxygen (O_2)	31.99	154.6	0.427
Carbon Monoxide (CO)	28.01	133.9	0.301
Carbon Dioxide (CO_2)	44.01	304.2	0.468
Nitrous Oxide (N_2O)	44.02	309.7	0.452
Nitrogen (N_2)	28.02	126.2	0.313
Ammonia (NH_3)	17.03	405.7	0.235

4.1.5. Brunauer-Emmett-Teller (BET) Model

The Langmuir model is based on the monolayer adsorption (11), which is controlled by the adsorbate/adsorbent interaction. Brunauer, Emmett, and Teller developed the BET method, which is applicable for multilayer adsorption including both Langmuir and S-shape isotherm. Derivations of the BET equation are found in the original literature (12) starting with the division of the surface into empty sites, one monolayer sites, two monolayer sites, and then assuming the random distribution of various types of sites (26).

BET theory is also based on the assumption that the active forces of condensation are responsible for the binding energy of multilayer adsorption (2). The linear form of the BET model, based on the assumption of a finite number of adsorbed layers on a free surface, is written:

$$1 / [W ((P_o / P) - 1)] = 1 / W_mC + (C - 1) (P / P_o) / (W_mC) \qquad 4.11$$

A straight line BET plot allows W_m and C to be obtained from the slope and intercept. The specific surface area is calculated using the occupied area of a single adsorbate molecule by Equation 4.8. The BET C constant is related to the energy of adsorption in the monolayer, which is also indicative of the interaction of adsorbate and adsorbent. C is expressed as a function of temperature by (5):

$$C = Exp [(E_A - E_L) / RT] \qquad 4.12$$

where E_A is the heat of adsorption of the gas in the first adsorbed layer, E_L is the heat of liquefaction of the gas, and R is the gas constant.

A Type II isotherm is characterized by C >>1, or $E_A > E_L$, where the attractive forces between adsorbate and adsorbent are greater than the attractive forces between gas molecules in the liquefied state. When $E_A < E_L$, the forces between adsorbate and adsorbent are small, signifying a Type III isotherm. It is also noted that Type IV and V isotherms are signified by almost filled pores at a pressure lower than the gas vapor pressure. This suggests that as the gas pressure increased, additional forces appear that make the heat of adsorption or binding energy in some higher layer to be greater than the heat of liquefaction (5).

The linear BET region for the nitrogen isotherm of many adsorbents is in the range of relative pressure of 0.05 to 0.35 (12). The monolayer is complete at a relative pressure of point B, the sharp knee point. The isotherm progressed to second layer or higher covered by BET (8). To obtain the best BET region, the best linear fit including point B for this range of isotherm is recommended. Other studies revealed that the

limited linear BET region is more restricted (3, 9), and is dependent on the system and operating temperature. The operating temperature, BET range as well as adsorbate cross-section area, σ, are listed in Table 4.2.

Table 4.2. Adsorbate Parameters (9)

Adsorbate gas	Temperature (K)	BET range	Close-packed σ (Å^2/molecule)	Customary σ (Å^2/molecule)
Nitrogen	77	0.13 – 0.20	16.2	16.2
Argon	77	0.10 – 0.19	13.8	13.8
Krypton	77	0.14 – 0.24	15.2	20.2
Xenon	77	0.16 – 0.25	16.8	17.0
Oxygen	77	0.13 – 0.20	14.1	14.1
Carbon dioxide	195	0.14 – 0.22	16.3	21.0
n-Butane	273	0.32 – 0.53	32.1	43.0
Benzene	293	0.25 – 0.51	30.7	43.0

When the adsorbent surface is covered by a monolayer of adsorbate, a fraction of the surface is still not covered. The uncovered fraction of the adsorbent surface, $(\theta_o)_m$, is dependent on the BET C constant, and a lower BET C constant will yield a higher uncovered fraction (13).

$$(\theta_o)_m = (C^{1/2} - 1) / (C - 1) \qquad 4.13$$

The fraction of surface covered by layers i molecules deep is:

$$(\theta_i)_m = C \ [(C^{1/2} - 1) / (C - 1)]^{i+1} \qquad 4.14$$

Most adsorbent surfaces are heterogeneous in energy because of the variation of the heat of adsorption on surface coverage. The BET theory was criticized for assuming the same energy for all adsorption sites on the surface. The BET theory also neglects the effect of interaction between neighbor molecules in the same layer. Due to the horizontal

forces between molecules at higher coverage, their separation is much less than a single diameter. Moreover, the heat of adsorption is assumed to be the same as the heat of condensation in higher layers, and the reduction of adsorption forces as the distance from the surface increases was neglected (3).

4.1.6. Barret-Joyner-Halenda (BJH) Model

The BJH Method is proposed by Barret, Joyner, and Halenda (16) to estimate the available porous volume and area, starting with open-ended cylindrical pores and assuming that all pores are filled with liquid at unity relative pressure. A layer of adsorbate molecules of statistical thickness t_1, is physically adsorbed on the pore adsorbent surface in which r_{p1} is the largest pore radius, and r_{k1} is the inner capillary radius. A schematic of the desorption mechanism is shown in Figure 4.3.

The pore volume (V_{p1}) and capillary volume (V_{k1}) relationship under equilibrium conditions is:

$$V_{p1} = V_{k1} \, r_{p1}^2 / \, r_{k1}^2 \qquad\qquad 4.15$$

V_{k1} is not measurable. To determine the desorbed pore volume, the relative pressure $(P/P_o)_1$ is lowered to $(P/P_o)_2$, and a measurable desorbed volume of ΔV_1 of adsorbate gas from the first pore is obtained. This desorption empties the capillary condensate and adsorbed layer Δt_1 from the largest pore. The desorbed volume of the first largest pore is:

$$V_{p1} = \Delta V_1 \, r_{p1}^2 / \, (r_{k1} + \Delta t_1)^2 \qquad\qquad 4.16$$
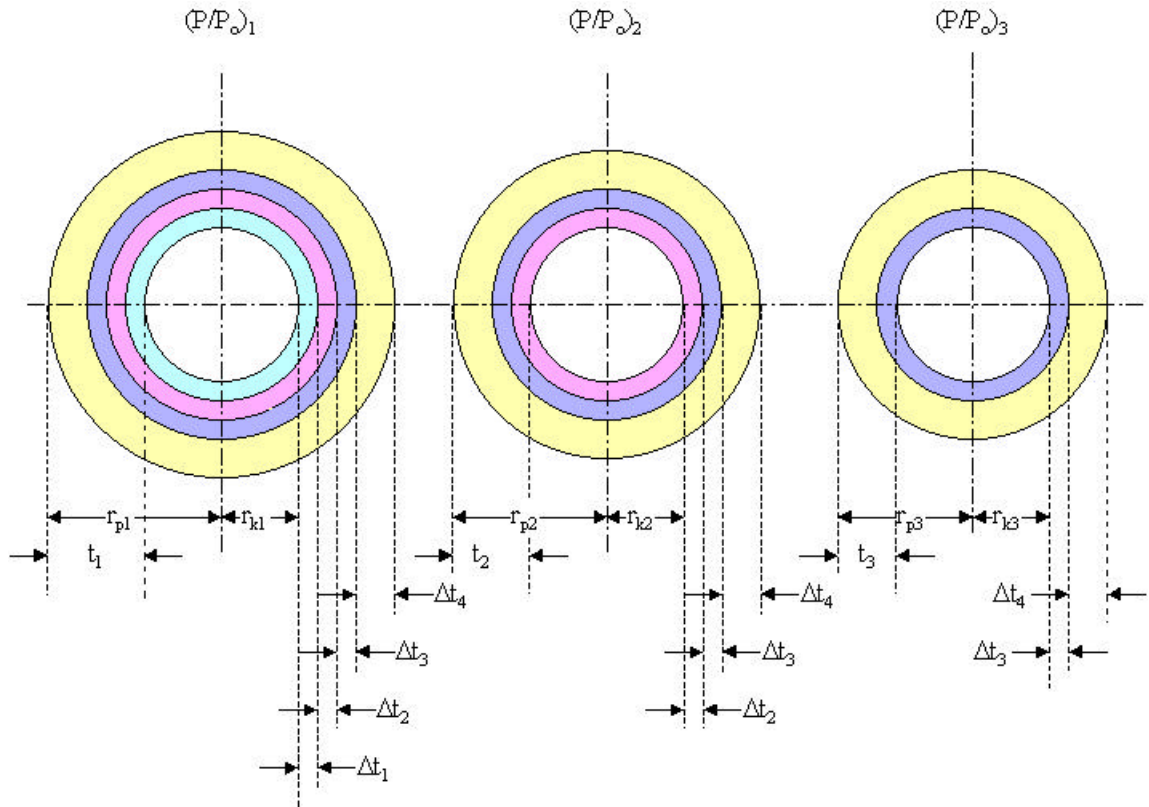
Figure 4.3. Desorption Mechanism of Three Different Pores at Reduction Over
First Three-Pressure Decrements (16)

When the pressure is lowered from $(P/P_o)_2$ to $(P/P_o)_3$, the measurable desorption

volume includes both the volumes from the second pore (ΔV_2) and from the second

thinning layer $(V_{\Delta t2})$. The desorption volume from second pore is:

$$V_{p2} = (\Delta V_2 - V_{\Delta t2})\, r_{p2}^{\,2} / (r_{k2} + \Delta t_2\,)^2 \qquad\qquad 4.17$$

The volume of second thinning layer $(V_{\Delta t2})$ is expressed in terms of the desorbed

gas average area (Ac_1) from the previous pore:

$$V_{\Delta t2} = \Delta t_2\, Ac_1 \qquad\qquad 4.18$$

The general form of the step wise desorption of the thinning layer is written from $j = 1$ to $n - 1$. The summation is the sum of average area of the "unfilled pores down to, but not including, the pore that is emptied of capillary condensate in the nth desorption" (16).

$$V_{\Delta tn} = \Delta t_n \, \Sigma \, Ac_j \qquad\qquad 4.19$$

The general form of step wise desorption volume is:

$$V_{pn} = (\Delta V_n - \Delta t_n \, \Sigma \, Ac_j) \, [r_{pn}^{2}/ (r_{kn} + \Delta t_n)^{2}] \qquad\qquad 4.20$$

Ac_j is not constant but varies with each desorption step. An alternative way to describe the desorption volume is shown in Figure 4.4. The relationship between pore area and Ac_j is:

$$Ac_j = C_j \, A_p \qquad\qquad 4.21$$
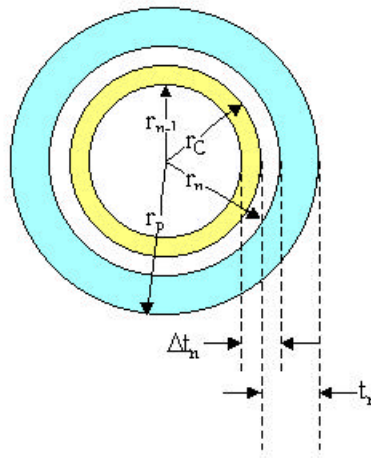
Figure 4.4. Change in Thickness (16)

$$C_j = (r_p - t_r) / r_p = r_C / r_p \qquad\qquad 4.22$$

where t_r is the thickness of the physically adsorbed layer at corresponding value of P/P_o.

The pore area is defined as:

$$A_p = 2V_p / r_p \qquad\qquad 4.23$$

The final form of Equation 4.20 is:

$$V_{pn} = (\Delta V_n - \Delta t_n \, \Sigma \, C_j \, A_p) \, [r_{pn}^2 / (r_{kn} + \Delta t_n)^2] \qquad\qquad 4.24$$

The BJH method is established based on the assumptions of cylindrical pores, adsorption on pore walls, and capillary condensation in the inner capillary volume (16). It is applicable in the desorption range from unity relative pressure down to the last point of BET region (~ 0.3).

4.1.7. The t Method

In the presence of mesopores, the t method can be used to find the micropore volume and surface area. This technique is based on BET theory but more information about the adsorption isotherm will be gained. The recommended range for the t method is relative pressures up to 0.75 (20). The t-curve (17) is a straight line through the origin as long as the multilayer is formed , and expressed in terms of adsorbed volume as a function of average thickness of adsorbed layer. The slope of the t-curve yields the specific surface area S, which is not necessarily equal to the S value from the BET method because of the variation of the C value in BET (18). The micropore volume can also be calculated from the intercept of the t curve after converting to the liquid volume. Thereby, the typical average thickness of the adsorbed layer in angstroms is written in terms of the adsorbed volume, which is obtained from the BET model (19):

$$t = (V_A / S) \, 10^4 = (M \, V_{SP} / 22414) \, (V_a / S) \, 10^4 \qquad\qquad 4.25$$

where V_A is the adsorbed volume of the gas adsorbate at STP (cm^3/g), and V_{SP} is the specific volume of adsorbate (cm^3/g).

For nitrogen adsorbate gas, the above equation is expressed as:

$$t = 15.47 \, (V_a / S) \qquad\qquad 4.26$$

The t method also assumes that the adsorbed layer behaves the same as liquid nitrogen, thus the adsorbed layer has the same density as the capillary condensed liquid. Therefore, the thickness of one statistical layer is given as the diameter of one nitrogen molecule.

$$3.54 = V_a / V_m \qquad\qquad 4.27$$

The t value can also be determined as a function of relative pressure for nitrogen adsorption based on the Halsey method by assuming that the adsorption energy in the second layer is equal to the liquefaction energy (21). In another words, the density and packing of the liquid monolayer are the same as for normal liquid nitrogen.

$$t = 3.54 \, \{5 / [\ln (P_o /P)]\}^{1/3} \qquad\qquad 4.28$$

The de Boer method is another method used to calculate the t values, which is applied to gas adsorption on a solid (26).

$$t = \{13.99 / [0.034 + \log (P_o /P)]\}^{1/2} \qquad\qquad 4.29$$

Three characteristic shapes of t curves are shown in Figure 4.5 (8). A t curve of type (a) suggests the absence of both micropore and capillary condensation at the adsorption isotherm. Type (b) consists of a portion with downward deviation and an upper linear portion. The downward deviation is due to the blocking of accessible

78

surface area in the micropore region by the adsorbate gas. The upper linear portion is

due to the multilayer growth either at the surface or in the intermediate pores. Type (c) is

comprised of an upward deviating section and a linear part due to the capillary

condensation of intermediate pores and multilayer growth at the external surface after

pore condensation, respectively (8). The t method is criticized for neglecting the effect of

pore filling by assuming the monolayer adsorption occurs at the pore walls or open

surface (17).
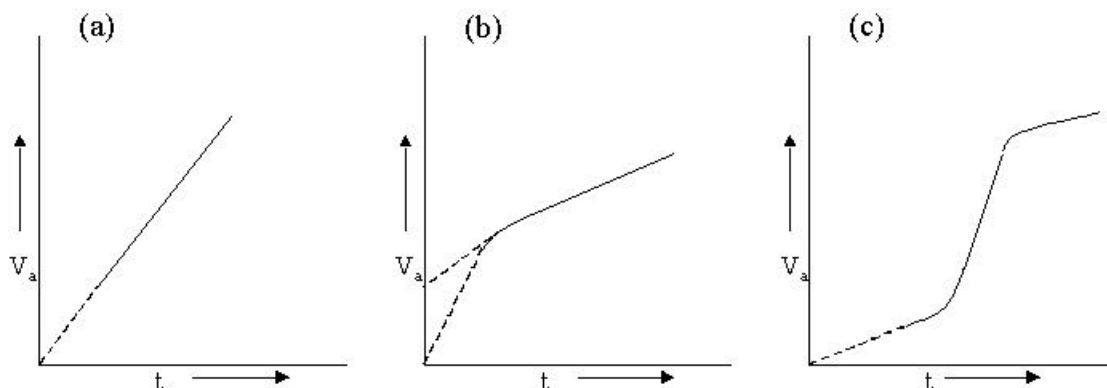
Figure 4.5. Characteristic t Curves, (a) External Surface Area or Intermediate Slit
Shaped Pores; (b) Micropore and External Surface Area; (c) Intermediate
Pores With Curve Wall (8)

4.2.   Instrumentation

The analysis is performed using a Quantachrome Autosorb 1C Instrument model

P/N 05061-C. The schematic of the system is illustrated in Figure 4.6. The instrument

includes temperature and pressure measurement, two out-gassing stations, a temperature

setting, the analysis station, the dewar station, the dewar status, and the cold trap system.

79
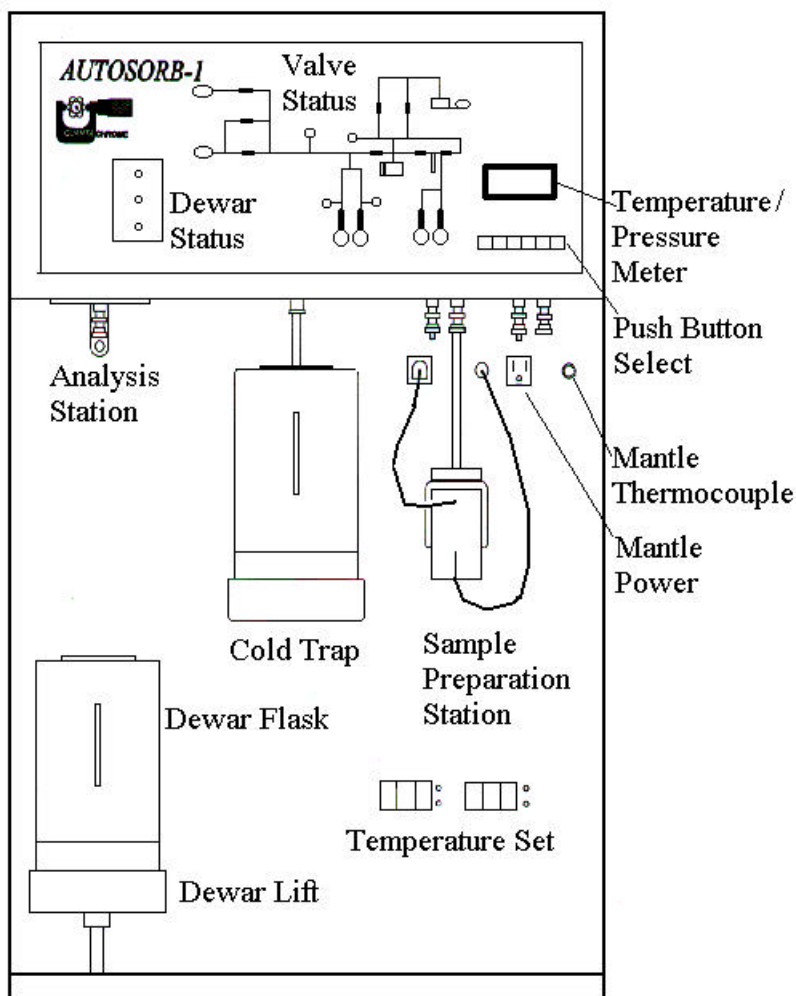
Figure 4.6. Schematic Diagram of Instrument (4)

A detailed schematic of the instrument is also shown in Figure 4.7. The inert gas at ambient temperature and about 7 psi enters the system through a coarse valve. The flowrate of the adsorbate gas at ambient temperature and about 5 psi entering the system is regulated by either a coarse or a fine valve. The main chamber of the system is called the manifold, at which the manifold temperature and pressure are measured and monitored by a temperature transmitter and two pressure transmitters of 100 and 10 torr.

The manifold temperature, (°C), manifold pressure (mmHg), the sample station pressure (mmHg), the P_o pressure (mmHg), and the outgassing temperature (°C) are shown in the meter display. The push button select is used to select the displayed reading on the meter. The manifold is isolated from other stations by 12 solenoid valves, which are automatically controlled by the system. The two LED color status valves indicated closed or open, which corresponds to yellow or green light, respectively. The manifold is also connected to a calibration chamber, which is employed for the manifold volume calibration.
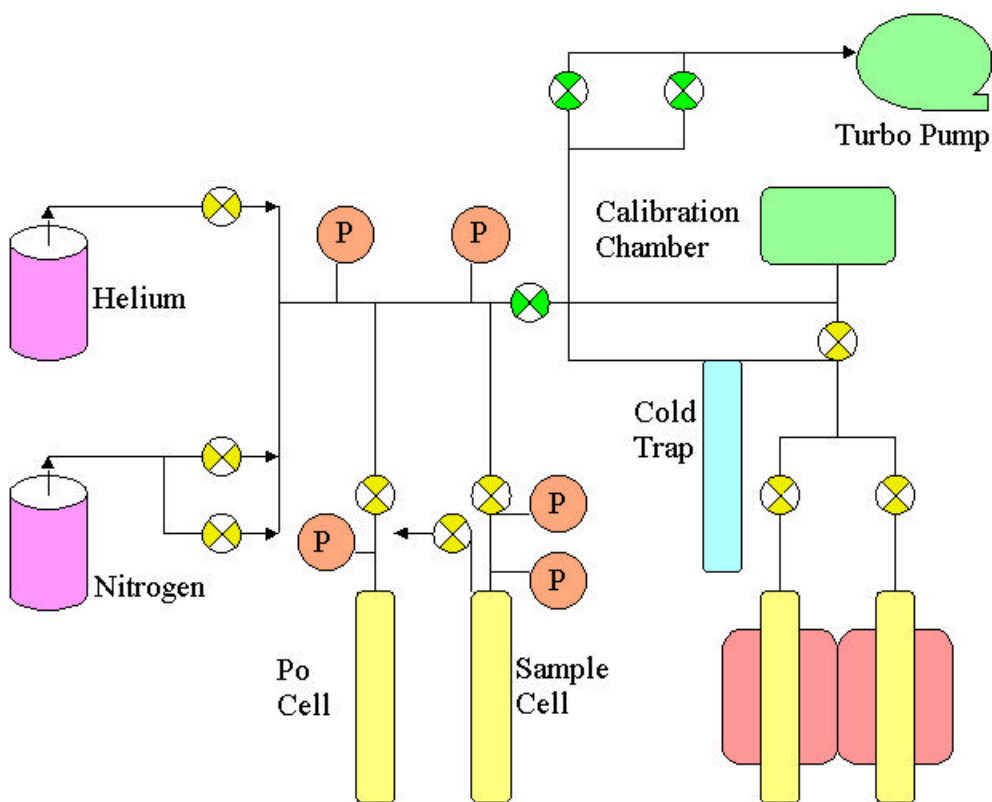
Figure 4.7. Detailed Schematic of Instrument

The analysis station consists of both the Po cell and the sample cell. The pressure of the Po station is monitored by a 1000 torr pressure transmitter, while the pressure of the sample station is also recorded by two pressure transmitters of 1000 and 1 torr. The cold trap is used prevent the diffusion of the sample degassing products from getting into the manifold. The cold trap Dewar flash is also filled with liquid nitrogen and mounted on the front of panel (4).

Prior to the analysis, the sample is pretreated in the outgassing station. The temperature setting allow individual control of the heating mantles. The system or the outgassing station can be evacuated through both or either fine or coarse valve by a turbo pump at which a Pirani gauge is used to monitored the pressure. The Dewar flask status is also indicated by the LED colors. The first blue "ON" indicates the contact of thermistor with liquid nitrogen. The second yellow "ON" indicates the Dewar down command, and the last green "ON" indicates the good status. The level is monitored by the thermistor, which hangs parallel to the sample cell.

4.2.1. Manifold Volume

The manifold volume is determined based on both the universal gas law and the pressure measurement with the aid of a metal sphere. The mass balance between sphere and manifold is illustrated in Figure 4.8.

Since the mass of gas is conserved, the mass balance equation is (2):

$$n = P_1 \, V_{man} / R \, T_1 = P_2 \, (V_{man} + V_{cal} - V_s) / R \, T_2 \qquad 4.30$$

With known values of P_1, P_2, T_1, T_2, V_{cal}, and V_s, the manifold volume is calculated according to the ratio of pressure and temperature. The manifold volume is internal reference volume for determining the quantity of gas adsorbed.

$$V_{man} = (V_{cal} - V_s) (P_2 / T_2) / [(P_1 / T_1) - (P_2 / T_2)] \qquad 4.31$$

where V_{man} is the manifold volume (cm^3), V_{cal} is the calibration chamber volume (cm^3), and V_s is the sphere volume (cm^3).
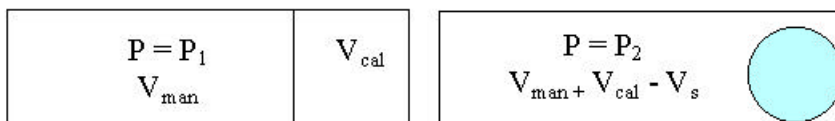
Figure 4.8. Manifold Volume Determination

4.2.2. Free Space Volume

The sample cells are different in size and shape due to the various forms and quantity of sample. Therefore, the free volume within the sample cell must be known in order to determine the amount of gas adsorbed on the sample. The free space volume is determined from the pressure difference in the manifold before and after the gas exchange from the manifold and the sample cell. Helium gas is used for free space volume determination because it is not adsorbed by the sample and behaves as an ideal gas. The measurement of gas quantities adsorbed by the sample is performed in a similar manner by subtracting the remaining gas quantities in the free space after equilibrium from the gas originally introduced into the free space. However, part of the sample cell is immersed in a liquid nitrogen bath, so two distinct temperature zones exist. In addition to

total free space volume, the gas quantities in the cold zone must be corrected for non-ideality. Figure 4.9 illustrates the free space measurement diagram (2).

At pressure P_2, the sample is not immersed in the cold bath, and the temperature, T_w remains at ambient temperature. Based on Figure 4.9B, the mass balance at equilibrium is:

$$(P_1 \, V_{man} / R \, T_1) = (P_2 \, V_{man} / R \, T_w) + (P_2 \, V_{fw} / R \, T_w) \qquad 4.32$$

Let $V_{fw} / R \, T_w = F_{fw}$, and $V_{man} / R \, T_1 = F_{man}$. Thus the total moles of gas is:

$$n_t = P_2 \, F_{man} + P_2 \, F_{fw} \qquad 4.33$$
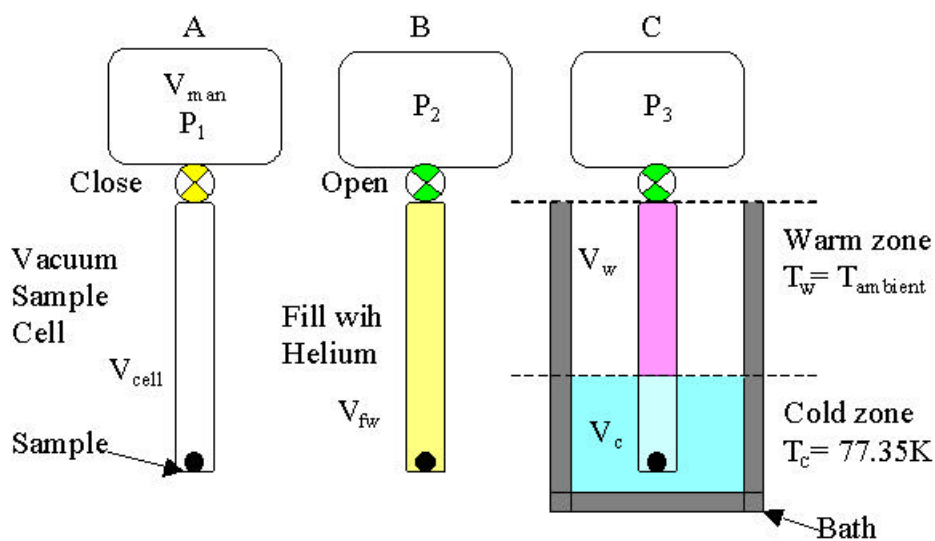
Figure 4.9. Schematic Diagram of Free Space Measurement Sequence (2)

When immersed in the liquid nitrogen bath, the physical volume of chamber, V_{fw}, is divided into two sections. V_w is the upper volume at temperature T_w, and V_C is the lower volume at temperature T_C.

$$V_{fw} = V_w + V_C \qquad\qquad 4.34$$

The total gas quantity in the system is still conserved during the measurement.

Therefore, the thermal equilibrium mass balance of Figure 4.9C is:

$$n_t = P_3 F_{man} + (P_3 V_w / R T_w) + (P_3 V_C / R T_C) \qquad\qquad 4.35$$

Or,

$$P_3 F_C = n_t - P_3 F_{man} - (P_3 V_w / R T_w) \qquad\qquad 4.36$$

Since $V_w = V_{fw} - V_C$

$$(P_3 V_w / R T_w) = (P_3 V_{fw} / R T_w) - (P_3 V_C / R T_w) \qquad\qquad 4.37$$

Let,

$$V_C / R T_w = (V_C / R T_C) (T_C / T_w) = F_C (T_C / T_w) \qquad\qquad 4.38$$

Substituting Equation 4.38 into Equation 4.37, then substituting Equation 4.37

into Equation 4.36, equation 4.36 becomes:

$$P_3 F_C = n_t - P_3 F_{man} - (P_3 V_{fw} / R T_w) + P_3 F_C (T_C / T_w) \qquad\qquad 4.39$$

Or,

$$F_C = (n_t - P_3 F_{man} - P_3 F_{fw}) / [P_3 (1 - T_C / T_w)] \qquad\qquad 4.40$$

Equation 4.36 is rearranged to express the quantity of gas in the free space of the

sample cell at P_3 and partially immersed in the cold bath. Let $F_{fc} = F_w + F_C$.

$$n_t - P_3 F_{man} = (P_3 V_w / R T_w) + P_3 F_C = P_3 F_{fc} \qquad\qquad 4.41$$

Substituting Equation 4.41 into Equation 4.40, the final expression of the cold

free space factor is:

$$F_C = (F_{fc} - F_{fw}) / (1 - T_C / T_w) \qquad\qquad 4.42$$

4.2.3. Gas Adsorbed Quantity

The amount of gas adsorbed is the difference between the total dosed amount and the gas remaining in the free space after some of it is adsorbed by the sample. Prior to the analysis, the sample is evacuated and cooled to liquid nitrogen temperature T_C. The manifold volume, V_{man}, is isolated from the sample cell and charged with adsorptive gas at P_1, and T_{man} is measured. A quantity of gas is dosed into the sample cell. Then the system pressure, P_2, is measured after equilibrium is approached. A quantity of gas dosed into the sample cell is written as (2):

$$n_{cell} = P_1 F_{man} - P_2 F_{man} \qquad\qquad 4.43$$

Since a portion of the sample cell is at liquid nitrogen temperature, a correction factor must be applied for the nonideal behavior. In order for the quantity of gas involved in the process to be determined accurately as a function of pressure, a nonideal correction factor γ is applied:

$$n = (PV / RT)(1 + \gamma P) \qquad\qquad 4.44$$

The quantity of gas adsorbed in the sample is expressed as (2):

$$n_A = n_{cell} - n_{fc} + n_C\, \gamma\, P_2 \qquad\qquad 4.45$$

Or,

$$n_A = P_1 F_{man} - P_2 F_{man} - P_2 F_{fc} + F_C\, \gamma\, P_2^{\,2} \qquad\qquad 4.46$$

The gas adsorbed from the initial dose and from each subsequent dose is calculated and reported as the adsorbed volume as a function of pressure.

4.2.4. Saturation Pressure Measurement

The saturation pressure can either be measured directly or manually entered by the operator. The saturation pressure measurement starts with evacuation of the P_o cell. Then adsorbate gas is charged into the P_o cell until saturation occurs. The pressure of the saturated gas is measured and recorded for each point along the isotherm, then used to calculate the relative pressure, P/P_o, for the isotherm.

4.2.5. Software

The functions of the instrument software include monitoring and controlling all operations during calibration, measurement, and data manipulation. Dosing the sample with the quantities of adsorbate gas at a target pressure and detecting the equilibrium pressure are the most critical functions. Figure 4.10 illustrates the dosing increment at equilibrium pressure at a restricted interval and pressure tolerance band (2).

After one data point is recorded, the instrument is ready for the next point. The gas is charged to the sample cell, which is then isolated from the manifold. The pressure drops as the gas is adsorbed into the sample. The shape of the pressure drop depends on the uptake rate of the sample. Two parameters that are set to guide the instrument during this process are the equilibration interval and the pressure tolerance. The equilibration interval is the time at which the pressure remains stable, while the pressure tolerance is the acceptable range of actual pressure according to target pressure.
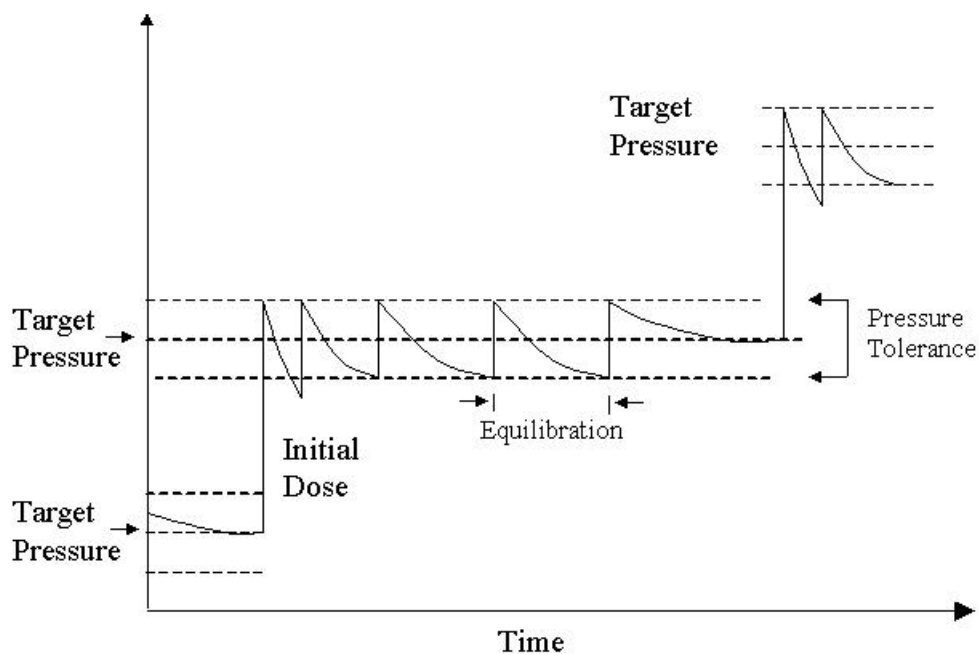
Figure 4.10. Pressure Equilibration (2)

4.2.6. Operating Parameters

The adsorbed volumes as a function of relative pressure were performed by the Quanta Chrome Autosorb 1C using the sphere for calibration and nitrogen as the adsorbate gas. Prior to the analysis, 2 to 3 catalyst pellets of 0.24 to 0.37g were outgassed at 200°C with Helium back-filled gas for 12 hours. The outgassing process was completed only if catalysts had passed the outgassing test of 5μ mmHg/min. Before the analysis, a 1 minute leak test was performed. The physisorption analysis was accomplished by nitrogen gas with fine evacuation while the P_o cell was in the P_o station for direct saturation pressure measurement, and maxi dose was on. The analysis points were selectively chosen in the micropore range, 20 adsorption and 20 desorption points.

Zero tolerance target pressure was also set with the equilibration time from 3 to 5 minutes.

4.3. Results and Discussion

Physisorption is an important attribute of catalysts, which may affect the activity, selectivity, and stability of the catalysts. Physisorption is the process where the gas molecules interact with the surface without sharing or exchanging electrons. Most methods of physisorption are based on nitrogen adsorption and desorption isotherms at liquid nitrogen temperature. Surface characteristics are determined by different methods including the multi-point BET, Langmuir, BJH model, and adsorbed thickness layer t method.

According to the kinetic theory of Herz-Knudsen (25), the adsorption rate is assumed to be the same as the collision rate of the nitrogen gas molecules at the adsorbent surface. Figure 4.11 shows that the molecular collision rate is linearly proportional to relative pressure, and up to 5.7×10^{23} nitrogen molecules strike one cm^2 surface per second. The collision rate is dependent on the gas molecule characteristics as well as the operating temperature and pressure, but not the adsorbent surface according to the Herz-Knudsen theory. As the operating pressure increases, different numbers of nitrogen gas molecules strike the surface. However, the adsorbent characteristics may influence the adsorption time or amount of gas adsorbed. Thereby, the assumption that the adsorption rate is the same as the collision rate of nitrogen gas molecules is unjustified in this case. Thus, the collision rate of the nitrogen gas molecules is simply

the number of gas molecules that strike the surface at the operating temperature and pressure.
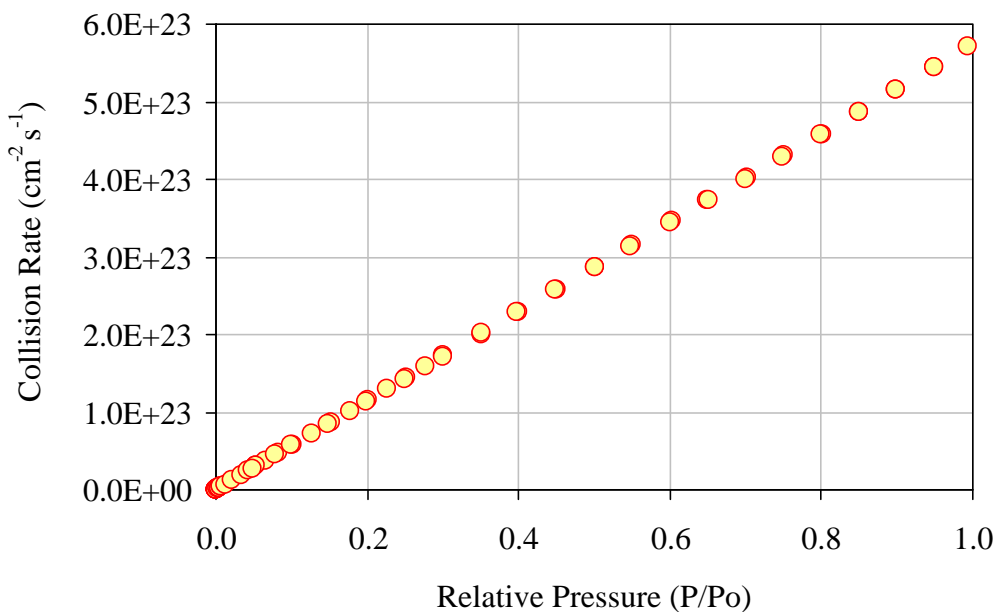
Figure 4.11. Collision Rate

Figure 4.12 shows the time of the adsorption at difference trials. Catalyst CB1(1) and CB1(3) take almost the same amount of time to adsorb the same dose of nitrogen gas, thereby their pore structures must be similar. However, aged catalyst CB1(1) takes a shorter time to adsorb indicating that some pore modifications have been occurred during the reaction.
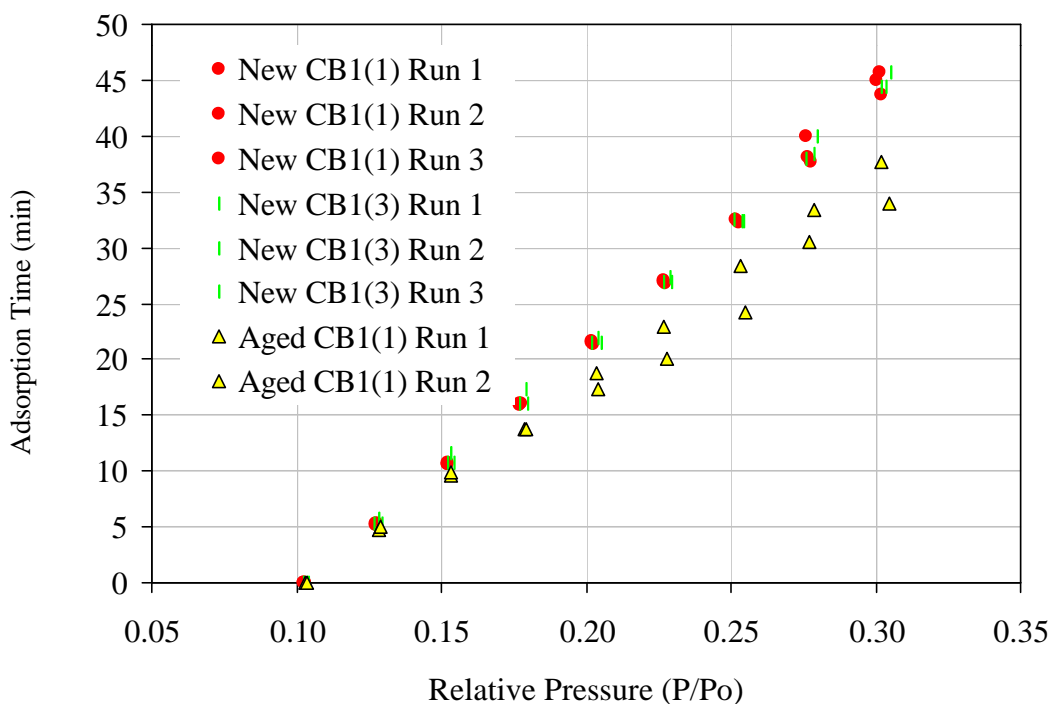
Figure 4.12. Adsorption Time

4.3.1. Adsorption-Desorption Isotherms

In order to obtain the adsorbent characteristics such as size, shape, and the distribution of capillaries, the multimolecular adsorption and desorption isotherm curves over the whole range of relative pressure are required. These are shown in Figures 4.13 and 4.14. The isotherms are concave in the low pressure region, and convex in the higher pressure region, while approximately linear in the intermediate region. The adsorption volume increases rapidly at low relative pressure due to the interaction of nitrogen gas with the first energetic region followed by the less energetic region. The monolayer of adsorbed molecules is completed at a relative pressure about 0.007, then the multilayers

are formed. The abrupt rise in adsorbed volume at a relative pressure of 0.75 to unity

indicates that capillary condensation has occurred during the adsorption process.
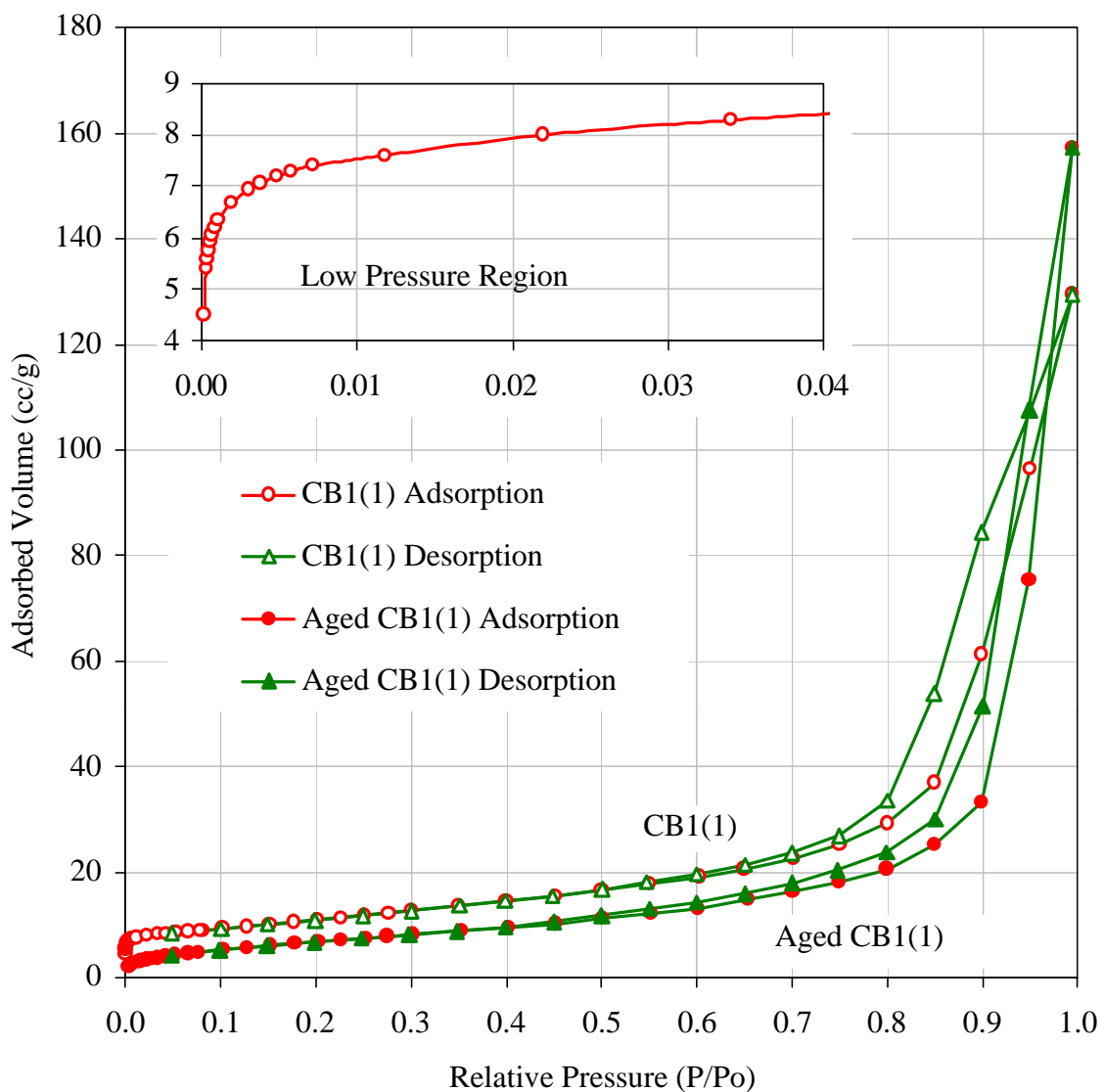
Figure 4.13. Adsorption and Desorption Isotherms of Fresh
CB1(1) and Aged B1(1) Catalysts
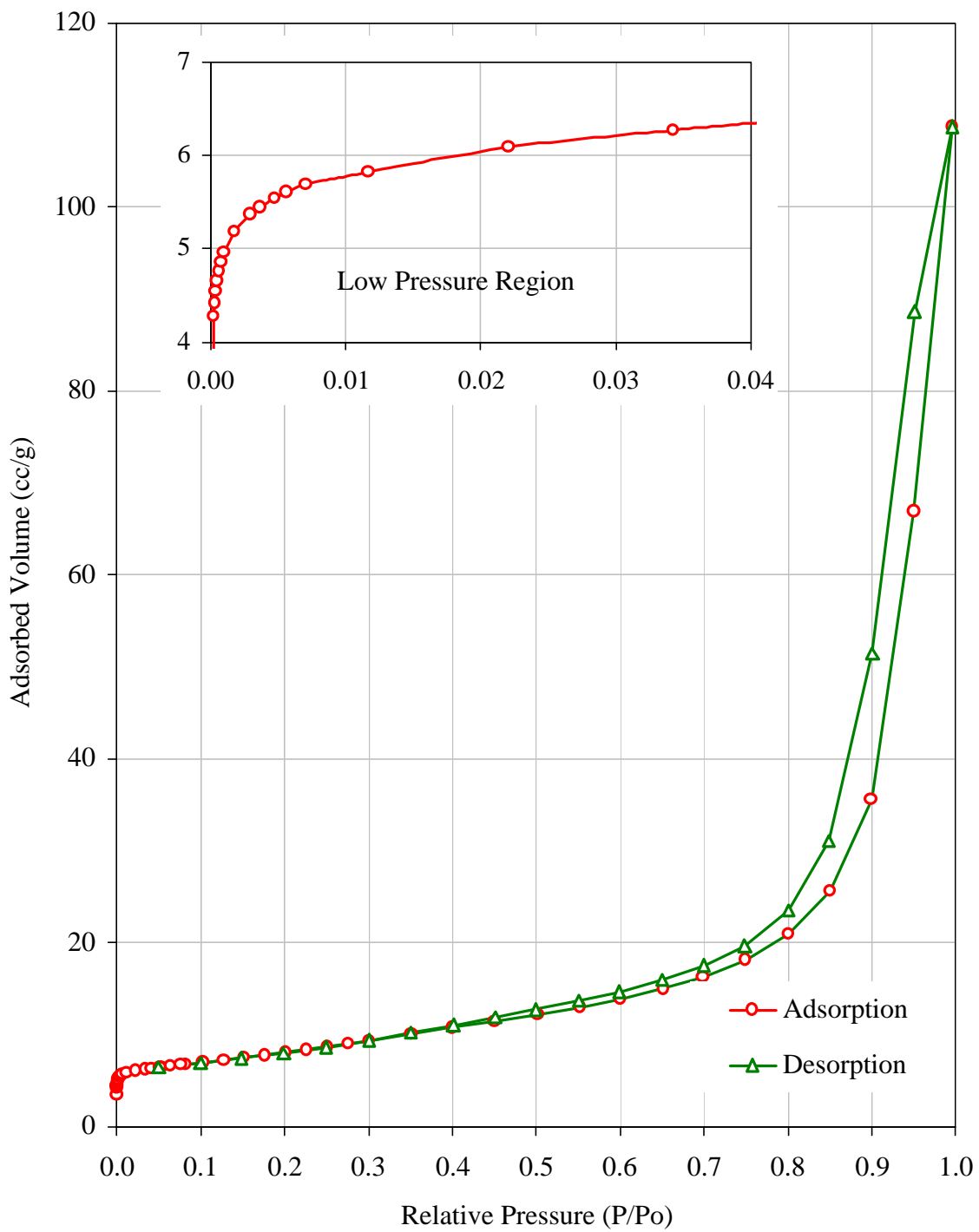
Figure 4.14. Adsorption and Desorption Isotherms of CB1(3) Catalyst

The desorption process involved the same series of steps in reverse direction. Thereby, a hysteresis loop is formed from the adsorption and desorption curve, which exhibited the mesoporous behavior due to the filling and emptying effects of the pores by capillary condensation (2, 4, 9, and 31). Catalyst CB1(1) isotherm occurs at higher adsorbed volume than CB1(3). The adsorptive capacity of CB1(1) is higher than CB1(3). Changes in the CB1(1) catalyst after reaction are also noticed at lower adsorption volumes, which may be due to the effect of sintering or blocking of pores during reaction. The similarity of the hysteresis shape exhibited indicates the existence of similar pore shapes shown in Figure 4.15. The hysteresis shape indicates (9) the existence of the aggregates of adsorbent containing parallel plates, slit shape pores, or wide capillaries.
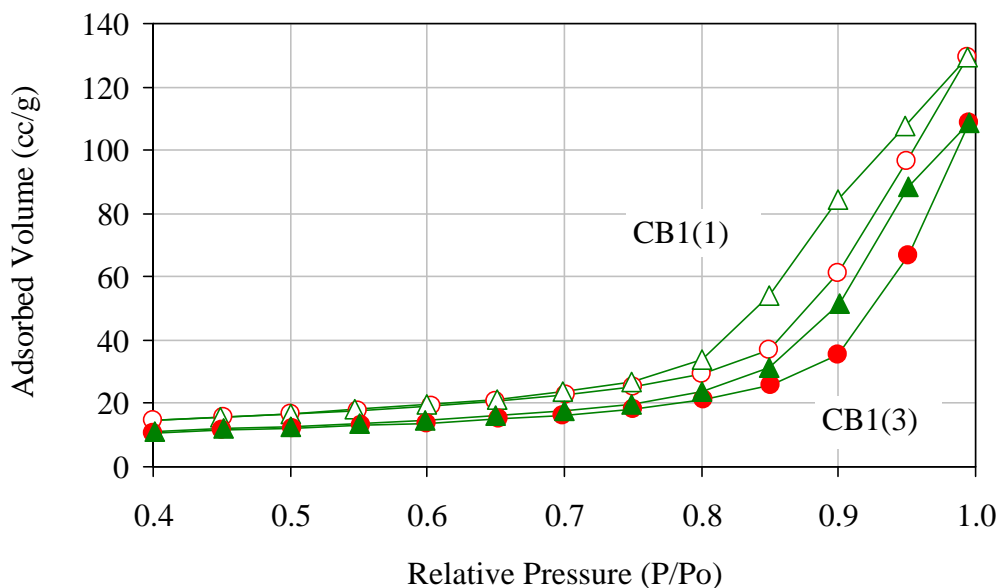
Figure 4.15. Hysteresis Loops

The Langmuir model for catalysts is shown in Figure 4.16. This model is based on the assumption that the desorption rate is the same as the condensation rate since the adsorbate gas only forms a monolayer, with only one molecule attached to each site and remaining on the surface for a finite time (7). The monolayer formation follows the Langmuir model at low relative pressure below 0.1. Therefore, the relative pressure range of Langmuir Model begins at a relative pressure of 0.1, down to the best linear fitted points. The Langmuir model is shown in Figure 4.16.
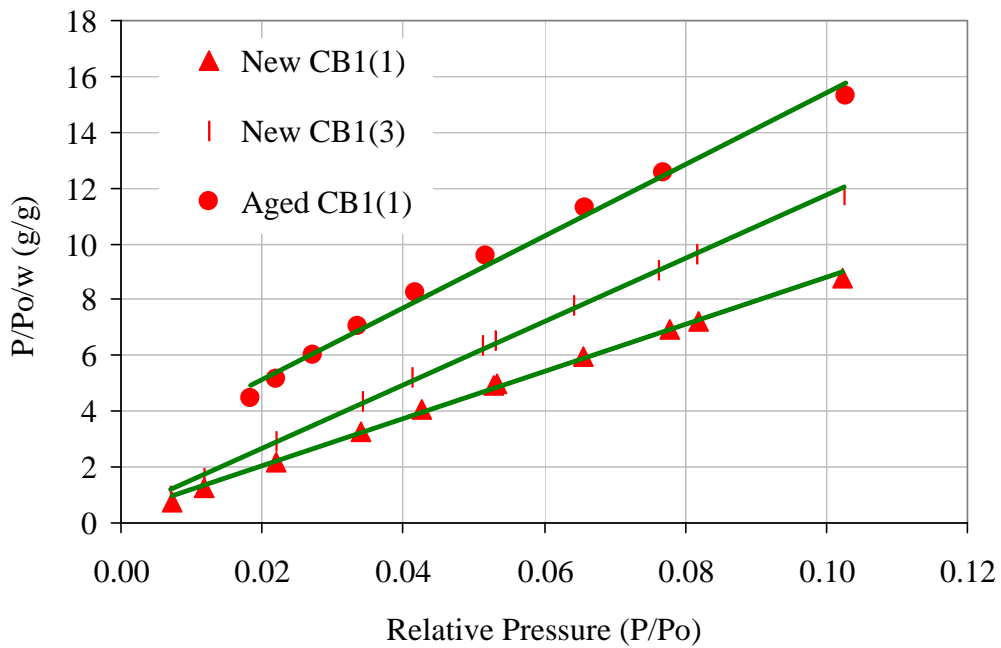
Figure 4.16. Langmuir Model

The Langmuir surface areas are 41.31, 30.76, 26.08 m^2/g compared to BET

Model surface areas of 39.43, 28.78, 26.62 m^2/g for CB1(1), CB1(3), and aged CB1(1),

respectively. The surface area of aged CB1(1) is less than the fresh CB1(1), which

confirms earlier isotherm behavior indicating that sintering had occurred during reaction,

thus resulting in modification of the catalyst structure. Therefore, catalyst preparation

methods have played an important part in catalyst accessible area, which affects the

productivity of catalyst.

4.3.3. BET Model

The traditional multipoint BET model is shown in Figure 4.17. This plot is nearly

linear between relative pressures of 0.05 and 0.35. The BET Model is applicable for

multilayer adsorption controlled by adsorbate-adsorbent interactions. BET and other

model results are shown in Table 4.3. The BET C constants, which are related to the

adsorption energy in the monolayer and indicative of adsorbate-adsorbent interactions,

indicated that heat of adsorption is greater than heat of liquefaction, or the attractive

forces between adsorbate gas molecules in the liquefied state are less than the attractive

forces between adsorbate gas molecules and the adsorbent surface (5). Catalyst CB1(3)

has the highest C constant or strongest adsorbate-adsorbent interactions while CB1(1)

after reaction exhibits the weakest adsorbate-adsorbent interactions. The BET Model

covers the relative pressure region of completed monolayer point progressing to second

layer or higher. When sufficient adsorption has occurred to form a monolayer, the

fraction of surface not covered by any adsorbate is a function of the BET C constant in

which a lower C constant will yield a higher uncovered fraction (14). Since CB1(3) has

the strongest adsorbate-adsorbent interactions, it has the lowest uncovered fraction of 7.16 %, while the uncovered fraction of CB1(1) after reaction is 14.66 %. The BET Model was criticized for neglecting lateral molecules' interactions and assuming the same energy for all adsorption sites. Since the surface interaction energy is decreased, and lateral interaction energy increased with adsorbed volume, the sum of these energies is nearly constant overall adsorption energy up to completion of the monolayer (32).
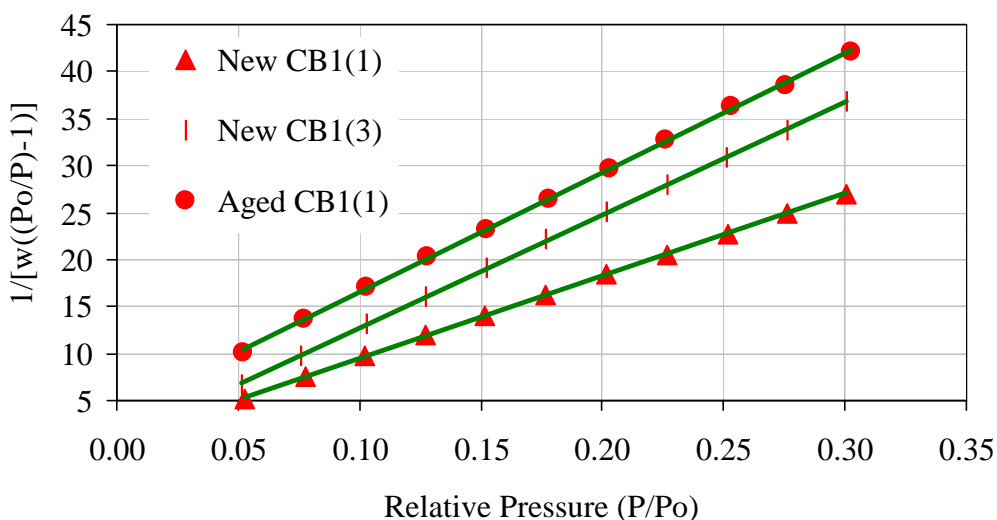
Figure 4.17. BET Model

4.3.4. BJH Model

The volume and area of porous catalysts can be estimated by the BJH Model. This is based on the assumption that the pores are open-ended cylinders and filled with liquid at unity relative pressure. The BJH Model is applicable in the desorption range from unity relative pressure down to the last point of the BET region of 0.35. According

to the literature, pores larger than 300 Å are ignored, and the computations are started at

a relative pressure of 0.967. This does not deny the existence of larger pores, which may

contain up to 10% of the total condensate volume. However, the number of large pores is

generally smaller than the number of smaller ones, hence their contribution to pore

volume and pore area distribution curves are generally less than 1% (16). A summary of

BJH results is also given in Table 4.3. The cumulative surface area is greater than the

BET surface area. The purpose of this method is not for the computation of areas, but for

the determination of the distribution of areas and volumes among pores of varying radii.

The desorption accumulative adsorbed area and volume of BJH model are shown in

Figure 4.18 and 4.19.
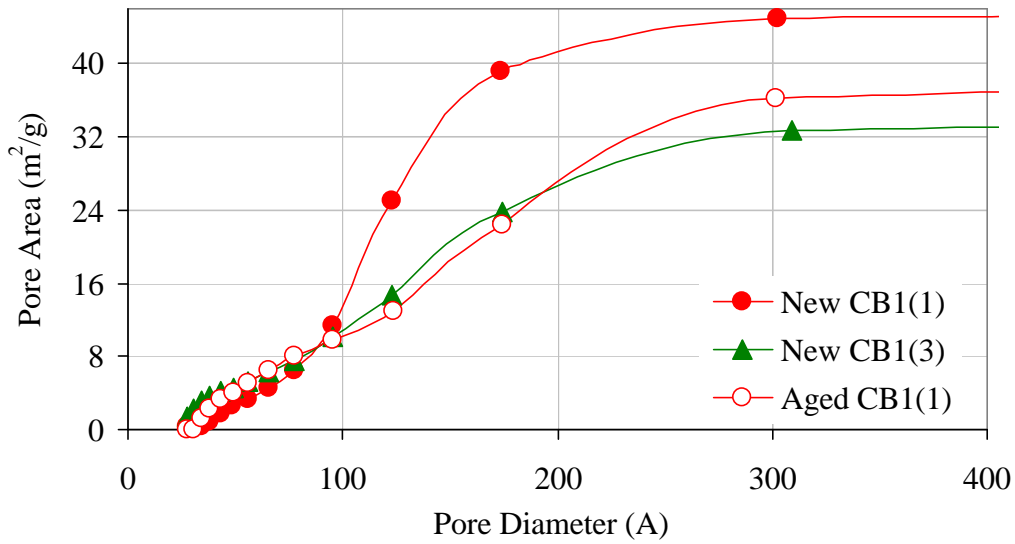
Figure 4.18. Accumulative Desorption Pore Area of BJH Model
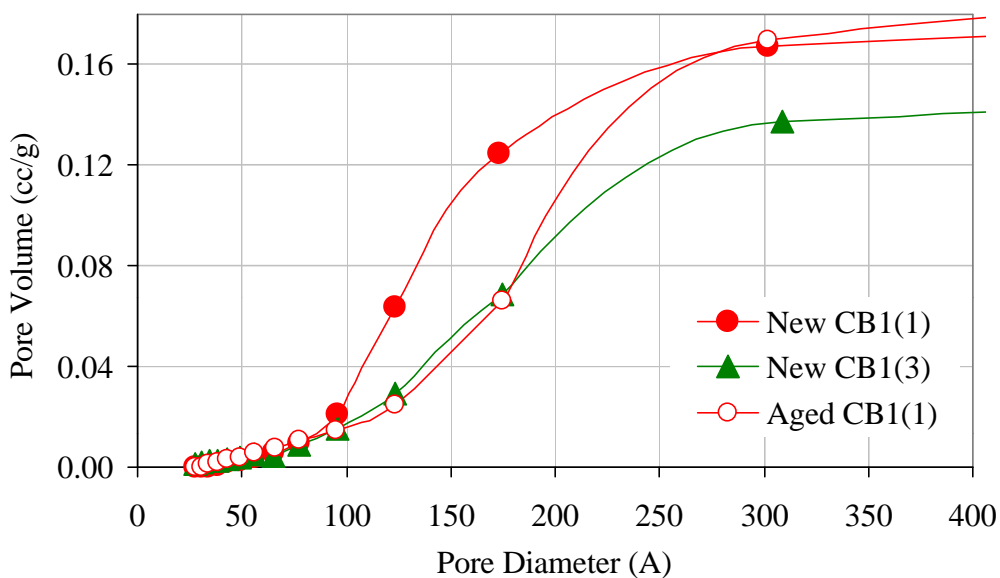
Figure 4.19. Accumulative Desportion Pore Volume of BJH Model

Both pore accumulative area and volume exhibit similar behavior for all pores up to 100 Å. As the pore diameter increases from 75 to 200 Å, the accumulative area of CB1(1) increases rapidly and higher than others where the maximum accumulative surface area is obtained at about 300 Å. Likewise, the accumulative volume of CB1(1) rises quicker, but CB1(1) after reaction has higher final accumulation volume. This may be due to the alteration of the pore structure at high temperature. The total accumulation volume of CB1(1) after reaction is higher than others. Area and volume distributions of the catalysts are shown in Figures 4.20 and 4.21. Obviously, there could be no rigidly "correct" distribution curve because the void spaces are not necessarily cylindrical pores (16). Catalyst CB1(1) observed to have a narrow distribution while CB1(1) after reaction and CB1(3) exhibit broad distribution. Based on the pore area distribution, the most

probable radius of 123 Å is observed for both CB1(1) and CB1(3), and 174Å for CB1(1) after reaction. Likewise, the pore volume maximum is achieved at 123Å for CB1(1), 174Å for both CB1(3) and CB1(1) after reaction. BJH model is applicable for catalysts with mesopores. Due to the shape of the hysteresis loops, the mesopore assumption should be valid in this case. However, the shape of these pores are proved to be the aggregates of adsorbent containing parallel plates, slit shape pores, or wide capillaries. Therefore, the assumption of open-ended pores may be insufficient.

Table 4.3. Physisorption Results

	CB1(1)	CB1(3)	Aged CB1(1)
Modified Langmuir Model			
Monolayer Weight (g/g)	0.0119	0.0088	0.0075
Area (m^2/g)	41.312	30.768	26.084
BET Model			
C Constant	123.56	168.58	33.868
Monolayer Weight (g/g)	0.0113	0.0083	0.0076
Surface Area (m^2/g)	39.432	28.780	26.626
Uncovered Fraction	0.0825	0.0715	0.1466
BJH Desorption Model			
Cumulative Desorption Surface Area (m^2/g)	45.600	33.170	37.770
Cumulative Desorption Pore Volume (cc/g)	0.2026	0.1695	0.2488
Desorption Pore Diameter (A)	123.10	174.50	174.40
de Boer T Method			
Micropore Area (m^2/g)	13.720	11.760	0.000
External Surface Area (m^2/g)	25.700	17.020	27.330
Total Area (m^2/g)	39.420	28.780	27.330
Halsey T Method			
Micropore Area (m^2/g)	10.85	9.858	0.000
External Surface Area (m^2/g)	28.580	18.920	27.330
External Surface Area (m^2/g)	39.430	28.778	27.330
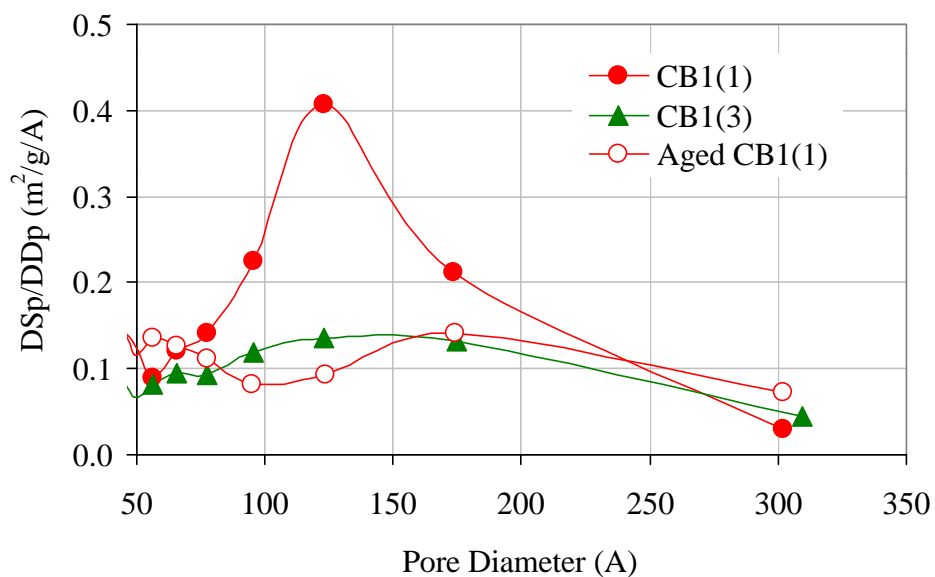
Figure 4.20. Desorption Area Distribution of BJH Model
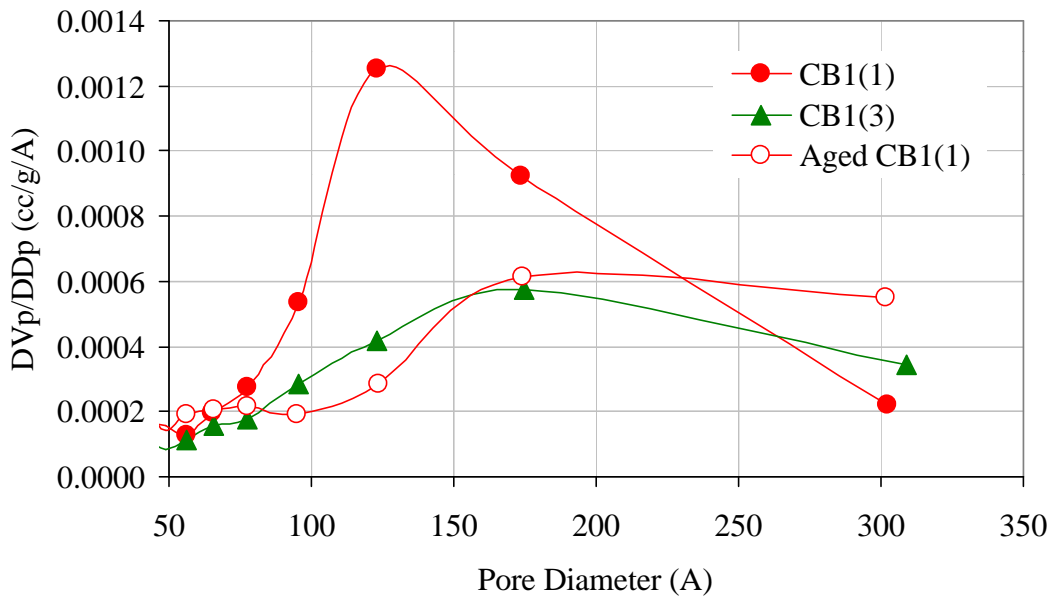
Figure 4.21. Desorption Volume Distribution of BJH Model

4.3.5.   The t Method

The characteristic t curves are shown in Figure 4.22. At the same average thickness, the de Boer method yields higher adsorbed volume compared to the Halsey method. The adsorbed volume from both methods is decreasing in the order of CB1(1), CB1(3), and CB1(1) after reaction. The first downward deviation at relatively low pressure shown in the characteristic t curve of CB1(1) and CB1(3) may be due to the blocking of accessible surface area in the micropore region (8, 17). Growth of the adsorbed layer at the surface or in the intermediate pores is indicated by the upper region following the capillary condensation in the wider pores (17). The characteristic t curves compared with the BET t curve are shown in Figure 4.23. The de Boer average thickness is in agreement with BET t curve in the relative pressure region less than 0.65. In addition, the Halsey equation is based on the assumption that the adsorbed layers behave as a normal liquid nitrogen layer, while the BET theory assumes that the adsorbed layer has the same density as the capillary condensed liquid. The Halsey equation depends on a monolayer thickness of 3.54 Å, while the t method from BET is evaluated according to the BET surface area. The differences between the Halsey and BET models are observed. The monolayer is completed at a statistical thickness of 3.54 Å, 2.5 Å, and 2.9 Å according to Halsey, de Boer, and BET, respectively. At these t values, the t curve deviates from the first downward region, indicating that more nitrogen is taken up corresponding to multimolecular adsorption. Most of the pores are filled at an average t value of about 11.5 Å, which corresponds to the relative pressure of 0.8. The t values used to evaluate surface area are recommended up to a relative pressure of 0.75 (17). The

chosen pressure range for the t-method surface area evaluation is from point B up to best linear fit of relative pressure range (~ 0.1). In the multimolecular adsorption region, the t curve should be a straight line through the origin for a nonporous material. The slope of this linear region gives the specific surface area. The extrapolation of the linear region to the adsorption axis gives a positive intercept equivalent to the micropore volume. From Table 4.3, the external surface areas of the fresh catalysts are lower than the BET surface area, but the sum of micropore and external surface area is in good agreement with surface area obtained from BET equation. All models concluded that CB1(1) had the highest total surface area, while CB1(1) after reaction had the lowest total surface area due to pore modification. In conclusion, the experimental data are well fitted to the models, and micropores are also existed in both fresh catalysts. Only the external area of catalyst CB1(1) after reaction is in good agreement with BET surface area due to the absence of micropores.
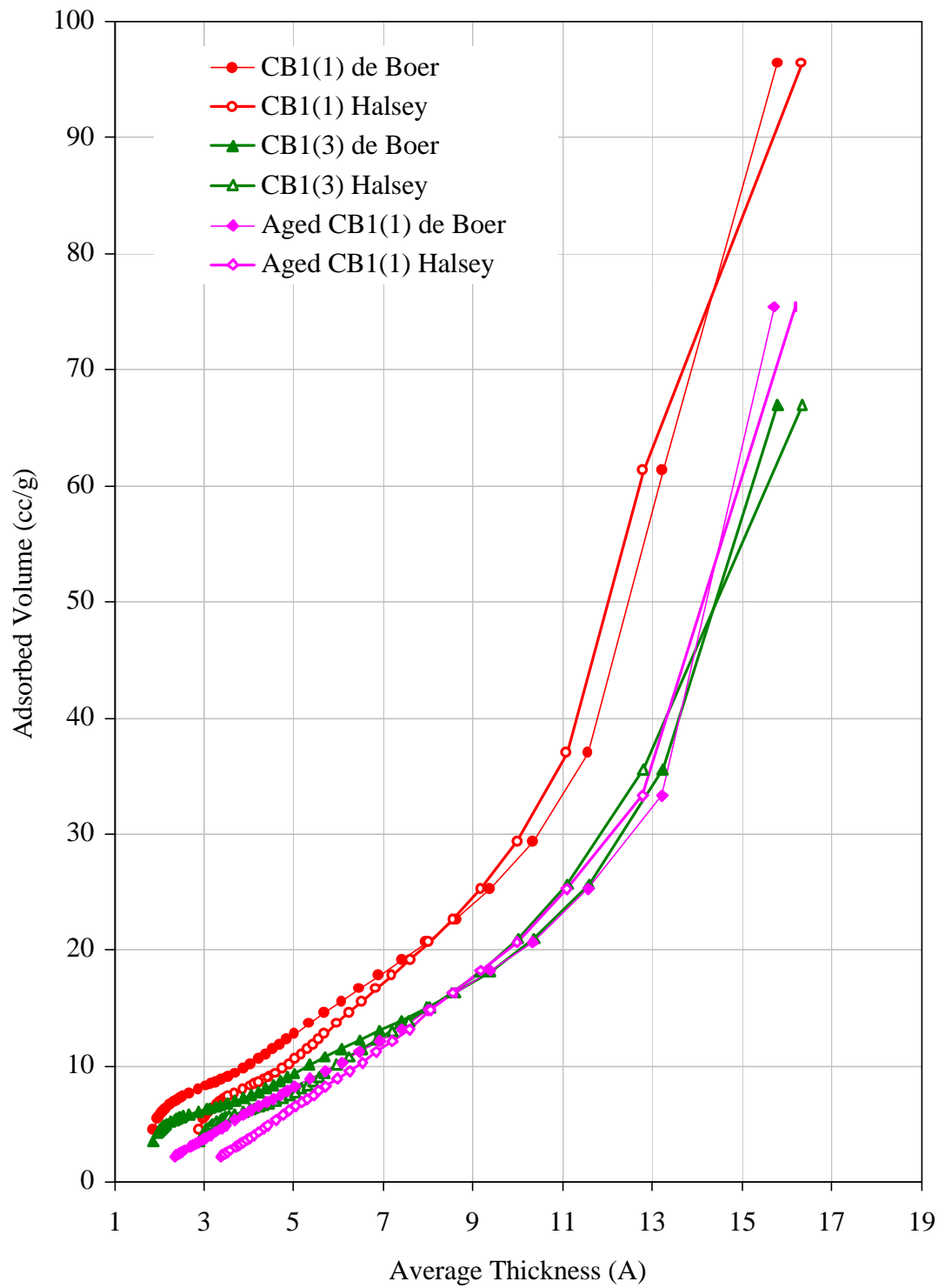
Figure 4.22. Characteristic t Curve

104
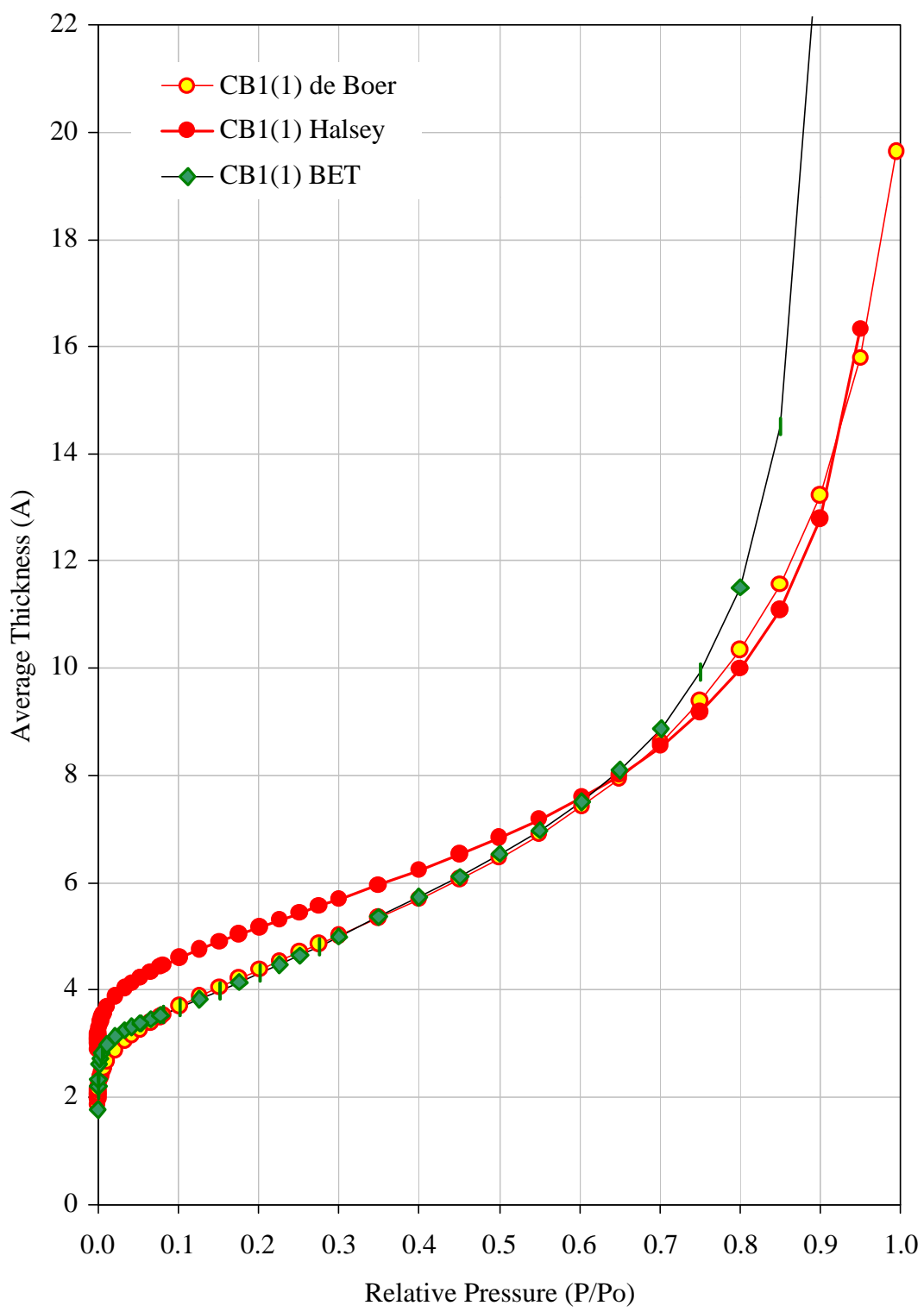
Figure 4.23. Characteristic t Curve Compared with Fitted BET Isotherm

4.4. References

1.   Knight, A., "Gas Adsorption", Innovative Teaching Lab, (1996).

2.   Webb, P., Orr, C., <u>Analytical Methods in Fine Particle Technology</u>, (Micromeritics Instrument Corporation, Norcross, GA: 1998).

3.   Gregg, S., Sing, K., <u>Adsorption, Surface Area and Porosity</u>, (Academic Press, New York: 1967).

4.   "Gas Sorption System Manual", Quantachrome Corporation, (1998).

5.   Brunauer, S., Deming, L. S., Deming, W. S., Teller, E., *Journal of the American Chemical Society*, <u>62</u>, 1723, (1940).

6.   "Chembed 3000 Manual", Quantachrome Corporation, (1996).

7.   Langmuir, I., *Journal of the American Chemical Society*, <u>40</u>, 1361, (1918).

8.   De Boer, J. H., "Surface Area Determination", International Union of Pure and Applied Chemistry in Conjunction with the Society of Chemical Industry, Proceedings of the International Symposium on Surface Area Determination, (1969).

9.   Rouquerol, F., Rouquerol, J., Sing, K., <u>Adsorption by Powders and Porous Solids: Principles, Methodology and Applications</u>, (Academic Press, London: 1999).

10.   Satterfield, C., <u>Heterogeneous Catalysis in Industrial Practice</u>, (McGraw-Hill, New York: 1991).

11.   Langmuir, I., *Journal of the American Chemical Society*, <u>37</u>, 1139, (1915).

12.   Brunauer, S., Emmett, P., Teller, E., *Journal of the American Chemical Society*, <u>60</u>, 309, (1938).

13.   Lowell, S., Shields, J., Charalambous, G., Manzione, J*., Journal of Colloid and Interface Science*, <u>86</u>, 191, (1982).

14.   Hill, T., *Journal of Chemical Physics*, <u>14</u>, 268, (1946).

15.   Lowell, S., *Powder Technology*, <u>12</u>, 291, (1975).

16.   Barrett, E., Joyner, L, Halenda, P., *Journal of the American Chemical Society*, <u>28</u>, 373, (1951).

17.   De Boer, J. H., Lippens, B. C., Lisen, B. G., Broekhoff, J. C. P., *Journal of Colloid and Interface Science*, <u>21</u>, 405, (1966).

18.   Lippens, B. C., De Boer, J. H., *Journal of Catalysis*, <u>4</u>, 319, (1965).

19.   Lippens, B. C., Lisen, B. G., De Boer, J. H., *Journal of Catalysis*, <u>3</u>, 32, (1964).

20.   De Boer, J. H., Lisen, B. G., Osinga, T. J., *Journal of Catalysis*, <u>4</u>, 643, (1965).

21.   Halsey, G. D., *Journal of Chemical Physics*, <u>16</u>, 931, (1948).

22.   Harkins, W. D., Jura, G., *Journal of the American Chemical Society*, <u>66</u>, 1366, (1944).

23.   Jura, G., Harkins, W. D., *Journal of the American Chemical Society*, <u>68</u>, 1941, (1946).

24.   Tompkins, F. C., <u>Chemisorption of Gases on Metals</u>, (Academic Press, New York: 1978).

25.   Masel, R. I., <u>Principles of Adsorption and Reaction on Solid Surfaces</u>, (John Wiley & Sons, Inc., New York: 1996).

26.   Wedler, G., <u>Chemisorption: An Experimental Approach</u>, (Butterworths, Boston: 1970).

27.   Laidler, K. J., <u>Catalysis</u>, Emmett, P. H., ed., (Reinhold, Volume 1, Chapter 3, New York: 1956).

28.   Young, D. M., Crowell, A. D., <u>Physical Adsorption of Gases</u>, (Butterworths, London: 1962).

29.   Ross, S., Olivier, J. P., <u>On Physical Adsorption</u>, (John Wiley & Sons, Inc., New York: 1964).

30.   de Boer, J. H., <u>The Structure and Properties of Porous Materials</u>, Everett, D. H., Stone, F. S., eds., (Butterworth, London: 1958).

31.   Brunauer, S., Mikhail, R. SH., Bodor, E. E., *Journal of Colloid and Interface Science*, <u>24</u>, 451, (1967).

32.   Lowell, S., Shields, J. E., <u>Powder Surface Area and Porosity</u>, (Chapman & Hall, New York: 1991)

CHAPTER V

SURFACE CHARACTERIZATION

5.1. X-Ray Photoelectron Spectroscopy Theory

Characterization of surface properties is definitely important to catalysts since most catalytic reactions occur on the surface. The surface is not only the top layers of adsorbent molecules but also the non-uniform transition layers. Generally, the chemical composition of the surface is significantly different from the interior bulk. The surface methods provide both qualitative and quantitative chemical information about surface composition (1).

XPS provides not only information about the atomic composition, but also the structure and oxidation states present in the sample. The basis of XPS originated from Einstein's photoelectric process. This process depends on the ejection of electrons during a collision with the surface, and the surface having enough energy to expel them (2). The schematic of the XPS process is shown in Figure 5.1. The surface is irradiated monoenergetic soft x-ray of Mg Kα or of Al Kα with hν incident energy. Higher incident energy (hν) than the inner shell electron energy will result in the excitation of the electrons, and eventually photoelectrons are emitted from the surface with a range of their kinetic energy. Moreover, the law of conservation of energy can be used to determine the final energy state of the emitted photoelectron (5).
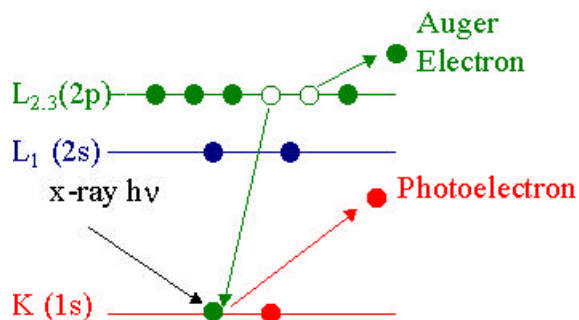
Figure 5.1. XPS Emission Process (3)

The photon penetrating power of an x-ray source is typically in the range of ten

microns below the surface. However, only electrons within 80 angstroms region can

leave the surface without losing energy and produce peaks in the spectra. Otherwise, the

electrons will lose energy due to inelastic collisions (3).

The relationship between kinetic energy, E_K, and binding energy, E_B, of the

emitted electron referenced to Fermi level is illustrated in Figure 5.2. It is also noted that

the sum of kinetic energies of the emitted electrons do not exceed the ionizing photon

energy according to the law of conservation of energy. Also, the kinetic energy of the

emitted electrons varies corresponding to the ion final states in the atom (3).

$$E_K = h\nu - E_B - \Phi_A \qquad\qquad 5.1$$

where Φ_A is the known spectrometer work function from the instrument calibration.

The binding energy, energy of an ion remaining after emission, is the energy

relative to the Fermi level (zero binding energy). In a solid, binding energy is defined as

the energy difference between initial and final states after the electron has been ejected.

Since the binding energy is unique for each element, the atomic concentration for each element can be identified.
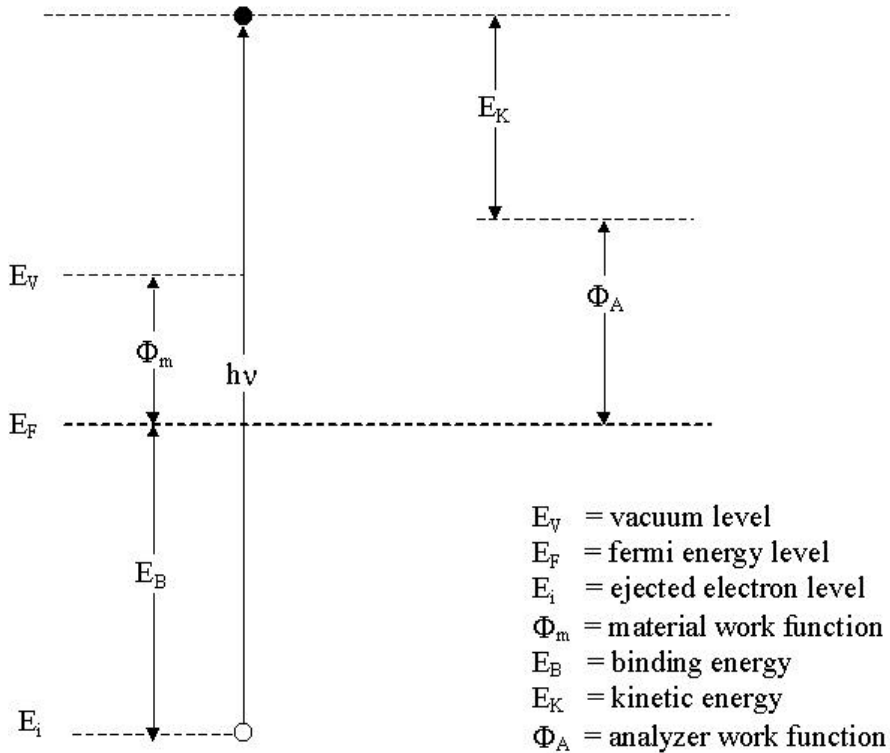
Figure 5.2. XPS Energy Level Diagram (5)

Moreover, the work function is not well defined in many cases and also can alter the binding energy value by several electron volts. After the photon ejection process, the electrons pass through one potential field to another when traveling from the sample into the analyzer (4). Also, after photoelectron emission, Auger electrons may be ejected due to the relaxation of remaining excited ions. The Auger kinetic energy is independent on the mode of initial ionization. It is the difference between the initial ionization energy

and double of final ion charge. Thus, the two types of emitted electrons from the

photoionization process are the photoelectron and Auger electron (3).

5.2.   Instrumentation

The analysis was performed by PHI model 1600 XPS instrument as shown in

Figure 5.3, in which only major components are illustrated. The components of the

surface analysis system are consisted of a x-ray source, a vacuum chamber, an electron

energy analyzer, an ion gun, and a signal processor.

Dual Anode X-Ray Source

Energy Analyzer

Ion Gun
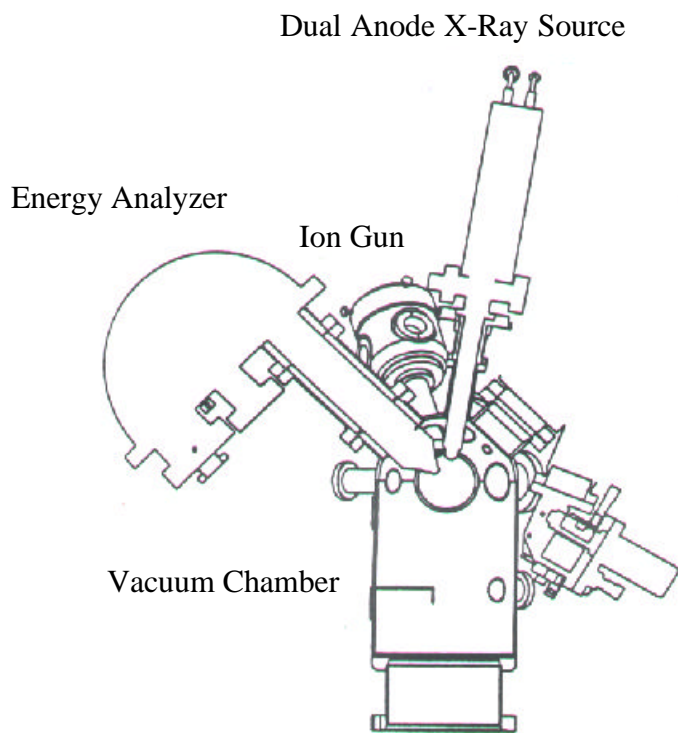
Vacuum Chamber

Figure 5.3. Schematic Diagram of PHI 1600 Model

5.2.1. Vacuum Requirements

In order for the photoelectron to travel from the surface to the analyzer without losing energy due to collisions with the gas molecules inside the chamber, a vacuum below 8.5×10^{-8} Torr must be maintained. The degree of contamination will be minimized under ultra high vacuum (UHV) thus eliminating the altering in data interpretation of XPS spectra. An ion gauge, about which the operation details can be found in the vacuum technology handbook (7), is used to monitor the pressure of the system. A turbomolecular pump and an ion pump are used to maintain UHV conditions.

5.2.2. X-ray Source

The Phi Model 1600 XPS system employed a dual-anode x-ray source. The exterior housing protects its delicate interior from the high voltage of the ultra high vacuum chamber. The anode, filament assemblies, and the cooling water attachment make up the body of the x-ray source. An illustration of the dual-anode x-ray source is shown in Figure 5.4 (6, 8).

The dual anode source has a two-face anode constructed from a thin magnesium (or aluminum) foil. Each of the anode's faces has a semi-circular filament at near ground potential. The electron accelerates through a 15 kV potential and bombards the magnesium anode foil to generate x-rays of Mg Kα at 1253.6 eV. The monochromatic and the standard x-ray source are located at 90° and 54.7° relative to the analyzer axis, respectively (3). The x-ray source is operated at 200 watts and 15 kV to provide the uniform flux of photons over the sample area of 1 cm^2 (6, 33).
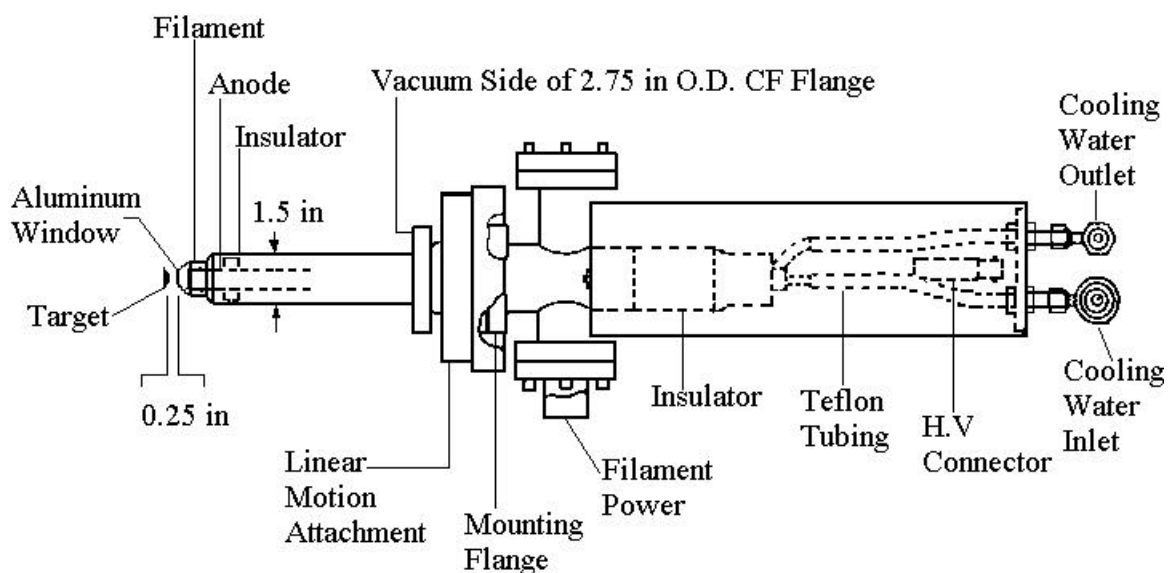
Figure 5.4. Dual Anode X-ray Source Schematic (8)

5.2.3. Electron Energy Analyzer

The Phi Model 1600 XPS employs a spherical capacitor analyzer (SCA) to measure the kinetic energy of the emitted photoelectrons. The SCA operates at a fixed energy window or pass energy (ΔE) to maintain the constant energy resolution ($\Delta E / E$) for which 46.95 and 23.5 eV are low and high resolution, respectively. Only electrons that have energy within this range will be accepted and then adjusted to this pass energy. While the SCA operates at a constant pass energy, the Omni Focus III lens is used to scan the spectrum (3, 6, 33).

5.2.4. Spectrum Interpretation

The electron spectra consist of the number of detected electrons (in kilo counts) as a function of their kinetic energy in a fixed energy interval. Only electrons that leave the surface without energy loss produce well-defined peaks. Other electrons undergo

113

inelastic loss processes before emerging to form the background (6). Elements of sample can be identified based on their characteristic binding energy according to the atomic orbital where the electrons are emitted. A survey scan of 0 to 1100 eV should be obtained first for elemental identification. In addition to a broad survey scan, narrower detailed scans provided the information about oxidation, quantitative analysis, peak deconvolution, and other data manipulation (6).

5.2.5. Angle-resolved XPS

To determine the atomic concentration gradient at different surface levels, angle-resolved XPS is employed by tilting the sample for the desired electron take-off angle. The take-off angle is the angle between the sample longitudinal axis and the entrance to the spectrometer parallel axis in which the limitation in this case is between 30° and 60° (3).

5.2.6. Software

The Phi Model 1600 system is controlled and operated by Windows-based software. The software data acquisition mode obtained the requested spectra such as survey or multiplex. The software is designed to convert the PCS data file to an ASCII file, and then the data are compiled and analyzed. XPSPEAK 4.1 program has also been used to provide the data analysis means for peak fitting, deconvolution, relative peak areas, and heights.

The XPS operating parameters are as follows: The UHV chamber pressure is less than 8.5 x 10^{-8} Torr, while the pretreatment chamber pressure is 7.5 x 10^{-3} Torr in which pure hydrogen is the treatment gas. Survey spectra are taken in the range of 0 – 1100eV with a pass energy of 46.95 eV and step size of 0.5 eV. Survey spectra are repeated 10 times with the acquisition time of 18 minutes. The pass energy of the high resolution spectra is 23.5 eV with the step size of 0.2 eV. The ratio of time / step is 50 ms. Finally the repeating scan number is 15 times.

5.3. Results and Discussion

XPS surface characterizations were performed on fresh catalyst after overnight outgassing at room temperature in the UHV chamber. The fresh catalyst was then moved to the pretreatment chamber and reduced under 7.5 x 10^{-3} Torr of flowing research-grade hydrogen. The pretreatment temperature was ramped at approximately 5°C per minute to 175°C and held at this temperature for one hour. The pretreated catalysts were then reanalyzed using XPS without exposure to air. The same catalysts were then pretreated again with hydrogen at the same pressure and a temperature of 225°C. The process treatment was repeated at 275°C. The depth profiles were obtained by analyzing the surface at 30° and 60° take-off angle. The aged catalysts were retrieved from the reactor after about one week under reaction conditions, and then analyzed after outgassing in the UHV chamber.

Survey spectra taken from the fresh, reduced and aged catalyst are shown in Figures 5.5 through 5.8. The percentages of all elements on the surface are shown in Figures 5.9 and 5.10. In fresh catalyst, the predominate peak due to O is readily apparent. Other features such as Cu, Cr, and Co are observed with only a trace amount of K present. Distinct oxidation states of Cu, Cr, and Co are present as well as their Auger features. Referring to Figures 5.9 and 5.10, after reduction at different temperatures, the C 1s peak decreases, and K 2p features are increased for CB1(1) catalyst at 30° angle. This may due to the migration of K to the surface during the reductive treatment when carbon contamination is reduced (28). Similar behavior is observed for K 2p at 60° angle, but C 1s features are increased up to the reduction temperature of 225°C, then decreased. At a 60° angle, similar behaviors of C 1s and K 2p are observed for CB1(3) catalyst. However, at 30° angle, C 1s features are increased while K 2p features are decreased. The O 1s peak decreases in intensity for both catalysts at 30° and 60° angle indicating that the oxygen content of the near surface region is reduced during the reductive treatment. This may be due partially to the elimination of O containing carbon contamination, or due to the reduction of metal oxide. Moreover, the Cu features are increased whereas Cr and Co features are almost unchanged indicating that the near surface region of the reduced catalyst is enriched in Cu. Cr and Co species are partially reduced under these conditions. Survey spectra taken from the aged catalyst show an increase in intensity of Cu features for both catalysts as well as K 2p features in CB1(1) catalyst. C 1s features are however reduced. Higher intensity of O 1s peak from the aged
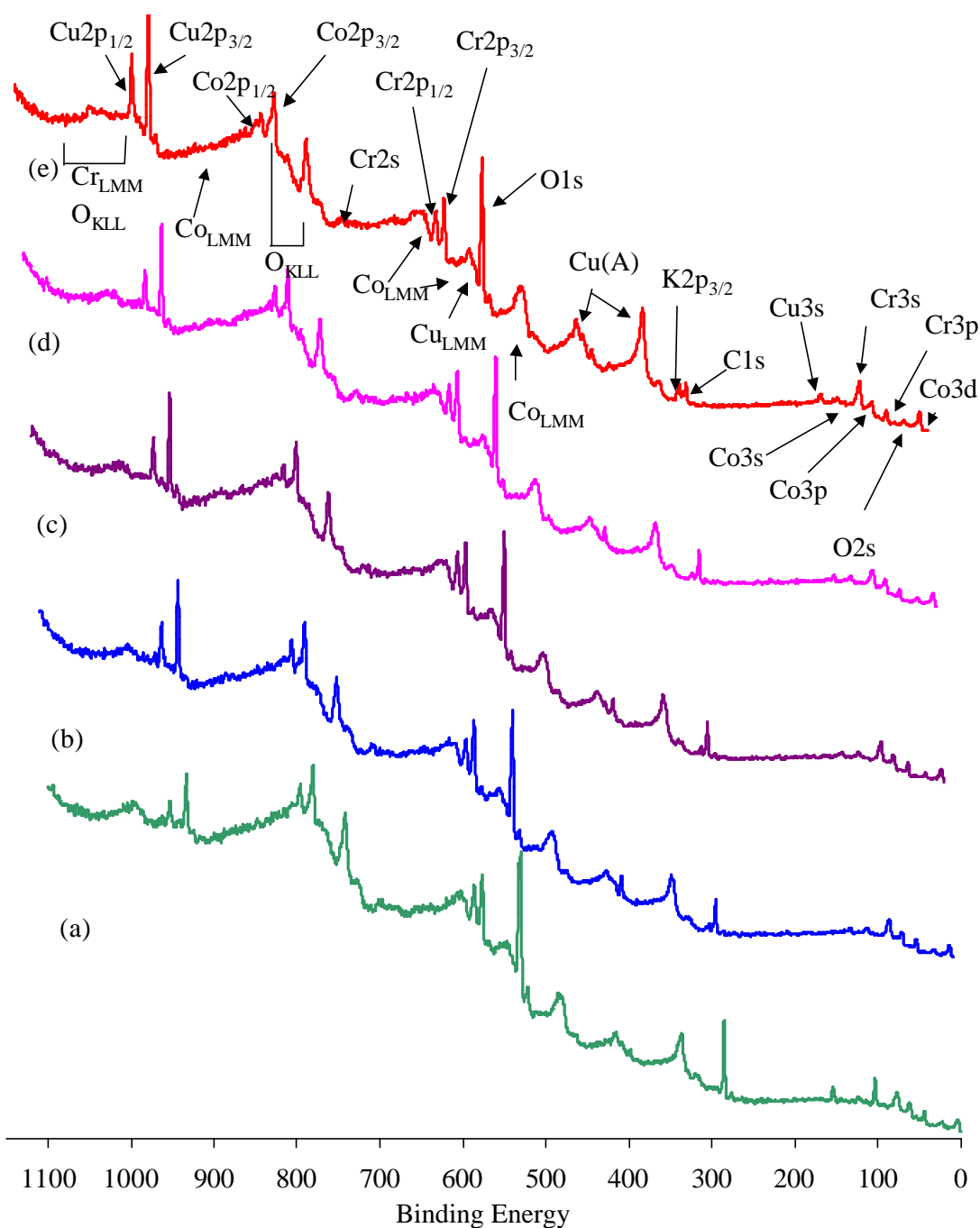
Figure 5.5. CB1(1) XPS Survey at 30° Angle, (a) After Outgassing, (b) 1 hr Reduction at 175°C, (c) 1 hr Reduction at 225°C, (d) 1 hr Reduction at 275°C of H$_2$ at 7.5x10^{-3} Torr, (e) Aged Catalyst

117
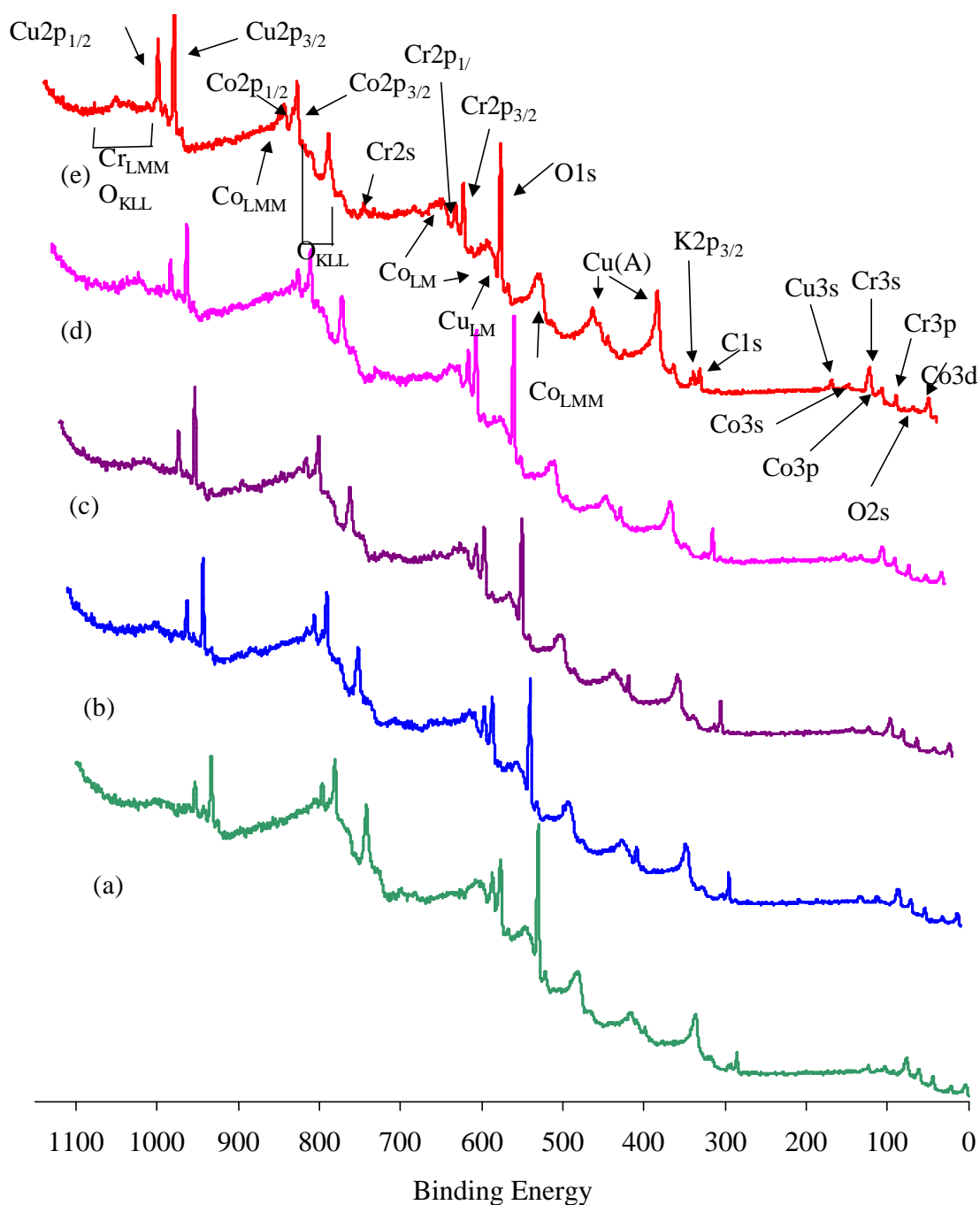
Figure 5.6. CB1(1) XPS Survey at 60° Angle, (a) After Outgassing, (b) 1 hr Reduction at 175°C, (c) 1 hr Reduction at 225°C, (d) 1 hr Reduction at 275°C of H_2 at 7.5x10^{-3} Torr, (e) Aged Catalyst

118
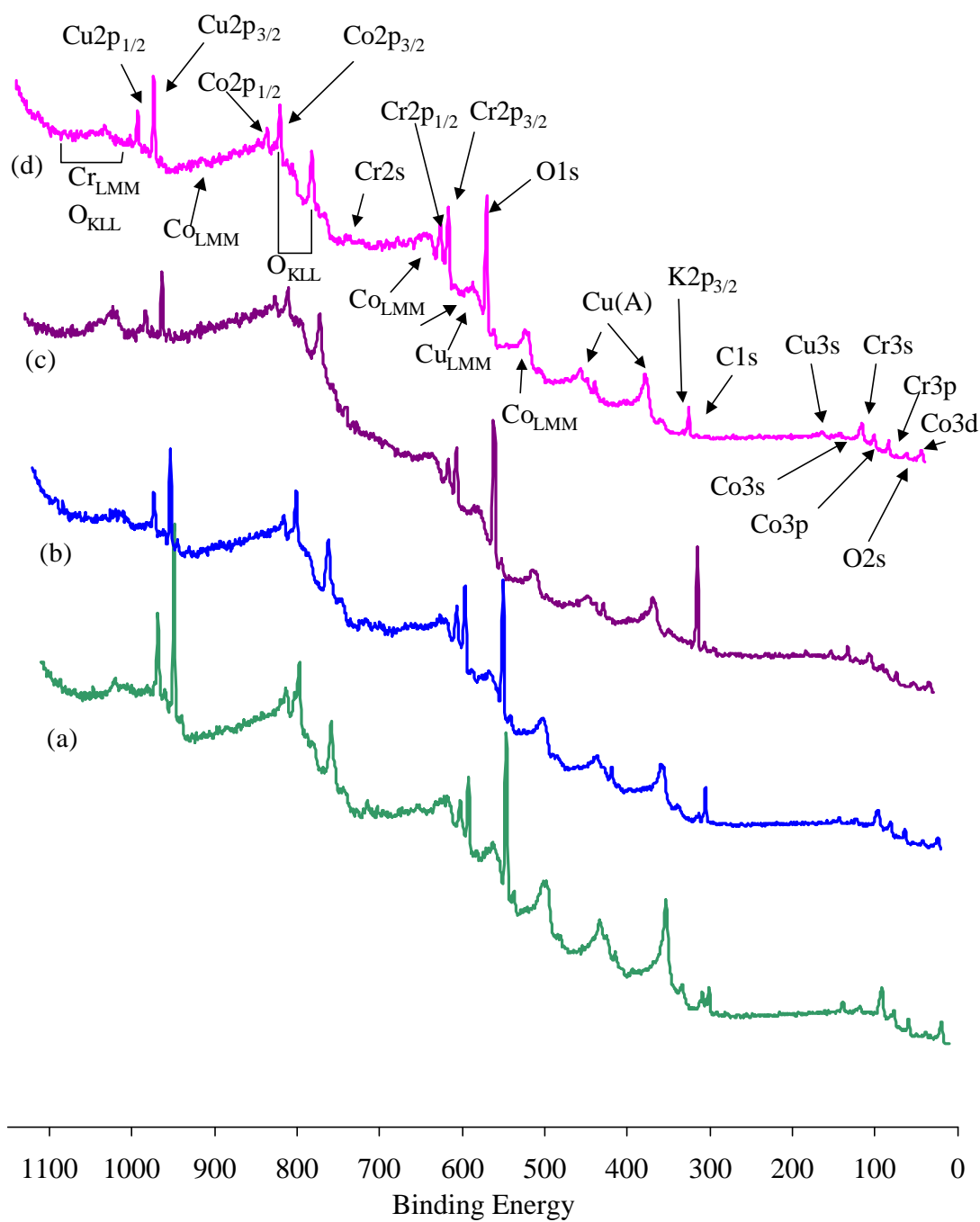
Figure 5.7. CB1(3) XPS Survey at 30° Angle, (a) After Outgassing, (b) 1 hr
Reduction at 175°C, (c) 1 hr Reduction at 225°C, (d) 1 hr
Reduction at 275°C of H$_2$ at 7.5x10^{-3} Torr

119
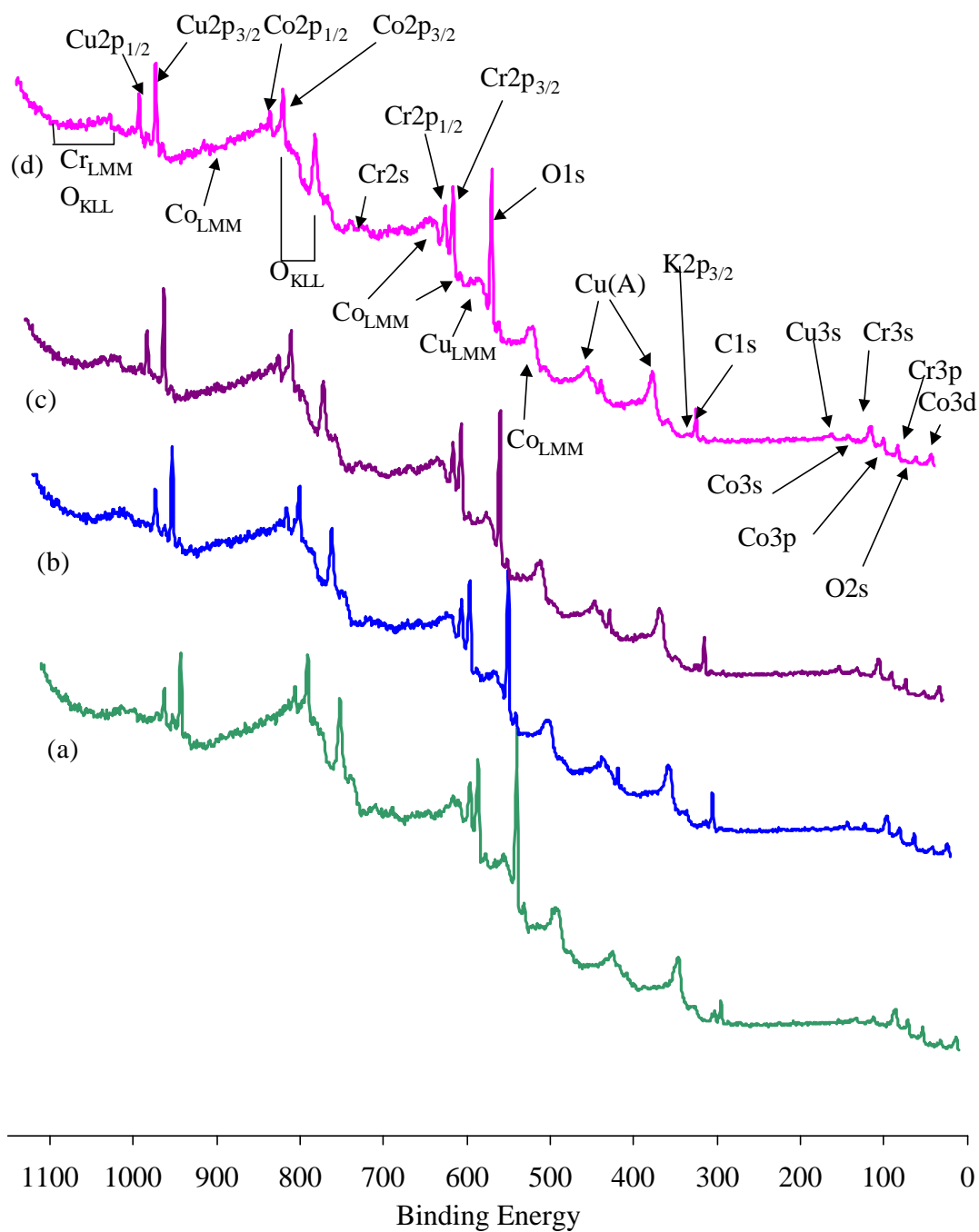
Figure 5.8. CB1(3) XPS Survey at 60° Angle, (a) After Outgassing, (b) 1 hr
Reduction at 175°C, (c) 1 hr Reduction at 225°C, (d) 1 hr
Reduction at 275°C of H$_2$ at 7.5x10^{-2} Torr
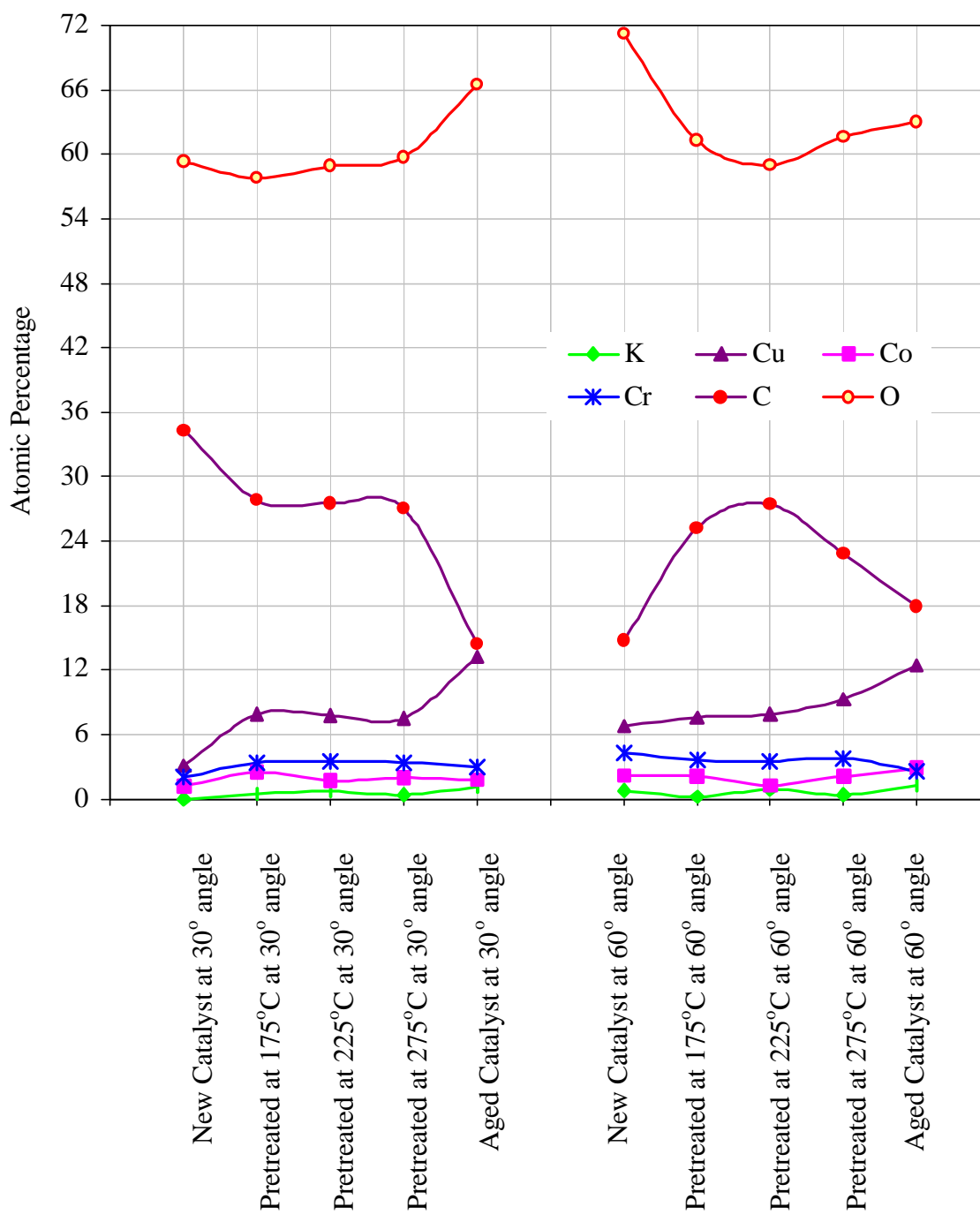
Figure 5.9. Atomic Percentage on the Surface of Catalyst CB1(1)
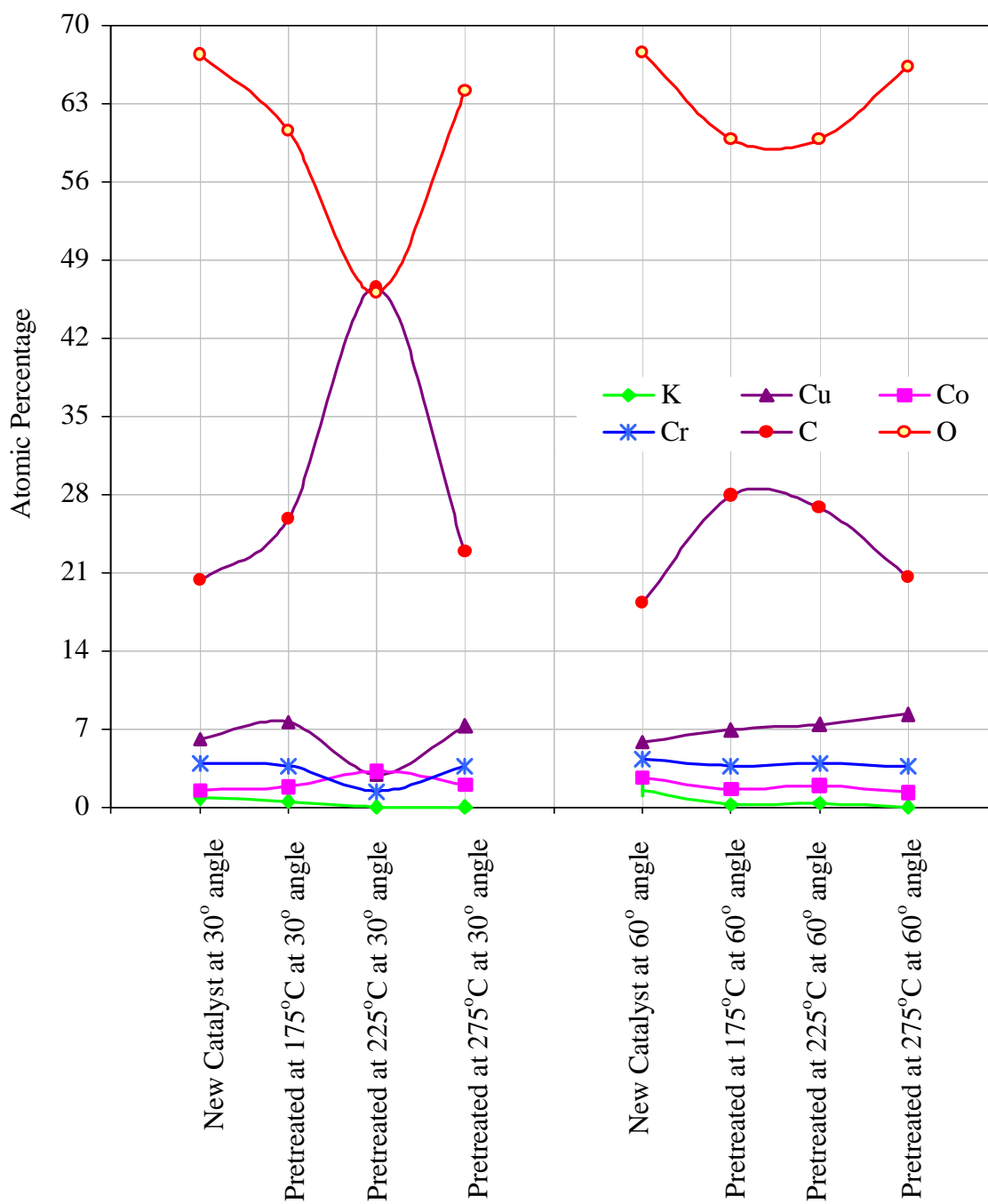
Figure 5.10. Atomic Percentage on the Surface of Catalyst CB1(3)

catalyst may be due to oxygen accumulation during the reaction process, or due to the

catalyst exposure to air. Major changes in reduction are only observed for Cu, C, and O

while K, Co, and Cr species are not significantly changed.

5.3.2. Copper High Resolution Spectra

The binding energies of the detected elements obtained from XPS high-resolution

spectra are calibrated based on 284.8 eV, the adventitious carbon 1s . This is used as a

reference for charge correction (3). The Cu $2p_{3/2}$ XPS spectra taken from the fresh,

reduced, and aged catalysts are shown in Figures 5.11 and 5.12. The peak

deconvolutions, shown in Figures 5.13 and 5.14, are based on the assumption that the

peaks are Gaussian. The Cu $2p_{3/2}$ peak has a BE value of 932.5 eV which corresponds to

either Cu^+ or Cu^0 species. Only through examination of Auger transition parameters can

the differentiation of Cu^+ and Cu^0 species be obtained (10). A shoulder in the Cu peak is

evident at 933.7 due to the presence of Cu^{2+} (3). The high-resolution spectra of fresh

catalyst exhibited other shoulders indicating that other forms of Cu other than Cu^+, Cu^0,

and Cu^{2+} are present. However, these forms disappeared with exposure to H_2, and Cu^0

species in the near-surface increased. A summary of atomic concentrations of Cu $2p_{3/2}$

peaks based on model area is shown in Table 5.1. Cu peak investigation showed that the

ratio of Cu^0/Cu^{2+} species is from 2.76 to 8.70 on the surface of CB1(1), 1.61 to 7.74 in

the bulk of CB1(1), 4.34 to 18.45 on the surface of CB1(3), and 4.26 to 14.03 in the bulk

of CB1(3). The Cu^{2+} species totally disappeared, and only Cu^0, with a much more

intensified and narrower peak, was detected in the catalyst after reaction. In addition, the

Cu^0 species is more intensified in CB1(3) than in CB1(1) catalyst, and more intensified
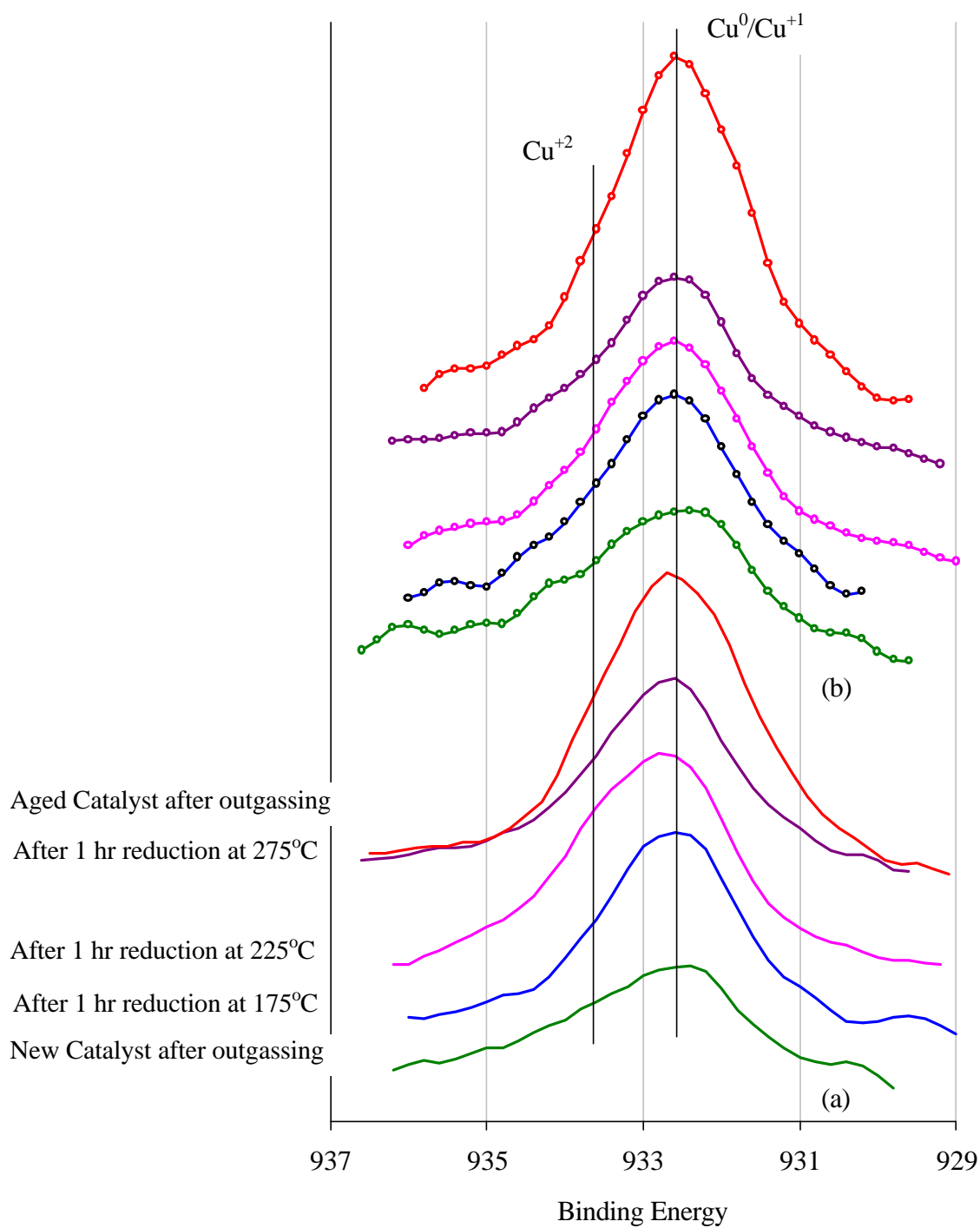
Figure 5.11. CB1(1) XPS High Resolution Spectra of
Cu 2p3/2 at (a) 30° Angle, (b) 60° Angle

124
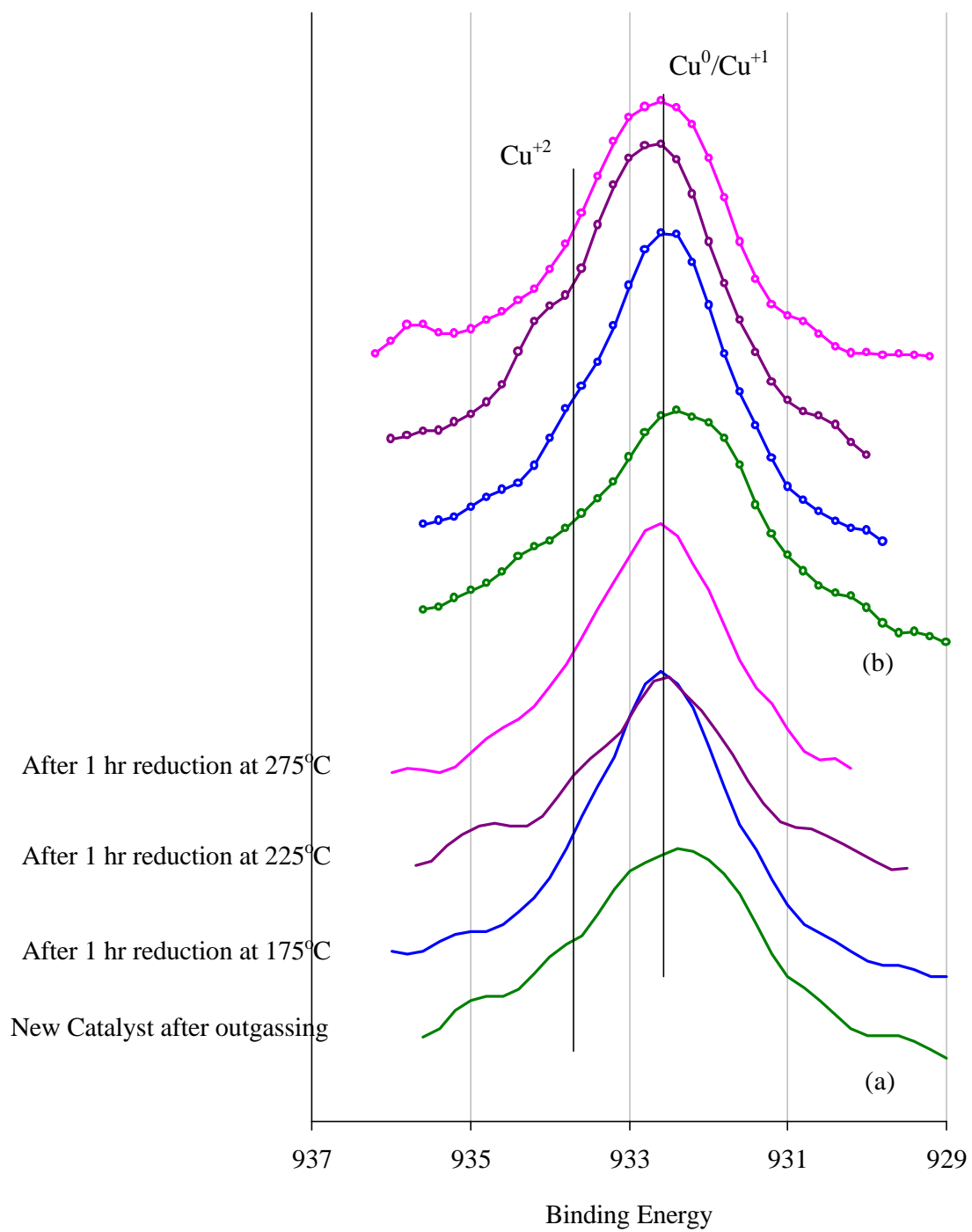
Figure 5.12. CB1(3) XPS High-Resolution Spectra of
Cu 2p3/2 at (a) 30° Angle, (b) 60° Angle

Aged Catalyst after outgassing

After 1 hr reduction at 275°C

After 1 hr reduction at 225°C

After 1 hr reduction at 175°C

New Catalyst after outgassing

(a)

(b)
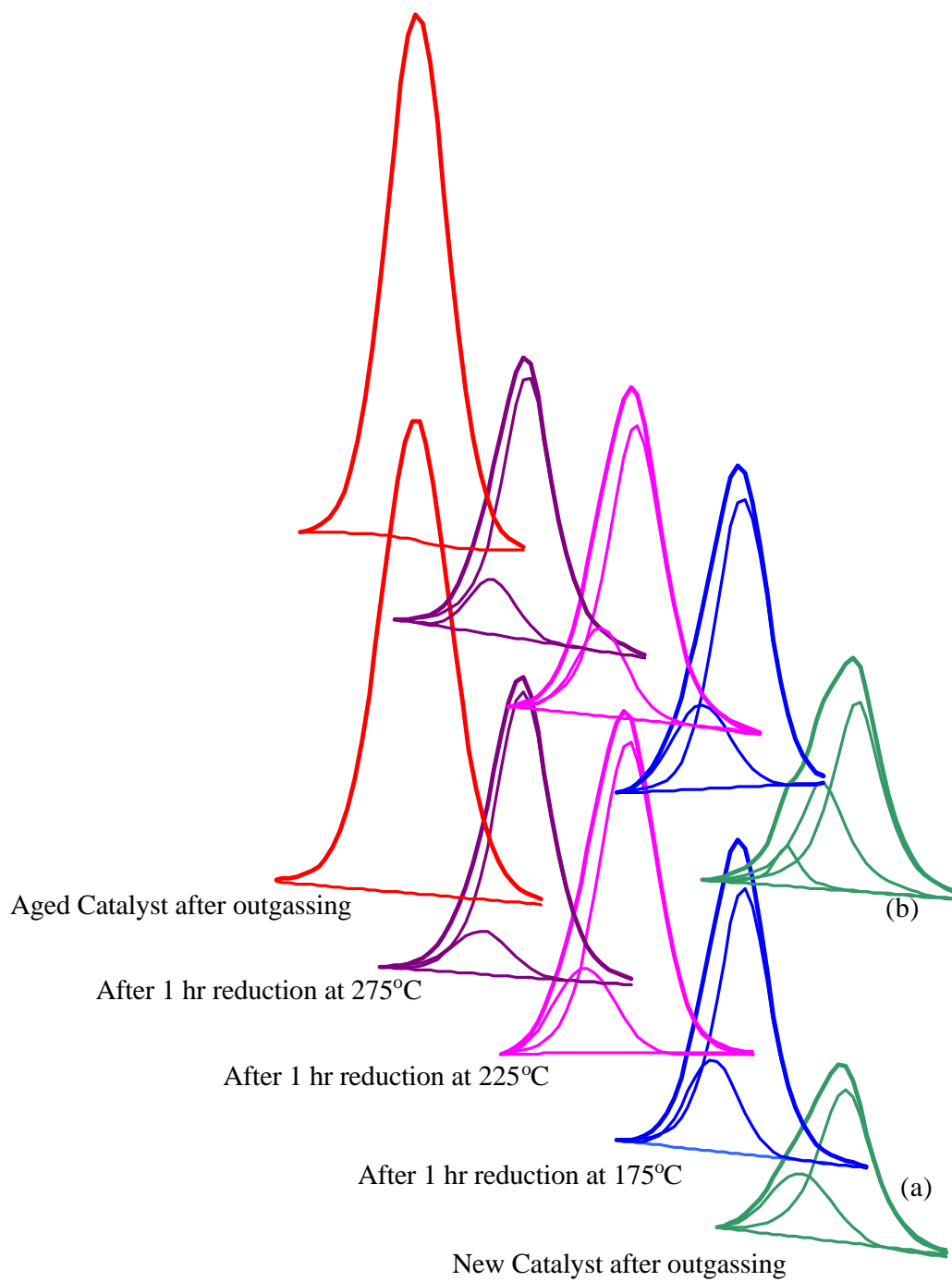
Figure 5.13. Cu 2p3/2 Peak Deconvolutions of XPS High-Resolution Spectra of CB1(1) at (a) 30° Angle, (b) 60° Angle

126

After 1 hr reduction at 275°C

After 1 hr reduction at 225°C

After 1 hr reduction at 175°C

New Catalyst after outgassing

(a)

(b)
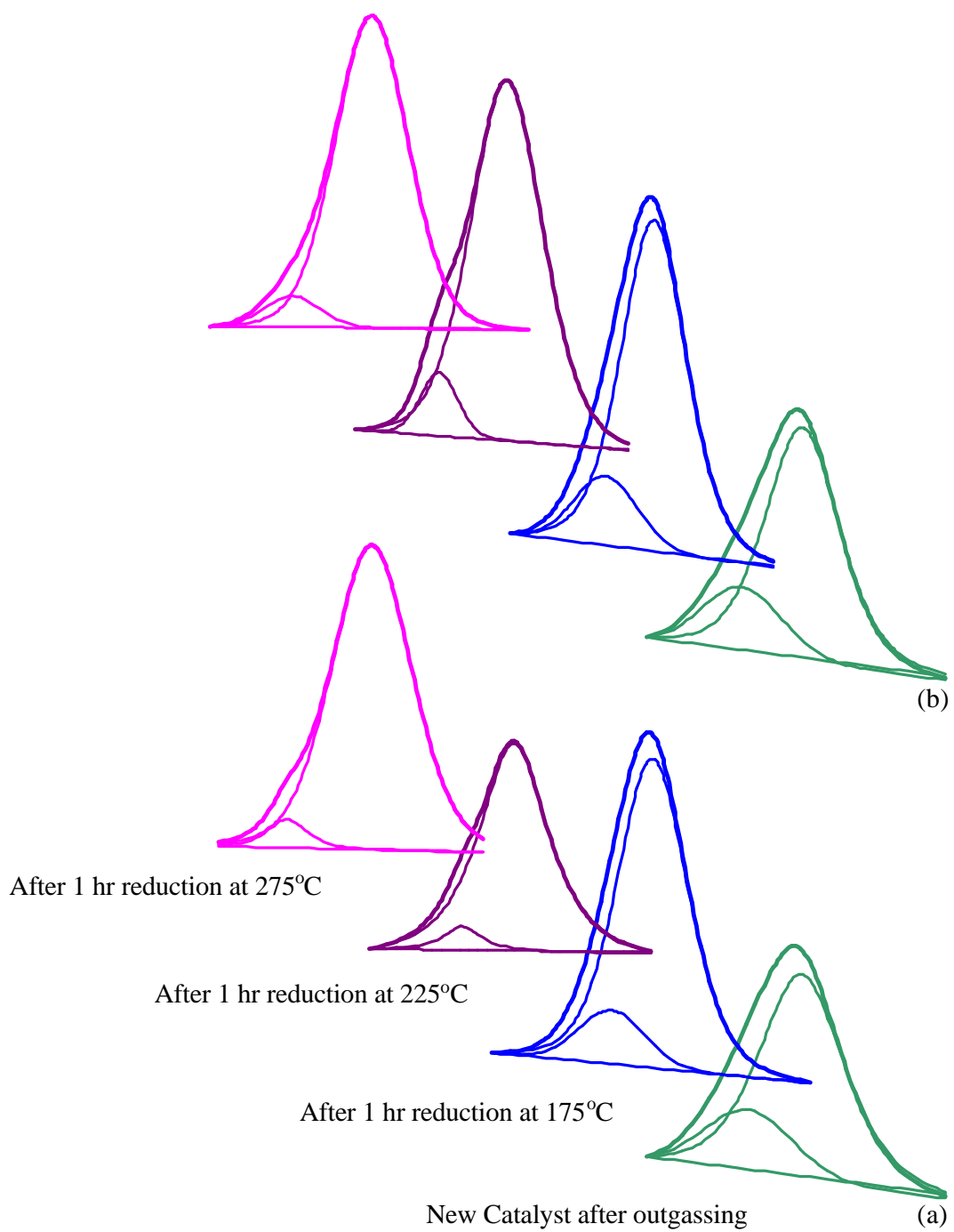
Figure 5.14. Cu 2p3/2 Peak Deconvolutions of XPS High-Resolution
Spectra of CB1(3) at (a) 30° Angle, (b) 60° Angle

on the surface than in the bulk of the fresh catalyst. These effects may be due to the partial reduction of Cu^{2+} species to copper metal, with the remainder being stabilized in Cu^+ state upon hydrogen exposure at high temperature (10, 17). Also, reduction in the Cu^{+2} shoulder indicates that the catalysts are reduced with increasing temperature. The results agree with Monnier et al. (12), who observed that reduction of CuO in Cu-Cr oxide catalyst to Cu^0 occurs upon exposure to H_2 at 270°C. Likewise, Apai et al. (13) and Capece et al. (14) have also stated that the CuO in Cu/Cr_2O_3 catalysts is reduced to Cu^0 upon pretreatment. According to the literature, the amount of stable surface Cu^+ sites was directly related to methanol production rate (15, 16). Both Cu^+ and Cu^0 sites are required for methanol synthesis since the Cu^0 and Cu^+ sites are essential for H_2 and CO adsorption, respectively. Courty et al. (18) speculated that Cu^+ species were stabilized in the spinel or as copper chromate phases, which were responsible for CO adsorption, while Cu^0 was responsible for CO desorption and C-C bond formation. The Cu peak observations also agree with Calafat et al. (11), who stated that Cu^{2+} species in CuZnCr catalyst are completely reduced after the reaction. Also, surface Cu species increase in the catalyst after reaction indicating that no loss in activity is observed because, according to Chinchen et al. (31), activity of catalyst is a function of copper metal concentration.

Table 5.1. Copper Species Concentration of Cu 2p3/2 Peaks

		Cu^0	Cu^{+2}	Cu^0/Cu^{+2}
F1 at 30° angle	Fresh	73.41	26.59	2.76
	Reduced at 175°C	79.96	20.04	3.99
	Reduced at 225°C	80.80	19.20	4.21
	Reduced at 275°C	89.69	10.31	8.70
	Age	100.00	0.00	
F1 at 60° angle	Fresh	61.62	38.38	1.61
	Reduced at 175°C	77.88	22.12	3.52
	Reduced at 225°C	80.01	19.99	4.00
	Reduced at 275°C	88.55	11.45	7.74
	Age	100.00	0.00	
F3 at 30° angle	Fresh	81.27	18.73	4.34
	Reduced at 175°C	88.71	11.29	7.86
	Reduced at 225°C	94.10	5.90	15.95
	Reduced at 275°C	94.86	5.14	18.45
F3 at 60° angle	Fresh	80.99	19.01	4.26
	Reduced at 175°C	86.34	13.66	6.32
	Reduced at 225°C	92.75	7.25	12.80
	Reduced at 275°C	93.35	6.65	14.03

5.3.3. Chromium High Resolution Spectra

The high-resolution XPS Cr $2p_{3/2}$ spectra are shown in Figures 5.15 and 5.16. The broad peak width indicates that a mixture of chemical states is present near the surface. They appear to be Cr^0, Cr^{1+}/Cr^{3+}, $Cr(OH)_x$, and Cr^{6+} at binding energies of 574.8, 576.5, 577.5, and 578.3 eV, respectively. The binding energy difference of Cr^{1+}/Cr^{3+} species in oxide form is not large enough to allow differentiation between the two species. However, no literature has been found to support the presence of Cr^{1+}. Reduction of Cr^{6+} species is observed with exposure to H_2. Cr^{6+} to Cr^{3+} reduction is
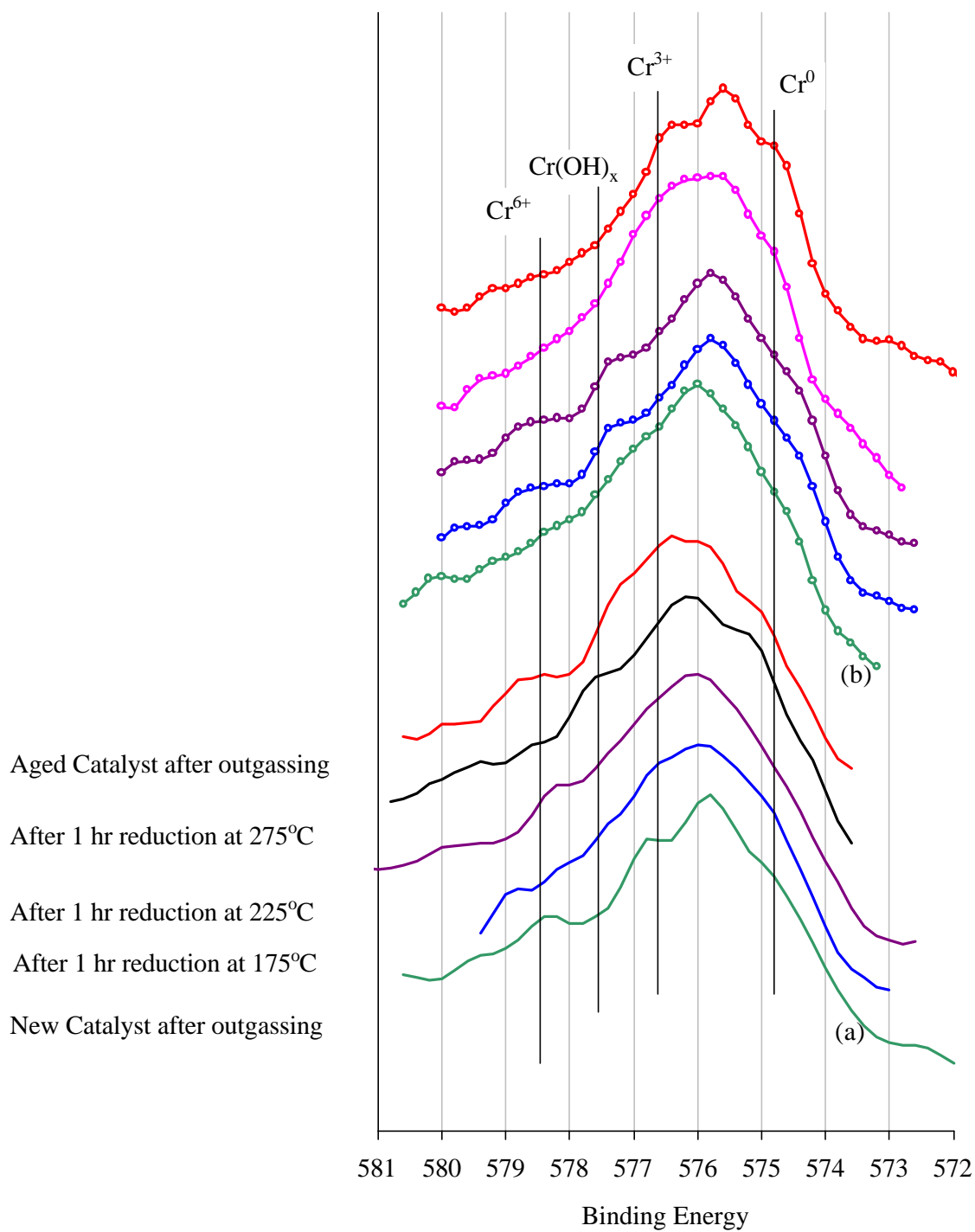
Figure 5.15. CB1(1) XPS High-Resolution Spectra of
Cr 2p3/2 at (a) 30° Angle, (b) 60° Angle

130
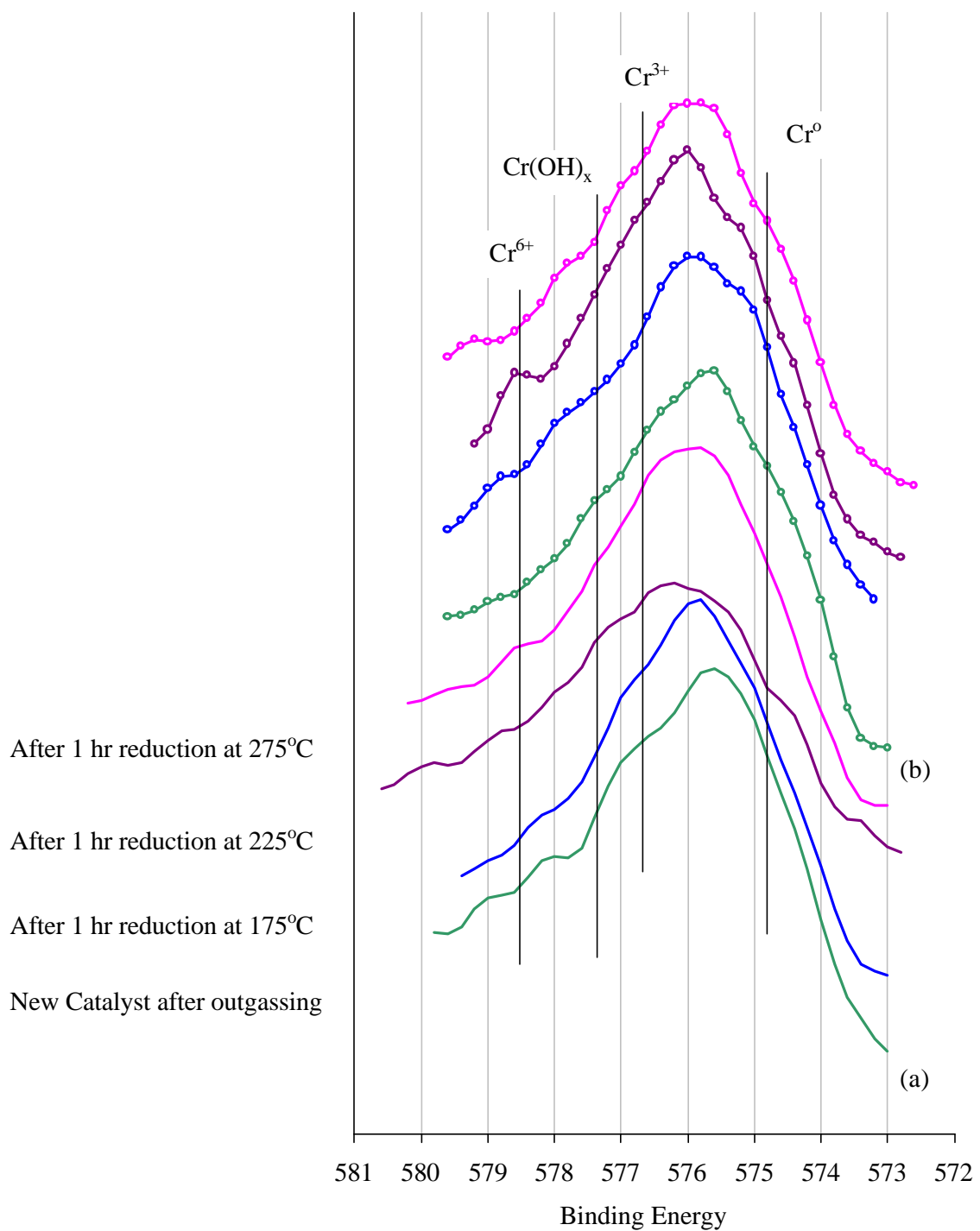
Figure 5.16. CB1(3) XPS High-Resolution Spectra of
Cr 2p3/2 at (a) 30° Angle, (b) 60° Angle

131

expected since a strong oxidizer metal salt was used to form the catalyst precursor (18). $Cr(OH)_x$ species are also observed at increasing pretreatment temperature. The change in Cr^{3+} shoulder shape indicates a reduction in Cr^{3+} since Cr^{3+} species are reducible (19). The increase in the shoulder at Cr^0 species region and shift in the binding energy indicates that other Cr species may be partially reduced to Cr^0 species. After the reaction, more Cr^o species are exhibited in the near-surface region.

5.3.4. Cobalt High Resolution Spectra

XPS high-resolution spectra of Co are shown in Figures 5.17 and 5.18. The primary peaks are assigned to Co^{2+}/Co^{3+} with the shoulder of Co^0 species. Again, Co^{2+}/Co^{3+} species differentiation could not be obtained due to the closeness of their binding energies. The spectra investigation do not agree with Sheffer et al. (10) that satellite peaks of $2p_{3/2}$ are more intensified in the reduced catalyst compared to fresh catalyst, and much more intensified in aged catalyst. Forst et al. (20) stated that the high intensity satellite peaks indicated the presence of Co^{2+} species, and less intense satellite structures of Co^{3+} species. Thus, Co in fresh catalysts was present as Co^{3+}, indicated by a low intensity satellite structure at about 9.4 eV from the $2p_{3/2}$ main peak. Likewise, observation of aged catalysts is in agreement with Calafat et al. (11) that Co was present as Co^{2+} species, mainly proven by the high intensity satellite peak at about 6 eV from the $2p_{3/2}$ peak. After reduction in situ by H_2, no significant changes in satellite peaks were observed which indicated no significant reduction from Co^{3+} to Co^{2+} at the maximum reduction temperature of 275°C. At 400°C, Fornasari et al. (26) observed the reduction

132
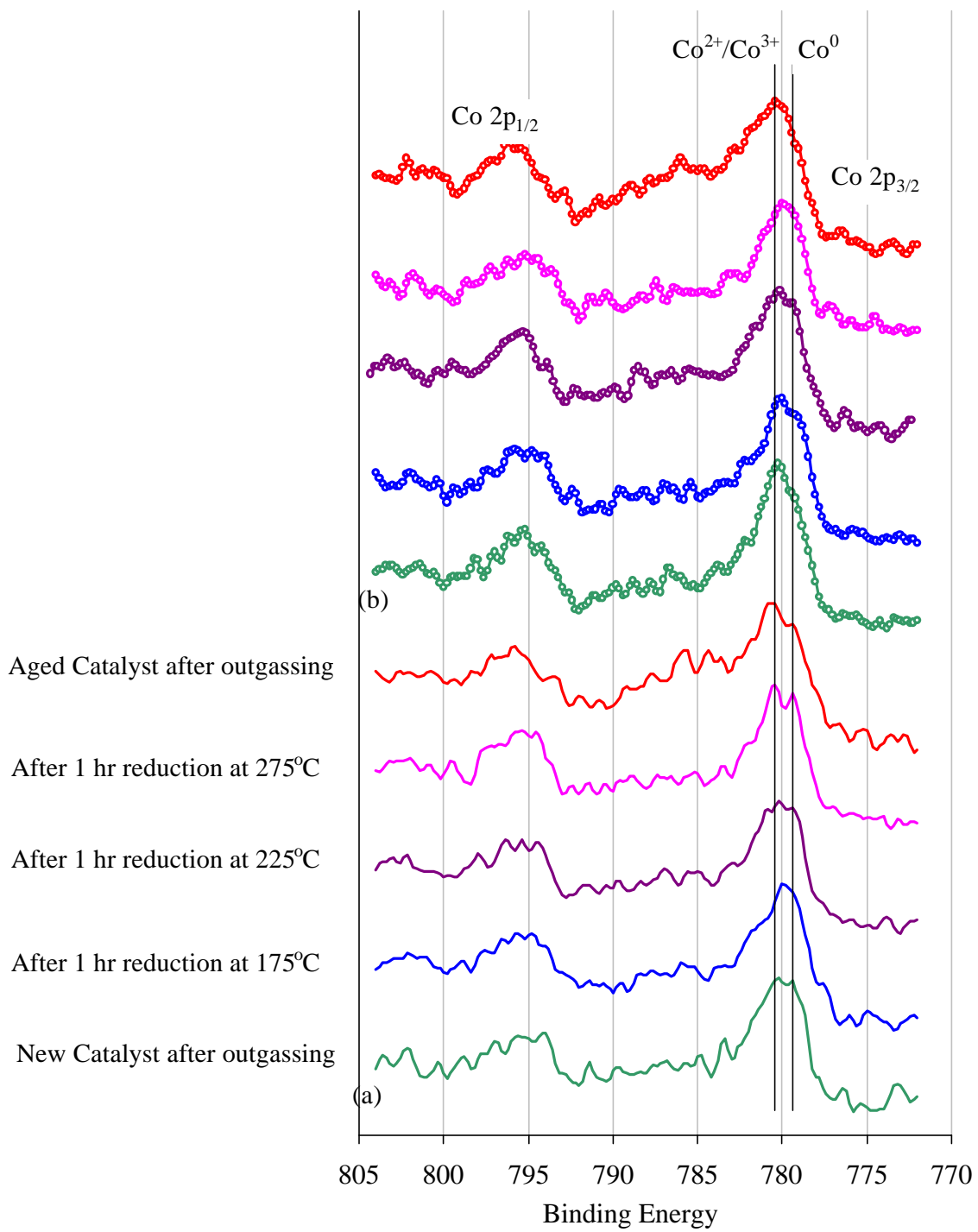
Figure 5.17. Co XPS High-Resolution Spectra of CB1(1) at
(a) 30° Angle, (b) 60° Angle

133

Co 2p$_{1/2}$ Co^{2+}/Co^{3+} Co^0 Co 2p$_{3/2}$

(b)

After 1 hr reduction at 275°C

After 1 hr reduction at 225°C

After 1 hr reduction at 175°C

New Catalyst after outgassing

(a)

805   800   795   790   785   780   775   770

Binding Energy
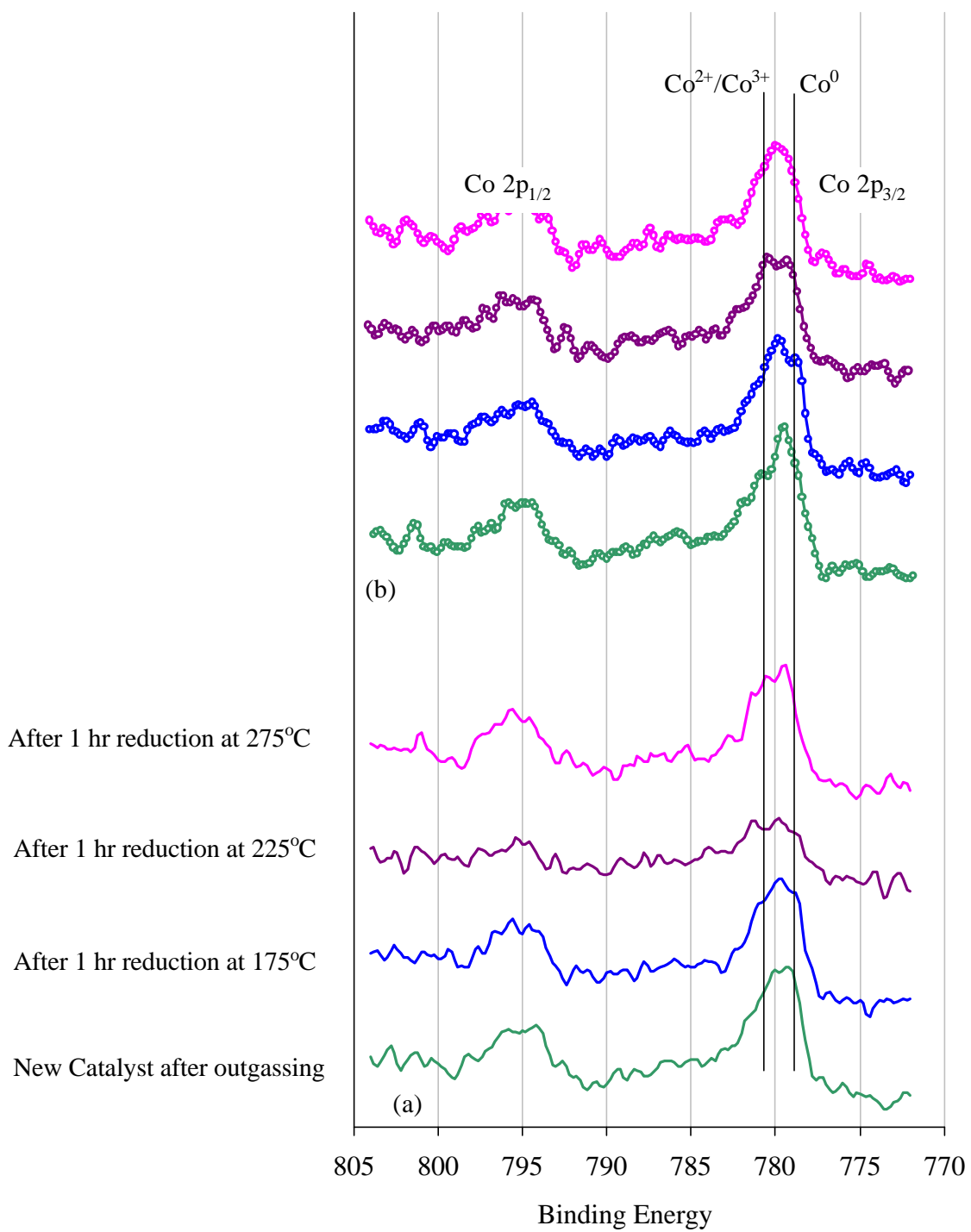
Figure 5.18. Co XPS High-Resolution Spectra of CB1(3) at
(a) 30° Angle, (b) 60° Angle

134

of Co^{3+} to Co^{2+} in Cu-Zn-Cr catalyst, and Sugi et al. (21) also observed that some Co^{2+} species are reduced to metallic state at 300°C in modified cobalt catalysts with the presence of Ru. Based on the observation and overlapping of O auger features/Co $2p_{3/2}$, no conclusive results about Co reduction could be made. In general, Co species on the near-surface region (30°) are less than deeper in the bulk (60°). Castner et al. (22, 23) also emphasized that Co species at near-surface regions can be substantially different from the bulk, and the direct comparison by using fraction of surface Co reduction is not advisable. Otherwise, the Co spectra investigation showed that the surface Co peaks varied significantly in size and shape with the temperature of reduction. Stiles et al. (32) stated that a tolerable quantity of cobalt may produce a catalyst that had the capability of producing ethanol, as well as propanol.

5.3.5. Potassium High Resolution Spectra

XPS high-resolution spectra of K2p are shown in Figures 5.19 and 5.20. However, no significant information concerning its chemical state can be obtained (10, 27). Potassium may exist in the form of K_2CrO_4 or $K_2Cr_2O_7$ (28, 30). The incorporation of potassium into the catalyst is small, and the strength in intensity of the potassium signal indicated that the aged catalyst surface was much more enriched in potassium than fresh or reduced catalyst surface.
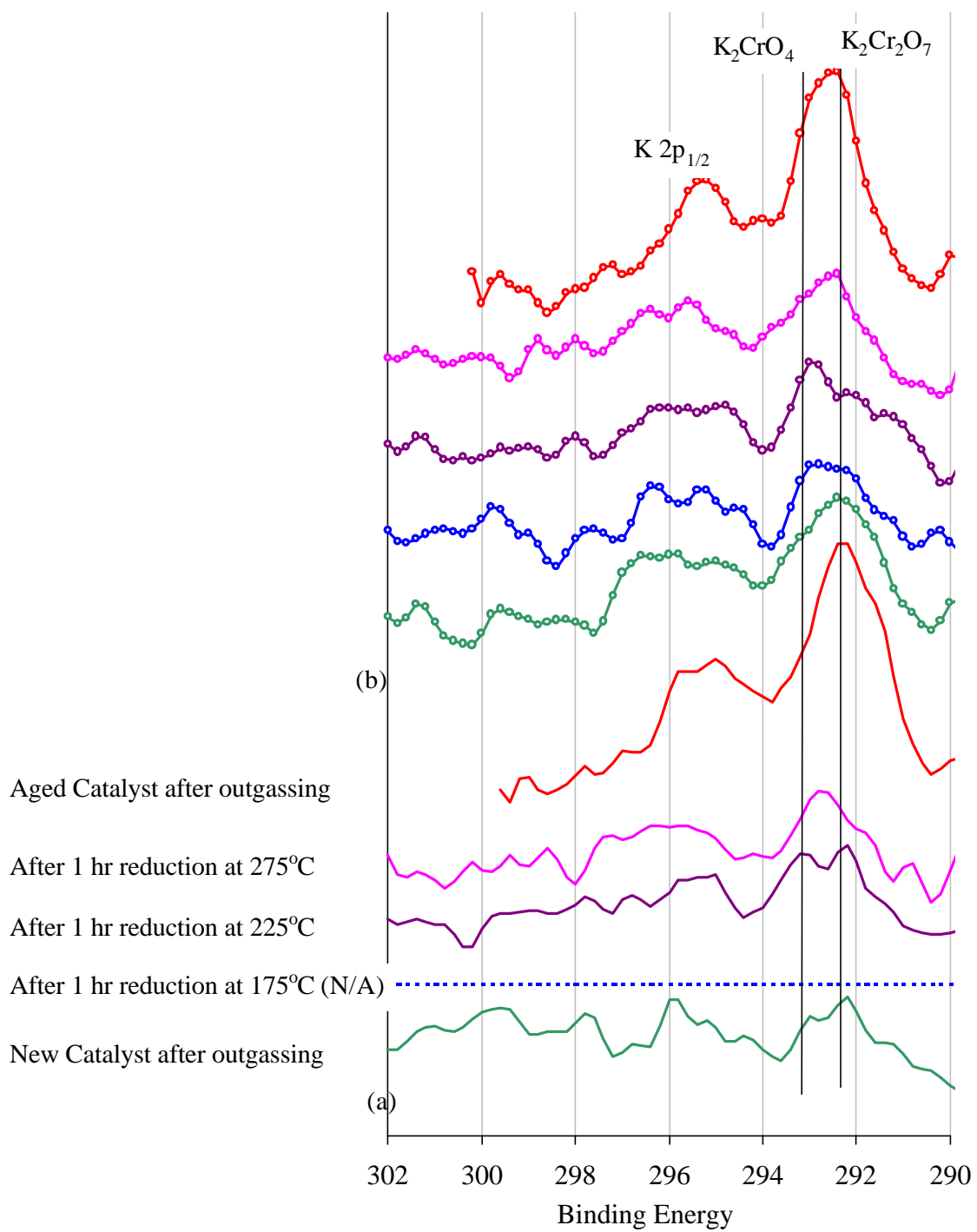
Figure 5.19. K XPS High-Resolution Spectra of CB1(1) at
(a) 30° Angle, (b) 60° Angle

136
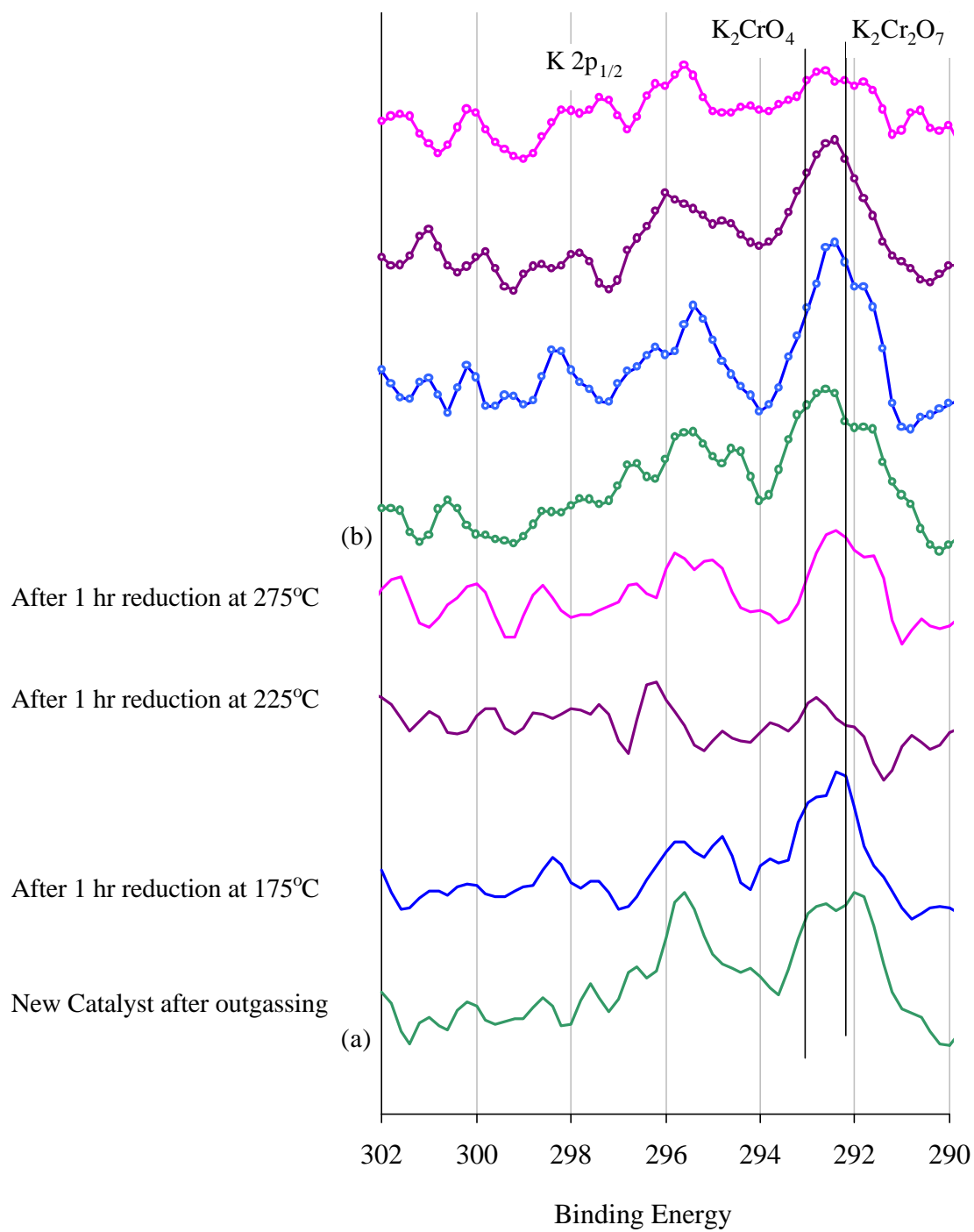
Figure 5.20. K XPS High-Resolution Spectra of CB1(3) at
(a) 30° Angle, (b) 60° Angle

137

5.3.6. Oxygen High Resolution Spectra

The high-resolution XPS O1s spectra taken from the catalysts and their peak deconvolutions are shown in Figures 5.21 through 5.24, respectively. A mixture of chemical states is observed due to the broad peak width. The primary peak at approximately 529.3 is assigned as O in metal oxide species. Most of the oxygen in the near surface region of the catalyst pellets is bound as metal oxide. Metal oxide concentration on the surface is equivalent to that in the bulk. A shoulder at 530.8 is due to the presence of O species in hydroxide groups. A shoulder at the binding energy of 532.0 may be due to the presence of adsorbed water (28). Metal oxide reduction increases in the order from fresh, pretreated, and after reaction catalyst, while the hydroxide concentration remains approximately the same, and water concentrations are greatly diminished. It is believed that more catalytic sites are exposed under hydroxide and water removal (28). The water concentration in CB1(3) is much lower than in CB1(1) catalyst. The abnormal observation of excess water presented in CB1(3) at 225°C may be due to exposure by air because of a power failure during the analysis, which is also proved by the excessively high concentration of adventitious carbon.
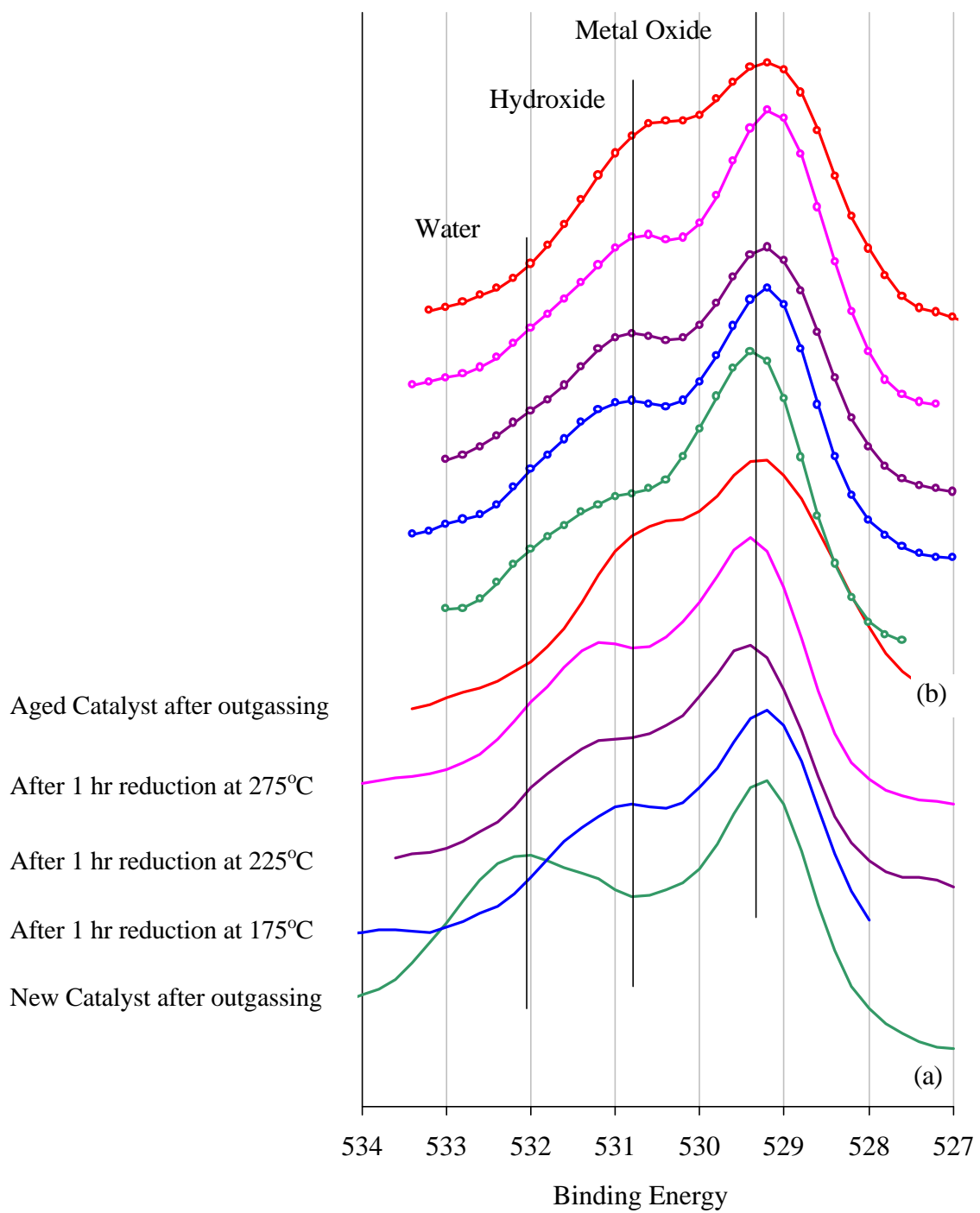
Figure 5.21. O1s XPS High-Resolution Spectra of CB1(1) at
(a) 30° Angle, (b) 60° Angle

Figure 5.22. O1s XPS High-Resolution Spectra of CB1(3) at (a) 30° Angle, (b) 60° Angle

140

Aged Catalyst after outgassing

After 1 hr reduction at 275$^{\mathrm{o}}$C

After 1 hr reduction at 225$^{\mathrm{o}}$C

After 1 hr reduction at 175$^{\mathrm{o}}$C

New Catalyst after outgassing

(a)

(b)
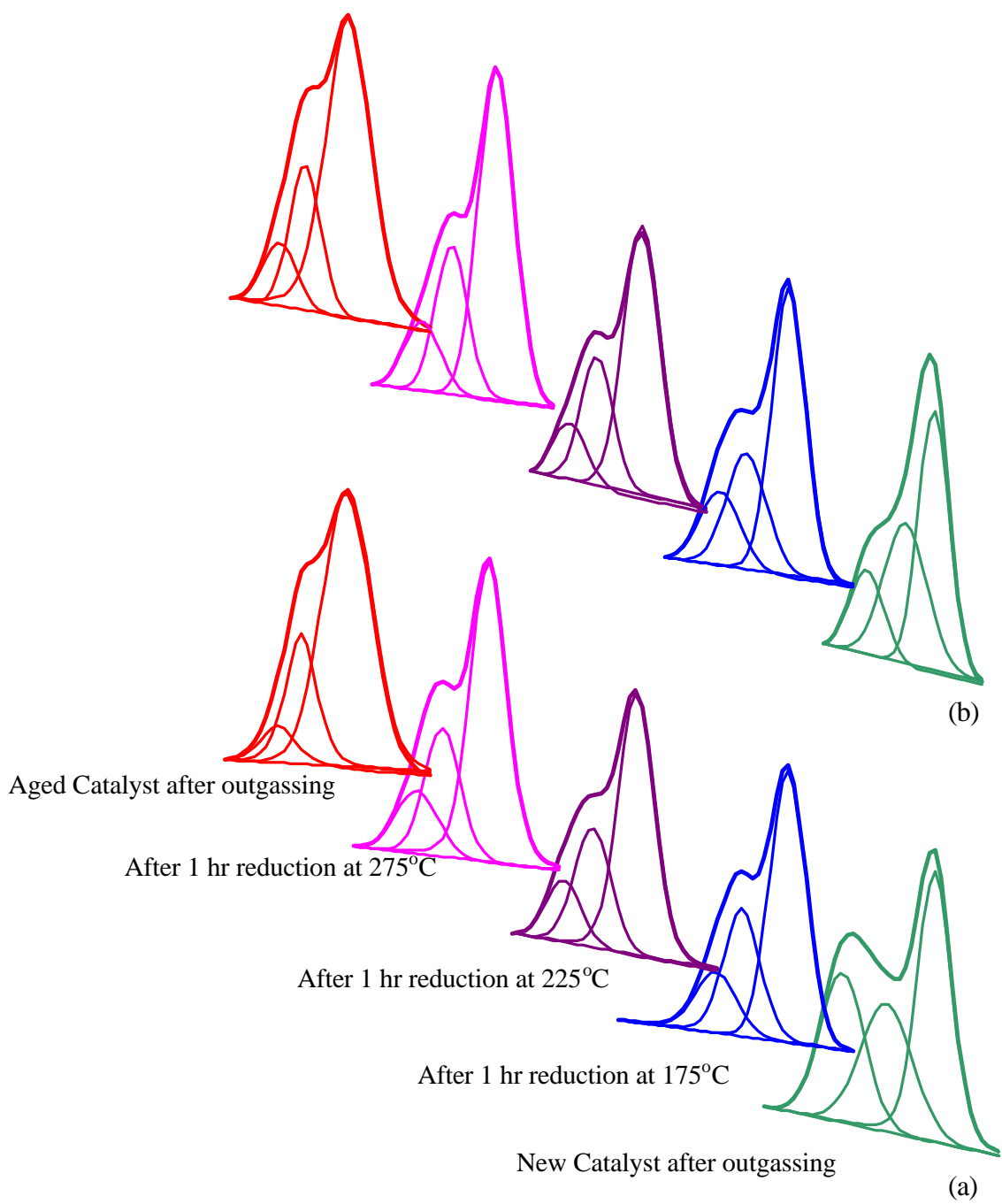
Figure 5.23. O1s Peak Deconvolutions of XPS High-Resolution
Spectra of CB1(1) at (a) 30$^{\mathrm{o}}$ Angle, (b) 60$^{\mathrm{o}}$ Angle

141

After 1 hr reduction at 275℃

After 1 hr reduction at 225℃

After 1 hr reduction at 175℃

New Catalyst after outgassing

(b)

(a)

Figure 5.24. O1s Peak Deconvolutions of XPS High-Resolution
Spectra of CB1(3) at (a) 30° Angle, (b) 60° Angle

142

<u>5.3.7. Carbon High Resolution Spectra</u>

The XPS C1s spectra obtained from both catalysts are shown in Figures 5.25 and 5.26. The peak at 284.8 is the C1s reference peak resulting from adventitious carbon (24, 29). The peaks or shoulders at 282.1, 286.1, 288.8 have been assigned to carbon in carbide, C with N, and carbonate structure, respectively. The surface C1s peak CB1(1) catalyst is greatly reduced in size after one-hour reduction at 175°C, but only small changes are observed with an increase in temperature. CB1(1) surface is more enriched in carbon than CB1(3). Increasing the pretreatment temperature of CB1(3) catalyst does not have significant effect on C1s peaks. Both catalysts show that before reduction, C1s concentration is much higher at the surface than in the bulk. The increase in temperature removed carbon from the surface but not in the bulk. The carbide peak is presented after pretreatment, but disappeared after the reaction. C with N shoulder increased with increasing temperature, and again disappeared after the reaction. Likewise, the carbonate peak is intensified with increasing temperature and more intensified after the reaction.
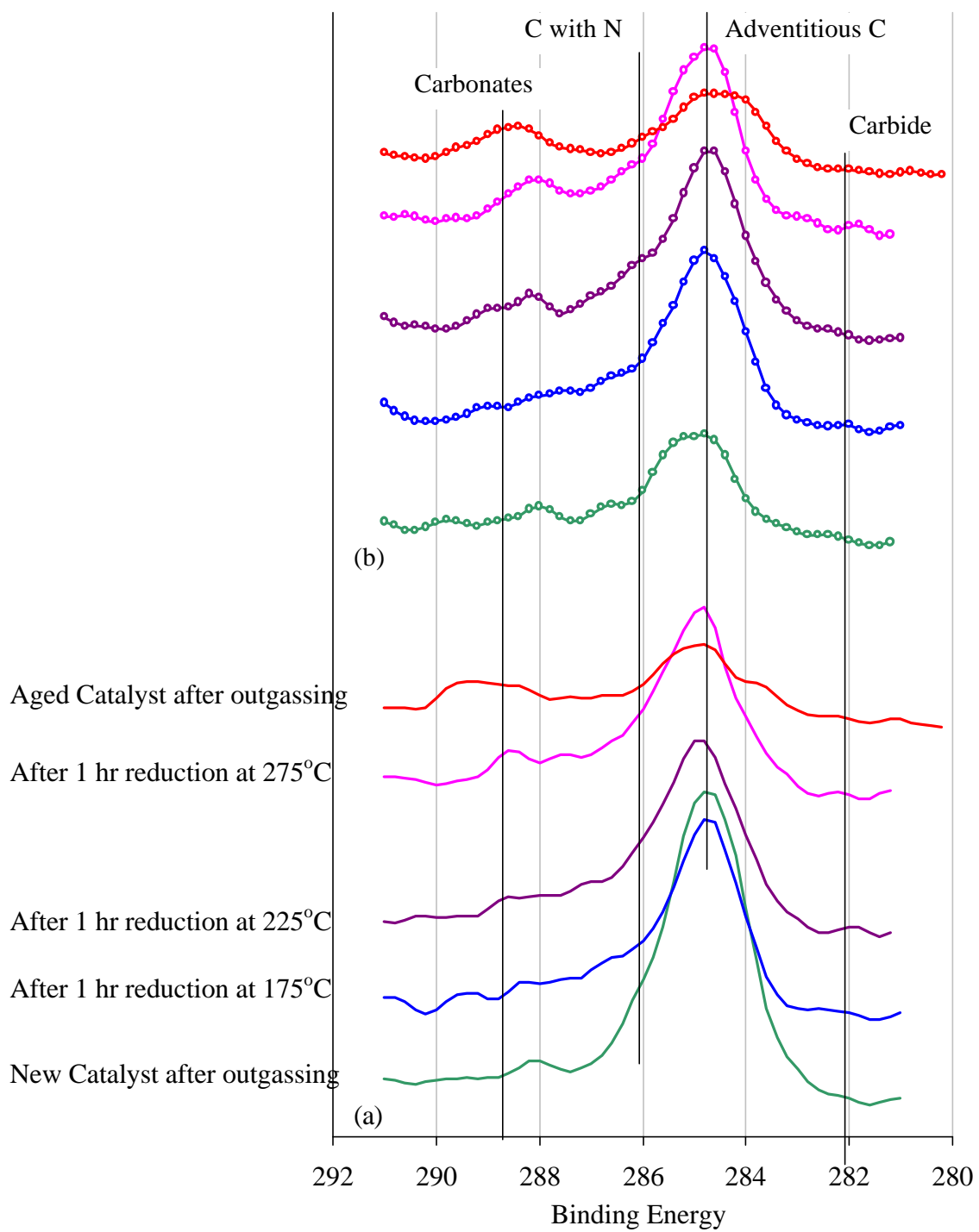
Figure 5.25. C1s XPS High-Resolution Spectra of CB1(1) at
(a) 30° Angle, (b) 60° Angle

144
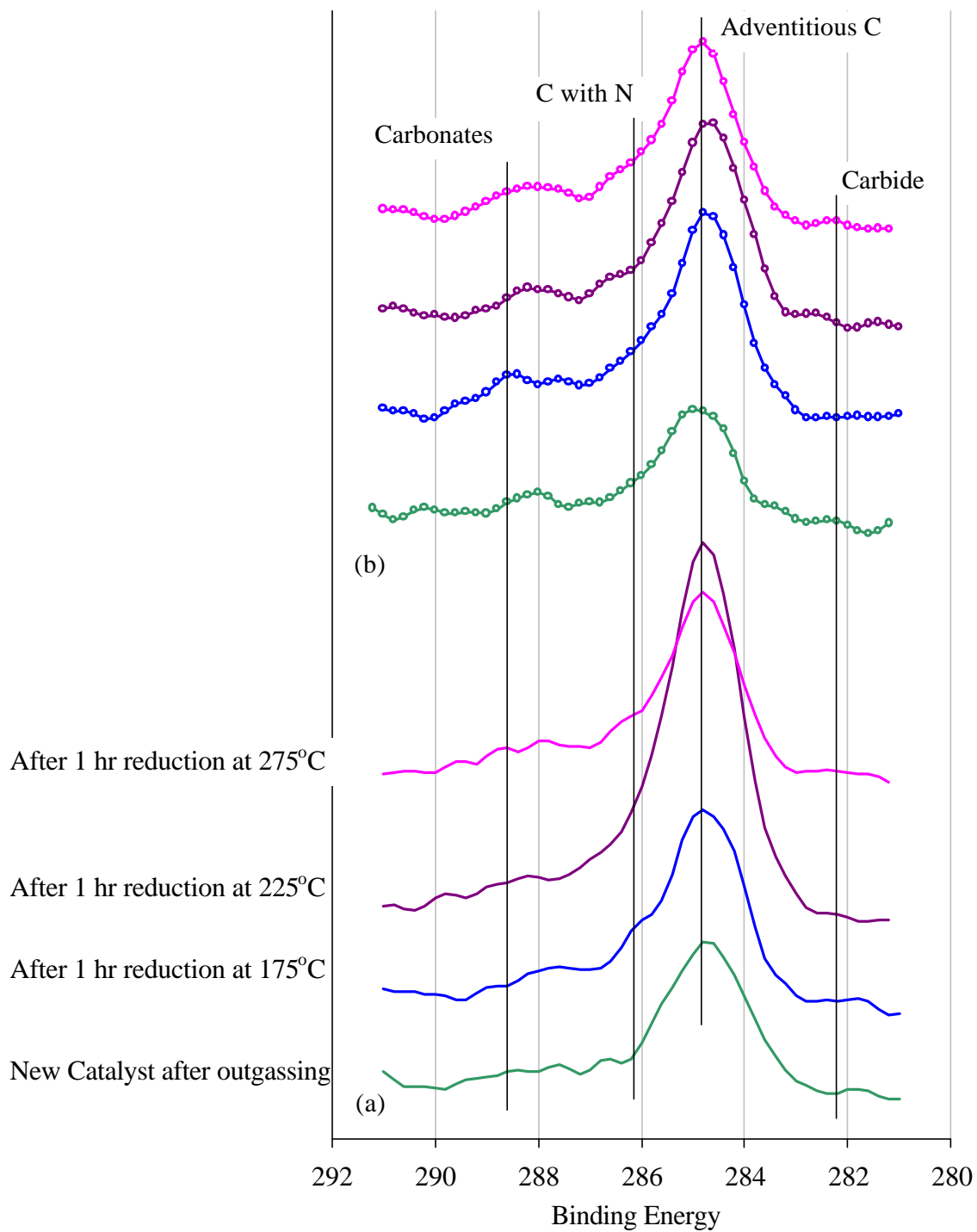
Figure 5.26. C1s XPS High-Resolution Spectra of CB1(3) at
(a) 30° Angle, (b) 60° Angle

145

5.4. References

1. Skoog, D., A., Holler, F. J., Nieman, T. A., Principles of Instrumental Analysis, (5th edition, Harcourt Brace College Publishers, Florida: 1998).

2. Atkins, P. W., Physical Chemistry, (5th edition, W. H. Freeman and Company, New York: 1994).

3. Moulder, J. F., Stickle, W. F., Sobol, P. E., Bomben, K. D., Handbook of X-ray Photoelectron Spectroscopy, Chastain, J., ed., (Perkin-Elmer Corporation, Minnesota: 1992).

4. Carlson, T. A., Photoelectron and Auger Spectroscopy, (Plenum Press, New York: 1978).

5. Tompkins, F. C., Chemisorption of Gases on Metals, (Academic Press, New York: 1978).

6. Singamsetty, C. S. K., XPS/ISS Characterization of Carbon Fibers for the Synthesis of Carbon Fiber/Epoxy Composites Containing an Elastometric Interphase, M. S. Thesis, Mississippi State University, (1995).

7. O'Hanlon, J. F., A User's Guide to Vacuum Technology, (John Wiley & Sons, New York: 1980).

8. "Surface Analysis Components Catalog", Physical Electrons, Eden Praire, MN.

9. Frost, D. C., Ishitani, A., McDowell, C. A., *Molecular Physics*, 24, 861, (1972).

10. Sheffer, G. R., King, T. S., *Journal of Catalysis*, 115, 376, (1989).

11. Calafat, A., Laine, J., *Journal of Catalysis*, 147, 88, (1994).

12. Monnier, J. R., Hanrahan, M. J., Apai, G., *Journal of Catalysis*, 92, 119, (1985).

13. Apai, G., Monnier, J.R., Hanrahan, M. J., *Journal of Chemical Society, Chemical Communications*, 212, (1984).

14. Capece, F. M., Di Castro, V., Furlani, C., Mattogno, C., Fragale, C., Gargano, M., Rossi, J., *Journal of Electron Spectroscopy Related Phenomenon*, 27, 119, (1982).

15. Klier, K., Chatikavanij, R. G., Herman, R. G., Simmons, G. W., *Journal of Catalysis*, 74, 343, (1982).

16.   Monnier, J. R., Hanrahan, M. J., Apai, G., *Journal of Catalysis*, 88, 523, (1984).

17.   Chu, P. - J., Gerstein, B. C., Sheffer, G. R., King, T. S., *Journal of Catalysis*, 115, 194, (1989).

18.   Courty, P., Durnad, D., Freund, E., Sugier, A., *Journal of Molecular Catalysis*, 17, 241, (1982).

19.   Tauster, S. J., Fung, S. C., Baker, R. T. K., Horsley, J. A., *Science*, 221, 1121, (1981).

20.   Frost, D. C., McDowell, C. A., Woolsey, I. S., *Molecular Physics*, 27, 1473, (1974).

21.   Sugi, Y., Takeuchi, K., Matsuzaki, T., Arakawa, H., *Chemistry Letters*, 1315, (1985).

22.   Castner, D. G., Santilli, D. S., "Catalytic Materials", Whyte, T., Dalla Betta, R., Derovane, E., Baker, R., Eds., Acs Symposium Series 248, American Chemical Society, Washington, D.C., 42, (1984).

23.   Castner, D. G., Watson, P. R., Chan, I., Y., *Journal of Physical Chemistry*, 93, 3188, (1989).

24.   Sheffer, G. R., Jacobson, R. A., King, T. S., *Journal of Catalysis*, 116, 95, (1989).

25.   Sheffer, G. R., King, T. S., *Journal of Catalysis*, 116, 448, (1989).

26.   Fornasari, G., Huysser, A. D., Mintchev, L, Trifiro, F., Vaccari, A., *Journal of Catalysis*, 135, 386, (1992).

27.   Sheffer, G., Investigation of the Catalytic Behavior and Chemical Nature of Alkali Promoted Copper and Copper-Cobalt-Chromium Oxide Catalysts for the Conversion of Synthesis Gas to Methanol and Higher Alcohols, Doctor of Philosophy Dissertation, Iowa State University, (1987).

28.   Epling, W. S., Reaction and Surface Characterization Studies of K and Cs Promoted, Zn/Cr Spinel, Higher Alcohol Synthesis Catalysts, Doctor of Philosophy Dissertation, University of Florida, (1997).

29.   Iranmahboob, J., Formation of Ethanol and Higher Alcohols from Syngas, A Doctor of Philosophy Dissertation, Mississippi State University, (1999).

30.   Minahan, D., Epling, W., Hoflund, G. B., *Journal of Catalysis*, 179, 241, (1998).

31.   Chinchen, G. C., Mansfield, K., Spencer, M. S., *Chemtech*, 692, (1990).

32.   Stiles, A. B., Chen, F., Harrison, J. B., Hu, X., Storm, D., Yang, H. X., *Ind. Eng. Chem. Res*., <u>30</u>, 811, (1991).

33.   Srinivasan, B., <u>An Investigation of the Gas Sensing Properties of Au/MnOx: Response to CO Exposure and Comparison to Pt/SnO$_2$</u>, M. S. Thesis, Mississippi State University, (1998).

CHAPTER VI

CONCLUSIONS AND RECOMMENDATIONS

6.1.   Conclusions

The results obtained from this study allow the following conclusions:

6.1.1.   Higher Alcohol Synthesis

Synthesis gas conversion studies over Cu-Co-Cr-K catalyst result in a yield in the range of 7 to 270 g kg-cat^{-1} hr^{-1}. Alcohol yield is in the range of 22 to 76 wt% for CB1(3) catalyst, and 10 wt % to 46 wt % for CB1(1) catalyst. Therefore, the catalysts are active for higher alcohol synthesis, and excessive exothermic heat is observed. Moreover,

- High temperature is more favorable for the production rate.

- Increasing pressure also has a significant effect on alcohol yields.

- Alcohol productivity is also benefited by increased space velocity

- Both methanol and higher alcohol productivity are higher in CO_2 free syngas, while water productivity is higher in CO_2 syngas.

- In general, CB1(1) is the preferred catalyst for high alcohol production compared to CB1(3).

149

- The temperature programmed reduction profiles do not show the individual reduction of surface metals. Also, depending on the temperature ramping rate, the catalyst reduction temperature ranged is from 170 to 190°C.

- Sintering of aged CB1(1) is observed by SEM with bigger agglomeration of cobalt oxide crystallites.

- In conclusion, CB1(1) catalyst was found to be a viable catalyst for the conversion of synthesis gas to higher alcohols.

6.1.2. Physisorption

According to the Langmuir, the BET, the de Boer t method, and the Halsey t method, the surface area of CB1(1), CB1(3), and CB1(1) after reaction are $39.9 \pm .9$ m^2/g, 28.9 ± 1.7 m^2/g, and 26.5 ± 0.3 m^2/g, respectively. Deactivation resulted from loss of active surface area at high temperature. Closing of pores can also influence the activation energy and poisoning characteristics of the surface. Furthermore,

- The strongest adsorbate-adsorbent interactions are observed with CB1(3) catalyst while aged CB1(1) exhibits the weakest interactions. Therefore, CB1(3) catalyst has the lowest surface uncovered fraction.

- According to the BJH model, the pore area maximum is obtained at 123 Å for CB1(1) and CB1(3), 174 Å for aged CB1(1). The pore volume maximum is achieved at 123 Å for CB1(1), 174 Å for both CB1(3) and aged CB1(1).

- The pore size distribution of the t method exhibits the presence of a set of pores of less than 2.5 Å, thereby, the pores may be the aggregates of slit-

150

shaped pores, open on all sides, giving no capillary condensation until high relative pressure. Also, no evidence of micropores has been observed except CB1(3) catalyst.

6.1.3. Surface Characterization

The predominate species on the catalyst surface are oxygen, carbon, and copper. Oxygen at near surface region is reduced during the pretreatment. Likewise, surface carbon species decreased after reduction. The near surface region of reduced catalyst is enriched with copper while chromium and cobalt features are almost unchanged. Also, more oxygen accumulation is noticed, and higher intensity features are observed in the copper peak in the aged catalyst. In addition,

- Other forms of copper species are present in fresh catalyst in addition to Cu^0, Cu^+, and Cu^{2+} features. When exposed to H_2, Cu^0 species in the near surface region increased while the Cu^{+2} shoulder was reduced. Likewise, higher near surface Cu^0 peaks are noticed while Cu^{+2} peaks totally disappeared in the catalyst after reaction. Cu^0 features are also more intensified in CB1(3) compared to CB1(1) catalyst. Besides, more Cu^0 species are on the surface compared to in the bulk.

- Chromium features in the near surface region appeared to be Cr^0, Cr^{1+}/Cr^{3+}, $Cr(OH)_x$, and Cr^{6+}. Two species of Cr^{1+} and Cr^{3+} could not be differentiated. Nevertheless, the presence of Cr^{3+} species has been proving by others, and reduction in Cr^{3+} species is observed. Increasing treatment temperature results in Cr^{6+} to Cr^{3+} reduction. Other Cr species are also partially reduced to

Cr^0 species. At last, more Cr^0 species in aged catalyst existed in the near surface region.

- The primary peaks of cobalt are assigned to Co^{2+}/Co^{3+}. The cobalt species in fresh catalyst is Co^{3+}, and in aged catalyst is Co^{2+}. Moreover, no significant reduction from Co^{3+} to Co^{2+} is observed during the reduction procedure. In general, less cobalt species are on the surface compared to in the bulk.

- Although, no significant information concerning the potassium chemical state can be obtained, potassium may exist in the form of K_2CrO_4 or $K_2Cr_2O_7$. The surface potassium is more enriched in aged catalyst comparing to fresh and reduced catalyst.

- The primary peak of O 1s is assigned to metal oxide species, which are greater in catalyst CB1(3) comparing to CB1(1). The surface metal oxide feature is equivalent to that in the bulk, and increased in the order from fresh, reduced, and after reaction catalyst. Hydroxide and water features are also presented in which both are greatly diminished under reduction. Also, water features are less in CB1(3) comparing to CB1(1) catalyst.

- The primary peaks of carbon are assigned to carbon in carbide, C with N, and carbon structure. The carbon features are greatly reduced after reduction, and an increase in temperature removed carbon from the surface but not in the bulk. Carbon species are also higher at the surface compared to in the bulk. Generally, CB1(1) surface is more enriched in carbon compared to CB1(3) catalyst surface. The carbide peak remained after reduction, but disappeared

after the reaction. C with N shoulder is higher with reduction temperature, and again disappeared after reaction. Similarly, the carbonate peak is intensified with increasing reduction temperature, and more intense after reaction.

6.2.   Recommendations

The previous conclusions indicate that the catalysts are active for higher alcohol synthesis. The following suggestions are recommended for future research:

- To further investigate the effect of metal content and metal distribution on catalyst activity and selectivity for higher alcohol synthesis, and also in order to achieve good metal stability.

- To study different ways to incorporate the various promoters and different active metals as well as their contribution to the catalytic reaction.

- To understand the chemical nature of the catalyst in order to optimize preparation procedures.

- To study supported catalyst as opposed to unsupported.

- To better understand the effect of reduction temperature and the reducibility of catalyst on catalyst life-time and sintering.

- To evaluate the deactivation of catalysts and to compare this deactivation with IFP catalysts.

- To study the effect of transport limitations and thermodynamic constraints.

- To study the carbon monoxide uptake, and to investigate the active metal surface of single metal catalyst.

APPENDIX A

LIQUID PRODUCT ANALYSIS

A.1.   Gas Chromatography

Gas chromatography is a powerful method for direct separation and analysis of gaseous samples and liquid solutions where the components are qualitatively and quantitatively determined. It can be categorized based upon the physical characterization where the stationary and mobile phases are in contact. The gas chromatography column employed is one in which the stationary phase is fixed in a narrow tube while the mobile phase is forced through under pressure (1). The solutes or analytes are separated from one another based on their relative vapor pressures and affinities for the stationary phase. This chromatographic process is called elution (4). Chromatographic theory is based on the assumptions of instantaneous equilibrium between the solute concentrations in each phase, minimal diffusion of solute in the mobile phase along the column axis, and uniformly wall-coated column (6).

The GC chromatogram is the detector response versus retention time and contains peaks corresponding to solute elution through the column. Retention time is the time it takes after sample injection for a peak to reach the detector. It is also noted that temperature plays an important role in GC retention. The more volatile components may be well resolved, but the less volatile materials will elute with longer retention time and have very broad peaks (3).

A.2.   Instrumentation

In gas chromatography, mixtures are separated into their components based on retention of the analyte between two phases. First, the sample is vaporized and injected

onto the head of the chromatographic column. The sample is then transported by an inert gaseous mobile phase through a fixed immiscible stationary liquid phase. The components distribute themselves at different degrees between the mobile and stationary phase. Components that are weakly held by the stationary phase move rapidly, and those are strongly held move slowly with mobile phase. The differences in mobility consequently separates components into bands that can be analyzed for quantitative and qualitative purposes (1).

The liquid analytes are automatically injected into the GC injection port by an autosampler HP Model 5973 based upon the set-up sequences. An HP 5890 GC with Poraplot Q column of 25 m in length and 0.25 mm diameter is employed for the separation according to the retention of analyte between mobile and stationary phase. The analyte travels through a capillary interface toward the HP 5971 Model mass spectrometer (2). The mass spectrometer consists of three components. The ion source produces ions by bombarding the sample with electrons. Ions are then sorted according to their mass to charge ratio by a quadrupole mass filter. These ions continue their journey by striking the detector or electron multiplier, which then produces a signal proportional to the number of ions striking. Finally, a chromatogram is acquired from the data acquisition software according to the ion abundance and retention time.

In the mass spectrometer, the ion source is heated under low vacuum. Electrons are produced from a tungsten filament by a collector voltage of 70 eV. This voltage is applied to the filament and defines the energy of electrons (4). When the electron strikes the neutral surface of the molecules, ions are produced due to electron interactions in

which molecules lose both incoming and bound electrons. Consequently, the molecule becomes an ion with a charge. Due to their reactive and high-energy possessive nature, the molecular ions fragment into neutral radical ions (2).

After ionization, the ions are separated by their mass to charge ratio by an electrical field. The mass analyzer of the MS is the quadrupole mass filter, which consists of four metallic strips (2 sets). One set is applied with positive DC voltage and the other with negative DC voltage of the same value. An oscillating voltage at 1 MHz is applied to all four strips. Due to the electric field of oscillation and DC voltage, the entering ion undergoes complex motions. The low-mass ion is pulled off toward the negative strips and never comes out of the mass filter. In contrast, the high-mass ion is oscillated toward the positive strips and is ejected from the side of the mass filter. Thus, only ions at a certain mass which have a stable oscillation will exit the quadrupole mass filter and travel toward the detector (2).

After the separation, the exiting ions from the mass filter hit the interior semi-conductive surface of the electron multiplier and electrons are ejected from the surface. Depending on the multiplier voltage, more or fewer electrons will be ejected. These electrons cascade down the horn and are accelerated by a potential difference to another portion of the semi-conductive surface where a larger cascade of electron results. This process is repeated several times until the weak electron inputs are magnified. Thus, the function of the electron multiplier detector is to convert the ion into electron currents at a higher order of magnitude. In order for the ions to travel from the ion source to the detector without colliding with other molecules or surfaces, a vacuum system consisting

of a high vacuum oil diffusion pump and a mechanical rough pump and is applied to provide an adequate mean free path. Information about the pumping system can be found elsewhere (5).

Before the mass spectrometer can be used to measure the masses of fragmentation ions, it must be tuned and calibrated. Tuning is done by adjusting the lens to ensure that the adjacent peaks overlap as little as possible and the relative peak height has the expected ratio on the mass axis. Calibration adjusts the signal frequency so that the mass axis corresponds to the expected mass fragment of the calibration compound. Calibration is done with a volatile liquid, perfluoro-t-butylamine (PFTBA), to ensure that the same compound under the same operating conditions on different machines will exhibit the same fragment of masses in the same relative amounts (7).

A.3. Operating Condition

$1\mu L$ of liquid sample was automatically injected into the GC Poraplot Q column of 25 m in length and 0.25 mm diameter. Prior to the analysis, the method for higher alcohol analysis had been created and is reproduced in Table A.1.

Table A.1. GC/MS Method of Higher Alcohol Analysis

Inlet B Flow Settings:	
Column Length:	25 m
Column Diameter:	0.25 mm
Gas:	He
Vacuum Compensation:	On
Pressure:	9.4 psi
Flow:	0.798 ml/min
Linear Velocity:	37.2 cm/sec
Split Flow:	0
GC Temperature Information:	
Injection B Temperature:	280°C
Detector B Temperature:	300°C
Auxiliary Temperature:	125°C
Oven Temperature:	175°C
Injector Information:	
Injection Source:	Auto
Injection Location:	Rear
Sample Washes:	2
Sample Pumps:	4
Sample Volume:	1 stop
Viscosity Delay:	0
Solvent A Washes:	2
Solvent B Washes:	2
On Column:	No
Purge A/B:	
Initial Value:	OFF
On Time:	0.00
Off Time	1.00

A.4.   Analysis Calibration

The calibration was performed using the mixtures of alcohols and acetonitrile as internal standard on a mass basis. The calibration standard was prepared as follows: Cap and record the tare weight of a 50 ml bottle. Each component was carefully injected by volume via syringe-tip burettes starting with methanol, ethanol, isopropanol, propanol,

159

butanol, and water. In Table A.2, approximate values for the required volume of each

component are recorded. These were used as a guide during the preparation of

gravimetric standard. The actual net mass of each component (Wi) was then recorded.

The acetonitrile, as internal standard, was simply added to each mixture, and its net mass

(Ws) was recorded. The calibration standards were stored in a refrigerator at 0 to 5°C

when not in use.

Table A.2. Estimated Volumes Required for Calibration Standards

		Water	Methanol	Ethanol	Acetonitrile	isoPropanol	Propanol	Butanol
	Density (g/ml)	1.0000	0.7910	0.7939	0.7860	0.7850	0.8040	0.8100
Mix #1	V(ml)	0.5000	35.0000	2.0000	5.0000	1.3000	3.0000	1.0000
	$W_{calculated}$ (g)	0.5000	27.6850	1.5878	3.9300	1.0205	2.4120	0.8100
	W_{actual} (g)	0.4398	27.6504	1.6010	3.9119	1.1021	2.4432	0.8083
Mix #2	Volume (ml)	1.0000	25.0000	5.0000	5.0000	0.5000	9.5000	1.5000
	$W_{calculated}$ (g)	1.0000	19.7750	3.9695	3.9300	0.3925	7.6380	1.2150
	W_{actual} (g)	0.9859	19.7058	3.9125	3.9228	0.3952	7.6774	1.1928
Mix #3	Volume (ml)	2.0000	20.0000	10.0000	5.0000	1.8000	8.0000	0.5000
	$W_{calculated}$ (g)	2.0000	15.8200	7.9390	3.9300	1.4130	6.4320	0.4050
	W_{actual} (g)	1.9903	15.8016	7.8584	3.9173	1.4018	6.4681	0.3958
Mix #4	Volume (ml)	2.5000	13.0000	15.0000	5.0000	4.7000	5.0000	2.0000
	$W_{calculated}$ (g)	2.5000	10.2830	11.9085	3.9300	3.6895	4.0200	1.6200
	W_{actual} (g)	2.4978	10.2911	11.8641	3.9230	3.6673	4.0504	1.6171
Mix #5	Volume (ml)	4.0000	6.0000	20.0000	5.0000	1.0000	6.0000	4.7000
	$W_{calculated}$ (g)	4.0000	4.7460	15.8780	3.9300	0.7850	4.8240	3.8070
	W_{actual} (g)	3.9812	4.7392	15.7317	3.8949	0.7923	4.8563	3.9156
Mix #6	Volume (ml)	7.0000	2.0000	25.0000	5.0000	3.0000	1.0000	3.0000
	$W_{calculated}$ (g)	7.0000	1.5820	19.8475	3.9300	2.3550	0.8040	2.4300
	W_{actual} (g)	6.9887	1.5590	19.8059	3.9054	2.3434	0.7761	2.4131
Mix #7	Volume (ml)	12.9000	3.5000	3.0000	5.0000	6.0000	7.0000	7.0000
	$W_{calculated}$ (g)	12.9000	2.7685	2.3817	3.9300	4.7100	5.6280	5.6700
	W_{actual} (g)	12.8373	2.7992	2.3689	3.8953	4.6713	5.6560	5.6621
Mix #8	Volume (ml)	9.0000	4.0000	7.0000	5.0000	7.4000	4.0000	9.0000
	$W_{calculated}$ (g)	9.0000	3.1640	5.5573	3.9300	5.8090	3.2160	7.2900
	W_{actual} (g)	8.9937	3.1578	5.5612	3.9390	5.7835	3.2636	7.2639

For each of the eight standards prepared, the measured weight of each component in each standard are recorded in table A.3. Also in Table A.3 are compiled the measured area and the computed area ratio (Ai / As) obtained from the chromatogram of each calibration standard. A calibration was generated for each analyte. The Calibration curves are presented in Figures A.1 to A.6. Linear Regression of the data on each curve was performed and the obtained slope and intercept are given on each figure.

A certified calibration standard was purchased from PolyScience. A sample was analyzed with the GC/MS and weight percentage of each component was determined using the calibration curves in Figures A.1 to A.6. The comparison of the calculated weight percentage with that supplied by the manufacturer is given in Table A.4. The mass of each oxygenate (Wi) in an analyzed sample was calculated using the ratio of area of oxygenate to that of the internal standard:

Wi = Ws [(Ai / As) – bi] / mi

where bi and mi are the intercept and slope of each oxygenate calibration curve, respectively.

The mass percentage of each oxygenate is obtained by:

wt % = (Wi / Wg)(100 %)

where Wg is the mass of sample.

Table A.3. GC/MS Higher Alcohol Analysis Calibration Standards

		Mix #1	Mix #2	Mix #3	Mix #4	Mix #5	Mix #6	Mix #7	Mix #8
Water	Wi(g)	0.4398	0.9859	1.9903	2.4978	3.9812	6.9887	12.8373	8.9937
H_2O	g / g IS	0.1124	0.2513	0.5081	0.6367	1.0222	1.7895	3.2956	2.2832
7732-18-5	Wt. %	1.29	2.91	5.87	7.35	11.70	20.62	37.76	26.43
	Ai		97,910	146,545	139,892	372,914	327,890	421,133	280,764
	Ai/As		0.0717	0.1063	0.1225	0.2465	0.3381	0.8224	0.5274
Methanol	Wi(g)	27.6504	19.7058	15.8016	10.2911	4.7392	1.559	2.7992	3.1578
CH_3OH	g / g IS	7.0683	5.0234	4.0338	2.6233	1.2168	0.3992	0.7186	0.8017
67-56-1	Wt. %	81.22	58.18	46.59	30.28	13.93	4.60	8.23	9.28
99.9%	Ai	6,688,660	4,442,807	3,207,740	1,794,967	1,176,104	214,665	230,947	260,594
	Ai/As	4.5222	3.2550	2.3275	1.5720	0.7773	0.2213	0.4510	0.4895
Ethanol	Wi(g)	1.6010	3.9125	7.8584	11.8641	15.7317	19.8059	2.3689	5.5612
CH_3CH_2OH	g / g IS	0.4093	0.9974	2.0061	3.0242	4.0391	5.0714	0.6081	1.4118
64-17-5	Wt. %	4.70	11.55	23.17	34.91	46.25	58.45	6.97	16.35
200 Proof	Ai	441,743	1,081,994	2,057,311	2,630,667	4,911,366	3,663,803	219,521	557,679
	Ai/As	0.2987	0.7927	1.4927	2.3039	3.2458	3.7775	0.4287	1.0475
Acetonitrile (IS)	Ws(g IS)	3.9119	3.9228	3.9173	3.923	3.8949	3.9054	3.8953	3.939
CH_3CN 99.9%	As	1,479,079	1,364,929	1,378,212	1,141,836	1,513,128	969,910	512,071	532,400
75-05-8									
Isopropanol	Wi(g)	1.1021	0.3952	1.4018	3.6673	0.7923	2.3434	4.6713	5.7835
$(CH_3)_2CHOH$	g / g IS	0.2817	0.1007	0.3578	0.9348	0.2034	0.6000	1.1992	1.4683
67-63-0	Wt. %	3.24	1.17	4.13	10.79	2.33	6.92	13.74	17.00
99.5%	Ai	374,634	99,344	445,514	1,008,411	268,770	507,871	560,325	720,015
	Ai/As	0.2533	0.0728	0.3233	0.8831	0.1776	0.5236	1.0942	1.3524
1-Propanol	Wi(g)	2.4432	7.6774	6.4681	4.0504	4.8563	0.7761	5.656	3.2636
$CH_3CH_2CH_2OH$	g / g IS	0.6246	1.9571	1.6512	1.0325	1.2468	0.1987	1.4520	0.8285
71-23-8	Wt. %	7.18	22.67	19.07	11.92	14.28	2.29	16.64	9.59
99.5%	Ai	630,345	2,138,890	1,551,827	735,509	1,442,759		465,089	253,654
	Ai/As	0.4262	1.5670	1.1260	0.6441	0.9535		0.9083	0.4764
1-Butanol	Wi(g)	0.8083	1.1928	0.3958	1.6171	3.9156	2.4131	5.6621	7.2639
$CH_3(CH_2)_3OH$	g / g IS	0.2066	0.3041	0.1010	0.4122	1.0053	0.6179	1.4536	1.8441
71-36-3	Wt. %	2.37	3.52	1.17	4.76	11.51	7.12	16.66	21.35
99.5%	Ai						47,886	90,308	149,611
	Ai/As						0.0494	0.1764	0.2810
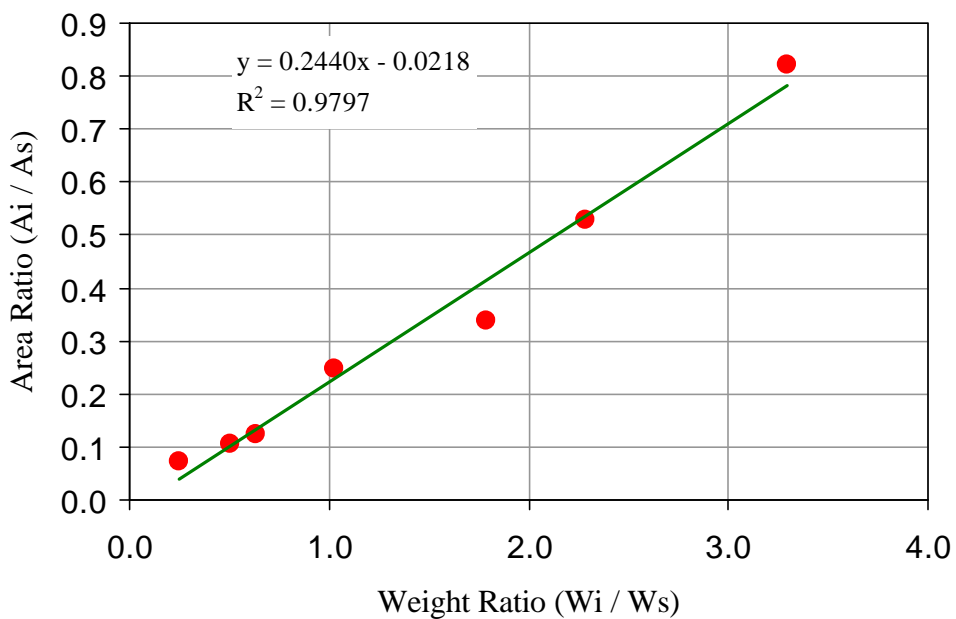
Figure A.1. Calibration Curve of Water
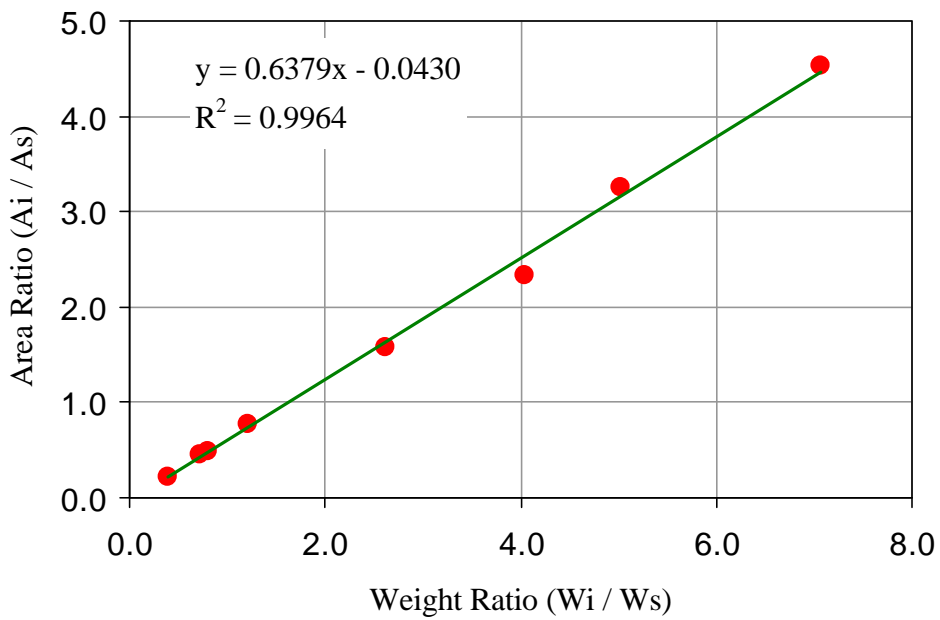
Figure A.2. Calibration Curve of Methanol
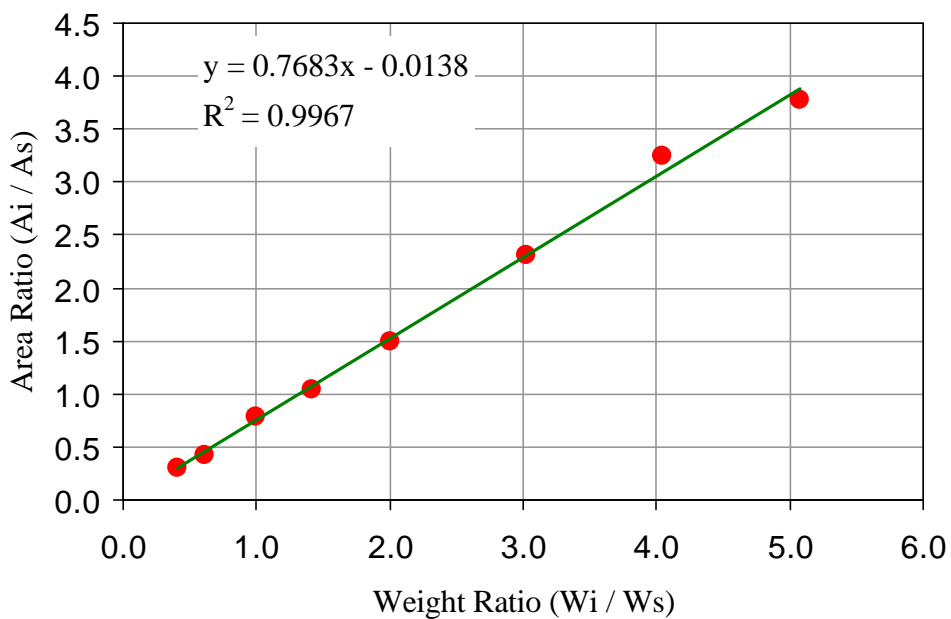
Figure A.3. Calibration Curve of Ethanol
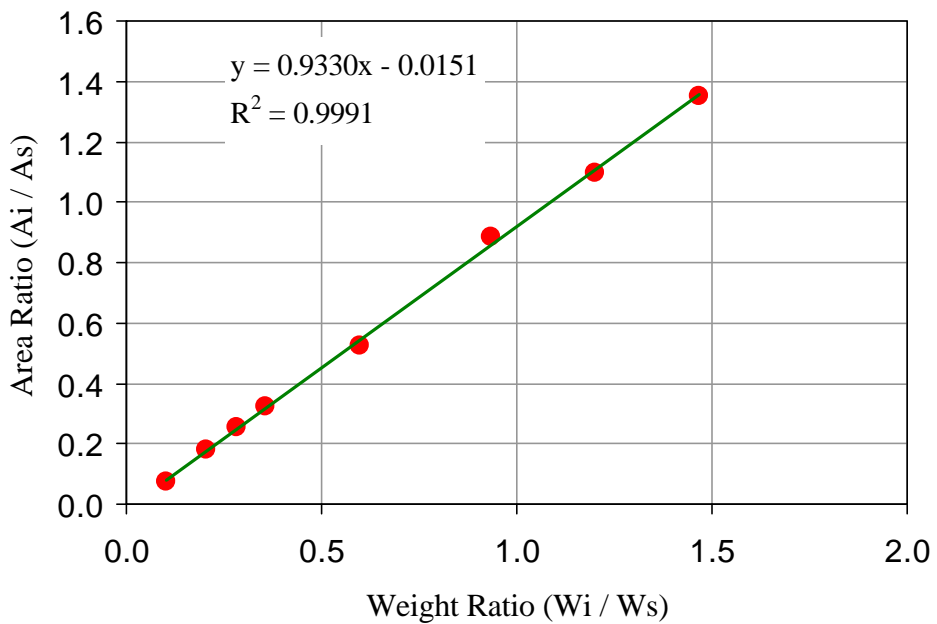
Figure A.4. Calibration Curve of isoPropanol
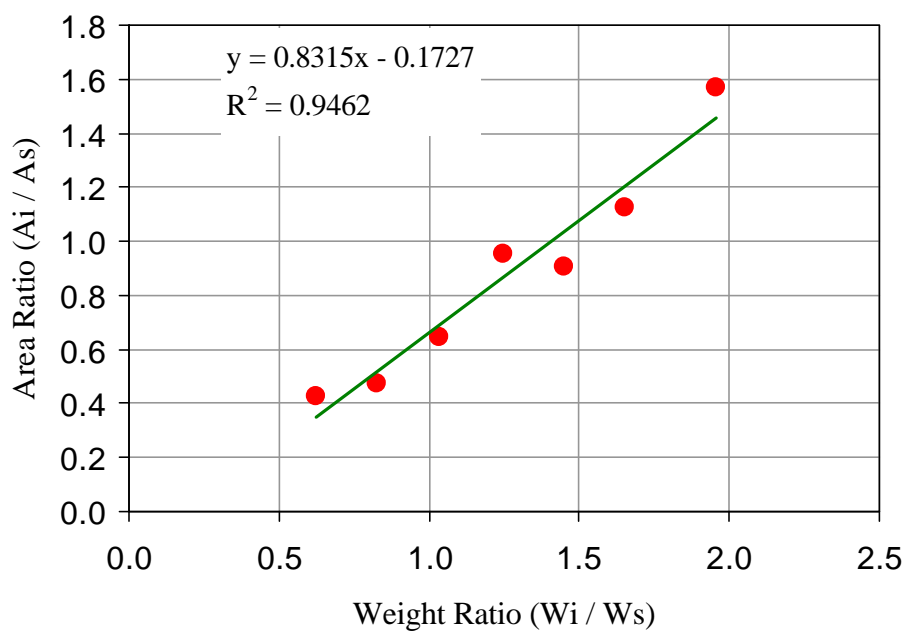
Figure A.5. Calibration Curve of Propanol
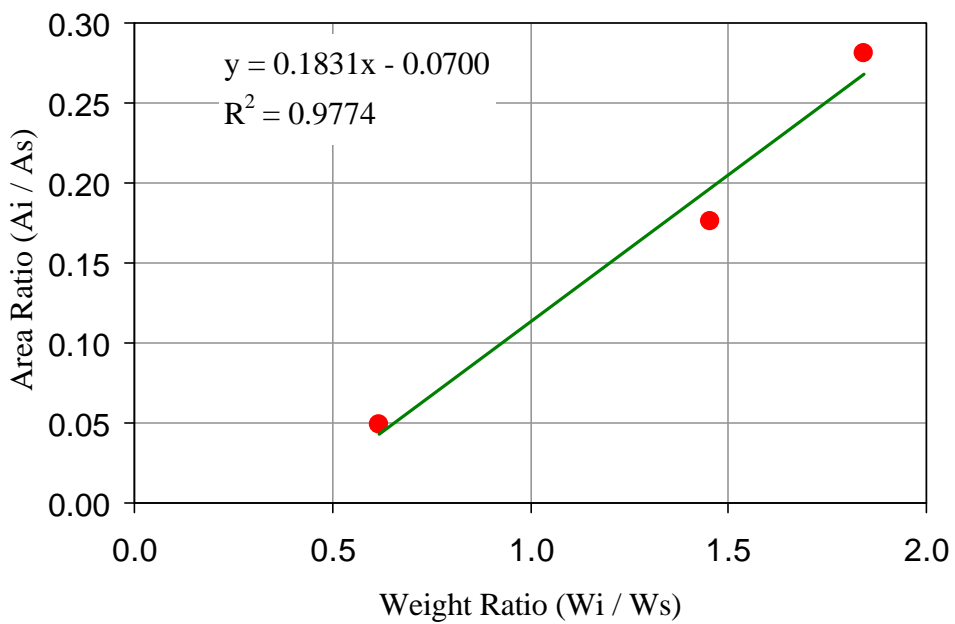
Figure A.6. Calibration Curve of Butanol

Table A.4. Standard Sample Analysis

Ws =	0.1390 g						
Component	Slope	Intercept	Ai / As	Wi (g)	Measure Wt. %	Actual Wt. %	Error %
Water	0.2440	-0.0218	0.0438	0.03736	3.0960	3.0437	0.017
Methanol	0.6379	-0.0430	3.0072	0.66464	55.0820	55.8297	0.013
Ethanol	0.7683	-0.0138	2.2249	0.40502	33.5660	33.0014	0.017
IsoPropanol	0.9930	-0.0151			None		
Propanol	0.8315	-0.1727	0.4232	0.09962	8.2560	8.1252	0.016
Butanol	0.1831	-0.0700			None		

A.5. Sample Analysis

The collected sample was filtered and transferred to a 1.5-ml vial. The mass of
each sample (Wg) was recorded along with the weight of Acetonitrile (Ws) added as
internal standard.

For CB1(1)R2 #1:

The average area ratio of methanol and acetonitrile for four runs was0.6756. The
weight of internal standard (Ws) in the mixture was 0.1718g, and the mass of sample
(Wg) was 1.4676 g. The calculated wt% of methanol is:

$W_{methanol}$ = (0.1718g)[(0.6756 + 0.0430)] / 0.6379

= 0.1935g

Wt% = (0.1935)(100) / (1.4676)

= 13.19 %

Table. A.5. GC/MS Selected Data Calculations

Component	H_2O	CH_3OH	C_2H_5OH	$(CH_3)_2OH$	C_2H_3OH	C_4H_9OH	Others OH
Slope	0.2440	0.6379	0.7683	0.9930	0.8315	0.7258	
Intercept	-0.0218	-0.0430	-0.0138	-0.0151	-0.1727	-0.1556	
Ret. Time	*2.99*	*3.49*	*4.59*	*6.30*	*7.68*	*15.29*	
Sample ID:	**CB1(1) R2 #1**		**Wg = 1.4676g**		**Ws = 0.1718g**		
Ai / As	1.5948	0.6756	0.1973				
Wi (g)	1.1382	0.1935	0.0472				
Wt%	77.56	13.19	3.22				6.04
Sample ID:	**CB1(1) R2 #2**		**Wg = 1.4379g**		**Ws = 0.1902g**		
Ai / As	1.0768	1.0675	0.3093	0.0128	0.0303		
Wi (g)	0.8563	0.3311	0.0800	0.0053	0.0464		
Wt%	59.56	23.03	5.56	0.37	3.23		8.25
Sample ID:	**CB1(1) R2 #3**		**Wg = 1.6075g**		**Ws = 0.1225g**		
Ai / As	2.1296	1.5766	0.3491				
Wi (g)	1.0801	0.3110	0.0579				
Wt%	67.19	19.35	3.60				9.86
Sample ID:	**CB1(1) R2 #4**		**Wg = 0.4630g**		**Ws = 0.1015g**		
Ai / As	0.7392	0.4309	0.0926				
Wi (g)	0.3166	0.0754	0.0141				
Wt%	68.37	16.29	3.04				12.31
Sample ID:	**CB1(1) R2 #5**		**Wg = 1.5653g**		**Ws = 0.1167g**		
Ai / As	2.1693	1.3023	0.2935				
Wi (g)	1.0479	0.2461	0.0467				
Wt%	66.95	15.72	2.98				14.35

A.6.   References

1.   Skoog, D. A., Holler, F. J., Nieman, T. A., <u>Principles of Instrumental Analysis</u>, (5th Edition, Harcourt Brace & Company, Florida: 1998).

2.   "HP 5971/5972 MSD Operation Student Manual", Hewlett Packard, (1994).

3.   Baugh, P. J., <u>Gas Chromatography: A Practical Approach</u>, (Oxford University Press, New York: 1993).

4.   McNair, H. M., Miller, J. M., <u>Basic Gas Chromatography</u>, (John Wiley & Sons, New York: 1998).

5.   Message, G. M., <u>Practical Aspects of Gas Chromatography / Mass Spectrometry</u>, (John Wiley & Sons, New York: 1984).

6.   Grob, R. L., <u>Modern Practice of Gas Chromatography</u>, (John Wiley & Sons, New York: 1985).

7.   McMaster, M., McMaster, C., <u>GC/MS A Practical User's Guide</u>, (Wiley-Vch, New York: 1998).

APPENDIX B

PHYSISORPTION MODEL CALCULATIONS

P/Po and V are obtained by Autosorb-1C

V_{ads} = V / w_{cat} = 1.76511 cm^3/0.2385g = 7.40 cm^3/g

Convert adsorbed volume (V_{ads}) to adsorbed weight,

W = M(PV_{ads}/RT)

W = (28.0134 g N$_2$/mol)(1atm)(7.4 cm^3/g catalyst)/

[(82.06 cm^3 atm mol^{-1}K^{-1})(273.2K)

= 0.0092 g N$_2$ /g catalyst

B.1. Langmuir Model

Table B.1. The Langmuir Data of CB1(1) Catalyst

Relative Pressure P / Po	Adsorbed Volume (V) (cm^3)	Adsorbed Volume (V_{ads}) (cm^3/g)	Adsorbed Weight (W) (g-gas/g-cat)	Langmuir Data P / Po / W (1 / g)
0.007156	1.765110	7.40	0.0092	0.7736
0.011786	1.811310	7.59	0.0095	1.2417
0.021931	1.907770	8.00	0.0100	2.1937
0.034067	1.976120	8.29	0.0104	3.2897
0.042638	2.012530	8.44	0.0105	4.0429
0.053325	2.050290	8.60	0.0107	4.9632
0.065632	2.099210	8.80	0.0110	5.9662
0.081882	2.156410	9.04	0.0113	7.2460
0.052795	2.053090	8.61	0.0108	4.9071
0.077748	2.143580	8.99	0.0112	6.9214
0.102382	2.232850	9.36	0.0117	8.7500

Plot (P / Po W) vs. (P / Po) of Catalyst CB1(1) run 3

Slope = 84.3105   Intercept = 0.3465

W_m = 1 / Slope = 0.0119

$$S \quad = \quad W_m \, \sigma \, N_A \, / \, m \, M$$

$$= \quad (0.0119 \text{ g/g}) \, (16.2 \text{ Å}^2/\text{molecules}) \, (6.023 \text{ x } 10^{23} \text{ molecules/mole}) \, /$$

$$[(28.0134 \text{ g/mole}) \, 1 \text{m}^2/(10^{10})^2 \text{ Å}^2] \qquad = \qquad 41.31 \text{ m}^2/\text{g}$$

B.2. BET Model

Table B.2. The BET Data of CB1(1) Catalyst

Relative Pressure $P \, / \, Po$	Adsorbed Volume (V) (cm^3)	Adsorbed Volume (V_{ads}) (cm^3/g)	Adsorbed Weight (W) (g-gas/g-cat)	BET Data $1/[w((Po \, / \, P)-1)]$ ($1 \, / \, g$)
0.052795	2.053090	8.61	0.0108	5.1806
0.077748	2.143580	8.99	0.0112	7.5049
0.102382	2.232850	9.36	0.0117	9.7480
0.127170	2.326250	9.75	0.0122	11.9520
0.151698	2.422560	10.16	0.0127	14.0863
0.176730	2.521700	10.57	0.0132	16.2449
0.201584	2.620490	10.99	0.0137	18.3860
0.226626	2.721270	11.41	0.0143	20.5490
0.251539	2.820480	11.83	0.0148	22.7381
0.276304	2.925050	12.26	0.0153	24.9080
0.300590	3.038130	12.74	0.0159	26.9947

Plot $1/[W \, ((Po \, / \, P) - 1)]$ vs. $(P \, / \, Po)$ of Catalyst CB1(1) run 3

Slope = 87.6162   Intercept = 0.7149

W_m = $1 \, / \, (\text{Intercept C})$

Slope = $(C - 1) \, / \, W_m C$

C = $(\text{Slope} \, / \, \text{Intercept}) + 1$ = 123.56

W_m = $1 \, / \, (0.7149)(123.56)$ = 0.0113 g N_2/g catalyst

S = $W_m \, \sigma \, N_A \, / \, m \, M$

$$= \text{(0.0113 g/g) (16.2 Å}^2\text{/molecules) (6.023 x 10}^{23}\text{ molecules/mole) / }$$

$$[(28.0134 \text{ g/mole}) \ 1\text{m}^2/(10^{10})^2 \ \text{Å}^2] \quad = \quad 39.43 \ \text{m}^2\text{/g}$$

$(\theta_o)_m \quad = \quad (C^{\frac{1}{2}} - 1) \ / \ (C - 1) \quad = \quad 0.0825$

$(\theta_i)_m \quad = \quad C[(C^{\frac{1}{2}} - 1) \ / \ (C - 1)]^{i+1}$

$(\theta_1)_m \quad = \quad 0.8417$

B.3. BJH Model

Data from CB1(1) Run 3

$t_n(\text{Å}) \quad = \quad 3.54 \ [5 \ / \ \text{LN(Po} \ / \ \text{P})]^{1/3} \quad = \quad 3.54 \ [(5 \ / \ \text{LN}(1 \ / \ 0.899514)]^{1/3}$

$\quad = \quad 12.79 \ \text{Å}$

$r_K(\text{Å}) \quad = \quad 4.15 \ / \ [\log(\text{Po} \ / \ \text{P})] \quad = \quad 4.15/(\text{LOG}(1 \ / \ 0.899514))$

$\quad = \quad 90.23 \ \text{Å}$

$r_P(\text{Å}) \quad = \quad \Delta t_n + r_K \quad = \quad 12.79 + 90.23$

$\quad = \quad 103.03 \ \text{Å}$

$r_K(\text{avg}) = \quad (90.23 + 58.47) \ / \ 2 \quad = \quad 74.35 \ \text{Å}$

$r_P(\text{avg}) = \quad (103.03 + 69.54) \ / \ 2 \quad = \quad 86.29 \ \text{Å}$

$\Delta t_n(\text{Å}) = \quad 12.79 - 11.07 \quad = \quad 1.72 \ \text{Å}$

$r_C(\text{Å}) \quad = \quad (103.03 - 68.54)/2 \quad = \quad 16.74 \ \text{Å}$

$t_r(\text{Å}) \quad = \quad r_{P \ avg} - r_C \quad = \quad 69.55 \ \text{Å}$

$\Delta V_{gas} \quad = \quad 84.48 - 53.94 \quad = \quad 30.54 \ \text{cm}^3\text{/g}$

$\Delta V_{liq} \quad = \quad \Delta V_{gas} \ \rho_{gas} \ / \ \rho_{liq} \quad \text{where} \ \rho_{gas} = 0.0012507 \ \text{g/cm}^3 \quad \rho_{liq} = 0.8121 \ \text{g/cm}^3$

$\Delta V_{liq} \quad = \quad 30.54 \ (0.0012507) \ / \ 0.8121 \quad = \quad 0.0472 \ \text{cm}^3\text{/g}$

Table B.3. The BJH Data of CB1(1) Catalyst

(P/Po)	Ads. Vol. (V) cm³	t_n Å	r_K Å	r_P Å	Avg r_K Å	Avg r_P Å	Avg Δt_n Å	r_C Å	t_r Å	ΔV_{gas} cc/g	ΔV_{liq} cc/g	Cj	Avg $[r_P/r_K+t_r]^2$	Δt_n $\Sigma(Cj\ Ap)$ cc/g	Pore Vol. Vp cc/g	Cum Vp cc/g	Ap m²/g	ΣCj Ap m²/g
0.9947	30.89	34.72				Å					0.034		1.03	0.000	0.350		0.00	0.00
0.9492	25.65	16.21	183.3	199.5	136.79	151.2	3.41	48.26	103.0	23.06	0.0356	0.9887	1.19	0.00000	0.04251	0.2058	5.62	5.56
0.8995	84.48	12.79	90.23	103.0	74.35	86.29	1.72	16.74	69.54	30.53	0.0472	0.9900	1.31	0.00096	0.06081	0.1708	14.10	19.51
0.8492	53.94	11.07	58.47	69.54	50.64	61.17	1.09	8.38	52.79	20.31	0.0314	0.9911	1.43	0.00213	0.04175	0.1283	13.65	33.04
0.7999	33.63	9.98	42.81	52.79	37.97	47.54	0.82	5.25	42.28	6.66	0.0103	0.9914	1.53	0.00270	0.01164	0.0674	4.90	37.89
0.7494	26.97	9.16	33.12	42.28	29.91	38.75	0.64	3.53	35.22	3.28	0.0051	0.9918	1.64	0.00241	0.00438	0.0257	2.26	40.13
0.6991	23.69	8.53	26.69	35.22	24.45	32.73	0.51	2.49	30.24	2.23	0.0034	0.9923	1.75	0.00203	0.00249	0.0141	1.52	41.64
0.6505	21.46	8.02	22.22	30.24	20.45	28.24	0.45	1.99	26.25	1.75	0.0027	0.9920	1.87	0.00187	0.00154	0.0097	1.09	42.73
0.5996	19.71	7.57	18.68	26.25	17.26	24.63	0.4	1.62	23.01	1.63	0.0025	0.9918	1.99	0.00173	0.00158	0.0072	1.28	44.00
0.5471	18.07	7.16	15.84	23.01	14.82	21.83	0.32	1.18	20.65	1.29	0.002	0.9926	2.12	0.00141	0.00121	0.0057	1.11	45.10
0.5005	16.79	6.84	13.8	20.65	12.87	19.55	0.33	1.1	18.44	1.26	0.0019	0.9917	2.25	0.00147	0.00106	0.0041	1.09	46.18
0.4487	15.53	6.52	11.93	18.44	11.16	17.53	0.29	0.92	16.61	0.97	0.0015	0.9916	2.4	0.00135	0.00035	0.0029	0.40	46.58
0.3985	14.56	6.22	10.39	16.61	9.75	15.85	0.26	0.76	15.08	0.89	0.0014	0.9917	2.57	0.00123	0.00039	0.0018	0.49	47.07
0.3508	13.67	5.96	9.12	15.08	8.53	14.36	0.27	0.73	13.63	0.95	0.0015	0.9906	2.74	0.00127	0.00055	0.0014	0.76	47.82
0.3001	12.71	5.69	7.94	13.63														

C_j $=$ $[r_P - (\Delta t_n / 2)] / r_P$ $=$ 0.9900

tr $=$ avg $\Delta t_n / 2$ $=$ 0.86

$[r_P/(r_K + t_r)^2]$avg $=$ $[86.29 / (74.35 + 0.86)]^2$ $=$ 1.31

Based on the assumption that all pore are fill at relative pressure,

Ap_1 $=$ 0 at P/Po $= 0.9947$

$(\Sigma C_j Ap)_0$ $=$ 0

$(\Sigma C_j Ap)_1$ $=$ 0

Vp_1 $=$ $[r_P/(r_K + t_r)]^2 [\Delta V_{liq} - \Delta t_{n1}(\Sigma C_j Ap)_0]$

$=$ $1.03 (0.0339 - 0)$ $=$ 0.3503 cm^3/g

Ap_2 $=$ $2 Vp_2 (10^4) / r_{P\,avg}$ $=$ $2 (0.04251) (10^4) / 151.29$

$=$ 5.62 cm^2/g

Cum Vp_2 $=$ $Vp_1 + $ Cum Vp_3 $=$ $0.3505 + 0.1708$

$=$ 2.058 cm^3/g

$\Delta t_{n3} (\Sigma C_j Ap)_2 =$ 1.72Å $(5.56$ m^2/g$)$ 0.0001 $=$ 0.00096 cm^3/g

Vp_3 $=$ $[r_P/(r_K + t_r)]^2 [\Delta V_{liq} - \Delta t_{n3} (\Sigma C_j Ap)_2]$

$=$ $1.31 (0.0472 - 0.00096)$ $=$ 0.06081 cm^3/g

Cum Vp_3 $=$ $Vp_2 + $ Cum Vp_4 $=$ $0.04251 + 0.1283$

$=$ 0.1708 cm^3/g

Ap_3 $=$ $2 Vp_3 (10^4) / r_{P\,avg}$ $=$ $2 (0.06081) (10^4) / 86.29$

$=$ 14.10 cm^2/g

$(\Sigma C_j Ap)_3$ $=$ $(\Sigma C_j Ap)_2 + C_{j3} Ap_3$ $=$ $5.56 + (0.9900)(14.10)$

$=$ 19.51 cm^2/g

B.4.   The t Method

Table B.4. The t Data of CB1(1) Catalyst

Relative Pressure P / Po	Adsorbed Volume (V) (cm³)	Adsorbed Volume (V_{ads}) (cm³/g)	BET t Data	Halsey t Data	de Boer t Data
0.000099	1.08	4.52	1.77	2.89	1.86
0.000251	1.29	5.41	2.12	2.99	1.96
0.000316	1.33	5.60	2.20	3.02	1.99
0.000398	1.37	5.76	2.26	3.05	2.02
0.000503	1.41	5.92	2.32	3.08	2.05
0.000631	1.45	6.06	2.38	3.11	2.08
0.000797	1.48	6.20	2.43	3.14	2.11
0.001008	1.51	6.34	2.49	3.18	2.15
0.001851	1.59	6.68	2.62	3.28	2.25
0.003004	1.66	6.94	2.72	3.37	2.34
0.003745	1.68	7.06	2.77	3.41	2.38
0.004799	1.71	7.19	2.82	3.46	2.44
0.005711	1.74	7.28	2.86	3.50	2.48
0.007156	1.77	7.40	2.90	3.55	2.53
0.011786	1.81	7.59	2.98	3.68	2.67
0.021931	1.91	8.00	3.14	3.87	2.87
0.034067	1.98	8.29	3.25	4.03	3.05
0.042638	2.01	8.44	3.31	4.13	3.16
0.053325	2.05	8.60	3.37	4.23	3.27
0.065632	2.10	8.80	3.45	4.33	3.39
0.081882	2.16	9.04	3.55	4.46	3.53
0.052795	2.05	8.61	3.38	4.22	3.27
0.077748	2.14	8.99	3.53	4.43	3.50
0.102382	2.23	9.36	3.67	4.60	3.70
0.127170	2.33	9.75	3.83	4.76	3.88
0.151698	2.42	10.16	3.98	4.90	4.05
0.176730	2.52	10.57	4.15	5.04	4.22
0.201584	2.62	10.99	4.31	5.17	4.38
0.226626	2.72	11.41	4.48	5.31	4.54
0.251539	2.82	11.83	4.64	5.44	4.70
0.276304	2.93	12.26	4.81	5.57	4.86
0.300590	3.04	12.74	5.00	5.69	5.02
0.350205	3.26	13.67	5.36	5.96	5.35

Relative Pressure P / Po	Adsorbed Volume (V) (cm^3)	Adsorbed Volume (V_{ads}) (cm^3/g)	BET t Data	Halsey t Data	de Boer t Data
0.400137	3.48	14.60	5.73	6.23	5.69
0.451316	3.71	15.58	6.11	6.53	6.07
0.500262	3.98	16.67	6.54	6.84	6.46
0.549933	4.24	17.79	6.98	7.19	6.90
0.602833	4.57	19.14	7.51	7.60	7.42
0.649502	4.93	20.67	8.11	8.01	7.95
0.701246	5.40	22.62	8.88	8.55	8.62
0.750159	6.03	25.29	9.92	9.17	9.38
0.800299	7.00	29.33	11.51	9.99	10.34
0.849783	8.82	36.98	14.51	11.09	11.56
0.899405	14.62	61.32	24.06	12.79	13.22
0.950309	22.99	96.41	37.82	16.33	15.79
0.994713	30.89	129.50	50.81	34.72	19.63

BET t model

S_{BET} = 39.43 m^2/g

t = 15.47 (V_a / S) = 15.47 (4.52 cm^3/g) / 39.43 cm^2/g

= 1.77 Å

Halsey t model

t = 3.54 [5 / LN(Po/P)]$^{1/3}$ = 3.54 [(5 / LN(1 / 0.000099)]$^{1/3}$

= 2.89 Å

de Boer t model

t = {13.99 / [0.034+(LOG(Po/P))]}$^{1/2}$

= {13.99 / [0.034+(LOG(1 / 0.000099))]}$^{1/2}$ = 1.86 Å

Plot V_a vs. t in the pressure range of 0.007155 to 0.10238 yields,

Slope = 1.848   Intercept = 0.8168

$A_{external}$ = 15.47 (slope) = 28.58 m^2/g

APPENDIX C

PHYSISORPTION DATA

C.1.   Standard Isotherm and BET Data

Table C.1. Standard Trial Analysis Data

Sample ID	Alumina, 3 white pellets
Description	Cat #2005-4399
Adsorbate	NITROGEN
Outgas Temperature	300 °C
Cross-Sectional Area	16.2 Å²/molecule
Outgas Time	12.0 hrs
Non-Ideality	6.58E-05
P/Po Tolerance	0
Molecular Weight	28.0134 g/mol
Equilibration Time	3 min
Station #	1
Bath Temperature	77.35 K

Table C.2. Run 1 Isotherm and BET Data of Standard
(89.4 min analysis time, 0.1319 g sample)

Relative Pressure (P/Po)	Adsorbed Volume (cc/g)	BET Data [1/(W((Po/P)-1))]
5.17E-02	19.6515	2.2210
7.68E-02	20.9680	3.1730
1.00E-01	22.0646	4.0300
1.25E-01	23.1836	4.9310
1.51E-01	24.3183	5.8390
1.76E-01	25.2879	6.7450
2.00E-01	26.2805	7.6020
2.25E-01	27.3945	8.5010
2.51E-01	28.2598	9.4720
2.76E-01	29.1039	10.4700
3.01E-01	30.1569	11.4200

Table C.3. Run 2 Isotherm and BET Data of Standard
(84.8 min analysis time, 0.1319 g sample)

Relative Pressure (P/Po)	Adsorbed Volume (cc/g)	BET Data [1/(W((Po/P)-1))]
5.1494E-02	19.6849	2.2070
7.6870E-02	21.0224	3.1690
1.0003E-01	22.1010	4.0240
1.2524E-01	23.1873	4.9400
1.5024E-01	24.1975	5.8460
1.7544E-01	25.1799	6.7610
2.0035E-01	26.1268	7.6730
2.2517E-01	27.0823	8.5860
2.4950E-01	28.1077	9.4630
2.7453E-01	29.0702	10.4200
2.9954E-01	29.9974	11.4100

Table C.4. Run 3 Isotherm and BET Data of Standard
(84.8 min analysis time, 0.1319 g sample)

Relative Pressure (P/Po)	Adsorbed Volume (cc/g)	BET Data [1/(W((Po/P)-1))]
5.1000E-02	19.5633	2.1960
7.6600E-02	20.9181	3.1710
1.0020E-01	22.0109	4.0460
1.2520E-01	23.0871	4.9590
1.5010E-01	24.0958	5.8650
1.7530E-01	25.0821	6.7790
2.0020E-01	26.0457	7.6890
2.2710E-01	27.2345	8.6300
2.5020E-01	28.1374	9.4880
2.7450E-01	29.1317	10.3900
2.9960E-01	30.1413	11.3600

Table C.5. Run 4 Isotherm and BET Data of Standard
(2328.3 min analysis time, 0.1247 g sample)

Relative Pressure (P/Po)	Adsorbed Volume (cc/g)	BET Data [1/(W((Po/P)-1))]
1.3392E-06	0.0041	
1.4465E-06	0.0139	
1.4639E-06	0.0236	
1.4956E-06	0.0430	
1.5402E-06	0.0624	
1.6209E-06	0.0915	
1.6580E-06	0.1108	
1.7619E-06	0.0000	
1.8232E-06	0.1785	
1.8762E-06	0.1881	
1.9012E-06	0.2168	
1.9548E-06	0.2361	
1.9778E-06	0.2456	
2.0335E-06	0.2552	
2.3968E-06	0.3395	
3.2524E-06	0.5056	
4.1233E-06	0.7089	
5.4775E-06	0.9908	
6.9093E-06	1.6453	
9.0970E-06	2.1113	
1.1867E-05	2.6416	
1.5565E-05	3.0030	
2.0408E-05	3.3979	
2.6622E-05	3.8461	
3.4692E-05	4.2077	
4.4951E-05	4.6575	
5.8079E-05	5.0734	
7.4747E-05	5.5086	
9.4960E-05	5.9393	
1.2132E-04	6.4063	
1.5418E-04	6.8720	
1.9598E-04	7.3464	
2.4757E-04	7.8259	
3.1328E-04	8.3152	
3.9532E-04	8.7914	
4.9907E-04	9.2720	

Relative Pressure (P/Po)	Adsorbed Volume (cc/g)	BET Data [1/(W((Po/P)-1))]
6.3106E-04	9.7593	
7.9834E-04	10.2437	
1.0009E-03	10.7091	
1.1671E-03	11.0309	
1.4777E-03	11.5257	
1.8267E-03	11.9673	
2.2763E-03	12.4314	
2.8275E-03	12.8914	
3.6397E-03	13.4311	
4.5415E-03	13.9054	
5.8550E-03	14.4563	
7.2059E-03	14.9092	
9.2353E-03	15.5008	
1.2624E-02	16.1500	
1.7057E-02	17.0362	
2.0271E-02	17.4964	
2.6594E-02	18.2817	
3.1533E-02	18.7889	
4.1316E-02	19.6566	
5.1613E-02	20.4459	2.1300
5.2796E-02	20.5640	2.1690
6.4717E-02	21.3654	2.5910
8.0615E-02	22.3160	3.1440
1.0071E-01	23.3445	3.8380
1.5016E-01	25.5795	5.5270
2.0004E-01	27.6470	7.2370
2.4931E-01	29.7019	8.9460
3.0069E-01	31.8651	10.8000
3.5014E-01	34.0383	
3.9918E-01	36.3859	
4.5209E-01	39.1093	
4.9977E-01	42.0332	
5.4951E-01	45.6468	
6.1023E-01	54.0780	
6.5046E-01	58.9485	
6.9934E-01	67.9405	
7.4942E-01	82.2684	
7.9914E-01	103.8582	
8.5037E-01	126.2062	
8.9988E-01	138.6164	

Relative Pressure (P/Po)	Adsorbed Volume (cc/g)	BET Data [1/(W((Po/P)-1))]
9.5028E-01	154.1236	
9.9580E-01	176.7551	
9.4986E-01	162.1812	
8.9873E-01	150.7438	
8.5056E-01	141.9803	
8.0025E-01	131.3988	
7.5037E-01	115.3556	
7.0050E-01	86.9386	
6.5047E-01	66.4771	
5.9956E-01	56.1709	
5.4939E-01	49.8996	
5.0076E-01	45.5363	
4.4923E-01	41.1441	
3.9974E-01	38.1014	
3.4779E-01	35.3730	
3.0038E-01	33.0353	
2.4984E-01	30.6755	
1.9926E-01	28.3422	
1.4900E-01	26.0059	
1.0045E-01	23.7105	
4.7018E-02	20.6215	

Table C.6. Run 5 Isotherm and BET Data of Standard
(98.6 min analysis time, 0.1247 g sample)

Relative Pressure (P/Po)	Adsorbed Volume (cc/g)	BET Data [1/(W((Po/P)-1))]
5.3365E-02	20.0132	2.2540
7.7465E-02	21.1947	3.1700
1.0098E-01	22.2249	4.0440
1.2592E-01	23.2959	4.9480
1.5090E-01	24.2582	5.8620
1.7599E-01	25.1965	6.7820
2.0080E-01	26.1140	7.6980
2.2718E-01	27.1358	8.6680
2.5069E-01	28.0121	9.5560
2.7541E-01	28.9666	10.5000
3.0032E-01	29.9172	11.4800

Table C.7. Run 6 Isotherm and BET Data of Standard
(97.9 min analysis time, 0.1247 g sample)

Relative Pressure (P/Po)	Adsorbed Volume (cc/g)	BET Data [1/(W((Po/P)-1))]
5.0692E-02	19.7810	2.1600
7.7350E-02	21.1249	3.1750
1.0110E-01	22.1626	4.0600
1.2605E-01	23.1717	4.9800
1.5080E-01	24.1560	5.8820
1.7590E-01	25.1237	6.7970
2.0090E-01	26.0557	7.7200
2.2580E-01	26.9758	8.6510
2.5064E-01	27.8797	9.5990
2.7489E-01	28.8848	10.5000
3.0020E-01	29.8655	11.4900

Table C.8. All Trials BET Analysis of Standard
(Calculations are in Appendix B)

	Area (m^2/g)	Slope	Intercept	BET C Constant	Correlation
Run 1	94.30	36.60	0.3345	110.4	0.999887
Run 2	93.83	36.79	0.3217	115.4	0.999958
Run 3	94.29	36.57	0.3632	101.7	0.999971
Run 4	99.59	34.63	0.3411	102.5	0.999975
Run 5	93.15	37.12	0.2719	137.5	0.999958
Run 6	92.93	37.19	0.2793	134.2	0.999970

C.2. Catalyst Isotherm and BET Data

C.2.1. CB1(1) Data

Table C.9. Trial Analysis Data of CB1(1) Catalyst

Report for Station	1
Sample ID	CB1(1) Fresh Catalyst
Sample Weight	0.2385 g
P/Po Tolerance	0
Gas Type	Nitrogen
Cross-Sectional Area	16.2 Å²
Molecular Weight	28.0134 g/mole
Non-Ideality Correction Factor	6.58E-05 /torr
Ambient Temperature	293.122 K
Analysis Temperature	77.347 K
Outgass Temperature	200°C
Outgass Time	13 hr

Table C.10. Run 1 Isotherm Data of CB1(1) Catalyst

Pressure (atm)	Saturation Pressure (atm)	Adsorbed Volume (cc / g)	Equilibration Time (min)	Analysis Time (min)	Flag
5.3385E-02	1.0034	2.0415	3	43.60	A M
7.7425E-02	1.0032	2.1349	3	48.95	A M
1.0242E-01	1.0033	2.2247	3	54.30	A M
1.2729E-01	1.0020	2.3126	3	59.65	A M
1.5203E-01	1.0017	2.4030	3	65.02	A M
1.7710E-01	1.0019	2.4970	3	70.40	A M
2.0200E-01	1.0019	2.5890	3	75.80	A M
2.2702E-01	1.0021	2.6832	3	81.20	A M
2.5196E-01	1.0017	2.7773	3	86.63	A M
2.7614E-01	1.0022	2.8843	3	94.27	A M
3.0151E-01	1.0024	2.9884	3	100.00	A M

A is the adsorption data point
M is the BET data point

Table C.11. Run 2 Isotherm Data of CB1(1) Catalyst

Pressure (atm)	Saturation Pressure (atm)	Adsorbed Volume (cc / g)	Equilibration Time (min)	Analysis Time (min)	Flag
5.3652E-02	1.0012	2.0414	3	42.27	A M
7.7077E-02	1.0020	2.1353	3	47.85	A M
1.0223E-01	1.0019	2.2295	3	53.20	A M
1.2721E-01	1.0011	2.3206	3	58.38	A M
1.5206E-01	1.0011	2.4107	3	63.75	A M
1.7703E-01	1.0010	2.5011	3	69.05	A M
2.0167E-01	1.0009	2.5972	3	74.77	A M
2.2659E-01	1.0009	2.6957	3	80.28	A M
2.5150E-01	1.0004	2.7926	3	85.70	A M
2.7641E-01	1.0001	2.8921	3	91.25	A M
3.0040E-01	1.0011	3.0003	3	98.17	A M

Table C.12. Run 3 Isotherm Data of CB1(1) Catalyst

Pressure (atm)	Saturation Pressure (atm)	Adsorbed Volume (cc / g)	Equilibration Time (min)	Analysis Time (min)	Flag
9.9578E-05	1.0025	1.0775	5	223.63	A
2.5156E-04	1.0028	1.2911	5	277.38	A
3.1677E-04	1.0032	1.3346	5	298.15	A
3.9879E-04	1.0029	1.3729	5	311.02	A
5.0447E-04	1.0031	1.4119	5	327.85	A
6.3290E-04	1.0033	1.4458	4	338.22	A
7.9973E-04	1.0037	1.4792	4	349.93	A
1.0122E-03	1.0038	1.5130	4	363.77	A
1.8587E-03	1.0042	1.5935	4	396.73	A
3.0181E-03	1.0047	1.6553	4	418.55	A
3.7622E-03	1.0045	1.6828	4	429.97	A
4.8218E-03	1.0049	1.7141	4	444.73	A
5.7378E-03	1.0046	1.7363	4	452.53	A
7.1855E-03	1.0042	1.7651	4	460.72	A L
1.1842E-02	1.0048	1.8113	4	468.35	A L
2.2039E-02	1.0049	1.9078	4	474.50	A L
3.4226E-02	1.0047	1.9761	4	480.07	A L

Pressure (atm)	Saturation Pressure (atm)	Adsorbed Volume (cc / g)	Equilibration Time (min)	Analysis Time (min)	Flag
4.2831E-02	1.0045	2.0125	4	486.02	A L
5.3023E-02	1.0043	2.0531	3	490.78	A M L
5.3546E-02	1.0041	2.0503	4	494.55	A L
6.5943E-02	1.0047	2.0992	4	500.53	A L
7.8108E-02	1.0046	2.1436	3	505.50	A M L
8.2260E-02	1.0046	2.1564	4	510.52	A L
1.0284E-01	1.0045	2.2329	3	515.53	A M T L
1.2768E-01	1.0040	2.3263	3	520.82	A M T
1.5238E-01	1.0045	2.4226	3	526.18	A M T
1.7754E-01	1.0046	2.5217	3	531.57	A M T
2.0258E-01	1.0049	2.6205	3	536.95	A M T
2.2762E-01	1.0044	2.7213	3	542.37	A M T
2.5266E-01	1.0044	2.8205	3	547.78	A M T
2.7750E-01	1.0043	2.9251	3	553.22	A M T
3.0197E-01	1.0046	3.0381	3	559.20	A M T P
3.5180E-01	1.0046	3.2599	3	566.13	A T P
4.0174E-01	1.0040	3.4823	3	573.10	A T P
4.5326E-01	1.0043	3.7147	3	580.57	A T P
5.0271E-01	1.0049	3.9758	3	588.73	A T P
5.5245E-01	1.0046	4.2438	3	597.28	A P
6.0538E-01	1.0042	4.5650	3	607.43	A P
6.5231E-01	1.0043	4.9302	3	619.05	A P
7.0432E-01	1.0044	5.3959	3	633.98	A P
7.5341E-01	1.0043	6.0325	3	652.48	A P
8.0360E-01	1.0041	6.9961	3	681.77	A P
8.5354E-01	1.0044	8.8203	3	726.58	A P
9.0328E-01	1.0043	14.6239	3	868.35	A P
9.5557E-01	1.0055	22.9934	3	994.27	A P
1.0005E+00	1.0059	30.8863	3	1140.95	A D P
9.5462E-01	1.0057	25.6478	3	1240.25	D P
9.0404E-01	1.0050	20.1476	3	1330.00	D P
8.5171E-01	1.0029	12.8653	3	1495.58	D P
8.0275E-01	1.0035	8.0213	3	1576.93	D P
7.5163E-01	1.0030	6.4330	3	1606.07	D P
7.0105E-01	1.0028	5.6498	3	1624.18	D P
6.5221E-01	1.0027	5.1174	3	1635.98	D P
6.0113E-01	1.0026	4.7004	3	1646.45	D P
5.4852E-01	1.0026	4.3106	3	1657.33	D P
5.0180E-01	1.0027	4.0039	3	1665.50	D P

Pressure (atm)	Saturation Pressure (atm)	Adsorbed Volume (cc / g)	Equilibration Time (min)	Analysis Time (min)	Flag
4.4973E-01	1.0022	3.7040	3	1674.20	D P
3.9947E-01	1.0024	3.4721	3	1684.50	D P
3.5173E-01	1.0025	3.2596	3	1691.50	D P
3.0075E-01	1.0022	3.0325	3	1697.03	D P
2.5036E-01	1.0029	2.8114	3	1702.78	D
1.9992E-01	1.0029	2.6100	3	1708.42	D
1.4925E-01	1.0025	2.4104	3	1713.78	D
1.0066E-01	1.0026	2.2248	3	1718.60	D
4.8552E-02	1.0033	2.0353	3	1726.63	D

A is the adsorption data point
D is the desorption data point
T is the statistical thickness data point
P is the pore size distribution point
L is the Langmuir data point
M is the BET data point

C.2.2. CB1(3) Data

Table C.13. Trial Analysis Data of CB1(3) Catalyst

Report for Station	1
Sample ID	CB1(3)
Sample Weight	0.3682 g
P/Po Tolerance	0
Gas Type	Nitrogen
Cross-Sectional Area	16.2 Å²
Molecular Weight	28.0134 g/mole
Non-Ideality Correction Factor	6.58E-05 /torr
Ambient Temperature:	292.15 K
Analysis Temperature:	77.347 K
Outgass Temperature:	200°C
Outgass Time:	12 hr

Table C.14. Run 1 Isotherm Data of CB1(3) Catalyst

Pressure (atm)	Saturation Pressure (atm)	Adsorbed Volume (cc / g)	Equilibration Time (min)	Analysis Time (min)	Flag
5.3674E-02	1.0100	2.3356	3	42.83	A M
7.8211E-02	1.0098	2.4222	3	47.97	A M
1.0340E-01	1.0102	2.5068	3	53.20	A M
1.2836E-01	1.0112	2.5927	3	58.97	A M
1.5350E-01	1.0122	2.6837	3	64.75	A M
1.7915E-01	1.0118	2.7773	3	70.55	A M
2.0424E-01	1.0115	2.8743	3	75.05	A M
2.2896E-01	1.0116	2.9769	3	80.57	A M
2.5391E-01	1.0116	3.0857	3	85.62	A M
2.7877E-01	1.0107	3.2034	3	91.58	A M
3.0358E-01	1.0095	3.3218	3	97.68	A M

Table C.15. Run 2 Isotherm Data of CB1(3) Catalyst

Pressure (atm)	Saturation Pressure (atm)	Adsorbed Volume (cc / g)	Equilibration Time (min)	Analysis Time (min)	Flag
9.9922E-05	1.0028	1.2823	5	247.30	A
2.5179E-04	1.0024	1.5762	5	313.57	A
3.1673E-04	1.0024	1.6269	5	329.58	A
3.9997E-04	1.0032	1.6731	5	343.37	A
5.0298E-04	1.0034	1.7143	5	356.92	A
6.3658E-04	1.0034	1.7533	4	367.88	A
7.9863E-04	1.0045	1.7891	4	381.08	A
1.0097E-03	1.0038	1.8251	4	397.30	A
1.8242E-03	1.0036	1.9092	4	429.67	A
2.9730E-03	1.0042	1.9758	4	450.90	A
3.7087E-03	1.0035	2.0054	4	462.40	A
4.7622E-03	1.0038	2.0391	4	474.40	A
5.6676E-03	1.0039	2.0626	4	481.80	A T
7.1022E-03	1.0050	2.0931	4	489.67	A L
1.1742E-02	1.0046	2.1418	4	495.62	A L
2.2149E-02	1.0033	2.2406	4	500.37	A L
3.4379E-02	1.0033	2.3069	4	506.42	A L

Pressure	Saturation Pressure	Adsorbed Volume	Equilibration Time	Analysis Time	Flag
(atm)	(atm)	(cc / g)	(min)	(min)	
4.1557E-02	1.0044	2.3404	4	511.38	A L
5.1469E-02	1.0043	2.3827	3	515.33	A M L
5.3260E-02	1.0031	2.3860	4	517.47	A T L
6.4441E-02	1.0034	2.4306	4	521.15	A T L
7.6392E-02	1.0035	2.4760	3	525.30	A M L
8.1987E-02	1.0042	2.4953	4	530.28	A L
1.0295E-01	1.0035	2.5718	3	535.30	A M T L
1.2778E-01	1.0033	2.6646	3	540.07	A M T
1.5267E-01	1.0026	2.7598	3	544.63	A M T
1.7760E-01	1.0037	2.8625	3	550.22	A M T
2.0252E-01	1.0032	2.9684	3	555.82	A M T
2.2727E-01	1.0035	3.0787	3	561.23	A M T
2.5194E-01	1.0036	3.1954	3	566.65	A M T
2.7700E-01	1.0031	3.3214	3	571.30	A M T
3.0181E-01	1.0033	3.4463	3	576.75	A M T P
3.5264E-01	1.0040	3.7154	3	583.98	A T P
4.0138E-01	1.0033	3.9720	3	590.65	A T P
4.5135E-01	1.0022	4.2284	3	597.47	A T P
5.0340E-01	1.0030	4.5094	3	606.80	A T P
5.5382E-01	1.0030	4.7967	3	617.35	A P
6.0124E-01	1.0022	5.1100	3	625.90	A P
6.5382E-01	1.0029	5.5341	3	638.00	A P
7.0107E-01	1.0030	6.0031	3	648.90	A P
7.5182E-01	1.0025	6.6889	3	663.97	A P
8.0277E-01	1.0022	7.7321	3	692.33	A P
8.5207E-01	1.0019	9.4543	3	731.27	A P
9.0124E-01	1.0020	13.1103	3	797.98	A P
9.5336E-01	1.0031	24.6431	3	985.35	A P
9.9895E-01	1.0034	40.0405	3	1164.80	A D P
9.5394E-01	1.0034	32.6540	3	1271.40	D P
9.0185E-01	1.0013	18.9443	3	1430.23	D P
8.5080E-01	1.0018	11.4478	3	1523.48	D P
8.0106E-01	1.0007	8.6819	3	1559.28	D P
7.4894E-01	1.0007	7.2368	3	1587.73	D P
7.0008E-01	1.0006	6.4633	3	1603.52	D P
6.5037E-01	1.0003	5.8697	3	1615.75	D P
5.9876E-01	1.0000	5.4021	3	1625.68	D P
5.5074E-01	1.0003	5.0477	3	1633.50	D P
5.0027E-01	1.0009	4.6979	3	1641.57	D P

Pressure	Saturation Pressure	Adsorbed Volume	Equilibration Time	Analysis Time	Flag
(atm)	(atm)	(cc / g)	(min)	(min)	
4.5083E-01	1.0001	4.3911	3	1648.40	D P
4.0106E-01	1.0003	4.0768	3	1655.55	D P
3.5014E-01	1.0006	3.7728	3	1661.93	D P
3.0070E-01	1.0005	3.4545	3	1678.23	D P
2.4982E-01	1.0002	3.1854	3	1684.10	D
1.9896E-01	1.0001	2.9533	3	1689.52	D
1.4850E-01	0.9999	2.7438	3	1694.88	D
9.9753E-02	1.0002	2.5601	3	1699.38	D
4.9713E-02	1.0005	2.3752	3	1706.57	D

Table C.16. Run 3 Isotherm Data of CB1(3) Catalyst

Pressure	Saturation Pressure	Adsorbed Volume	Equilibration Time	Analysis Time	Flag
(atm)	(atm)	(cc / g)	(min)	(min)	
5.3572E-02	0.9999	2.3404	3	44.87	A M
7.7361E-02	0.9996	2.4277	3	49.82	A M
1.0241E-01	0.9997	2.5147	3	54.73	A M
1.2701E-01	1.0001	2.6079	3	60.08	A M
1.5212E-01	0.9998	2.7011	3	65.45	A M
1.7703E-01	0.9999	2.7970	3	70.83	A M
2.0183E-01	0.9995	2.8970	3	76.22	A M
2.2660E-01	0.9996	3.0026	3	81.62	A M
2.5102E-01	1.0000	3.1194	3	87.27	A M
2.7611E-01	1.0001	3.2427	3	92.70	A M
3.0210E-01	0.9995	3.3671	3	99.08	A M
3.5164E-01	0.9998	3.6134	3	106.10	A
3.9919E-01	1.0001	3.8630	3	113.82	A
4.5103E-01	1.0000	4.0937	3	120.22	A
4.9959E-01	0.9997	4.3393	3	127.33	A
5.4998E-01	0.9995	4.6290	3	135.57	A
6.0206E-01	0.9993	4.9967	3	145.40	A
6.5284E-01	0.9996	5.3945	3	156.93	A
7.0030E-01	0.9996	5.8953	3	172.48	A
7.4970E-01	0.9991	6.5488	3	188.13	A
7.9971E-01	0.9993	7.6029	3	211.18	A
8.4844E-01	0.9993	9.4201	3	247.50	A

Pressure	Saturation Pressure	Adsorbed Volume	Equilibration Time	Analysis Time	Flag
(atm)	(atm)	(cc / g)	(min)	(min)	
8.9819E-01	0.9986	13.6210	3	330.33	A
9.5045E-01	1.0010	26.7314	3	520.53	A
9.9669E-01	1.0021	41.8258	3	674.72	AD
9.5273E-01	1.0034	34.1455	3	791.77	D

Table C.17. Run 4 Isotherm Data of CB1(3) Catalyst

Pressure	Saturation Pressure	Adsorbed Volume	Equilibration Time	Analysis Time	Flag
(atm)	(atm)	(cc / g)	(min)	(min)	
5.4457E-02	1.0199	2.3209	3	42.50	A M
7.9007E-02	1.0169	2.4029	3	46.97	A M
1.0426E-01	1.0174	2.4802	3	51.08	A M
1.2960E-01	1.0167	2.5590	3	56.02	A M
1.5425E-01	1.0155	2.6505	3	61.32	A M
1.7981E-01	1.0139	2.7328	3	65.92	A M
2.0503E-01	1.0144	2.8199	3	70.52	A M
2.2982E-01	1.0141	2.9135	3	75.92	A M
2.5449E-01	1.0136	3.0213	3	82.18	A M
2.7982E-01	1.0119	3.1330	3	87.13	A M
3.0515E-01	1.0114	3.2369	3	91.58	A M
3.5555E-01	1.0110	3.4912	3	103.33	A
4.0533E-01	1.0113	3.7117	3	109.48	A
4.5678E-01	1.0121	3.9366	3	115.67	A
5.0675E-01	1.0102	4.1911	3	127.23	A
5.5468E-01	1.0063	4.4784	3	134.73	A
6.0485E-01	1.0061	4.7315	3	142.10	A
6.5502E-01	1.0061	5.0882	3	152.25	A
7.0564E-01	1.0055	5.4897	3	161.87	A
7.5382E-01	1.0058	6.1165	3	175.73	A
8.0537E-01	1.0059	7.0657	3	203.38	A
8.5519E-01	1.0059	8.5266	3	233.55	A
9.0405E-01	1.0051	12.0268	3	294.35	A
9.5332E-01	1.0045	23.6745	3	492.13	A
9.9985E-01	1.0047	39.8843	3	659.98	AD
9.5588E-01	1.0058	32.3670	3	771.00	D
9.0638E-01	1.0060	18.9615	3	915.92	D

Pressure	Saturation Pressure	Adsorbed Volume	Equilibration Time	Analysis Time	Flag
(atm)	(atm)	(cc / g)	(min)	(min)	
8.5564E-01	1.0059	11.2880	3	995.43	D
8.0468E-01	1.0048	8.3065	3	1031.35	D
7.5127E-01	1.0037	6.8568	3	1052.25	D
7.0274E-01	1.0038	6.0748	3	1067.60	D
6.5242E-01	1.0039	5.4814	3	1080.47	D
6.0074E-01	1.0040	5.0478	3	1090.00	D
5.4773E-01	1.0036	4.6567	3	1101.68	D
4.9956E-01	1.0034	4.3527	3	1108.32	D
4.5215E-01	1.0039	4.0701	3	1115.10	D
4.0205E-01	1.0030	3.7761	3	1121.73	D
3.5147E-01	1.0029	3.4745	3	1128.32	D
3.0119E-01	1.0032	3.2207	3	1135.18	D
2.4983E-01	1.0030	3.0010	3	1140.65	D
1.9903E-01	1.0013	2.7992	3	1146.07	D
1.5034E-01	1.0012	2.6360	3	1150.87	D
9.9763E-02	1.0009	2.4664	3	1155.38	D
4.9977E-02	1.0015	2.3059	3	1162.83	D

C.2.3. Aged CB1(1) Data

Table C.18. Trial Analysis Data of Aged CB1(3) Catalyst

Report for Station	1
Sample ID	Aged CB1(1)
Sample Weight	0.0991 g
P/Po Tolerance	0
Gas Type	Nitrogen
Cross-Sectional Area	16.2 Å²
Molecular Weight	28.0134 g/mole
Non-Ideality Correction Factor	6.58E-05 /torr
Ambient Temperature	291.876 K
Analysis Temperature	77.347 K
Outgass Temperature	200°C
Outgass Time	13 hr

Table C.19. Run 1 Isotherm Data of Aged CB1(1) Catalyst

Pressure (atm)	Saturation Pressure (atm)	Adsorbed Volume (cc / g)	Equilibration Time (min)	Analysis Time (min)	Flag
4.7136E-03	1.0030	0.2442	5	61.77	A
6.0994E-03	1.0036	0.2602	5	68.35	A
7.8383E-03	1.0033	0.2765	5	74.72	A
1.2689E-02	1.0033	0.3026	4	80.17	A
1.5870E-02	1.0030	0.3218	4	84.32	A
1.8455E-02	1.0032	0.3315	4	89.30	A
2.2341E-02	1.0032	0.3460	3	93.25	A
2.7317E-02	1.0034	0.3648	3	97.18	A
3.3745E-02	1.0034	0.3867	3	101.12	A
4.1804E-02	1.0034	0.4123	3	104.18	A
5.1843E-02	1.0034	0.4410	3	107.45	A M
5.3292E-02	1.0035	0.4407	3	108.97	A
6.6310E-02	1.0032	0.4691	3	113.43	A
7.7077E-02	1.0033	0.4930	3	117.40	A M
8.2083E-02	1.0036	0.5030	3	121.38	A
1.0318E-01	1.0035	0.5441	3	126.03	A M
1.2821E-01	1.0034	0.5882	3	130.70	A M
1.5335E-01	1.0031	0.6278	3	135.65	A M
1.7847E-01	1.0030	0.6634	3	139.82	A M
2.0349E-01	1.0030	0.6962	3	144.80	A M
2.2701E-01	1.0031	0.7293	3	149.00	A M
2.5313E-01	1.0031	0.7664	3	154.42	A M
2.7867E-01	1.0027	0.8017	3	159.45	A M
3.0202E-01	1.0028	0.8341	3	163.78	A M
4.0344E-01	1.0026	0.9835	3	169.52	A
5.0332E-01	1.0025	1.1477	3	174.58	A
6.0122E-01	1.0028	1.3657	3	183.35	A
7.0215E-01	1.0026	1.6637	3	191.48	A
8.0087E-01	1.0022	2.1463	3	202.47	A
9.0152E-01	1.0021	3.5458	3	232.10	A
9.9765E-01	1.0022	4.3940	3	437.92	AD
9.0124E-01	1.0031	5.2118	3	565.00	D
8.0154E-01	1.0032	2.3700	3	594.85	D
7.0122E-01	1.0028	1.8026	3	605.73	D
5.9699E-01	1.0025	1.4340	3	616.10	D
5.0010E-01	1.0029	1.1834	3	622.43	D

Pressure	Saturation Pressure	Adsorbed Volume	Equilibration Time	Analysis Time	Flag
(atm)	(atm)	(cc / g)	(min)	(min)	
4.0063E-01	1.0029	0.9794	3	627.90	D
2.9930E-01	1.0029	0.8303	3	633.25	D
1.9878E-01	1.0029	0.6900	3	638.50	D
9.8790E-02	1.0027	0.5355	3	643.55	D

Table C.20. Run 2 Isotherm Data of Aged CB1(1) Catalyst

Pressure	Saturation Pressure	Adsorbed Volume	Equilibration Time	Analysis Time	Flag
(atm)	(atm)	(cc / g)	(min)	(min)	
3.1796E-03	1.0117	0.2195	5	71.93	A R
3.8504E-03	1.0115	0.2297	5	77.92	A R
4.8527E-03	1.0107	0.2427	5	83.57	A R
6.1884E-03	1.0107	0.2570	5	90.58	A R
7.9387E-03	1.0104	0.2724	5	95.52	A R
1.2748E-02	1.0096	0.2990	4	102.02	A L R
1.5968E-02	1.0093	0.3170	4	106.40	A L R
1.8586E-02	1.0096	0.3255	4	107.93	A L R
2.2308E-02	1.0093	0.3402	3	111.72	A L R
2.7533E-02	1.0093	0.3584	3	115.65	A L R
3.3954E-02	1.0090	0.3783	3	119.60	A L
4.2121E-02	1.0087	0.4016	3	122.03	A L
5.2192E-02	1.0081	0.4277	3	125.98	A M L
6.6226E-02	1.0080	0.4611	3	130.95	A L
7.7399E-02	1.0076	0.4847	3	134.03	A M L
1.0362E-01	1.0079	0.5335	3	138.97	A M T L
1.2885E-01	1.0075	0.5725	3	143.92	A M T
1.5337E-01	1.0074	0.6142	3	148.90	A M T
1.7912E-01	1.0072	0.6491	3	152.67	A M T
2.0432E-01	1.0070	0.6795	3	156.23	A M T
2.2791E-01	1.0070	0.7099	3	159.02	A M T
2.5471E-01	1.0068	0.7399	3	163.13	A M T
2.7689E-01	1.0061	0.7826	3	169.43	A M T
3.0462E-01	1.0069	0.8164	3	172.85	A M T P
3.5485E-01	1.0064	0.8814	3	176.52	A T P
4.0481E-01	1.0063	0.9466	3	180.52	A T P
4.5499E-01	1.0064	1.0177	3	184.87	A T P

Pressure (atm)	Saturation Pressure (atm)	Adsorbed Volume (cc / g)	Equilibration Time (min)	Analysis Time (min)	Flag
5.0365E-01	1.0062	1.1158	3	190.77	A T P
5.5506E-01	1.0061	1.2048	3	195.82	A P
6.0489E-01	1.0058	1.3032	3	201.38	A P
6.5737E-01	1.0054	1.4689	3	210.35	A P
7.0428E-01	1.0054	1.6178	3	217.52	A P
7.5340E-01	1.0050	1.8059	3	224.95	A P
8.0396E-01	1.0051	2.0493	3	233.68	A P
8.5420E-01	1.0050	2.5031	3	246.95	A P
9.0338E-01	1.0048	3.3028	3	268.25	A P
9.5178E-01	1.0029	7.4753	3	363.58	A P
9.9701E-01	1.0026	15.5760	3	499.15	A D P
9.5120E-01	1.0024	10.6620	3	592.12	D P
9.0302E-01	1.0033	5.1105	3	691.50	D P
8.5347E-01	1.0038	2.9834	3	725.00	D P
8.0284E-01	1.0043	2.3564	3	741.57	D P
7.5042E-01	1.0042	2.0206	3	752.55	D P
7.0306E-01	1.0043	1.7812	3	760.98	D P
6.5336E-01	1.0043	1.5837	3	768.30	D P
6.0191E-01	1.0047	1.4186	3	774.72	D P
5.5260E-01	1.0042	1.2943	3	780.25	D P
5.0207E-01	1.0043	1.1715	3	785.35	D P
4.5149E-01	1.0041	1.0545	3	790.40	D P
4.0044E-01	1.0039	0.9464	3	795.22	D P
3.4983E-01	1.0042	0.8749	3	800.00	D P
2.9928E-01	1.0044	0.8099	3	803.55	D P
2.4897E-01	1.0042	0.7335	3	808.37	D
1.9892E-01	1.0042	0.6730	3	813.07	D
1.4879E-01	1.0042	0.6064	3	817.63	D
9.8842E-02	1.0036	0.5246	3	822.15	D
4.8820E-02	1.0037	0.4190	3	829.37	D

APPENDIX D

XPS DATA AND CALCULATIONS

The atomic concentration of metals was obtained using either using survey or high resolution spectra. The concentrations reported in the chapter 5 were determined from selectively chosen peaks and automatically calculated by the XPS software from the survey spectra. The atomic concentrations from high resolution spectra were calculated for the comparative purposes using both the area under peaks and the height of peaks in arbitrary units. The atomic concentration was calculated by:

$$C_x \quad = \quad n_x / \sum n_i \quad = \quad (I_x / S_x) / \sum (I_x / S_x) \qquad D.1$$

where C_x is the atomic concentration, I_x is the area or height of the peak, and S_x is the atomic sensitivity factor obtained from the PHI Chemical States Handbook of Physical Electronics Devision - The Perkin-Elmer Corporation.

The atomic sensitivity factors are not universal but depend upon the specific spectrometer. The atomic concentration, C_x, are valid to within the range of 10 to 20 %.

Table D.1. Atomic Concentration from the Survey Spectra Using Peaks Area

	Fresh Catalyst	Reduced at 175°C	Reduced at 225°C	Reduced at 275°C	Aged Catalyst
CB1(1) at 30°					
K 2p3/2	0.0	0.5	0.7	0.4	1.1
Cu 2p1/2	3.1	7.9	7.8	7.5	13.2
Co 2p1/2	1.2	2.5	1.7	2.0	1.8
Cr 2p3/2	2.0	3.4	3.5	3.4	3.0
C 1s	34.3	27.8	27.5	27.0	14.4
O 1s	59.3	57.8	58.9	59.7	66.5
CB1(1) at 60°					
K 2p3/2	0.8	0.2	0.9	0.4	1.3
Cu 2p1/2	6.8	7.6	7.9	9.3	12.4
Co 2p1/2	2.2	2.1	1.3	2.1	2.9
Cr 2p3/2	4.3	3.6	3.5	3.8	2.6
C 1s	14.7	25.2	27.4	22.8	17.9
O 1s	71.2	61.3	59.0	61.6	63.0
CB1(3) at 30°					
K 2p3/2	0.8	0.5	0.0	0.0	
Cu 2p1/2	6.1	7.6	2.9	7.3	
Co 2p1/2	1.5	1.8	3.2	2.0	
Cr 2p3/2	3.9	3.7	1.4	3.7	
C 1s	20.3	25.8	46.5	22.9	
O 1s	67.4	60.6	46.1	64.1	
CB1(3) at 60°					
K 2p3/2	1.5	0.2	0.3	0.0	
Cu 2p1/2	5.8	6.9	7.4	8.3	
Co 2p1/2	2.6	1.6	1.9	1.3	
Cr 2p3/2	4.3	3.7	3.9	3.6	
C 1s	18.3	27.9	26.8	20.6	
O 1s	67.6	59.8	59.8	66.3	

Table D.2. Atomic Concentration from the High Resolution Spectra Using Peak Height

	CB(1) at 30°			CB(1) at 60°			CB(3) at 30°			CB(3) at 60°		
	Height	I_x / S_x	%	Height	I_x / S_x	%	Height	I_x / S_x	%	Height	I_x / S_x	%
Cu 2p3/2	$S_x =$	3.55										
Fresh Catalyst	925	261	3.10	1558	439	5.62	1346	379	4.55	1485	419	5.08
Reduced at 175°C	2090	589	7.44	1914	540	7.38	1936	546	6.90	1901	536	6.80
Reduced at 225°C	2164	610	8.18	2204	621	8.07	1113	314	3.46	1967	555	6.69
Reduced at 275°C	1967	555	7.22	1658	468	6.17	1486	419	6.47	1612	454	5.81
age	2966	836	12.37	3543	999	13.25						
Cr 2p3/2	$S_x =$	1.58										
Fresh Catalyst	1033	652	7.76	1414	893	11.42	1475	932	11.18	1508	953	11.57
Reduced at 175°C	1178	744	9.39	1252	791	10.81	1396	882	11.16	1209	764	9.69
Reduced at 225°C	1236	781	10.47	1252	791	10.28	772	488	5.38	1441	910	10.98
Reduced at 275°C	1198	757	9.85	1346	851	11.22	1191	752	11.61	1340	847	10.83
age	1042	658	9.74	1283	811	10.75						
K 2p3/2	$S_x =$	0.98										
Fresh Catalyst	110	113	1.34	147	150	1.91	131	133	1.60	135	137	1.67
Reduced at 175°C	143	146	1.84	106	108	1.47	139	141	1.79	168	171	2.17
Reduced at 225°C	111	113	1.51	136	138	1.79	95	96	1.06	121	123	1.48
Reduced at 275°C	112	114	1.49	120	122	1.61	82	84	1.29	51	52	0.67
Aged Catalyst	341	347	5.14	275	280	3.72						
Co 2p1/2	$S_x =$	1.21										
Fresh Catalyst	349	289	3.43	644	533	6.81	517	427	5.13	495	409	4.97
Reduced at 175°C	430	356	4.50	649	537	7.34	462	382	4.83	405	335	4.25
Reduced at 225°C	414	342	4.59	506	419	5.44	238	197	2.17	450	372	4.49
Reduced at 275°C	502	415	5.41	458	379	5.00	436	360	5.56	503	416	5.32
Aged Catalyst	395	326	4.83	563	465	6.17						
O 1s	$S_x =$	0.71										
Fresh Catalyst	2351	3307	39.33	3222	4531	57.95	3262	4588	55.05	3502	4925	59.82
Reduced at 175°C	2664	3746	47.31	2508	3528	48.22	2727	3835	48.53	2799	3937	49.97
Reduced at 225°C	2460	3460	46.38	2509	3529	45.87	1972	2773	30.57	2885	4058	48.94
Reduced at 275°C	2655	3734	48.59	2755	3874	51.12	2287	3217	49.65	2846	4003	51.20
Aged Catalyst	2461	3461	51.21	2699	3796	50.35						
C 1s	$S_x =$	0.30										
Fresh Catalyst	1121	3786	45.03	377	1273	16.28	555	1873	22.48	412	1391	16.89
Reduced at 175°C	692	2338	29.52	536	1812	24.78	627	2118	26.79	632	2136	27.12
Reduced at 225°C	638	2154	28.88	650	2196	28.54	1540	5202	57.36	673	2274	27.43
Reduced at 275°C	624	2109	27.45	558	1885	24.88	488	1648	25.43	606	2046	26.17
Aged Catalyst	334	1129	16.70	352	1188	15.75						